TU Delft

Delft University of Technology

Electron beam technology for single nanometer fabrication

Scotuzzi, Marijke

DOI
10.4233/uuid:11a7a961-9f25-46f5-bf07-dc5765afcd59

Publication date
2019

Document Version
Final published version

Citation (APA)
Scotuzzi, M. (2019). *Electron beam technology for single nanometer fabrication*. [Dissertation (TU Delft), Delft University of Technology]. https://doi.org/10.4233/uuid:11a7a961-9f25-46f5-bf07-dc5765afcd59

Important note
To cite this publication, please use the final published version (if applicable).
Please check the document version above.

Copyright
Other than for strictly personal use, it is not permitted to download, forward or distribute the text or part of it, without the consent of the author(s) and/or copyright holder(s), unless the work is under an open content license such as Creative Commons.

Takedown policy
Please contact us and provide details if you believe this document breaches copyrights.
We will remove access to the work immediately and investigate your claim.

This work is downloaded from Delft University of Technology.
For technical reasons the number of authors shown on this cover page is limited to a maximum of 10.

Electron Beam Technology for Single Nanometer Fabrication

Electron Beam Technology for Single Nanometer Fabrication

Proefschrift

ter verkrijging van de graad van doctor
aan de Technische Universiteit Delft,
op gezag van de Rector Magnificus Prof. dr. ir. T.H.J.J. van der Hagen,
voorzitter van het College voor Promoties,
in het openbaar te verdedigen op maandag 9 September 2019 om 10:00 uur

door

Marijke SCOTUZZI

Master of Science in Electronic Engineering,
Università degli Studi di Brescia, Italy,
geboren te Brescia, Italie.

Dit proefschrift is goedgekeurd door de promotoren.

Samenstelling promotiecommissie bestaat uit:

Rector Magnificus,	voorzitter
Prof. dr. ir. P. Kruit,	Technische Universiteit Delft, promotor
Dr. C.W. Hagen,	Technische Universiteit Delft, promotor
Onafhankelijke leden:	
Prof. dr. M. Huth,	Goethe-Universität, Frankfurt am Main, Duitsland
Prof. dr. ir. J.P.H. Benschop,	Universiteit Twente
	ASML B.V.
Prof. dr. P. G. Steeneken,	Technische Universiteit Delft
Prof. dr. G.Q. Zhang,	Technische Universiteit Delft
Dr. A. Mohammadi-Gheidari,	Technische Universiteit Delft
	Thermo Fisher Scientific

This research is supported by the European project *Single Nanometer Manufacturing for beyond CMOS devices* (grant agreement No 318804 (SNM))

Printed by: ProefschriftMaken

Front & Back: Simona Bonafini Illustrations.

Copyright © 2019 by M. Scotuzzi

ISBN 978-94-6380-454-7

An electronic version of this dissertation is available at
http://repository.tudelft.nl/.

[...] Così tra questa
Immensità s'annega il pensier mio:
E il naufragar m'è dolce in questo mare.

Giacomo Leopardi

Contents

Summary xi

Samenvatting xvii

1 Introduction to Single Nanometer Manufacturing 1

2 Charged Particle Single-Digit Nanometer Manufacturing using Electron Beam Induced Deposition 7

2.1 Electron Beam Induced Deposition . . . 7
2.2 Fabrication of a Coulomb blockade device by Electron Beam Induced Deposition . . . 11
2.2.1 Fabrication of the single electron transistor by EBID . . . 13
2.2.2 Electrical characterization . . . 17
2.2.3 Conclusions . . . 19
2.3 Metrology of sub-20 nm nanostructures . . . 21
2.3.1 The TUD instrumentation . . . 21
2.3.2 The benchmark sample . . . 22
2.3.3 Analysis of the SEM images . . . 25
2.3.4 Analysis of the AFM measurements . . . 30
2.3.5 Measurement results . . . 35
2.3.6 TEM benchmark . . . 37
2.3.7 Conclusions . . . 43

3 Pattern transfer using etching masks made by EBID 45

3.1 Introduction . . . 45
3.2 Pattern transfer into silicon . . . 47
3.2.1 Experiments . . . 48
3.2.2 Results and discussion . . . 54
3.2.3 Summary and Conclusion . . . 60
3.2.4 Remarks on the line width measurement . . . 62
3.3 Pattern transfer into ITO . . . 63
3.3.1 Plasma etching of ITO using photoresist mask . . . 63
3.3.2 Pattern transfer into ITO using etch masks made by EBID . 67

3.4 Pattern transfer into TiN. 73
3.5 Conclusions 77
3.6 Pattern transfer into thin membranes. 78
3.6.1 EDX analysis on the EBID structures 82
3.6.2 Results and discussion 83
3.7 Conclusions 86

4 EBID stamps for Nano Imprint Lithography 89
4.1 Introduction 89
4.2 State of the art of nano imprint lithography 91
4.3 Definition of the experiment. 96
4.3.1 Design of the process flow for the fabrication of NIL stamps 96
4.3.2 Experimental methods 97
4.4 NIL using a replica of an EBID master - TiN on Pyrex 101
4.4.1 Fabrication of the EBID master 103
4.4.2 Results. 105
4.4.3 Discussion 111
4.5 NIL using an EBID master - Cr on Glass 112
4.5.1 Fabrication of the NIL stamp by EBID 114
4.5.2 Results. 116
4.5.3 Discussion 120
4.6 NIL using an EBID master - Mo on Glass 122
4.6.1 Fabrication of the second NIL stamp by EBID 124
4.6.2 Results. 126
4.6.3 Discussion 129
4.7 Conclusions 131

5 Multi Beam Scanning Electron Microscopes 133
5.1 The 196 MBSEM 133
5.2 Electronics control 137
5.3 Multi Beam EBID. 141
5.4 Conclusions 146

6 Design of a Multi Beam Splitting and Blanking Unit 149
6.1 Introduction 149
6.2 Requirements for a Multi Beam Unit 151
6.3 First order optics 155
6.3.1 On-axis aberrations. 156

6.4 Considerations on Coulomb Interactions . . . 158
6.5 Analysis of the three options . . . 164
6.5.1 Can we increase the number of beams even further? . . . 166
6.5.2 Final considerations and conclusions . . . 168
6.6 Optimization of the MBU final design . . . 170
6.6.1 Optimization and fine tuning of the parameters . . . 171
6.6.2 On-axis performance . . . 174
6.7 Final geometry . . . 178
6.7.1 Off-axis performance . . . 179
6.8 Simulations with EOD . . . 183
6.9 Field Curvature . . . 185
6.10 Coulomb interactions . . . 190
6.11 Blanker design . . . 195
6.11.1 Simulation of the blanker in COMSOL . . . 200
6.11.2 Analysis of the crosstalk . . . 206
6.12 Summary and conclusions . . . 211

7 Mechanical design and fabrication process of the Multi Beam Unit 215
7.1 Introduction . . . 215
7.2 Requirements on the mechanical design . . . 218
7.3 Mechanical design . . . 223
7.4 Fabrication of the beam splitting unit . . . 229
7.5 Fabrication of the blanker array . . . 231
7.6 Assembly of the stack of electrodes . . . 235
7.7 Summary and conclusions . . . 238

8 Multi Beam Unit - Experimental results 239
8.1 Introduction . . . 239
8.2 Experimental setup . . . 241
8.3 Initial results . . . 244
8.4 Multi beam EBID . . . 249
8.5 The blanker array . . . 250
8.5.1 Voltage test on the blanker electrodes . . . 254
8.6 Conclusions . . . 257

9 Conclusions 261

References 267

Curriculum Vitæ 285

List of Publications 287

Acknowledgements 289

Summary

To follow Moore's law and the trend of devices to keep shrinking, the nanotechnology industry is challenged in finding a suitable technique for the mass production of integrated circuits with critical dimension in the sub-10 nm range. At the time this project started, EUV lithography, that employs light with a wavelength of 13.5 nm and thus requires the scanner to be kept under vacuum, was encountering difficulties in making its way into high volume manufacturing. Therefore different technologies were being explored as alternative to EUVL. The European project Single Nanometer Manufacturing for beyond CMOS devices (SNM) [1] aims at developing a manufacturing platform that routinely provides sub-10 nm resolution. To achieve that, fabrication processes based on Nano Imprint Lithography (NIL) are investigated. NIL is a low cost, high resolution and high throughput patterning technique, suitable for the mass production of devices. In NIL, a UV-transparent stamp is pressed on top of a substrate covered with polymer, called the NIL resist. The features on the stamp are imprinted in this polymer, that hardens under the exposure of UV light. The features on the polymer are then transferred into the underlying substrate using etching processes. To fabricate these stamps, we propose to use electron beam induced deposition (EBID).

EBID is a high resolution and direct write technique that allows the patterning of structures in the sub-10 nm range. In EBID, an electron beam is scanned over a sample surface inside a vacuum chamber, which can be that of a scanning electron microscope (SEM). In the presence of a gas, the electron beam interacts with the precursor molecules, which dissociate into a volatile part, that is pumped out of the system and a non-volatile part, that sticks to the sample surface. EBID is capable of writing structures smaller than 3 nm FWHM in a scanning electron microscope. Moreover, unlike commonly used lithographic techniques, such as Electron Beam Lithography (EBL) and photolithography, EBID does not require any resist. This implies that process steps such as resist coating, development and lift-off are not required. However, EBID suffers from two main disadvantages, that limit its possible large scale applications. First, EBID has limited speed. Commonly, one electron beam has to scan the field of

interest spot by spot, or pixel by pixel, to locally deposit the material and form the desired structures. The throughput can be increased by employing many electron beams in parallel. This can be achieved in a multi-beam SEM (MB-SEM), where within one column multiple beamlets are generated and focused at the sample. The second limitation of EBID is related to the low conductivity of the deposits obtained. In the EBID community, many studies are carried out not only in investigating post deposition treatments, such as annealing, but also new gas precursors, where the carbon content, which is the main responsible for the high resistivity, is as little as possible.

EBID reveals to be a valid attractive lithographic technique for the fabrication of single electron transistors. These devices consist of Pt/C nanowire and nanodots transistors, integrated within Si nanodevices.

As an example of the attractiveness of EBID as a device fabrication technique a single electron transistor was made. This device consists of two Pt/C nanowires and a Pt/C nanodot in between, all integrated in a chip with predefined Si contact electrodes. The nanodot was as small as 20 nm and the device showed single-electron current oscillations and 'Coulomb diamond' electrical characteristics at room temperature. The fabrication of such small devices brings into the spotlight the challenges in metrology, to determine the size of features in the device. Typically, features are imaged using scanning electron microscopes with either secondary electron or backscattered electron imaging. Lines of rectangular cross section, with an enhanced secondary electron yield at the edges, have bright edges in SEM images and reproducible methods can be found to define the width of these lines. However, when lines have Gaussian shaped cross sections, such as EBID lines, it is less clear what criteria to apply to define the line width. A method that makes use of the inflection point in electron image intensity profiles is used to estimate line widths of Gaussian lines. Furthermore, a benchmark action is reported, in which metrology instrumentation, mainly SEMs and AFMs, available among the partners of the SNM project, are compared to a reference measurement. The analysis of the benchmark sample measured by AFM results in values that are larger compared to the reference value, most likely due to the critical dependence on probe shape correction. Values obtained by electron microscopy lie very close to the reference value.

One of the objectives of this thesis is to develop a process for the fabrication

of devices using Nano Imprint Lithography (NIL). In this work, we present an alternative way to fabricate NIL stamps making use of EBID. The main advantage of employing EBID instead of EBL is that coating the wafer with resist and undergoing post-exposure steps, such as development and lift-off, are avoided. However, when patterning EBID structures in the sub-10 nm range, the aspect ratio that can be achieved is typically very small. A way to increase the height of these structures is to transfer them into an underlying layer using an etching process. Pattern transfer of EBID lines of 7.4 nm width into silicon is achieved using chlorine and fluorine chemistries, resulting in slightly broader lines of 14.3 nm. However, NIL stamps must be UV transparent and we need to use glass substrates. ITO is a transparent and conductive material that can be deposited on top of glass wafers. While the transfer of EBID structures into ITO is possible with BCl_3 chemistry, the roughness of ITO is not compatible with the dimensions of the structures that we want to deposit. TiN is a compound that can be deposited by ALD and thus results in atomically flat surfaces. Studies on the selectivity of TiN towards silicon oxide and vice versa demonstrate that this is a more promising approach for the fabrication of NIL stamps by EBID.

Essentially, there are two ways to fabricate NIL stamps. The structures can be patterned on a silicon wafer, called the master. Later, these features are imprinted on a transparent substrate, called the replica. The replica is then used in the large scale NIL process. In this case, the features patterned on the NIL master are positively imprinted on the final wafer. Otherwise, structures can be directly patterned on the NIL stamp, that is then used in large scale NIL and imprinted onto the wafers. When using a replica, we observed some damaged lines on the imprinted wafers that we suspect to originate from the NIL stamp. While the width of the lines dramatically decreases from the EBID master to the last (ninth) imprinted sample, the height tends to remain constant. Fabricating NIL stamps directly with EBID requires the glass template used as stamp to be coated with a UV-transparent and conductive layer. First the glass template was covered with a 10 nm layer of chromium, that has a transmittance higher than 38%. While the line width is in general maintained, the height of the structures on the ninth imprint is always smaller than that on the EBID stamp. Because during the EBID deposition some charging effects were noticed and could have a negative impact, a second NIL template was coated with molybdenum. With more precautions, lines as small as 8 nm could be deposited. Also in this case we observed that the line width is in general maintained, while the height reduced considerably. In general, it is not trivial to image such small structures

on the imprinted wafers because of the presence of the polymer, which charges heavily under the electron beam. Because of that, the smallest structures could not be found on the imprinted substrates.

While EBID was demonstrated to be a suitable technique for patterning devices in the sub-10 nm range and for fabricating NIL stamps, attention was also directed to the problem of the low throughput. The speed of EBID can be increased in a multi beam scanning electron microscope (MBSEM). In Delft, a MBSEM that delivers 196 beams was recently developed. In this system, the beam splitter is placed in the source module of a commercially available SEM. To drive the voltages to the extra electrodes enclosed in the multi beam source module, a second Feg Gun Source control Unit (FGSU), controlled via a I^2C network, is added to the original one, which was operating in a Canbus network. To effectively control the two units, the two networks were integrated into one, controlled via a LabView program. The MBSEM is also used to demonstrate high throughput and large area patterning, where a 14 x 14 array of pillars as small as 57 nm was fabricated. The main limitation that was encountered here is the absence of an individual beam blanker. The 196 beams are switched on and off simultaneously and therefore different structures for different beamlets cannot be patterned.

A large part of this thesis is focused on the design and fabrication of a multi beam blanker array capable of turning a single beam SEM into a multi beam SEM. The multi beam unit (MBU) is designed to fit the variable aperture port of SEMs and consists of a beam splitter and a multi beam blanker array. The beam splitter consists of a multiple lens array (MLA), consisting of 5 μm apertures, that splits and focuses the beamlets at the blanker plate, which is placed 4 mm below the MLA. The MBU splits the single beam above the intermediate lens of an FEI Nova Nano Lab 650 SEM into 25 beamlets, each carrying 50 pA current, which are subsequently focused at the sample by the final lens. The total probe size, including the contributions from the on-axis and off-axis aberrations, is approximately 1.63 nm for a 5 kV acceleration voltage. Statistical Coulomb interaction calculations are shown not to deteriorate the performance of the system and are effectively negligible. A major challenge is the fabrication of the blanker array. It consists of an array of 2 μm apertures at a pitch of approximately 8.6 μm. Because of the limited space between the apertures, the fabrication of the blanking electrodes is not trivial. For this reason, a simplified blanker unit is designed. It consists of a macro-blanker, whose role is to de-

flect all the beamlets, and three micro-blankers, that can be activated one at a time to "un-blank" one beam. This simplified blanker unit serves as a proof-of-concept prototype. Simulations in COMSOL prove that when a voltage of ±50 V is applied to the macro-deflectors, a voltage of 25 V on the micro deflector is needed to "un-blank" the selected beamlet.

An alignment tool is designed to perform fine correction in X, Y and Z axis as well as rotation around X and Y, to position the MBU in the correct location inside the electron column. The MBU is mounted on a rigid support where flexible printed circuit cables carry the voltages for the macro-electrodes. The MBU is protected against unwanted collisions by a grounded shield. In parallel, the fabrication process of the MLA and the blanker unit led to separate chips that were stacked in a specially developed alignment tool based on a 6-degrees of freedom PI-hexapod system.

Finally, proof-of-concept experiments demonstrate that the MBU delivers an array of 5x5 beamlets focused at the sample. In such a configuration, an array of pillars is patterned by EBID, resulting in structures of 90 nm in diameter. Voltage test on the electrodes of the blanker unit have shown that no breakdown between neighboring blankers occurs. This unit can in the future be used to demonstrate the blanking of each beamlet and to determine the probe size of one beamlet at a time.

Samenvatting

Om de wet van Moore en de trend van steeds kleiner wordende componenten te kunnen blijven volgen, wordt de nanotechnologie-industrie uitgedaagd om een geschikte techniek te vinden voor de massaproductie van geïntegreerde schakelingen met een kritische afmeting in het sub-10 nm-bereik.
Toen dit projekt van start ging worstelde EUV-lithografie, waarbij gebruik wordt gemaakt van licht met een golflengte van 13,5 nm en waarbij de scanner onder vacuüm moet worden gehouden, met problemen bij het opschalen naar de productie van grote hoeveelheden. Daarom wordt er naar andere technologieën gekeken als alternatief voor EUVL. Het Europese project Single Nanometer Manufacturing for beyond CMOS devices (SNM) [2] richt zich op de ontwikkeling van een productieplatform dat routinematig sub-10 nm resolutie levert. Om dat te bereiken worden fabricageprocessen op basis van Nano Imprint Lithografie (NIL) onderzocht. NIL is een techniek die een lage kostprijs, hoge resolutie en hoge doorvoersnelheid bij het schrijven van patronen combineert, en is geschikt voor de massaproductie van componenten. Bij NIL wordt een UV-transparante stempel gedrukt op een substraat bedekt met een polymeer, de zogenaamde NIL-fotogevoelige laag. De elementen op de stempel worden in dit polymeer gedrukt, dat uithardt onder invloed van UV-licht. Vervolgens worden de elementen in het polymeer met behulp van etsprocessen overgebracht naar het onderliggende substraat.
Om deze stempels te vervaardigen, stellen we voor om elektronenstraal - geïnduceerde depositie (EBID) te gebruiken.

EBID is een directe schrijftechniek met hoge resolutie die het schrijven van patronen in het sub-10 nm bereik mogelijk maakt. Bij EBID wordt een elektronenstraal gerasterd over een monsteroppervlak in een vacuümkamer, bijvoorbeeld die van een raster elektronenmicroscoop (SEM).
Bij de aanwezigheid van een precursorgas vindt er interactie plaats tussen de elektronenbundel en de precursormoleculen, die dissociëren in een vluchtig deel, dat weggepompt wordt uit het systeem, en een niet-vluchtig deel, dat blijft kleven aan het monsteroppervlak. EBID is in staat om structuren met een volledige breedte op de helft van het maximum (FWHM) kleiner dan 3

nm in een raster elektronenmicroscoop te schrijven. In tegenstelling tot de gebruikelijke lithografische technieken zoals elektronenstraallithografie (EBL) en fotolithografie, heeft EBID bovendien geen fotogevoelige laag nodig. Dit betekent dat processtappen zoals het aanbrengen van een gevoelige laag, de ontwikkeling daarvan en lift-off niet nodig zijn. EBID heeft echter twee belangrijke nadelen, die de mogelijke grootschalige toepassingen ervan beperken. Ten eerste heeft EBID een beperkte snelheid. Gewoonlijk moet één elektronenstraal het relevante gebied punt voor punt, of pixel voor pixel, aftasten om het materiaal lokaal te deponeren en de gewenste structuren te vormen. De doorvoer kan worden verhoogd door veel elektronenbundels parallel te gebruiken. Dit kan worden bereikt in een multi-bundel SEM (MB-SEM), waarbij binnen een kolom meerdere bundels worden gegenereerd en gericht worden op het monster. De tweede beperking van EBID is gerelateerd aan de lage geleidbaarheid van de verkregen deposieten. In de EBID-gemeenschap worden veel studies uitgevoerd naar niet alleen post-depositiebehandelingen, zoals gloeien, maar ook naar nieuwe precursorgassen, waarbij het koolstofgehalte, hoofdverantwoordelijke voor de hoge weerstand, zo klein mogelijk is.

EBID blijkt een goed en aantrekkelijke lithografische techniek te zijn voor de fabricage van enkel-elektron transistoren. Deze componenten bestaan uit Pt/C nanodraad- en nanopunt-transistoren, geïntegreerd in Si nano - componenten.

Als voorbeeld van de aantrekkelijkheid van EBID als een fabricagetechniek voor componenten werd een enkel-elektron transistor gemaakt. Deze component bestaat uit twee Pt/C nanodraden en een Pt/C nanopunt ertussen, geïntegreerd in een chip met voorgedefinieerde Si-contactelektroden. De nanopunt was slechts 20 nm groot en de component vertoonde enkel-elektron stroomfluktuaties en 'Coulomb diamant' elektrische eigenschappen bij kamertemperatuur. De fabricage van dergelijke kleine componenten brengt de uitdagingen in de metrologie duidelijk naar voren, d.w.z. het bepalen van de grootte van de structuren in de component. Kenmerkend is dat de structuren worden afgebeeld met behulp van raster elektronenmicroscopen gebruikmakend van secundaire elektronen of terugverstrooide elektronen voor de beeldvorming. Lijnen van rechthoekige doorsnede, met een verhoogde secundaire elektronenopbrengst aan de randen, hebben heldere randen in SEM-beelden en reproduceerbare methoden kunnen worden gevonden om de breedte van deze lijnen te bepalen.

Wanneer lijnen echter Gaussisch gevormde doorsneden hebben, zoals EBID -lijnen, is het minder duidelijk welke criteria moeten worden toegepast om de lijnbreedte te bepalen. Een methode die gebruik maakt van het buigpunt in elektronenbeeld-intensiteitsprofielen wordt gebruikt om de lijnbreedte van Gaussische lijnen te schatten. Verder wordt er gerapporteerd over een kwantitatieve vergelijking, waarbij meetinstrumenten, voornamelijk SEM's en AFM's, die beschikbaar zijn bij de partners van het SNM-project, worden vergeleken aan de hand van een referentiestandaard.
De analyse van de referentiestandaard, gemeten met de AFM's, resulteert in waarden die groter zijn dan de referentiewaarde, wat waarschijnlijk het gevolg is van de uiterst gevoelige afhankelijkheid van de correctie voor de vorm van de aftaster. Waarden verkregen door elektronenmicroscopie liggen zeer dicht bij de referentiewaarde.

Één van de doelstellingen van dit proefschrift is het ontwikkelen van een proces voor de fabricage van NIL componenten. In dit werk presenteren we een alternatieve manier om NIL-stempels te maken met behulp van EBID. Het grote voordeel van het gebruik van EBID in plaats van EBL is dat het aanbrengen van een fotogevoelige laag op het substraat en het doorlopen van stappen na de belichting, zoals ontwikkeling en lift-off, worden vermeden. Echter, bij het schrijven van EBID-structuren in het sub-10 nm-bereik is de hoogte-breedteverhouding die kan worden bereikt meestal zeer klein. Een manier om de hoogte van deze structuren te vergroten is om ze over te brengen in een onderliggende laag met behulp van een etsproces. De overdracht van een patroon van EBID lijnen van 7,4 nm breedte in silicium wordt bereikt met behulp van chloor- en uorgebaseerde chemie, wat resulteert in iets bredere lijnen van 14,3 nm. Echter, NIL stempels moeten UV-transparant zijn en daarom moeten we glazen substraten gebruiken. ITO is een transparant en geleidend materiaal dat op glazen substraten kan worden aangebracht. Terwijl de overdracht van EBID structuren naar ITO mogelijk is met BCl3 chemie, is de ruwheid van ITO niet compatibel met de afmetingen van de structuren die we willen deponeren. TiN is een verbinding die middels ALD (atomaire laag depositie) kan worden gedeponeerd en resulteert in een vlak oppervlak, met atomaire precisie. Studies van de selectiviteit van TiN ten opzichte van siliciumoxide en vice versa tonen aan dat dit een veelbelovende aanpak is voor de fabricage van NIL-stempels met behulp van EBID.

In wezen zijn er twee manieren om NIL-stempels te vervaardigen. Ten eerste

kunnen de structuren op een silicium substraat, master genaamd, worden aangebracht. Later worden deze structuren op een transparant substraat, de replica genaamd, overgebracht. De replica wordt dan gebruikt in het NIL-proces op grote schaal. In dit geval worden de kenmerken van de NIL-master positief op het uiteindelijke substraat overgebracht. Ten tweede kunnen structuren direct op het NIL-stempel worden aangebracht, dat vervolgens voor grootschalige NIL wordt gebruikt en op de substraten wordt geprint. Bij het gebruik van een replica hebben we enkele beschadigde lijnen op de bedrukte substraten waargenomen waarvan we vermoeden dat ze afkomstig zijn van het NIL- stempel. Terwijl de breedte van de lijnen drastisch afneemt van de EBID-master naar het laatste (negende) bedrukte substraat, blijft de hoogte van de lijnen ongeveer constant. Voor het rechtstreeks vervaardigen van NIL-stempels met NIL is het nodig dat het als stempel gebruikte glazen sjabloon voorzien is van een UV-transparante en geleidende laag. Eerst werd het glazen sjabloon bedekt met een 10 nm dikke laag chroom, die voor meer dan 38% transparant is. Terwijl de lijnbreedte in het algemeen behouden blijft, is de hoogte van de structuren op de negende afdruk altijd kleiner dan die op het EBID-stempel. Omdat tijdens de EBID-depositie wat opladingseffecten werden waargenomen die een negatieve effekt zouden kunnen hebben, werd een tweede NIL-sjabloon met molybdeen gecoat. Met wat meer voorzorgsmaatregelen konden lijnen tot 8 nm worden gedeponeerd. Ook in dit geval zagen we dat de lijnbreedte over het algemeen behouden blijft, terwijl de hoogte van de lijnen aanzienlijk afnam. In het algemeen is het niet triviaal om zulke kleine structuren op de bedrukte substraten af te beelden vanwege de aanwezigheid van het polymeer, dat sterk oplaadt door de elektronenstraal. Hierdoor konden de kleinste structuren niet worden gevonden op de bedrukte substraten.

Naast dat aangetoond werd dat EBID een geschikte techniek is voor het aanbrengen van patronen voor componenten in het sub-10 nm bereik en voor het vervaardigen van NIL-stempels, werd er ook aandacht besteed aan het probleem van de lage doorvoersnelheid. De snelheid van EBID kan worden verhoogd in een multi-bundel raster elektronenmicroscoop (MBSEM). Er is onlangs in Delft een MBSEM ontwikkeld die resulteert in 196 bundels. In dit systeem wordt de bundelsplitser in de bronmodule van een in de handel verkrijgbare SEM geplaatst.
Om de voltages op de extra elektroden in de multi-bundel bronmodule aan te brengen, werd een tweede FEG bronbesturingseenheid (FGSU), aangestuurd via een I2C netwerk, toegevoegd aan de oorspronkelijke, die in een CANBUS

netwerk actief was. Om de twee eenheden effectief te kunnen besturen, werden de twee netwerken geïntegreerd in één netwerk, bestuurd via een LabView-programma. De MBSEM wordt ook gebruikt ter demonstratie van de hoge doorvoersnelheid en het aanbrengen van patronen op een groot oppervlak, waarbij een raster van 14 x 14 pilaartjes met een grootte tot 57 nm werd gefabriceerd. De belangrijkste beperking hier was de afwezigheid van een individuele bundelonderbreker. De 196 bundels worden gelijktijdig in- en uitgeschakeld en daarom kan niet elke bundel een andere structuur schrijven.

Een groot deel van dit proefschrift is gericht op het ontwerp en de fabricage van een matrix van bundelonderbrekers voor multi-bundel toepassingen, zodanig dat een SEM met een enkele bundel omgevormd kan worden in een SEM met meerdere bundels. De multi bundeleenheid (MBU) is zo ontworpen dat deze past in de poort waarin de variabele apertuur van een SEM gemonteerd is, en uit een bundelsplitser en een matrix van bundelonderbrekers bestaat. De bundelsplitser bestaat uit een matrix van micro lenzen (MLA), ieder met een opening van 5 µm diameter, die de bundels splitst en focust op de bundelonderbrekerplaat, die 4 mm onder de MLA is geplaatst. De MBU splitst de enkele bundel boven de intermediaire lens van een FEI Nova Nano Lab 650 SEM in 25 bundels, die elk 50 pA aan stroom bevatten, en vervolgens door de eindlens op het substraat worden gefocusseerd. De totale grootte van het focus, inclusief de bijdragen van de aberraties op en naast de optische as, is ongeveer 1,63 nm, wanneer een versnelspanning van 5 kV wordt gebruikt. Uit berekeningen van de statistische Coulomb interacties blijkt dat de prestaties van het systeem daardoor niet verslechteren, en deze kunnen aldus verwaarloosd worden. Een grote uitdaging is de fabricage van de matrix van bundelonderbrekers. Deze bestaat uit een matrix van openingen met een diameter van 2 μm op een steek van ongeveer 8,6 μm. Vanwege de beperkte ruimte tussen de openingen is de fabricage van de elektroden van de onderbreker verre van triviaal. Om deze reden is een meer eenvoudige onderbrekereenheid ontworpen. Deze bestaat uit een macro-onderbreker, die alle bundels tegelijk moet afbuigen, en drie micro-onderbrekers, die één voor één kunnen worden geactiveerd om het onderbreken van één bundel ongedaan te maken. Deze eenvoudige onderbrekereenheid dient als een prototype voor het aantonen van het concept. Simulaties in COMSOL bewijzen dat wanneer een spanning van ± 50 V op de macro-onderbrekers, of afbuigers, wordt gezet, een spanning van 25 V op de micro-afbuigers nodig is om de geselecteerde bundel door te laten.

Een speciale uitlijn inrichting is ontworpen om precieze correcties uit te voeren op de positie van de MBU in de elektronenkolom, met translaties in de X-, Y- en Z-as richting en rotaties rond de X- en Y-as. De MBU is gemonteerd op een stijve drager waarbij exibele printkabels de spanningen voor de macro-elektroden toevoeren. De MBU is beschermd tegen beschadiging door middel van een geaarde afscherming. Parallel hier aan werd het fabricageproces ontwikkeld van de matrix van micro lenzen (MLA) en de onderbrekereenheid als afzonderlijke chips, die gestapeld en uitgelijnd werden met behulp van een speciaal ontwikkeld uitlijngereedschap, gebaseerd op een PI-hexapod-systeem met 6 vrijheidsgraden.

Tot slot, experimenten die het concept aantonen hebben laten zien dat de MBU een reeks van 5x5 bundels oplevert die gefocusseerd zijn op het substraat. In een dergelijke konguratie is een reeks van pilaartjes geschreven met EBID, resulterend in structuren van 90 nm in diameter. Spanningstests op de elektroden van de onderbrekereenheid hebben aangetoond dat er geen doorslag tussen naburige onderbrekers optreedt. Deze eenheid kan in de toekomst worden gebruikt om het onderbreken van elke bundel aan te tonen en om de grootte van het focus van elke individuele bundel te bepalen.

1

Introduction to Single Nanometer Manufacturing

If I have seen further than others, it is by standing upon the shoulders of giants.

Isaac Newton

In 1965, Gordon Moore was asked by Electronics Magazine to predict the future of the semiconductor industry. Moore was, by that time, the owner of Fairchild Semiconductor company, founded by Moore himself. Years later, together with his general manager Robert Noyce, Moore left Fairchild Semiconductor to establish Intel corporation. What probably Moore did not expect back in 1965 was that the predictions that he made would become the drive for the evolution of processors. This prediction, known as Moore's law, says that the number of transistors on an integrated circuit doubles every year [2]. A few years later Moore's law was announced. The remarkable speech held by Richard Feynman titled "There's plenty of room at the bottom" marks the origin of the

Nanotechnology field [3]. In 1974, Robert Dennard and his team at IBM research wrote an article [4] describing the scaling rules for MOSFETs (Metal Oxide Semiconductor Field Effect Transistors), that include device dimension and power consumption [5]. Both Moore's law and Dennard's scaling represented the main drive in the semiconductor industry to keep pushing the resolution with which devices are patterned. While Dennard's scaling faces problems because of thermal noise that limits the scaling of the voltages used in devices, and because of the impossibility of increasing the clock speed further, Moore's law was adapted by predicting that the shrinking of transistor area lowers the cost of transistors by 30% per year [6]. We recently witnessed a third reformulation of Moore's law, also referred to as third era, where the scaling of devices is replaced by "scaling out" [7]. In this formulation, innovation in device fabrication is led by 3D integration, employment of new materials, memory on processors and more.

Nowadays, however, the main driver in the semiconductor industry still relies on the trend of device shrinking. New processes are developed, new patterning strategies are being employed in order to fabricate smaller and smaller devices. In this scenario, the most important player in the manufacturing of devices is lithography. Lithography is the step where devices are being "drawn" on the silicon wafer and it is the most critical step as it defines the minimum dimension with which features can be patterned. In the early 1960s, the first circuits boards were printed using shadow printing, which soon evolved into projection printing, introduced in the 1970s. In 1978, the world witnessed the first stepper, which utilized an automated wafer handling and alignment tool. From the 1980s, improvements in the exposure tools focused on reducing the wavelength of the light used during the exposure and employing bigger and bigger wafers, to both reduce the critical dimension of the features that could be printed and increase the throughput. The introduction of excimer laser sources with wavelength in the DUV (Deep Ultra Violet) range gave a sudden boost in the performance of scanner and stepper systems [8]. KrF sources that emit light with 248 nm wavelength were introduced in 1997 and were soon replaced in 2001 by ArF sources, that brought down the emission wavelength to 193 nm [9]. The resolution of DUV tools was further improved with the introduction of "wet" systems, or immersion lithography. While in dry systems the exposure is performed in air, in wet systems a medium, typically water, is led in between the projection lens and the wafer in order to increase the numerical aperture, and thus the resolution of the system [10]. Because new technologies,

like EUVL (Extreme Ultra Violet Lihography), delayed their entrance in mass production, tricks like self aligned double patterning helped in overcoming the limitation of lithographic tools in device shrinkage [11].

EUV lithography, developed by ASML, uses light with a wavelength of 13.5 nm. Because of such short wavelength, the scanner must work under vacuum, to prevent the light to be absorbed. EUV technology takes along drastic changes in the optical system of the exposure tool, which once comprised of lenses for DUV technology, is now replaced with mirrors [12]. The challenges in the development of such a sophisticated tool required more time than anticipated and, by the time this project started, this technology had not yet made its entrance in the high volume manufacturing industry. It was not yet clear how EUV technology will perform in mass production, and the battle with competing lithographic techniques still remained open.

As alternative to EUVL, Nano Imprint Lithography (NIL) emerges as a low cost, high resolution and high throughput patterning technique. In NIL, a stamp with nanostructures is pressed on top of a wafer coated with polymer, called NIL resist, which is cured under UV-light. In this step, the nanostructures on the stamp are imprinted, or duplicated, into the resist. The stamp is then removed from the wafer and the structures are then transferred into the underlying wafer by an anisotropic etching processes. Nano imprint lithography is not limited by wave diffraction, scattering or interference unlike conventional lithographic methods [13]. Reviews on nano imprint lithography can be found in literature [14] [15] [16] [17]. While NIL is demonstrated to be a suitable technique for the fabrication of features in the sub-20 nm range, the fabrication of NIL stamps requires high resolution patterning techniques. Typically, NIL stamps are made by electron beam lithography (EBL). EBL is a maskless lithographic technique where a beam scans the surface of a substrate covered with an electron-sensitive resist. The induced changes in the chemistry of the resist cause that, depending on the tone of the resist, the exposed area, or the non-exposed area, is being removed after the development of the resist. While the resolution in EBL depends on the chemical composition of the resist and how electrons are scattered within the resist layer, EBL is considered a suitable technique for patterning structures well below 10 nm [18]. However, with this technique several pre-patterning and post-exposure steps are required and involve the coating of the wafer with resist, development and lift-off of the resist.

This thesis investigates the opportunity of using Electron Beam Induced Deposition for the fabrication of NIL stamps as alternative to EBL. EBID is a high resolution and direct write technique, where, similarly to EBL, a beam is scanned over a sample surface. When a gas precursor is led into the chamber, which can be that of a scanning electron microscope (SEM), in the proximity of the beam, the electrons dissociate these complex molecules into a volatile part, that is pumped out of the system, and a non-volatile part, that sticks to the substrate forming the deposit. Literature offers a variety of review papers on focused electron beam induced processing and its future perspective [19] [20] [21] [22] [23] [24] [25] [26] [27]. When using the Pt precursor $MeCpPtMe_3$, EBID deposits have typically a low content of metal, that is surrounded by a "soup" of carbon. This means that the deposits have typically low conductance, which is one of the main limitations of EBID. The low quality of EBID deposits originates from the fact that the gas precursors typically come from other applications, such as Chemical Vapour Deposition (CVD), and they are not optimized for EBID. Another main disadvantage of EBID, like EBL, is the low throughput, which is determined by the inherently low speed of single-electron-beam systems. While in photolithography fields in the mm range can be exposed at once, in electron beam methods, the beam has to scan step by step, or pixel by pixel.

The low throughput is a bottleneck of electron beam systems, including scanning electron microscopes. To overcome this limitation, multiple beamlets can be used in one tool to speed up the performance. For lithography purposes, Mapper has developed a maskless lithography technology, based on parallel beam writing, where up to 65,000 beams could be focused at the sample surface [28] [29]. Recently, a pre-production tool was installed in CEA-Leti, targeting a throughput of 650,000 beams [30]. In the field of electron microscopes, Zeiss has launched a few years ago a high resolution and high throughput multi-beam SEM with up to 91 beamlets [31]. This system, which comprises secondary electron detection, is used to speed up the image acquisition in fields like biology research and in the semiconductor industry. In Delft, a multi-beam SEM (MBSEM) was developed using a commercially available FEI Nova Nano SEM 200 scanning electron microscope. The source module of this microscope was replaced with a multi-beam source module, where an aperture lens array split the electron beam emitted from a Schottky source into an array of 14 x 14 beams, delivering at the sample up to 196 beams. The imaging systems developed for this MBSEM are based on the detection of transmitted

electrons and secondary electrons [32]. The main limitation, for lithography purposes, of such an instrument is the absence of a blanker array that is capable of switching on and off each beam individually.

This thesis aims at developing a process based on electron beam technology for the fabrication of devices in the sub-10 nm range. The idea is to make use of Nano Imprint Lithography as a patterning method for high volume manufacturing and fabricate the stamps by electron beam induced deposition. EBID is suitable for the deposition of small structures. However, when patterning in the sub-10 nm range, the aspect ratio is very small and these structures are very thin. A possible way to overcome this limitation is to transfer these structures into an underlying layer. Moreover, MBSEMs can be used to pattern the EBID structures to overcome the limitation of the low throughput. The work presented in this thesis is part of the European project "Single Nanometer Manufacturing for beyond CMOS devices" (SNM) [1], which aims at achieving sub-10 nm resolution patterning using NIL as lithographic technique and stamps made by both Scanning Probe Microscopy (SPM) and EBID.

This thesis starts with analyzing EBID as a technique for high resolution patterning of functional electron devices. Chapter 2 deals with the fabrication of a single electron transistor consisting of a Pt/C nanowire and nanodots, integrated within Si nanodevices. To be able to fabricate such a device a wide range of parameters needs to be optimized and controlled. Following, the attention is focused on Metrology that plays an important role when determining the size of features, which can be non trivial. An activity aimed at comparing metrology tools with a reference measurement is presented here.

In chapter 3, the pattern transfer of EBID structures into underlying layers is demonstrated. The aim of this study is to improve the aspect ratio of the shallow EBID structures, keeping in mind that this step could be of use in the fabrication of NIL stamps. In fact, for this purpose, UV-transparent substrates are required and the pattern transfer must happen in layers that are not only transparent, but also conductive. Because of the difficulties encountered in determining the size of the etched features, a further investigation of the pattern transfer into thin membranes aims at achieving a more reliable measurement of the lateral dimensions by inspection in transmission electron microscopes.

The fabrication of NIL stamps is described in chapter 4. There are essentially two ways for fabricating NIL stamps. In a first approach, the structures can be patterned on a silicon wafer, called master. Later, these features are im-

printed on a transparent substrate, called replica. The replica is then used in the large scale NIL process. In a second approach, the structures are directly patterned on top of the NIL glass template using EBID. The fidelity in the imprinting of such structures in terms of line width and line height is studied.

The description of the features and capabilities of the Delft multi-beam SEM is presented in chapter 5. In this system, the beam splitter is placed in the source module of a commercially available SEM. The analysis of the control electronics is presented here and the improvements made in the integration of the control unit of the multi beam source unit are described. This chapter also deals with the experiments on large area and high throughput patterning using EBID in the Delft MBSEM.

A question that chapter 6 addresses is: how can an individual beam blanking array be integrated in the MBSEM? In the past, attempts in integrating a blanking array in the source module, below the multiple lens array failed. This happened because of the unfriendly conditions in the source module, including high vacuum level and high voltage. What if the multi beam splitting and blanking unit are re-designed? This chapter discusses the requirements that the new multi-beam system needs to meet and possible alternative designs. The evaluation of the performance of the possible alternatives is based on the analysis of the first order optics as well as on-axis aberrations. This chapter evolves then in the detailed discussion of the off-axis performance and stochastic Coulomb interactions. Lastly, the design of the blanker array is presented, followed by a simulation of its working principle.

The mechanical design and the fabrication process of the multi-beam splitting and blanking unit are addressed in chapter 7. The integration of the unit into a scanning electron microscope requires the development of a tool that is capable of placing and aligning the unit into the optical axis of the SEM column. The microfabrication processes for the fabrication of the multi aperture plate and the blanker array are presented.

Chapter 8 reports initial proof-of-concept experiments that demonstrate the splitting of the beam into multiple beamlets and how they can be focused at the sample surface. Then, the results of initial tests with a first prototype of a simplified design of the blanker array are described and the conclusions are reported in chapter 9.

2

Charged Particle Single-Digit Nanometer Manufacturing using Electron Beam Induced Deposition

A thinker sees his own actions as experiments and questions, as attempts to find out something. Success and failure are for him answers above all.

Friedrich Nietzsche

2.1 Electron Beam Induced Deposition

Single nanometer structures, i.e. structures with dimensions smaller than $10nm$, are not easy to fabricate. Standard lithography techniques, such as resist-based electron beam lithography, do not routinely provide $sub-10nm$ resolution.

Electron Beam Induced Deposition (EBID) is a high resolution direct write lithography technique, that is capable of writing single-digit nanometer patterns.

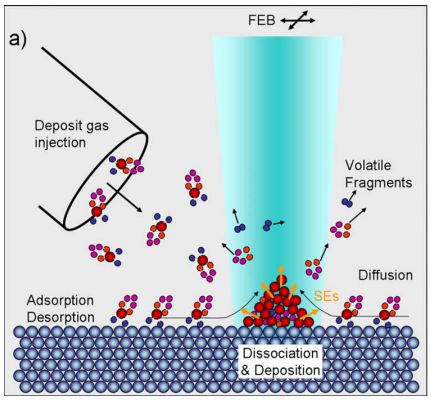

Figure 2.1: Schematics of the working principle of Electron Beam Induced Deposition [21]. A nozzle, from which the gas precursor is flown into the system, is positioned close to the sample surface. The gas molecules diffuse on the sample surface and are dissociated by the electron beam. The non volatile components stick to the sample surface, forming the deposit, while the non-volatile fragments are pumped out of the system.

As shown in figure 2.1, an electron beam is focused onto a sample in a vacuum chamber, which can be that of a Scanning Electron Microscope (SEM), and made to react with a precursor gas, let into the SEM through a nozzle positioned in proximity of the substrate. The gas molecules are dissociated into a volatile part, that is pumped out of the SEM, and a non-volatile part, that remains on the sample surface, forming a deposit. Typical precursors are $W(CO)_6$ and $MeCpPtMe_3$, that lead to tungsten and platinum deposits, respectively. However, a larger variety of materials is available, among which gold [33] [34], iron [35], cobalt [36], carbon and silicon dioxide [20].

EBID is a one-step high resolution patterning technique, that takes benefit from the capability of modern electron microscopes to focus the electron beam in a spot as small as a few tenth's of a nanometer. The high spatial resolution of EBID has been demonstrated by Van Dorp et al. [37], who patterned dots of $1nm$ diameter in a $200kV$ Scanning Transmission Electron Microscope (STEM), as shown in figure 2.2a. The dots were patterned using the $W(CO)_6$ precursor on a $30nm$ thick Si_3N_4 membrane [37], that was plasma-cleaned in an Ar/O_2 mixture to reduce the effect of hydrocarbon contamination. Using an SEM, van Oven et al. patterned $2.9nm$ FWHM lines on a silicon bulk substrate

using the $MeCpPtMe_3$ precursor [38]. The dense lines, that are shown in figure 2.2b, have a pitch of $6nm$ and were patterned in a multiple passes writing strategy not only to reduce the proximity effect, but also to enhance the precursor replenishment, allowed by a waiting time between passes.

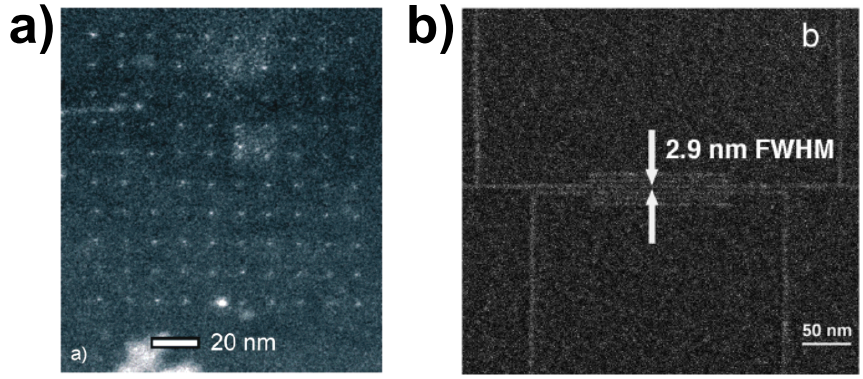

Figure 2.2: a) 10 x 10 array of dots with an avarage diameter of $1nm$ patterned in a $200kV$ STEM [37]. b) SEM micrograph of the dense lines with a pitch of $6nm$, where the smallest line has a width of $2.9nm$ FWHM [38].

The spatial resolution of EBID also depends on the dissociation cross-section of the precursor gas, that typically has a peak up to an energy range of a few 100's of eV [19] and partly overlapping the energy distribution of the secondary electrons (SE) that are generated in the substrate and emitted from its surface [39]. Also electrons that are generated in the deposited structure itself contribute to the dissociation process, and enhance the growth of the structure [40]. Also proximity effects play a role in the size of EBID patterns, as electrons scattered from neighboring structures also contribute in dissociating adsorbed precursor molecules [41] [42] [43]. Defining the correct writing strategy is therefore of extreme importance to achieve pattern sizes in the sub-10 nm range.

However, electron beam lithography techniques, such as EBID, are serial writing techniques and therefore inherently slow. To enhance the writing speed, multi-beam systems can be used. Post et al. [44] demonstrated that the throughput of EBID can be enhanced by a factor of 196, when using a **multi-beam scanning electron microscope** (MB-SEM) that delivers 14 x 14 beams to the sample surface, with the same characteristics as a state-of-the-art single beam

SEM [45] [46]. Figure 2.3 shows a single-beam SEM image of the 14 x 14 array of dots patterned with the multi-beam SEM at $15kV$, using a single 20s exposure.

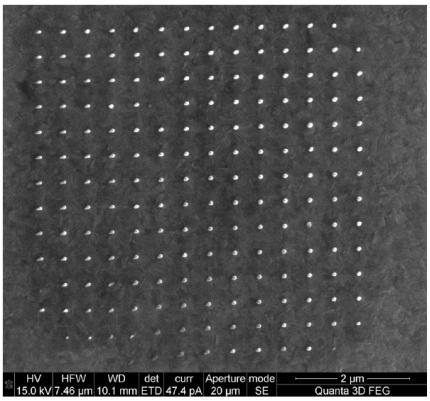

Figure 2.3: Single-beam SEM image of the 14 x 14 array of EBID dots patterned in the multi-beam SEM [46].

Another drawback of electron beam induced deposition is the purity of the patterned structures [47]. As most of the precursor gas consists of carbon, a large quantity of this element is found in the deposits along with the metal. Moreover, the presence of hydrocarbons in the SEM chamber, or on the sample surface itself, contributes in increasing the low purity of the deposits. Because EBID is often used for patterning conductive leads to nanostructures, it is desirable that the resistance of the deposits is very low. There is a variety of techniques used to purify EBID deposits and they differ depending on the precursor. Botman et al. have listed a number of possible techniques published in literature [48], where the common pathway for purity improvement is heating (before or after the deposition) and working in a favourable residual gas environment, achieved for instance by thoroughly plasma-clean the SEM chamber. The metal content of platinum and gold structures can be improved by post-deposition treatments in oxygen-rich atmosphere at both high temperature [49] and low temperature [50] [51] [52], or by exposing the structures with water [53]. Other purification techniques involve an irradation step with a laser beam [54] [55], or an e-beam post-irradiation step under oxygen flux [56]. Water-assisted deposition was recently proven to enhance the purity of gold structures [57]. Purification techniques have also been studied for tungsten [58], iron [59], ruthenium [60] and cobalt [61] precursors.

In this chapter, we present how electron beam induced deposition can be used for the fabrication of functional devices in the $10nm$ scale. In a world where dimensions are getting smaller and smaller, also metrology plays a cru-

cial role in not only determining the size of these objects, but most importantly in providing reliable measurement protocols. We then therefore focus on a metrology study aimed at comparing measurement methods and analysis methods within the SNM consortium. The aim of this study is to compare measurements of benchmark samples done in different laboratories with different measurement tools.

2.2 Fabrication of a Coulomb blockade device by Electron Beam Induced Deposition[‡]

Nowadays the CMOS technology is pushing for reduced device dimensions and new device structures to meet the increasing demands on improvements in speed, complexity and packing density of integrated circuits. When the dimension of structures reduces below the $10nm$ scale, where quantum effects start to play a role, challenging barriers are encountered in the physics and technology of devices. In this scenario, advanced lithographic techniques such as scanning probe lithography (SPL) [62] [63], electron beam lithography (EBL) [64] [65] and nano imprint lithography (NIL) [66] [67] have received increased attention in the fabrication of "beyond CMOS" sub-10 nm electronic devices.

Single electron transistors are types of sub-10 nm devices that have received an increased attention lately. Single electron transistors (SETs) consist of a source and a drain electrode, with a conducting island in between, and a nearby gate electrode. An electron that has tunneled from the source into the island might create a Coulomb repulsion, preventing other electrons to tunnel to the island, leading to an increase of the resistance of the device. In the presence of such a Coulomb blockade, the current-to-voltage characteristics, also known as I-V curve, of the device has a staircase-like shape, only for sufficiently unequal conductance of the drain/island and source/island. Wang et al. developed SETs by connecting the source and the drain electrodes with silicon nanowires with a width down to 30 nm [68]. The silicon nanowires were patterned on the silicon top layer of a silicon-on-insulator (SOI) wafer using electron beam lithography (EBL). The Si core of the nanowires was decreased in size down to $5nm$ by passivating the sample in a thermal oxidation step. I-V curves of such devices, that were measured at different temperatures, down to $8K$, show the Coulomb

[‡]This paragraph is published as:
Durrani, Z. A. K., Jones, M. E., Wang, C., Scotuzzi, M. and Hagen, C. W., Electron transport and room temperature single-electron charging in 10nm scale PtC nanostructures formed by electron beam induced deposition, *Nanotechnology 28 (2017) 474002*

blockade demonstrating the tunnelling of the electrons in the device. This particular fabrication process can be quite tedious, requiring many trials to end up with a small enough island.

Electron beam induced deposition (EBID) is emerging as a suitable high resolution lithographic technique for the fabrication of devices in the single-digit nanometer scale. The spatial resolution of EBID is determined by the probe size, and by the convolution of the energy dependent spatial distribution of incident electrons with both the electrons emitted from the substrate, and the energy dependent cross section for dissociation of precursor molecules at the substrate surface. The dissociation cross-section, which typically has a peak in the energy range at a few 100 eV, to some degree can overlap the energy distribution of the secondary electrons (SE) generated in the substrate and emitted from the surface. Electrons that are generated in the deposited structure itself also contribute to this dissociation process, and enhance the growth of the structure. Proximity effects resulting from electrons scattered during the exposure of neighbouring structures further contribute to dissociating adsorbed precursor molecules, thus affecting EBID pattern sizes. Hence, defining the correct writing strategy is of great importance to achieve pattern sizes in the sub-10 nm range.

EBID is demonstrated to be a valid technique for device fabrication, with applications ranging from electrical connections to nanowires and nanotubes [69] [70] [71] [72], to growth of nanowires [73] [74] [75] [76] [77] [78] [79] [80], fabrication of Pt tips for field emission electron sources [81] [82], field emission arrays [83] [84], nanopore nanomachining for molecule detection and DNA sequencing [85], patterned catalyst deposition [86] [87], and lithographic mask repair [88]. EBID is also used in the field of 3D nanoprinting [91] [92], nanomagnetism [89] [90], plasmonics [93] and photonics [94].

In this paragraph, we present the fabrication of single electron transistors (SET) by EBID using the Pt/C precursor, integrated in a silicon-on-insulator (SOI) chip. The SOI chips were pre-patterned with heavily doped n-type source and drain with a $\approx 100nm$ nanogap, where the EBID nanostructures forming the heart of the SET must be deposited. The geometry of a SET, shown in figure 2.4, consists of two nanowires patterned by EBID that extend from the pre-patterned source and drain electrodes and an EBID nanostructure, or the quantum dot, deposited in the gap formed between the two EBID leads. The

size of the gap between the electrodes and the EBID quantum dot should be smaller than 10 nm. This device is a good candidate for expressing single electron transistor behaviour at room temperature, but other devices consisting of nanowire-only Pt/C deposits, where the tunneling of electrons could occur in between the Pt grains, are also studied.

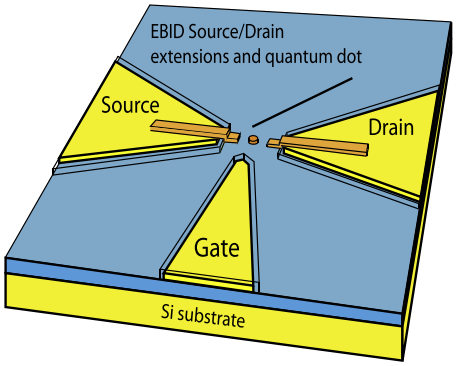

Figure 2.4: Schematic diagram of the device structure showing the silicon source, drain and gate electrodes together with the EBID Pt/C leads and nanodot structure.

2.2.1 Fabrication of the single electron transistor by EBID

The substrate where the SETs are to be fabricated is an SOI (silicon-on-insulator) wafer, with a $\approx 12nm$ thick top Si layer and $\approx 30nm$ buried oxide layer. The top Si layer was heavily doped with phosphorous at $\approx 10^{20}cm^{-3}$. 10 mm x 10 mm chips are used for device fabrication, each of which holds a 4 x 4 array of circuits. In each circuit, 8 device structures are defined, where the source, drain and gate electrodes can all be addressed independently. The device structures are defined in the Si layer using electron beam lithography using a Vistec VB6-HR machine operating at 100 kV. Figure 2.5a shows a low magnification SEM image of the pre-patterned devide on the SOI wafer, showing the 8 individual transistors. It will be seen that each device has a unique source and gate, but there are common drains between devices 1 and 2, 3 and 4, 5 and 6 and 7 and 8. A nanogap in the silicon between the source and drain was left for the deposition of the EBID patterns, as shown in figure 2.5b.

The final device consisting of the extensions of the drain and source contacts and the nanodot is fabricated using electron beam induced deposition. In

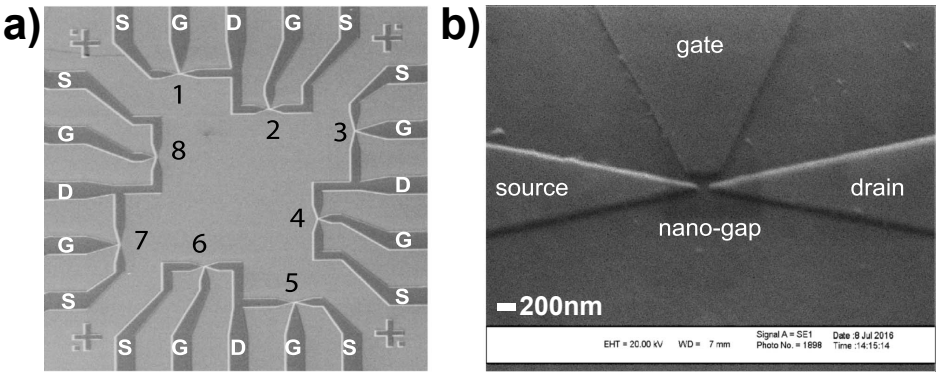

Figure 2.5: a) A low magnification SEM micrograph annotated to show the central area containing 8 device structures (numbered), each with a nanogap between the source and common drain, and a single side gate. The distance between the crosses is 200μm. b) SEM image of the pre-patterned device showing the source, drain and gate electrodes.

order to achieve high resolution patterning with EBID, a large group of parameters must be optimized for a successful deposition. First of all, the **electron beam settings** define the size of the electron beam at the sample, and hence the minimum size of the deposited structure. The higher the beam voltage and the lower the beam current, the smaller the probe size. We used a 19kV electron beam at a working distance of 5.25mm because it was the highest acceleration voltage available when using the Ultra High Resolution (UHR) mode. In this mode, a stronger magnetic lens, with a field that surrounds the pole-piece, focuses the beam in a small probe onto the sample surface. The choice of the beam current can be a compromise between probe size and acceptable contrast in the SE images. We used a probe current of 39pA, which leads to a beam diameter of $< 2nm$, to get enough signal on the SE detector during the focusing of the beam. The **geometry** of the set up, defined as the working distance and the position of the GIS nozzle must be optimized for the gas flow. In the FEI Nova Nano Lab 650 SEM, this is achieved by holding the sample at a eucentric height with the gas injection nozzle located approximately 100μm above the sample surface. The **operating conditions** of the SEM also play a crucial role: the SEM chamber must be thoroughly cleaned with oxygen plasma for 2 hours and before starting the deposition, the chamber vacuum level must have reached a sufficiently low base vacuum (better than $\approx 2 \cdot 10^{-6} mbar$). The choice of the **precursor gas** also influences the EBID patterning in terms of flux, adsorption and desorption of the precursor molecules and electron beam in-

duced dissociation cross section. In this experiment, we used the Pt precursor gas, trimethyl (methylcyclopentadienyl)-platinum ($MeCpPtMe_3$), with the deposited patterns expected to consist of Pt grains in a C matrix with a Pt:C ratio of approximately 1:5 [49]. Lastly, the **writing strategy** must be carefully studied and optimized. To pattern SET devices, the following strategy, shown in figure 2.6, was adopted:

a) First, the beam is finely focused to its smallest spot on surrounding particles and on the edge of the electrode itself. Then, the magnification is set to 240000, the beam is blanked and the gas is led into the chamber. It is of utmost importance that the gas flow stabilizes on the sample surface, which takes approximately 20 minutes. During this time, we do not encounter defocus of the beam, nor substantial drift.

b) First, the two connecting lines are patterned. The two lines are defined by the patterning software as a sequence of pixels and each pixel is exposed by the beam for an amount of time called the dwell time. The lines are both patterned starting from the electrode towards the island position and the space reserved for the island is set to be $50nm$. Each line is exposed for 4000 passes and in each pass the line pixels are exposed for $2\mu s$. Therefore, the total exposure time for each pixel is $8ms$. The pattern generator first completes one line and then writes the second one.

c) When the two lines are patterned, the beam is blanked and the gas is pumped out of the chamber. The device is then imaged to locate the exact position of the gap. The island is then defined as a circle with a diameter of $2nm$, patterned with a dwell time of $4ms$ and only 2 passes.

It is recognised that EBID processes also deposits a halo. This was not cleaned because the amount of material deposited was so little and spread over quite a large area and as such would not have formed a conducting layer. At $19keV$, the energy at which the deposition was performed, the diameter of the disk from which the backscattered electrons are emitted is $2.47\mu m$ [95]. Assuming a worst case scenario that the number of electrons generated by the backscattered electrons, SE2, is equal to the number of electrons directly generated by the primary electrons, SE1, and that the SE1 electrons are emitted from an area with a diameter of $\approx 3nm$ (a convolution of the probe size and the inelastic mean free path), the surface density is approximately $\approx 1.5 \cdot 10^{-6}$ times smaller than the SE1 surface density. On this basis an estimate of the number of atoms deposited in the $100nm$ wide gap between source and drain

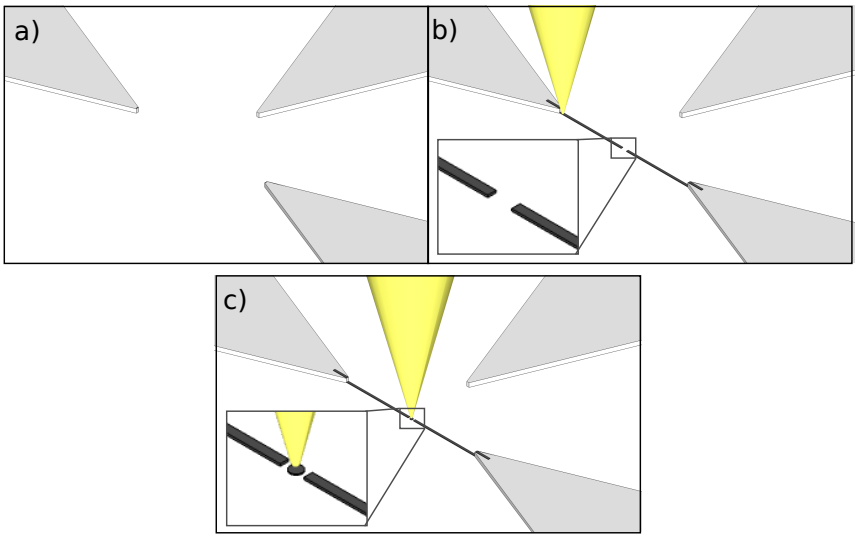

Figure 2.6: Schematic showing the writing strategy.

electrodes, assuming a continuous 20 nm wide EBID line of $10nm$ height and 100 nm length, is about $\approx 7.4{\cdot}10^5 mbar$ atoms. Assuming that the same number of atoms is deposited in the halo, of diameter $2.47\mu m$, the number of atoms per nm^2 is only 0.12, leading neither to a closed conducting surface layer nor likely to have an effect on the electrical characteristics of the nano-island devices.

Figure 2.7a shows the structure of the silicon source, drain and gate electrodes of device 1 prior to the nanowires and nanodot deposition: the source and drain are separated by a $200nm$ gap and the gate is positioned perpendicularly. Figure 2.7b shows the extended electrodes and nanodot deposited by EBID. As estimated from the SEM image, the gap to the island on the left hand side is $9.7nm$, that on the right hand side $4.5nm$, with the dot diameter being $22.5nm$, as shown in figure 2.7c. Further SEM images of the same device at different magnification, taken at a tilt angle of 45° are shown in (d + e). Finally, with such small deposits, usually the aspect ratio is ≈ 1–2. Using this aspect ratio, and inspection of SEM images, we estimate that the deposit thickness is $\approx 10nm$.

Figure 2.8 shows the SEM images of the pre-defined source-drain-gate structures of an another device (a) and the nanoleads and nanodot patterned by EBID, that define the single electron transistor (b-d). The size of the left hand side gap and the right hand side gap is $7nm$ and $3nm$ respectively, while the nanodot is $\approx 11nm$ in diameter, measured from the top down SEM image.

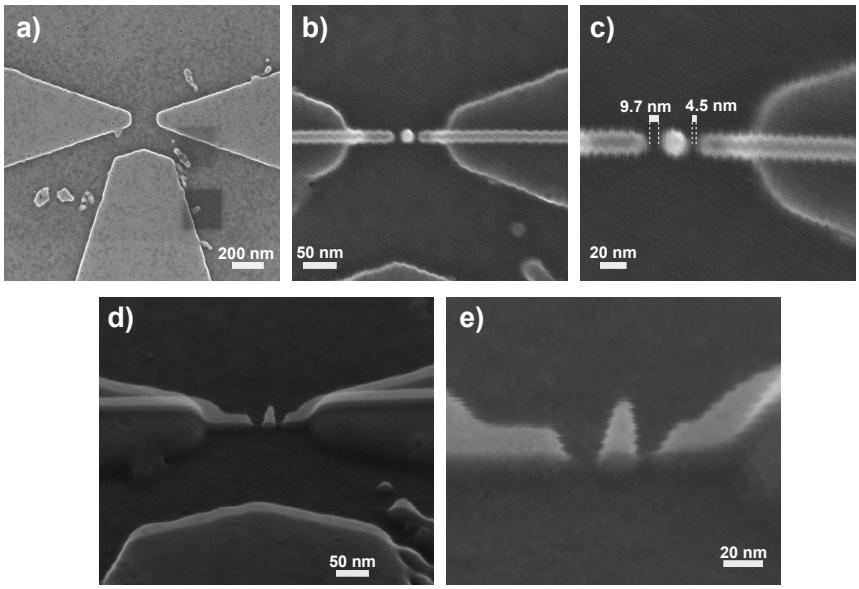

Figure 2.7: On the top row, SEM micrograph of the predefined source drain and gate electrodes (a) and of the extended electrodes deposited by EBID and the nanodot (b-c) deposited in between of device 1. The gap left of the island is $9.7nm$, the gap to the right $4.5nm$, and the island diameter is $22.5nm$, as estimated from the SEM image. On the bottom row, SEM images of the same device taken with a tilt angle of 45 deg (d-e).

2.2.2 Electrical characterization[‡]

The electrical characterization at room temperature of the drain–source current versus drain and gate voltage, the temperature dependent measurements and subsequent data analysis of the results were carried out by Durrani, Jones and Wang at the Imperial College facility.

Room temperature (RT = $290K$) measurements of the drain - source current vs. drain and gate voltage were performed using a 4-point probe station in conjunction with either an Agilent 4155B parameter analyser or a combination of Keithley 236 source measurement units (SMUs) interfaced with a computer. Subsequent data analysis of the results was undertaken using Matlab programmes. For the temperature dependent measurements, from $290-8K$,

[‡]We acknowledge Durrani, Z. A. K., Jones, M. E. and Wang, C for performing the electrical measurements and the analysis.

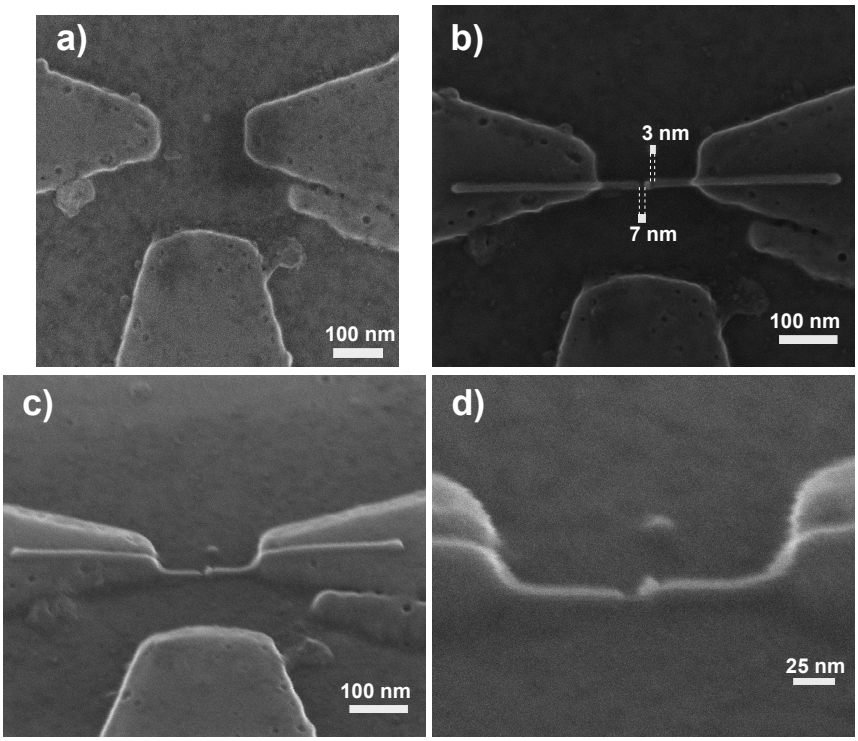

Figure 2.8: On the top row, top down SEM images of the pre-patterned source-drain-gate structure of a further device and the EBID patterned single electron transistor (b). On the bottom, SEM micrograph of the same patterned device, under a tilt angle of 45 deg (c-d).

samples of interest were wire bonded into chip carriers and inserted in a CTI-Cryogenics closed cycle helium cryostat.

The RT drain current (I_{ds}) and drain conductance (g_{ds}) vs. drain (V_{ds}) and gate (V_{gs}) voltage characteristics of a Pt/C nanodot device (Device 1, SEM image in figure 2.7) are shown in figure 2.9. The nanodot is $\approx 20nm$ in diameter, with $\approx 50nm$ long Pt/C nanowire electrodes on either side, isolated by few-nanometer scale gaps from the nanodot. The nanowire electrodes lead to Si point-contact regions. The measured data for I_{ds} vs. V_{ds}, V_{gs} using a 3D plot are shown in figure 2.9(a). I_{ds} is seen to increase non-linearly with V_{ds}, in a symmetrical manner for $\pm V_{ds}$. Current oscillations with a period $\Delta V_{gs} \approx 0.5V$ are seen, with finer, irregular fluctuations superimposed on these from one I_{ds} - V_{ds} sweep to the next. The main current oscillations can be better investigated

by using moving average (over 7 points) thin-plate spline fits to the data (figure 2.9b). A logarithmic plot of the magnitude of drain conductance $|g_{ds}|$, extracted from the smoothed data in (b), and plotted vs. V_{ds} and V_{gs} as a log scale colour, planar image is shown in figure 2.9c. The plot of $log|g_{ds}|$ allows diamond-like regions, marked 'A' and 'B', to be seen, within which g_{ds} is small, for small V_{ds} values and $0 < V_{gs} < 1.2V$. The corresponding oscillation in g_{ds} continues for $V_{gs} > 1.2V$, however, full diamond-like regions are not seen, as there is a low conductance region near $V_{ds} = 0V$ which cannot be modulated to larger g_{ds} values in a manner similar to the area between diamonds 'A' and 'B'. The I_{ds} vs. V_{ds} characteristics at different values of V_{gs}, offset from each other, are shown in figure 2.9d using a 2D plot. Here, the relative extent of modulation of I_{ds} curves by V_{gs} can be observed. The gate modulation of I_{ds} vs. V_{gs}, at constant V_{ds}, are shown on a linear scale in figure 2.6e and log 2.9f. Both the measured data (scatter points) and the spline fits to these are shown.

The electrical characteristics of figure 2.9 may be attributed to the formation of a room temperature single-electron transistor (SET) [96] [97]. Here, the diamond-like regions A and B, and the gate oscillation in I_{ds} may be associated with Coulomb diamonds, and gate modulated single-electron current oscillations, respectively [96]. The likely origin of the charging island, leading to SET behaviour, is the $\approx 20nm$ scale Pt/C nanodot (figure 2.7b). An alternative hypothesis is the existence of nanocrystals within the Pt/C nanowire electrodes. In the former case, the tunnel barriers isolating the charging island are the nanogaps between the nanodot and the electrodes. In the later case, the origin of the tunnel barriers is less clear, and the existence of potential barriers at grain-boundaries surrounding the charging nanocrystals would be necessary.

2.2.3 Conclusions

Electron beam induced deposition is a valid attractive lithographic technique for the fabrication of devices in the sub-10 nm range. Contrary to electron beam lithography, EBID is a direct write technique that does not require resist to be spun on the sample surface, alignment procedures and post-patterning steps, such as lift-off and metallization. For applications such as the definition of smaller devices within a pre-patterned chip, EBID was demonstrated to be a good candidate.

In this paragraph, we have presented the fabrication of devices consisting of EBID Pt/C nanowire and nanodot transistors, integrated within Si nanodevices. The Pt/C nanostructures were deposited across $\approx 100nm$ wide nanogaps

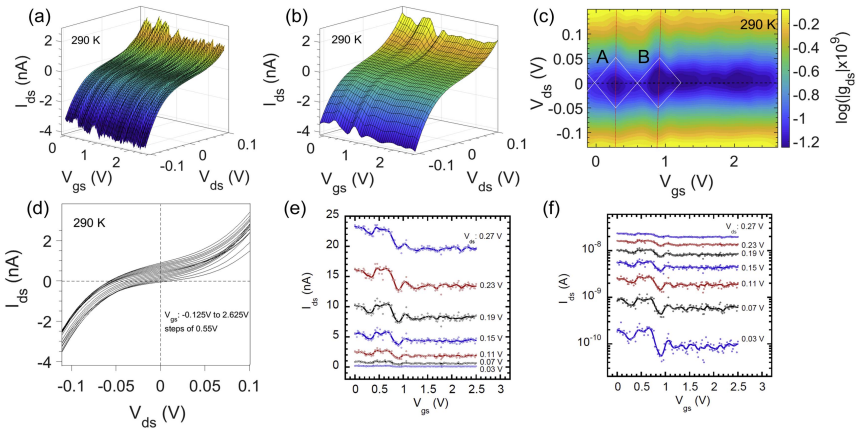

Figure 2.9: Room temperature electrical characteristics of a $\approx 20nm$ nanodot device (device 1). (a) A 3D plot showing I_{ds} as a function of V_{ds} and V_{gs}. (b) Data of (a) re-plotted following an averaged, thin-plate spline fit, to show more clearly the oscillation of I_{ds} versus V_{gs}. (c) $Log|g_{ds}|$, plotted using a linear colour scale, as a function of V_{ds} and V_{gs} and showing two diamond-like regions highlighted in white. (d) A 2-D plot of I_{ds} as a function V_{ds}, for values of V_{gs} from $-0.125V$ to $2.625V$, in steps of $0.55V$ superimposed. Curves are offset from each other for clarity. (e) Ids as a function of V_{gs} at 7 values of V_{ds}, from $0.03V$ to $0.27V$. (f) Data of (e) re-plotted using a log scale for I_{ds}, to highlight current oscillations at the lowest V_{ds} values.

between heavily doped n-type Si source and drain point-contact regions, fabricated in silicon-on-insulator material. Pt/C nanodots were fabricated having a minimum diameter $\approx 20nm$, with Pt/C nanowire electrodes on either side bridging a $\approx 100nm$ wide nanogap between the Si source and drain regions.

A single-electron transistor, operating at room temperature, was formed by the $\approx 20nm$ nanodot device. Here, single-electron current oscillations and 'Coulomb diamond' electrical characteristics were observed at RT. In the Pt/C nanowire devices, the p-type semiconducting nature of the devices was determined from gate measurements, and temperature dependences from 290 to 8 K. Current transport was seen to be a combination of thermally-activated and tunnelling transport of holes across potential barriers along the current path, formed at the Pt/C interface and/or at grain boundaries within the Pt/C deposit.

Device 1 in figure 2.7b shows a behavior that can be attributed to a SET behavior at room temperature that indicates a very strong RT single-electron effect. The nanodot in device 1 is rather large, $\approx 20nm$ in size, such that the total

capacitance $C_t \sim 3.2aF$ is not small enough for very strong room-temperature single-electron charging effects. However, in comparison with typical Si point-contact QD transistors [97], where some randomness in the location of the QD within the point-contact exists, the use of an EBID nanodot allows greater flexibility in the precise placement of the nanodot within a pre-defined device structure. In a more recent paper by Di Prima [98], Coulomb oscillations were observed in a single electron transistor fabricated by EBID at temperature as low as 0.3 K, demonstrating stable transistor operation.

2.3 Metrology of sub-20 nm nanostructures

Metrology is the science of measurements and has underpinned all the industrial revolutions. Its roots lay in the French Revolution, with the aim of standardizing the unit of length. In nanotechnology and in the semiconductor field, where researchers as well as industries are constantly demonstrating the fabrication of devices on the nanoscale, metrology plays a role of utmost importance. Metrology not only defines and establishes a common understanding of units of measurements, but also finds its application in the chain of traceability, in linking measurements to a reference standard. Within the Single Nanometer Manufacturing for Beyond CMOS devices (SNM) project, great attention was paid to metrology. In collaboration with VSL, the Dutch institute of metrology, a task-force on metrology was instantiated, involving all the project partners. The SNM benchmark was performed to compare and evaluate the capabilities of the participants to quantify the line width of an isolated line, the pitch of a regular dense line structure and the position of the individual lines within this dense line structure. The goal of this task-force was to investigate the measurement methods adopted by all partners and compare them to the reference standard. Two types of instrumentation were used in this benchmark task force: scanning probe microscopes in the form of regular atomic force microscopes (AFMs) or lithographic devices in AFM read-back mode were used, and charged particle microscopes (CPM) in the form of SEM and HIM (Helium Ion Microscope).

2.3.1 The TUD instrumentation

As part of the metrology benchmark task-force, the instrumentation used by us (TUD) consists of a scanning electron microscope (FEI Nova Nano Lab 650 dual beam SEM) and an atomic force microscope (Bruker Dimension fast-scan

Instrument	Bruker Dimension fast-scan Atomic Force Microscopy
Ambient conditions	Cleanroom class 10000, 20 +/−0.2 C
Measurement procedure	• Load a new cantilever in the AFM • Align the laser and photodetector • Autotune the tip • Load sample such that the lines under measurement are perpendicular to the fast scanning axis of the tip • Set the number of samples per scan line to maximum(16384) and scan rate to 1.96 Hz • Reduce Z limit to 500 nm to increase dynamic range of the Z axis • Tune signal by maximizing integral and proportional gain up to the point where the tip starts resonating, then reduce gain

Table 2.1: Instrument details, ambient conditions and measurement procedure of the Bruker fast-scan AFM

AFM). In table 2.1 and 2.2 the instruments details, the ambient conditions and the measurement procedures are described.

2.3.2 The benchmark sample

The benchmark sample [courtesy of IMEC] that was used for this task is a cut-out of a silicon wafer, with areas that contain blocks of dense Si lines, capped with Si_3N_4. The searching geometry patterned on the wafer allows the user to easily identify the block of interest. Each block consists of 24 lines with a pitch of approximately $0.05\mu m$. Along the direction of the lines, this pattern is disrupted every $3\mu m$ by the local discontinuation of the lines 1, 2, 4, 5, 7, and 8. This creates isolated parts of lines 3 and 6. In this benchmark activity the width (CD) of the isolated part of line 3 on this specific location will be determined. In addition, the position of the lines in the block in the vicinity of this specific local disruption will be evaluated, as well as the local pitch.

Figures 2.10a and 2.10b show the SEM micrograph of the regions of interest, taken with the TLD (Through the Lens) detector with beam spot size 1 (corresponding to a probe current of approximately $12pA$) and spot size 2 (corre-

Instrument	Nova Nano Lab 650 Dual Beam Scanning Electron Microscope
Ambient conditions	The microscope is not in a cleanroom, but in a regular laboratory
Measurement procedure	• The microscope chamber was cleaned with 2h oxygen plasma cleaning ($15W$) • The sample was loaded and clamped on a heavy block in order to limit vibrations and drift • The chamber pressure was $4.16 \cdot 10^{-6}$ mbar. • The working distance was set at the eucentric height ($5.4mm$). • The measurements were performed in UHR (Ultra High Resolution) mode. • Acceleration voltage: $18.5kV$, beam current: $39pA$ (Spot 2) and $12pA$ (Spot 1). Field of View (FoV): $1.4\mu m \times 1.4\mu m$. dwell time = $3\mu s$ • In between two measurements, refocus and astigmatism adjustment was performed

Table 2.2: Instrument details, ambient conditions and measurement procedure of the FEI Nova Nano 650 SEM

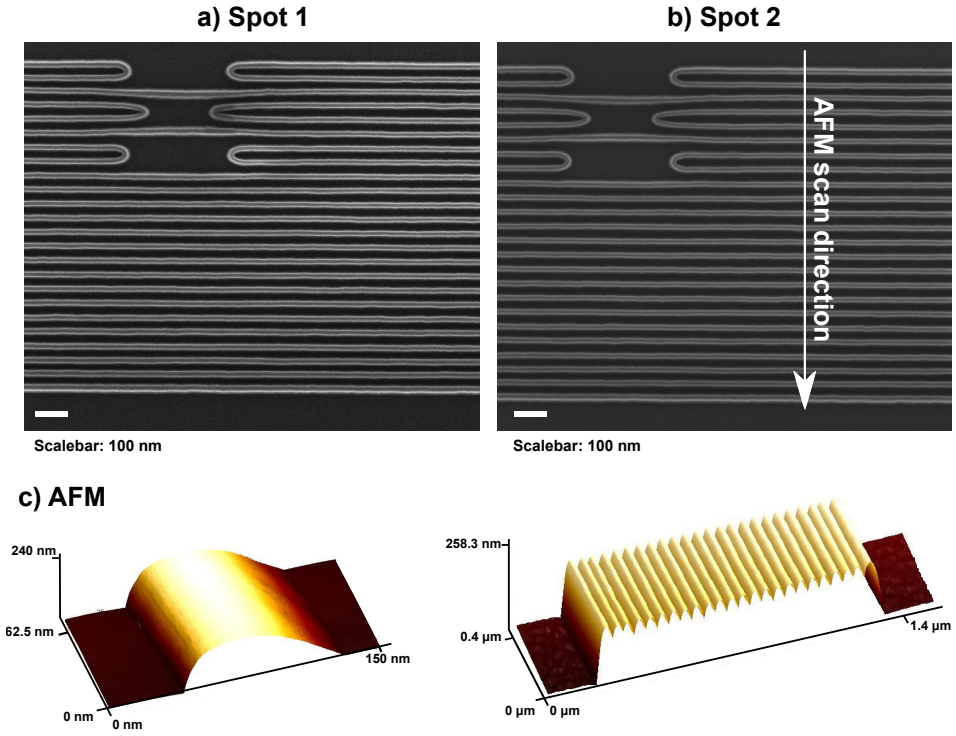

Figure 2.10: a) and b) Images of the benchmark sample on the region of interest, that consists of 24 lines taken with the FEI Nova Nano Lab 650 SEM. The images were taken at $18.5kV$ in Spot 1 (a) and Spot 2 (b), corresponding to a beam current of approximately $12pA$ and $39pA$ respectively. The images were taken from the Through the Lens Detector (TLD). c) 3D reconstruction of the AFM scan over the third line from the top and over the 24 lines, as indicated in the SEM micrograph in b), using the Bruker fast-scan AFM.

sponding to a probe current of approximately $39pA$), using a $18.5kV$ beam in immersion mode (UHR). Figure 2.10c shows the 3D reconstruction of the AFM scan of the third line from the top and of the 24 lines, as indicated by the arrow of figure 2.10b. The asymmetric shape of the third line profile in figure 2.10c indicates that the AFM tip used in this analysis has an asymmetric shape. From the SEM images and the AFM scans, the width of the lines and the position of the lines with respect to the third line were measured.

2.3.3 Analysis of the SEM images

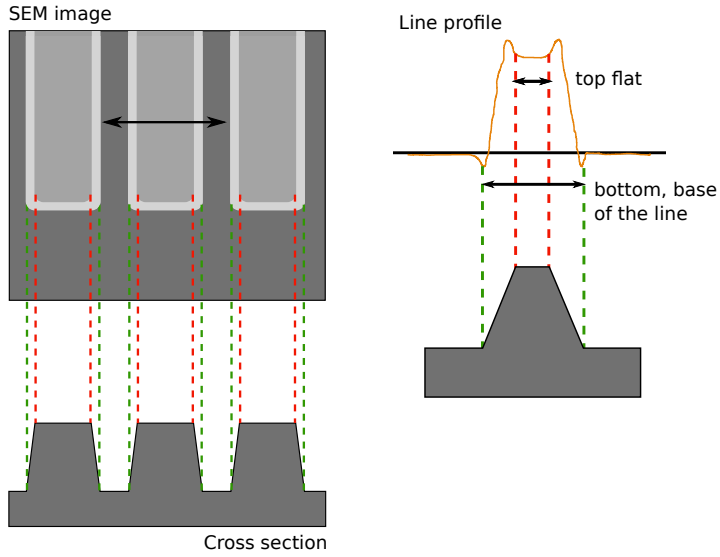

Figure 2.11: On the left, illustration of a secondary electron image of three lines and, below, their cross section. The brighter areas in the image correspond to the sidewalls of the lines. On the right, illustration of a line profile extracted from the SEM image. The line profile has an M-shape, where the peaks in intensity correspond to the sidewalls of the lines emitting more secondary electrons.

Typically, the width of lines having a gaussian profile is measured using either the FW50 value, namely the full width at 50% of the area under the profile, or the FWHM value, namely the full width at half maximum. When imaging with a secondary electron detector, the contrast of the lines at the edges is enhanced because more secondary electrons are emitted from those areas. Figure 2.11 shows a schematic of an SEM image of three lines and their cross section. The sidewalls of these lines generate more secondaries, creating an enhanced

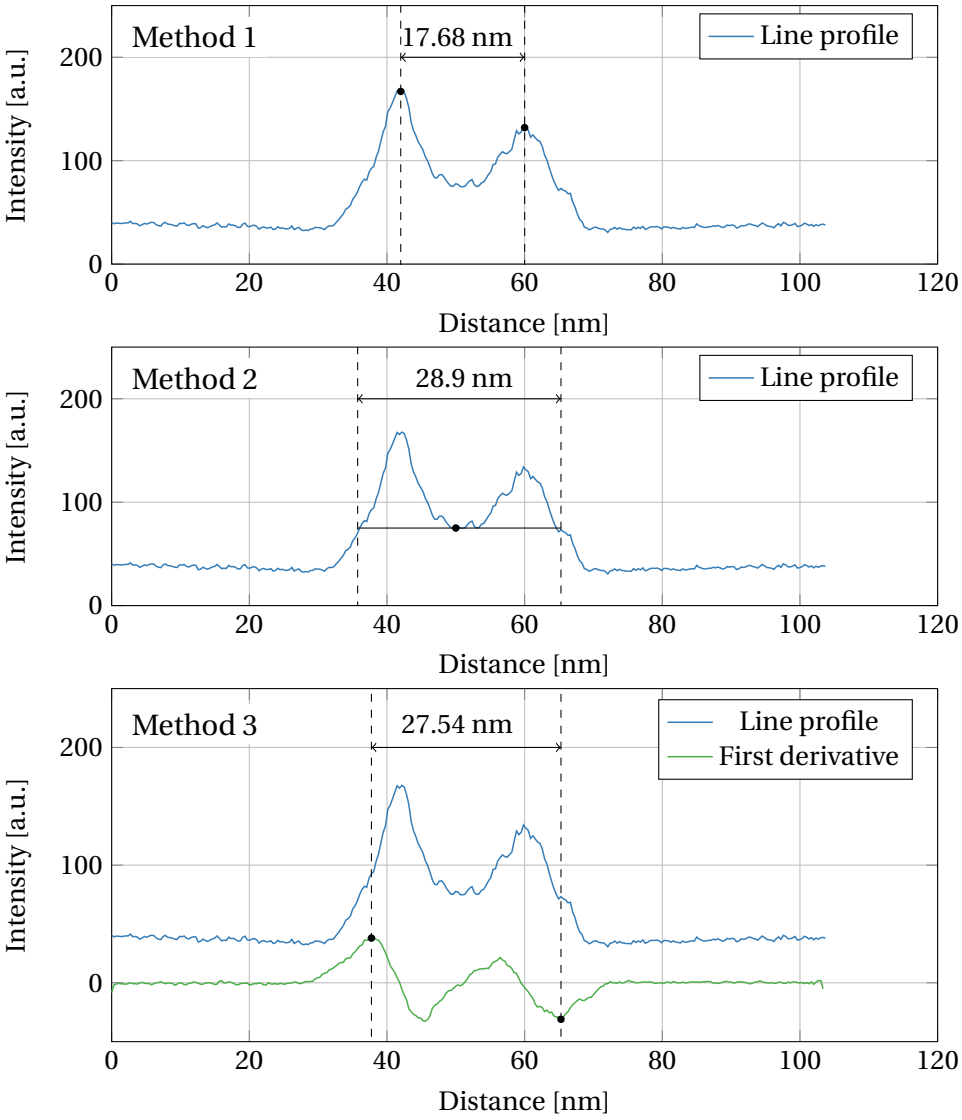

Figure 2.12: Profile of the third line integrated along a distance of approximately $100nm$ measured from the SEM images taken with spot 1 ($\approx 12pA$ beam current). The profile has an M-shape profile, which makes it difficult to establish the width using known criteria. Here we present three methods to calculate the width of M-shaped lines profiles. In the first method, the width of the line is measured as the distance between the two peaks. In the second method, the width is measured at the same height as the local minimum located between the two peaks. In the third method, the width is measured as the distanve between the first local maximum and the second local minimum of the derivative of the M-shaped line profile.

contrast in the SEM image. The profile of such line has an M-shape, where the peak in intensity is reached just outside the top flat.

In case of M-shaped line profiles, there is no clear definition of FW50 nor FWHM values and measuring the width of these lines is not trivial. Figure 2.12 shows three methods to define the width of M-shaped lines, taking as example the third line profile of the SEM image acquired with Spot 1, as shown in figure 2.10a. The first method to define the width is by measuring the distance between the two peaks of the M-shaped line profile. However this is an underestimation of the line width as it is an estimation of the top flat only. In this case, we measured a line width of $17.68nm$. In the second method, the line profile is measured at the height of the local minima in between the two peaks and in this case a width of $28.9nm$ is measured. This method could work if the flat in between the two peaks is narrow enough and presents a well defined local minimum. This cannot be applied in cases where the line profile is more similar to that illustrated in figure 2.11. The third method consists of calculating the derivative of the line profile, which shows two alternating peaks and dips [99]. The width of the line is measured from the first peak and the second dip of the derivative, namely the first and the last change in slope of the edges of the line. In this case, a line width of $27.54nm$ is measured.

Figure 2.13a shows the line profiles of the third line taken from the SEM images with spot 1 and spot 2 with the TLD detector. The profiles have an M-shape and it is noticeable that the profile taken with spot 1 is broader than that taken with spot 2. Changing spot required a change in brightness and contrast, which can explain the different size of the two profiles. In figure 2.13b the derivatives of the line profiles for spot 1 and spot 2 are shown. The width of these two lines is calculated using the second and the third method described in figure 2.12 and is shown in table 2.3. The width of the third line measured with beam spot 1 is $\approx 29nm$ if measured with method 2 and $\approx 27nm$ if measured from the derivative of the line profile. In case of beam spot 2, therefore larger beam current, the width is $\approx 26nm$ with method 2 and $\approx 25nm$ with method 3. The width of the line measured with spot 1 is larger than that measured from the image taken with spot 2, which has a larger spot size at the sample.

The difference in width measurement can be explained by the amount of drift that was measured by imaging the structure at high resolution with the two beam settings. Figure 2.14 shows two SEM images taken from the TLD detector with spot 1 (on the left) and spot 2 (on the right). The number of pixels

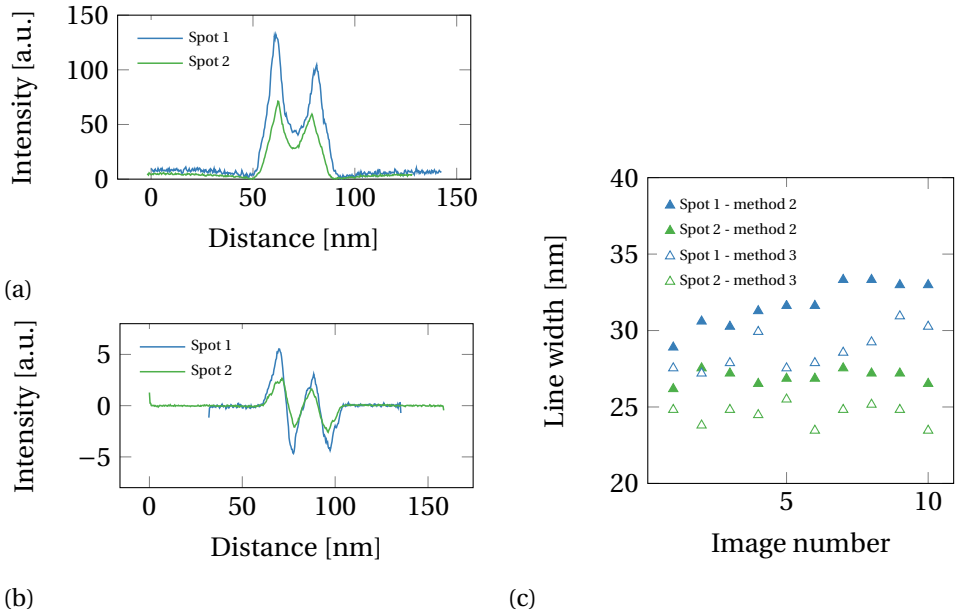

Figure 2.13: a) Profile of the third line measured from the SEM images taken with spot 1 ($\approx 12pA$ beam current) and spot 2 ($\approx 39pA$ beam current). b) Derivatives of the lines profiles in a) for beam spot 1 and beam spot 2. c) Line width calculated using the second method and the third method of figure 2.12 of the third line of ten images taken with spot 1 and spot 2.

Beam spot	Method 2	Method 3
Spot 1	$28.9nm$	$27.54nm$
Spot 2	$26.18nm$	$24.82nm$

Table 2.3: Width of the third lines measured with method 2 and method 3 from figure 2.12.

of these images is 1024 x 1024, the dwell time $3\mu s$, the horizontal field of view $512nm$ and no image avaraging and no image integration was selected. The beam settings were those selected for the acquisition of the image served for the analysis shown in figure 2.13. In a smaller box, the image was refreshed after $30s$. In the first image, taken with spot 1, a drift towards south was measured to be $28nm$, whereas on the second image it was $6nm$ towards north. The speed of the drift is in the first case $56nm/min$ whereas in the second case $12nm/min$.

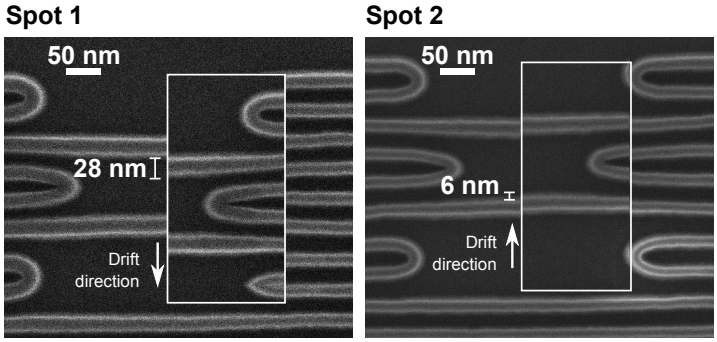

Figure 2.14: High magnification SEM images taken from the TLD detector of the area shown in figure 2.10, with dwell time $3\mu s$ and resolution of 1024 x 1024 pixels. On the left, the image is taken with spot 1, whereas on the right with spot 2. In the smaller boxes, the images were refreshed after a waiting time of $30s$. The drift measured on the left is $28nm$ and that on the right is $6nm$ and in opposite directions.

The images acquired for the benchmark task force have a resolution of 4096 x 4096 pixels, dwell time of $3\mu s$ and the total frame time is approximately $50s$. The third line is approximately 70 pixels wide, therefore it takes approximately $0.85s$ to scan the portion of the frame containing the third line. Within this time-frame, the drift towards south in case of spot 1 is approximately $0.8nm$ and the drift towards north is approximately $0.17nm$. Assuming the drift is constant, the lines imaged in spot 1 will appear broader by $0.8nm$, whereas those imaged in spot 2 will appear smaller by $0.17nm$. This alone is not sufficient to explain the difference in the measurement taken with spot 1 and spot 2. Anther factor that can contribute and can explain this difference can be a miscalibration of the magnification in the two different current settings.

The pitch and the position of the lines was measured from the line profile across the 24 lines, as shown in figure 2.15. The pitch between lines is measured as the distance between the dips of each line profile, whereas the position of the lines with respect to the third line is defined as the distance between the n-line

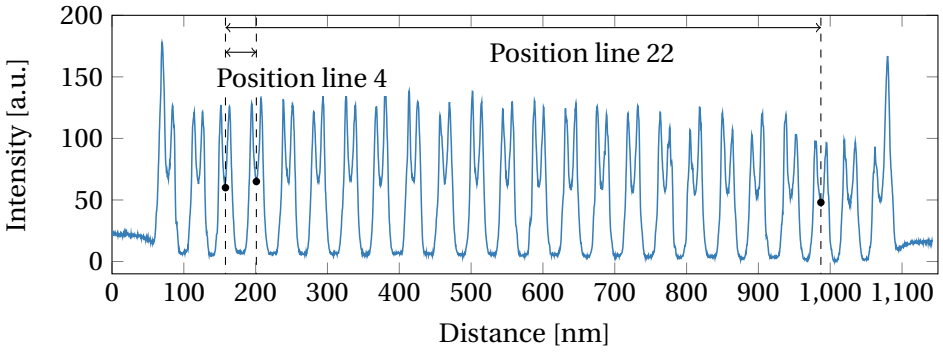

Figure 2.15: Line profile of the SEM images take with spot 1 showing the 24 lines with M-shpaed profiles. How the position of the lines is measured is highlighted in this graph. The position of a line is the position of minimum between the two peaks. The position of lines 4-22 is measured as the distance to the third line, as shown here for line 4 and line 22.

and the dip of the third line, as shown in figure 2.15.

Figure 2.16a shows the line profile of an image taken with spot 1 and a second line profile of an image taken with spot 2. With a Matlab code, the position of the dips in each profile is determined and the pitch and the position of lines 4-22 with respect to the third line was measured. Figures 2.16b and 2.16c show the resulting pitch and line position for images taken with spot 1 and spot 2. The pitch between lines has an average value of $\approx 44nm \pm 2.5nm$ and the two sets of measurements reveal the same trend.

2.3.4 Analysis of the AFM measurements

An atomic force microscope (AFM) consists of a proping tip attached to a cantilever spring. Because of the force between the tip and the sample, the cantilever is deflected. Images are taken by scanning the sample relative to the probing tip and digitizing the deflection of the lever or the z-movement of the piezo as a function of the lateral position x, y [100]. In atomic force microscopy, conductive and non-conductive samples can be imaged, with, in some cases, atomic resolution. In our study, we used a Bruker fast-scan AFM located in a cleanroom environment, as specified in table 2.2.

AFM is best suited for precise height measurement, whereas for lateral dimension reliable analysis is done by deconvolving the tip shape from the mea-

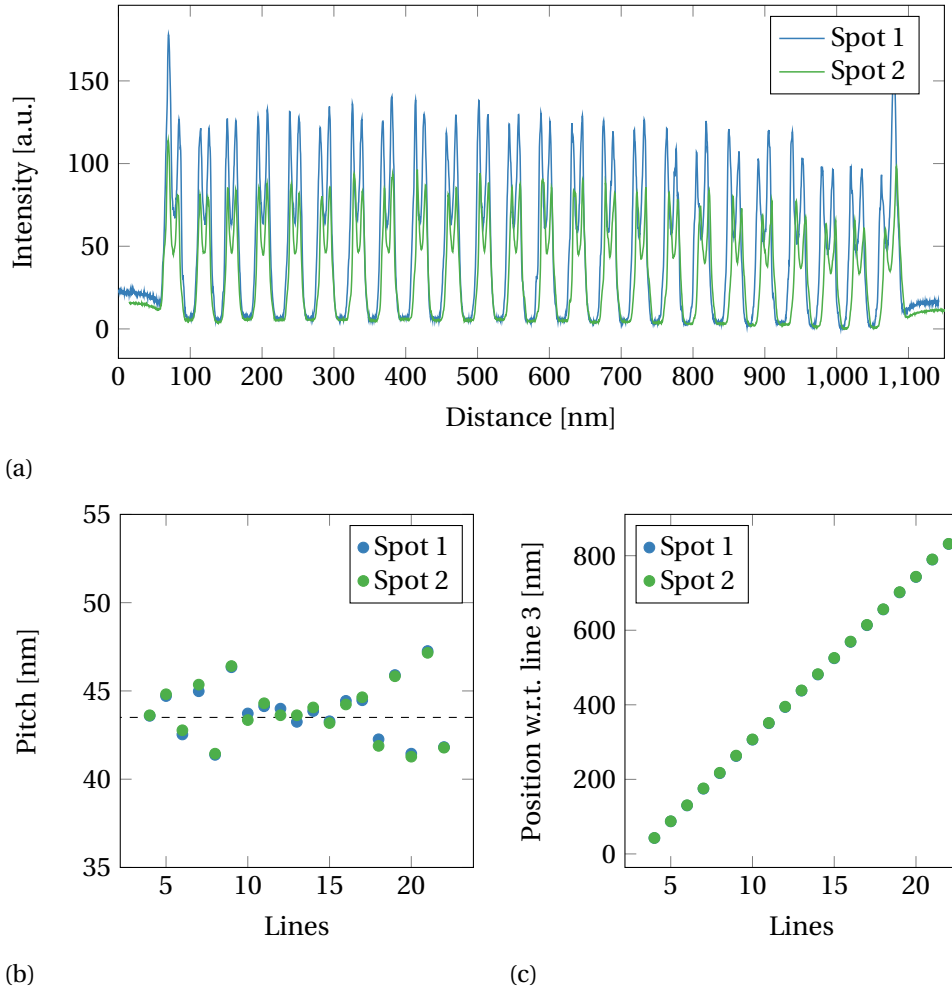

Figure 2.16: a) Line profile of the SEM images taken with spot 1 and spot 2, showing the 24 lines with M-shaped profiles. b) Pitch between the lines, for images take with spot 1 and spot 2. The dashed line indicates the average pitch of $\approx 44nm \pm 2.5nm$ calculated from these measurements. c) Line position with respect to line 3, for SEM images taken with spot 1 and spot 2.

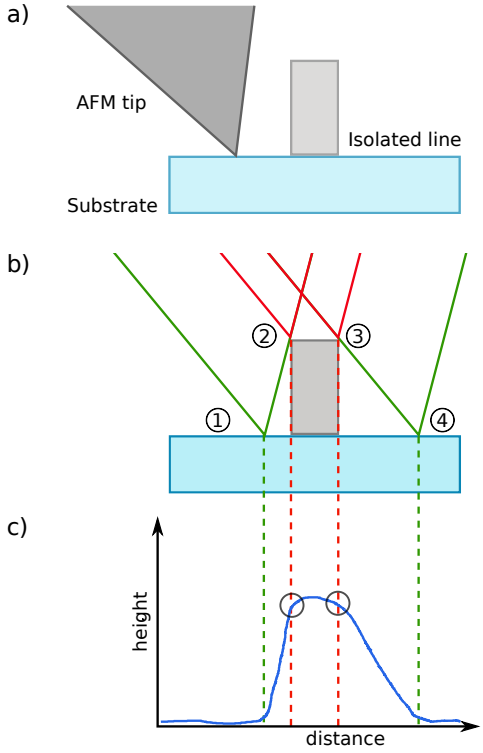

Figure 2.17: Explanation of the measurement of the critical dimension done by atomic force microscopy.

surement. Figure 2.10c shows the 3D reconstruction of the scanned area across line number 3. This reconstruction shows how an asymmetric tip leads to a profile with sidewalls with different slope. Figure 2.17a shows a schematic of an asymmetric tip scanning over a line. The tip is scanned over the line and it touches the top of the line (1) while the very end of the tip is still scanning the bottom surface. The tip is lifted because of the interaction with the upper left corner and then the very end of the tip reaches the top left corner (2). The tip then scans the top flat on the line, until the very end of the tip reaches the top right corner of the line (3). Because the slope of the tip now has decreased, the end of the tip will reach the substrate much further away than where the line actually ends (4). The obtained line profile, shown in figure 2.17 appears to be much broader than the line itself. The best way to reconstruct the line profile is to perform a tip-deconvolution. In this case, however, this was not possible because the sample used to measure the shape of the tip was not available. But in our analysis, we noticed that when the very end of the tip reached the two upper corners, there is a little bump in the profile. We therefore measured the distance between these two bumps to measure the line width, as appeared to be more consistent with what resulted from the SEM analysis.

Figure 2.18a shows the height profile of the 24 lines from the AFM analysis. The pitch is measured as the distance between two neighbouring peaks, whereas the position of the lines with respect to line 3 is the distance between the peak of the line and the third line peak. An accurate estimation of the width of the line is in this case not trivial because the shape of the tip was asymmetric. We took as line width the distance between bumps that are visible in the AFM profile and we believe belong to the very end of the tip bouncing of the corner of the line. In this case, we measured a line width of $24nm$. Lastly, the measurement of the line position from the AFM scan is shown in figure 2.18c and it is here compared to the line position measured with the SEM, spot 1 and spot 2. The slope of the AFM position measurement differs from the slope of the SEM position measurements and the position of line 22 with respect to line 3 measured from the SEM image is approximately $831nm$, whereas that measured from the AFM is $855nm$. This means that the either the SEM or the AFM set up may suffer from sample drift.

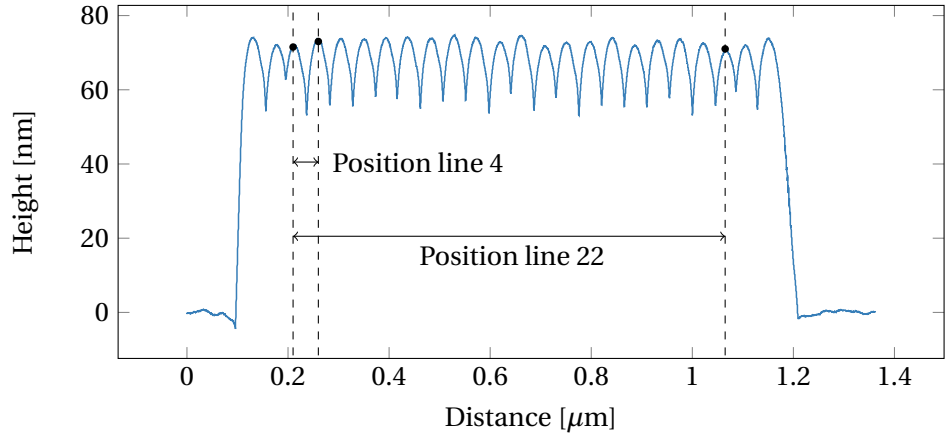

(a)

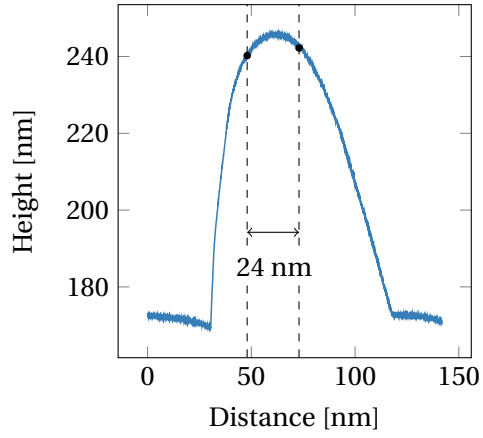

(b)

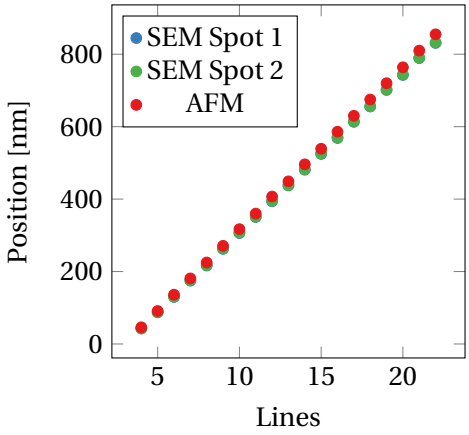

(c)

Figure 2.18: a) AFM profile of the 24 lines showing how the position of lines 4-22 was measured with respect to line 3. b) AFM line profile of the third line. The width of the line is measured by looking at the small bumps in the profile, as explained in figure 2.17 c) Pitch of lines 4 to 22 with respect to the third line, measured from the SEM line profiles (in spot 1 and 2) and from the AFM line profiles.

2.3.5 Measurement results

Figure 2.19 shows the results of the task force within the SNM project, for AFM and CPM instruments. The CD width of the third line is shown in figures 2.19a and 2.19b. The line width measured with the AFM from the partners results to be bigger than that measured by VSL, where the tip-deconvolution was applied, because of the convolution with the tip shape that broadens the line profile. The measurement performed by us (indicated in this graph here as B002) is actually smaller than that measured by the reference AFM, meaning that the method we used to determine the line width is an underestimation. In case of SEMs and HIM, here referred to as CPM, the measurements are closer with the reference value. The results for the pitch are shown in figures 2.19c and 2.19e. In case of AFMs, if the pitch is measured as the distance between consecutive peaks, there is little influence from the shape of the tip and the results are more reliable compared to the reference results. The results of the line position for AFMs and CPMs are shown in figures 2.19e and 2.19f: the presented graphs for the line position data are displayed as the difference from the reference values as measured by VSL. In this case, the accuracy of the measurement of the line position critically depends on the correct lateral calibration coefficient. Correction with a calibration coefficient that is either too small or too large will result in an increasing difference with respect to the reference value, that can be either positive or negative, as shown in figures 2.19e and 2.19f. One of the AFM results additionally shows a non linear difference, indicating a residual non-linearity in the movement of the scanning probe or scanning stage (TUIL-NPMM). The maximum observed difference of about 20 nm for the position of the final line with an average reference position value of $847 nm$ corresponds to a relative error of the calibration factor of 2.4%.

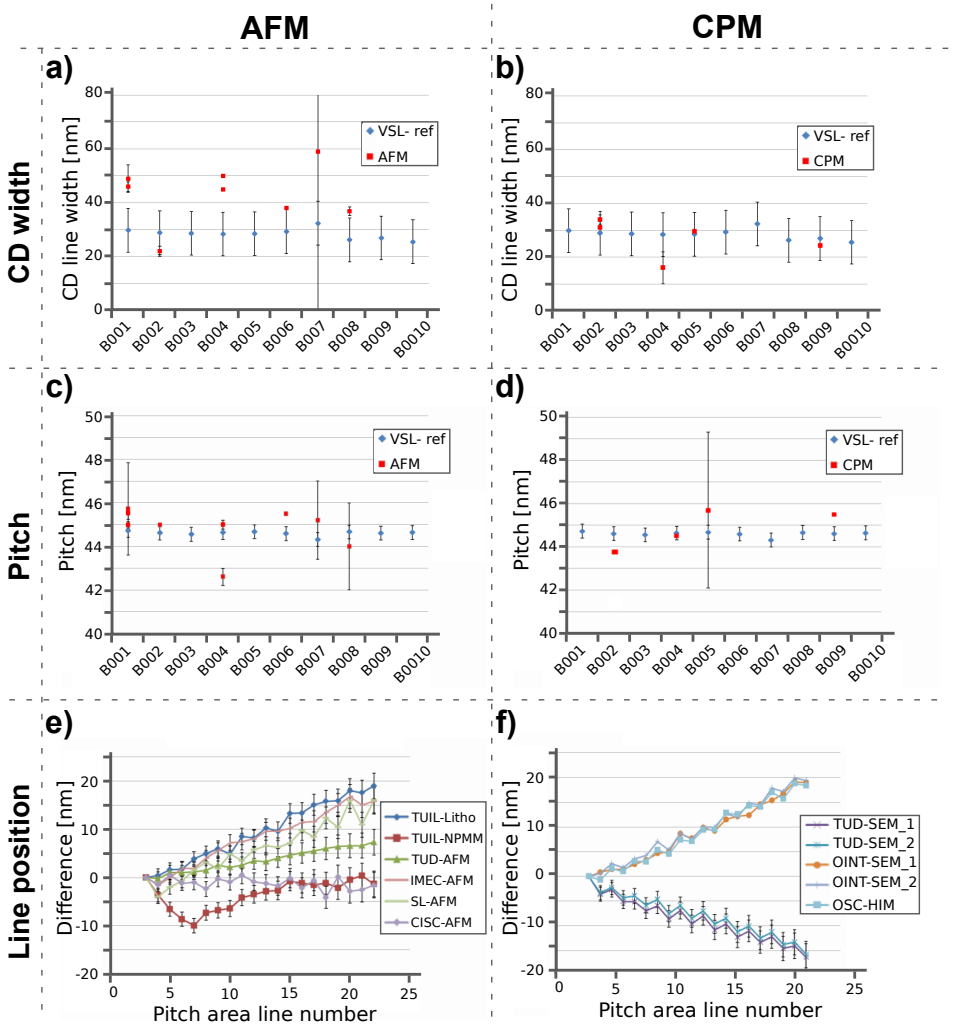

Figure 2.19: Results of the benchmark task force among all partners in the SNM project compared to the reference, measured by VSL. a) and b) Measurement of the CD width of the third line with the AFM and CPM respectively. c) and d) Measurement of the average pitch from the AFM and CPM. d) and e) Measurement of the line position from AFM and CPM.

2.3.6 TEM benchmark

A second benchmark task force was set up by VSL to compare TEM instruments within the partners of the SNM project. The sample was made by VSL and consists of a SiN TEM membrane in a silicon carrier. On top of the flat side of the sample silica nanoparticles were deposited such that they do not cluster. This way individual nanoparticles can be imaged and measured. The sizes of features on the benchmark sample are measured with different TEM instruments as well as SEMs and AFMs among the participants.

The instrumentation we used for the second benchmark task-force are two SEMs (FEI Nova Nano Lab 650 dual beam SEM and the FEI Verios XHR 460 SEM) and a NanoAnalytik in-situ AFM. The nanoparticles were imaged in the SEMs using beam voltages and beam currents that are listed in table 2.4. The resulting images are shown in figure 2.20.

The images *Nova-1*, *Nova-2* and *Nova-3* show regions with nanoparticles on top of the membrane. Nova-1 and Nova-2 were acquired using $5kV$ beam voltage and $1.6nA$ beam current, whereas Nova-3 was acquired with a $16.5kV$ and $2.3nA$ beam. For these images we used the UHR mode, or also called immersion mode. The SEM image *Nova-4* depicts particles that are lying on the silicon bulk substrate, in a region outside the thin membrane. In this case, a $16.5kV$ beam voltage and $11pA$ beam current was used, in immersion mode. The SEM micrographs at the bottom of figure 2.20 display areas with nanoparticles on the thin membrane and were taken with the FEI Verios 460 SEM, at $1kV$ (*Verios-1*) and $5kV$ (*Verios-2*), with $25pA$ current, in immersion mode. For both these images, the monochromator was switched on. The dwell time was selected to be $10\mu s$, apart from the image *Verios-1*, where a dwell time of $0.1\mu s$ with 8 averaged frames was selected to compensate for charging that was noticeable in that region. Table 2.4 also lists the horizontal field of view (HFW) of the images acquired with the two microscopes.

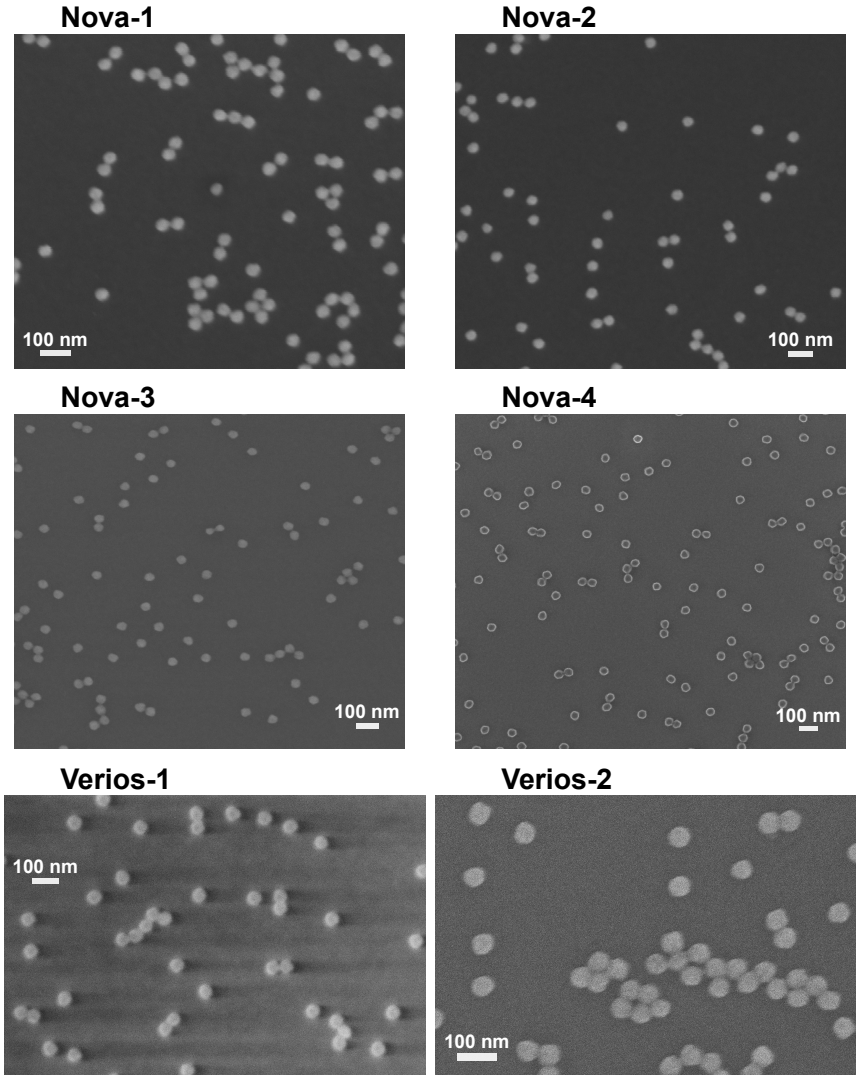

Figure 2.20: SEM micrograph of the nanoparticles taken with the FEI Nova Nano Lab 650 SEM and the FEI Verios 460 SEM. All images are taken from areas on the thin membrane, apart from image *Nova-4*, that was acquired in a region on the bulk substrate. The beam settings with which these images were taken are described in table 2.4.

Image	Beam energy	Beam current	Dwell time	Averaging	HFW
Nova-1	$5kV$	$1.6nA$	$10\mu s$	0	$1.28\mu m$
Nova-2	$5kV$	$1.6nA$	$10\mu s$	0	$1.6\mu m$
Nova-3	$16.5kV$	$2.3nA$	$10\mu s$	0	$1.7\mu m$
Nova-4	$16.5kV$	$11pA$	$10\mu s$	0	$2.13\mu m$
Verios-1	$1kV$	$25pA$	$0.1\mu s$	8	$1.6\mu m$
Verios-2	$5kV$	$25pA$	$10\mu s$	0	$1.03\mu m$

Table 2.4: Imaging settings for the two microscopes. Note that HFM is the horizontal field view.

The analysis of the benchmark sample was performed using the NanoAnalitik in-situ AFM, mounted in the FEI Nova Nano Lab 650 SEM, as shown in figure 2.19a. The AFM is mounted to fit below the electron-beam column and under a tilting angle, in order not to touch the ion-column, which is positioned under an angle of 52 deg on the right of the electron column. On the left of the electron column, the grid of the ETD detector is visible. Figure 2.21 shows an SEM micrograph of a sample that is being scanned with the in-situ AFM, where the cantilever and the tip are visible.

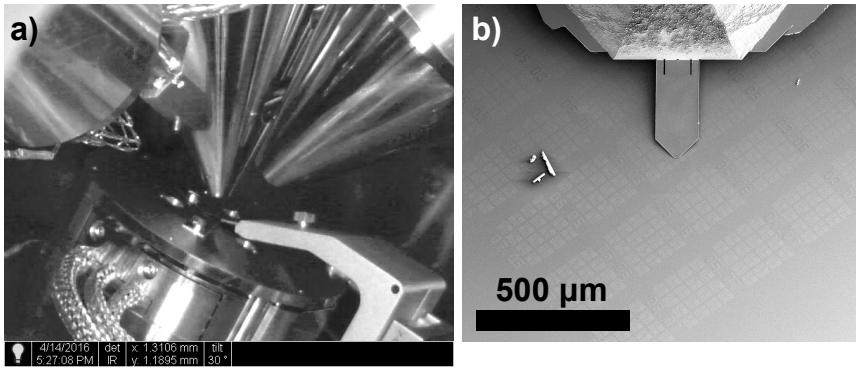

Figure 2.21: a) Image from the CCD camera inside the chamber of the Nova Nano Lab SEM showing the electron colum, the ion column, the ETD detector and the tilted stage, where the AFM is located. b) SEM micrograph showing the AFM cantilever while scanning the sample.

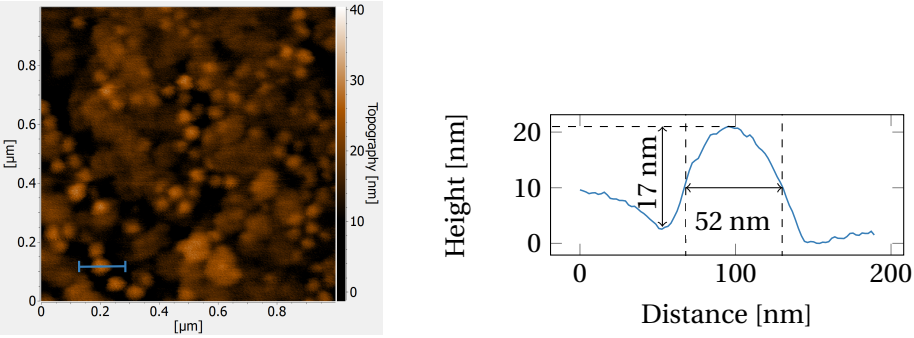

Figure 2.22: a) AFM image of the scanned area containing nanoparticles on a region outside the window and b) AFM profile of the particle highlighted in the figure on the left. The height of the particle is approximately $17nm$, whereas the width of the particle is $52nm$

However, because of the small size of the sample, it was not possible to clamp the sample to the AFM support, which would be ideal for avoiding drift. Using C-tape would indeed cause too much drift and the measurements could not be performed. Therefore, the AFM was mounted on the SEM stage, but the SEM door was left open, such that the AFM could be positioned at zero tilt. This way, however, it was quite difficult to navigate on this sample and only images of particles outside of the membrane of moderate quality were obtained. An example is the image on the left of figure 2.22, where the nanoparticles are clearly visible, but in a background that is very non-uniform. The height profile of the particle highlighted in the AFM scan is plotted on the right of figure 2.22. The width of the particle at half maximum (FWHM) is $52nm$, whereas the height is approximately $17nm$. As the particles are spherical, the broadening of the particles lateral dimension is caused by the tip not being infinitely small.

We carried out ten measurements on particles in each image and from those values we calculated the average value as well as the standard deviation. In table 2.5 the resulting particle sizes are shown for the instruments that were used in this task-force. The particle size was determined "by eye" from the SEM image. We chose this method because of the images being rather noisy. Also, the contrast of the particle in image *Nova-4* enhances the edges of the particle and drops in the middle, forcing us to use a different measurement method than in the other images. The particle size was measured therefore by loading the images in ImageJ [101] and measuring the particle from one border to the opposite. In case of the AFM analysis, the height of the particle was measured instead from the height profile. The height of the particles determined by the

AFM analysis is considerably smaller than that measured from the SEM image. The reason could be that the particle lay in a very rough background, giving misleading results. Also in this case, measurements of the height of the particles were performed on ten different particles.

Instrument	Image	Result [nm]
FEI Nova Nano Lab 650	Nova-1	46.9 ± 3.8
	Nova-2	58.5 ± 3.4
	Nova-3	41.8 ± 3.5
	Nova-4	48.2 ± 2.5
FEI Verios 460	Verios-1	51.5 ± 3.8
	Verios-2	47.3 ± 4.2
NanoAnalitik In-Situ AFM	AFM-1	13.1 ± 6.9

Table 2.5: Average particle size over a sample of 10 measurements on the images of figures 2.20 and 2.22.

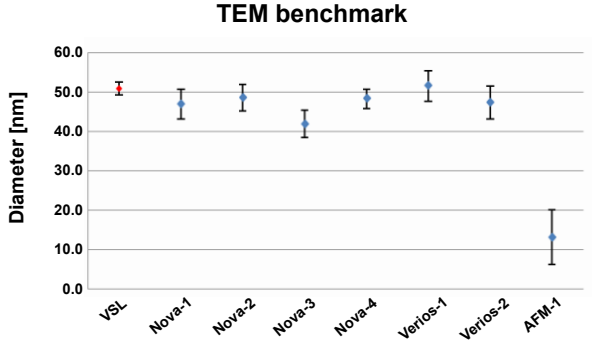

Figure 2.23: Results of the benchmark measurements using the nanoparticle sample. The reference averaged diameter measured at VSL is in line with the averaged diameter measured with the FEI Nova Nano Lab 650 and the FEI Verios 460 SEMs.

The sample was shipped back to VSL, where the analysis on the reference AFM was performed. The final results are shown in figure 2.23, where the measurements taken from the two FEI scanning electron microscopes and the in situ-AFM are compared with the reference measurement. The normalized error $| E_n |$ gives an indication of the error of the participant measurement with

respect to the reference value measured at VSL and it is calculated using the formula:

$$E_n = \frac{r_{lab} - R}{\sqrt{U^2(r_{lab})) + U^2(R)}} \tag{2.1}$$

Where r_{lab} is the measurement result of the participant, R is the reference value, $U(r_{lab})$ is the expanded measurement uncertainty for the result from the participant and $U(R)$ is the expanded measurement uncertainty for the reference value. $| E_n |$ describes the comparability of the measurement result with respect to the reference value, where absolute values of $| E_n |$ larger than 1 indicate an inconsistency with respect to the reference value. For all practical purposes this means that the difference between the measurement and the reference is too large given the stated uncertainties. The resulting normalized errors for our measurements are listed in table 2.6.

Instrument	Image	$\| E_n \|$
FEI Nova Nano Lab 650	Nova-1	0.9
	Nova-2	0.6
	Nova-3	2.3
	Nova-4	0.9
FEI Verios 460	Verios-1	0.2
	Verios-2	0.8
NanoAnalitik In-Situ AFM	AFM-1	5.3

Table 2.6: Average particle size over a sample of 10 measurements on the images of figures 2.20 and 2.22.

One of the results on sample *Nova-3* resulted in an $|En|$ value of 2.3. This measurement was taken for high voltage and high current settings, namely $16.5keV$ and $2.3nA$, in contrast to the other ones that were taken at lower voltage and/or lower current settings. For the In-Situ AFM result an $|En|$ value of 5.3 was calculated. This could be a result of the observation that the measured area by the Nanoanalytik AFM shows a very rough background. Such a rough background was not observed for areas at and near the membrane indicating that the measurement was taken at an area that does not represent the same or similar conditions as during reference measurements. Diameter measurements based on the particle height of particles on a rough background are more difficult to interpret and could lead to inaccurate results because a well defined reference plane is not available.

2.3.7 Conclusions

Defining the critical dimension of lines from images taken with a secondary electron detector is not trivial. In case of line profiles that have an M-shape the common definition of FW50 and FWHM cannot be applied, so the width must be determined with alternative ways. We have explored three methods for determining the line width: the first considers the line width as the distance between the two peaks, the second the distance at the height of the dip between the two peaks and the third the distance of the first peak and the second dip of the derivative of the line profile. While the first method is an underestimation of the width because it measures only the top flat of the line, the second and the third seem to be a more accurate estimation as they take into account the non-vertical sidewalls of the lines. Moreover, different imaging conditions may introduce unwanted effects that may broaden, or shrink, the line width, such as drift. The line pitch and the line position is then determined by the distance between two neighbouring peaks or the distance between the line peak and the reference peak. While AFM can measure the height of the structures with extreme high resolution, it is not the most reliable technique for width measurements as the line profile is the result of the physical profile of the line convoluted with the tip shape. In case of AFM, the pitch and the line position can be determined by the position of the peaks of each line.

The analysis results of the benchmark samples allows for a comparison of the performance of the instrumentation and analysis tools that were used to measure the required parameter values for those measurements that were stated with a measurement uncertainty. Bearing in mind these boundary conditions, the analysis of the CD line width measured by AFM results in values that are larger compared to the reference value most likely due to the critical dependence on probe shape correction, and for CPM very close to the reference value. The pitch results are both larger and smaller compared to the reference value for both techniques, and typically agree within slightly more than $1nm$ or approximately 2.4%. The line position analysis shows a linearly increasing difference (both positive and negative) for both techniques that were used in this benchmark, i.e. AFM and CPM. This can be attributed to an error in lateral calibration factor. This hypothesis is substantiated by the observation that the errors in the pitch and position are strongly correlated. A comparison between the two different types of instruments reveals a majority of positive differences for the AFM instruments while the CPM results are either too small or too large, the cumulative error is $20nm$, corresponding to 2.4%. The results from the benchmark provide a reference frame required for comparison

of measurement results from individual partners, and provides a typical value of the uncertainty, or confidence level, of the measurement results.

In the second task-force aimed at benchmarking the transmission electron microscopes in the consortium, silica nanoparticles on a SiN thin membrane were prepared and distributed among the partners. We imaged the samples with two scanning electron microscopes and an in-situ AFM. The size of the particles was determined "by eye" from the SEM images, whereas in case of the AFM analysis the size was determined by the height of the particles. The normalized error $|En|$ gives a hint on how accurate the measurements are with respect to a reference measurement. While the difference between the reference measurement and the measurement from the in-situ AFM is very large, those of the SEM images are smaller than 1 and therefore are consistent with the reference measurement. The only exception is for image *Nova-3*, where the measured average size of the particle is much smaller than the reference measurement.

The task-force on metrology aimed at evaluating the measuring methods among the SNM partners and comparing them to reference measurements. On one side, measuring M-shaped lines with the third method described in figure 2.12 resulted to be in line with the reference measurement. On the other side, AFM is not the ideal instrument for the measurement of CD width if not equipped with a tip-deconvolution function. Even though we tried to retrieve the position where the tip overstepped the two corners of the lines, this lead to measurements that were still far from the reference measurements. Also the measurement "by eye" on the silica nanoparticles confirmed to be accurate with respect to the reference measurement, in case of the SEM images.

3

Pattern transfer using etching masks made by EBID

Life would be tragic if it weren't funny.

Stephen Hawking

3.1 Introduction

Single nanometer structures, i.e. structures with dimensions smaller than $10nm$, are not easy to fabricate. Standard lithography techniques, such as resist-based electron beam lithography, do not routinely provide $sub-10nm$ resolution. Moreover, being serial writing techniques, they are inherently slow and not suitable for large area manufacturing. For large area manufacturing of single nanometer structures and devices it would be great when a fast and low-cost technique such as **Nano Imprint Lithography** (NIL) could be used. NIL is a non-conventional lithography technique with which nanostructures are fabricated through mechanical deformation of a soft polymer by pressing a

mold (or stamp) in it, at a controlled temperature and pressure. NIL is a massively parallel lithography technique and therefore extremely suitable to pattern large areas. But, a big challenge of this technique is the fabrication of high-resolution stamps. In the case of UV-assisted NIL, also known as Step and Flash Imprint Lithography (SFIL), the resist is cured with UV light, therefore transparent stamps are required. For thermal-NIL, the resist is cured thermally, hence the candidate material for molds can be silicon because of its hardness and high mechanical strength [14]. High resolution NIL stamps can be fabricated by depositing features on top of a substrate. Optical lithography is generally used for micron-scale features and Electron Beam Lithography (EBL) for patterning nano-scale features. These deposits form a mask for a subsequent anisotropic Reactive Ion Etch (RIE) into the underlying substrate, leading to the surface features required for NIL molds. $Sub-15nm$ nano imprint molds can be fabricated by using Electron Beam Lithography with hydrogen silsesquioxane (HSQ) resist by, either direct deposition of the features on top of the silicon substrate, or by transferring these deposits into the underling silicon substrate, to increase the aspect ratio of the patterns [102].

We propose to use EBID to fabricate stamps even for sub-10 nm NIL. For SFIL direct deposition of a UV transparent material on a transparent substrate would be possible, but it requires a suitable precursor that leads to transparent deposits. Instead we first study the fabrication of masks made by EBID, and transfer the masks into the Si substrate underneath using plasma etching to gain experience with sub-10 nm pattern transfer. These silicon samples can subsequently be used in nanoimprint lithography as masters for the fabrication of replicas, that serve as imprint templates. In order to directly fabricate NIL templates by EBID, UV-transparent samples need to be used. In this case, suitable substrates are Pyrex, or glass, coated with a conductive layer, that has to be UV-transparent as well. We investigated the pattern transfer into coating layers, that are both transparent and conductive: ITO, i.e. indium tin oxide, and TiN. ITO can be deposited very easily in a sputter coater, leading, however, to a very rough surface. On the other hand, TiN is deposited using Atomic Layer Deposition (ALD), leading to an atomically flat surface, that is preferred when patterning at the nanoscale. In this chapter, experimental results on the pattern transfer of EBID structures into silicon, ITO and TiN are presented and discussed. When patterning structures in the $sub-10nm$ scale, imaging the structures themselves and measuring their size is a challenge, because of the low contrast in SEM imaging. Repeating the experiment using thin membranes

allows imaging in transmission electron microscopes (TEM), leading to high resolution imaging. Hence, experiments on the pattern transfer into SiN thin membranes are also carried out, where the patterning is done in a scanning electron microscope and the imaging in a high acceleration voltage TEM.

3.2 Pattern transfer into silicon[‡]

The pattern transfer process of features in the $sub-10nm$ scale in itself is quite a challenge. Guan et al. demonstrated the pattern transfer into silicon of masks made by EBID using $W(CO)_6$ or $C_{10}H_8$ as a precursor, resulting in silicon nanowires with a width of $33nm$ [103]. The etching process, which is based on SF_6 and C_4F_8, leads to a selectivity of approximately 21. They even succeeded in fabricating nanopillars with sizes down to $13.5nm$, and a selectivity of 18, using a bilayer approach with an EBID mask on top of a polymethylmethacrylate mask. However, the authors do not expect that the bilayer approach has an inherently superior resolution over a single-layer approach. Notargiacomo et al. reported on the pattern transfer of ion and electron deposited Pt masks by using Reactive Ion Etching, where pattern transfer of lines with width down to $100nm$ is obtained with fluorine chemistry [104]. The same chemistry was used by Heerkens et al., who demonstrated the pattern transfer into silicon of $20nm$ wide lines deposited using EBID from a platinum precursor. They achieved a selectivity of the Pt-EBID lines to silicon of approximately 6 [105]. The pattern transfer of EBID masks can be used for many applications, e.g. gold bow-tie antennas with $10nm$ gap spacing were fabricated on AFM tips [106]. Fleischer et al. presented a process for the fabrication of nano-cones by focused electron beam deposition of a local etch mask on a metallized non-planar surface, and argon ion etching. The smallest resulting cone had a diameter of $60nm$ and height of $55nm$ [107]. Recently Weppelman et al. [108] presented the fabrication of narrow-gap nanostructures made by electron beam induced deposition and transferred into the underlying metal layer using a chromium sacrificial layer as etching mask. However, as far as we know, the pattern transfer of $sub-20nm$ EBID structures without the use of sacrificial layers has not been reported yet.

[‡]This section is published as:
Scotuzzi M., Kamerbeek M.J., Goodyear A., Cooke M. and Hagen, C. W., Pattern transfer into silicon using sub-10 nm masks made by electron beam-induced deposition, *J. of Micro/Nanolithography, MEMS, and MOEMS, 14(3), 031206 (2015)*

We present here the results of experiments that were carried out to gain experience towards etching with $sub-20nm$ EBID masks. As $sub-10nm$ structures deposited by EBID are also very shallow, with a typical aspect ratio of one, the pattern transfer into an underlying layer is a method by which the aspect ratio of the structure can be increased. High resolution EBID patterns were deposited onto a silicon substrate, serving as a mask for the subsequent etching process. Two sets of EBID masks, one with somewhat larger structures between 20 and $40nm$ and one with structures between 8 and $20nm$, were fabricated using the platinum precursor $MeCpPtMe_3$ (methyl- tri-methyl-cyclo-pentadienyl platinum) in an FEI Nova Nano Lab 650 Dual Beam system. The masks consist of arrays of dots and sets of lines, with sizes in the range between $40nm$ and $8nm$. We used different etching processes, based on hydrogen bromide, chlorine and fluorine chemistries, that are known to etch silicon.

3.2.1 Experiments

Basically two sets of experiments were performed. The first experiments were carried out to get some experience with pattern transfer into silicon using EBID structures as etching mask. Larger structures are preferred, because they are easier to find after the etching process. The second set of experiments then is carried out to demonstrate the pattern transfer into silicon of $sub-10nm$ EBID masks, with deposits of size down to $8nm$.

The quality of the etching process is mostly determined by the directionality of the etching. Preferably the etch is anisotropic, very selective and results in smooth surfaces after etching. To determine the directionality of the etching is challenging as the resulting structures are really small. The change in width of the structures gives an indication of the directionality.

The inspection of the masks, before and after etching, is done both in an FEI Nova Nano Lab 650 Scanning Electron Microscope (SEM) and in a Bruker Nanoscope V Atomic Force Microscope (AFM). The lateral dimension of the structures is manually measured in the SEM images, while the height is calculated from the AFM profile.

The smoothness of the resulting surface after etching is an important factor with the goal in mind to fabricate single-digit nanometer devices. To characterize the etching process usually the etch selectivity is determined, defined as the

ratio of the etching rate of the substrate material to the etching rate of the mask material. Because of the dimensions of the structures, it is difficult to measure the selectivity of the tested etching processes. Hence, we chose to characterize the process by the height ratio, defined as the ratio between the height of the mask before etching and the height of the structure after etching. This parameter gives a hint to what the etching rates of the materials are. A large height ratio is preferred because it leads to higher aspect ratio structures.

The first set of $20-40nm$ EBID masks was fabricated using the Platinum precursor $MeCpPtMe_3$ in an FEI Nova Nano Lab 650 Scanning Electron Microscope, using a $30kV$ beam focused in a $40pA$ spot, which corresponds to a probe size of $< 2nm$, in High Resolution (HR) mode. We used silicon substrates partially covered by $60nm$ of molybdenum. Because the total size of the EBID mask is only $4\mu m$, a search pattern is necessary to be able to retrieve the structures after pattern transfer. Hence, an array of 13x13 circular holes of approximately $10\mu m$ diameter has been lithographically opened in the molybdenum layer using photoresist as a mask, leading to a visible structure that can be easily retrieved. Figure 3.1 shows the process flow for the sample fabrication. The sacrificial layer (photoresist) is deposited on top of the silicon substrate. By means of optical lithography, the array of circles is transferred into the photoresist (PR) layer. A molybdenum layer is deposited on the sample surface after which the resist is removed in a lift-off process. The EBID structures are then deposited inside one of these circles, directly on the silicon surface.

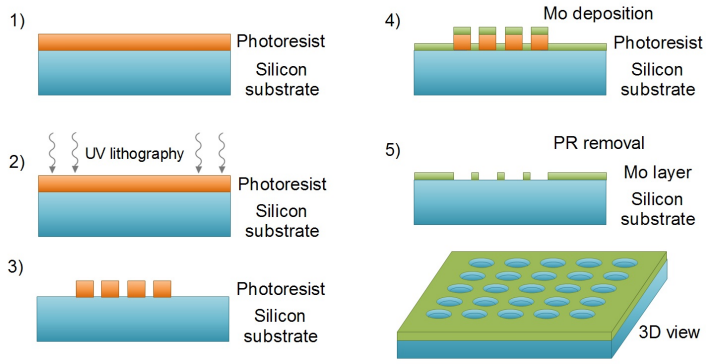

Figure 3.1: Process flow for the fabrication and 3D view of the search pattern on the Si sample.

The EBID masks, patterned with the Pt precursor, typically consist of car-

Array	**Size of each pixel** (dot)	**Dwell time**	**Number of passes**
A (top left)	15x15	$400ns$	1000
B (top right)	10x10	$800ns$	1000
C (bottom left)	5x5	$1\mu s$	1000
D (bottom right)	5x5	$400ns$	1000

Table 3.1: Electron beam induced deposition (EBID) parameters for the $20-40nm$ masks.

bon (85%) and platinum (15%). The first set of masks consists of four arrays of 5 by 5 dots, with a size in the $sub-40nm$ range. Figures 3.2a and 3.2b show the SEM micrograph and the AFM image of one of the patterned EBID masks, whilst Table 3.1 shows the patterning parameters for each array of dots. Each dot is defined as a square, the size of which is determined by the number of pixels exposed by the electron beam and the pixel to pixel distance. The latter was chosen equal to the diameter of the electron beam. The beam is scanned from one spot (pixel) to the next one following a serpentine writing strategy. The beam resides at each pixel for a certain amount of time, called the dwell time. The whole pattern is written 1000 times (the number of passes), We will refer to array A as the top left array of dots, B the top right, C the bottom left and D the bottom right. The diameter of the dots varies from 40 nm to 19 nm, while the height of the dots in Array A is approximately 4.7 nm.

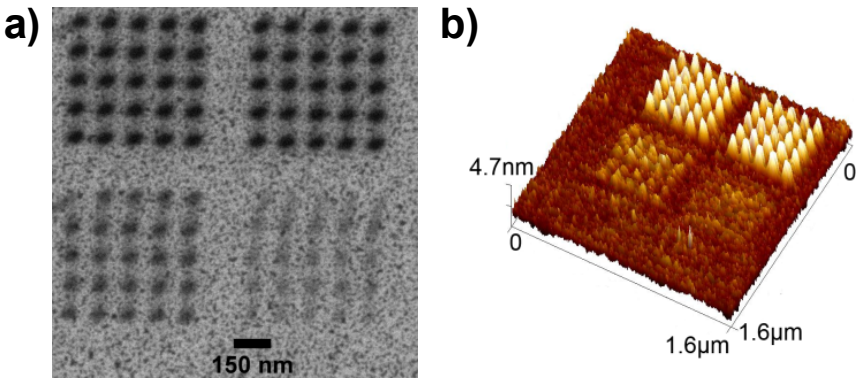

Figure 3.2: a) SEM micrograph of the $20-40nm$ EBID masks. b) AFM 3D view of the $20-40nm$ EBID mask.

Because the mask is shallow it is important that the chosen chemistry is very selective towards the EBID structures. The etching process used to transfer the EBID structures into the underlying silicon is carried out by Inductively Coupled Plasma (ICP) etching, performed in a PlasmaLab System 133 ICP380 at the Oxford Instruments Plasma Technology (OIPT) facility in the UK. Plasma based etching allows processes to be carried out at relatively low temperature by lowering the activation energy of the chemical etching reactions. Moreover, plasma etching allows a wide area to be processed, providing uniform etching and control over the direction of etching. Figure 3.3 shows the schematic of the ICP etching tool. By applying a combination of RIE power at the lower electrode and ICP power to the coils around the upper chamber, a better control over the ion density and the ion energy is provided. The wafer is mechanically clamped to the fluid-cooled lower electrode and helium is used as the sample backside cooling gas for better control over the wafer temperature. The backside cooling gas mixes with the etching gas in the chamber, but it has almost zero impact on the process, being light, hard to ionise and chemically inactive. The sample pieces were bonded to a carrier wafer to ensure good temperature control. A gas inlet leads the gas mixture into the chamber, that is at a controlled pressure and temperature [109].

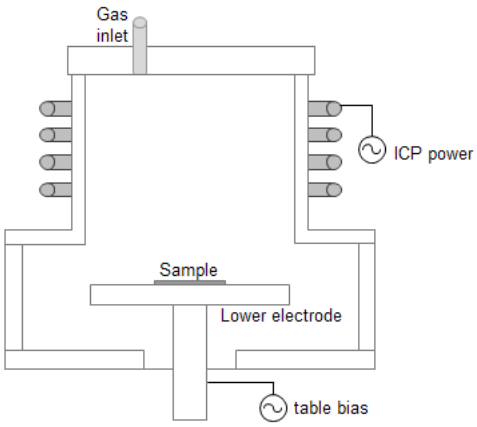

Figure 3.3: ICP RIE plasma etching tool used in the OIPT facility.

These masks are etched using hydrogen bromide HBr, chlorine Cl_2 and boron trichloride (BCl_3/Cl_2) chemistries, that are known to selectively etch silicon when using carbon-based masks. These etching processes are carried out by using both ICP and RIE power. HBr chemically reacts with silicon atoms

on the surface, forming Si_xBr, a compound with low volatility [109]. This characteristic makes HBr to be a highly anisotropic silicon etchant, in which Si_xBr forms a sidewall protective layer. Chlorine is also known to etch silicon either in a pure form or as part of the gas mixture BCl_3/Cl_2 [110]. When using either pure Cl_2 or BCl_3/Cl_2 chemistry, silicon atoms bind to Cl_2 forming the volatile compound $SiCl_x$, that can be pumped out of the system. Chlorine etching is strongly crystallographic, leading to an anisotropic etch profile [111]. Once the properties of each chemistry are determined, they can be further tested on even smaller EBID masks, to demonstrate the pattern transfer of $sub-10nm$ structures.

For that purpose the second set of $8-20nm$ EBID masks was fabricated in the same setup as the first set of masks, with a $20kV$ beam, focused in a $40pA$ spot, but now in Ultra High Resolution (UHR) mode. In this case we used a different substrate than the molybdenum-silicon one. The reason for that is that the smoothness of the molybdenum layer makes focusing of the electron beam a difficult process. We decided to use the same search pattern, but instead of depositing a metal layer outside the array of circular holes, we plasma-etched the Silicon for a very short time using SF_6 and oxygen such that black silicon is formed at approximately $20nm$ below the un-etched silicon surface. Figure 3.4 shows the process flow of the fabrication of the black silicon samples used for the fabrication of the 8 – 20 nm EBID masks.

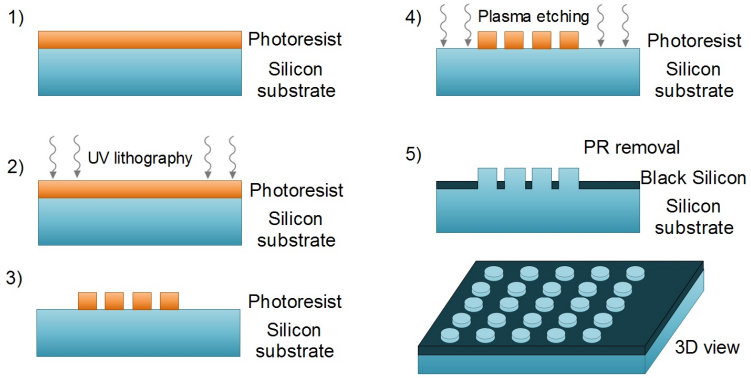

Figure 3.4: Process flow for the fabrication and 3D view of the optimized search pattern on the Si sample.

In this configuration, the EBID patterns are deposited inside the circles

on top of un-etched silicon, surrounded by the pillar-shaped black silicon, on which focusing the beam is really easy. Figure 3.5a shows a $8-20nm$ EBID mask. It consists of three arrays of 5 by 5 dots and 9 sets of lines. The dots have sizes of approximately $20nm$, $13nm$ and $7nm$ and a height of $7nm$, $2.5nm$ and $1nm$, for the top left, central and right array respectively. Each set of lines consists of 10 lines with $100nm$, $50nm$ and $20nm$ spacing. The width of these lines is $17nm$, $10nm$ and $8nm$, whilst the height is $5nm$, $2nm$ and $0.8nm$ for the first, second and third column respectively. Figure 3.5b shows the high resolution image of the $8n$m set of lines, with $50nm$ spacing.

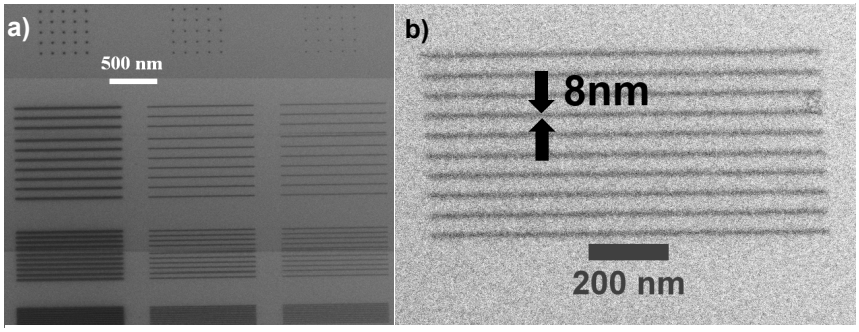

Figure 3.5: a) SEM micrograph of the $sub-20nm$ EBID mask. b) High resolution SEM micrograph of the $8nm$ lines at $50nm$ spacing.

Table 3.2 shows the deposition parameters and the designed pixel size of each structure of the mask. In this case a single pass patterning mode is chosen, instead of a multi-pass strategy. The deposition occurs in the current limited regime in which there is an abundant supply of precursor molecules. Hence the resulting deposits will not be affected by the chosen writing strategy (single pass or multi-pass), as demonstrated by Hari et al. [112]. The multi-pass strategy is preferred because it is less sensitive to the proximity effect.

The sample fabrication and subsequent inspection, that needs to be done before and after the etching, is a very time consuming process, hence the amount of samples available is limited. Therefore, the etching chemistries for the $8-20nm$ masks have to be chosen carefully. The chemistries chosen are hydrogen bromide (HBr), chlorine (Cl_2) and fluorine (SF_6/C_4F_8), for reasons that will be discussed later. Chemical etching by fluorine is known to be isotropic, therefore it is necessary to add a component that provides anisotropic etching. We used

Array	Size (pixel)	Dwell time	Number of passes
D-A (top left)	12x12	$100\mu s$	1
D-B (top centre)	8x8	$100\mu s$	1
D-C (top right)	5x5	$100\mu s$	1
Set of lines	**Size (pixel)**	**Dwell time**	**Number of passes**
L-A (left)	1000x1	$1ms$	1
L-B (centre)	1000x2	$100\mu s$	1
L-C (right)	1000x1	$100\mu s$	1

Table 3.2: EBID parameters for the $8-20nm$ masks.

an SF_6 plasma, that is known to etch silicon easily, and by adding C_4F_8 a fluorocarbon film is deposited that protects the sidewalls of the etched structure and sustains the anisotropy of the etching process. However, the ratio between carbon and fluorine needs to be tuned carefully, because polymer deposition can occur when the F-to-C ratio is too small.

3.2.2 Results and discussion

Initial experiments were carried out on $20-40nm$ etching masks to demonstrate the possibility of using EBID masks for nano-patterning into underlying silicon. In this case, HBr, Cl_2 and BCl_3/Cl_2 chemistry were chosen because of their affinity to etch silicon better than carbon, i.e. the main element in the EBID deposit when using the Pt precursor. In case of HBr, helium, that is used as a sample backside cooling gas, is also pumped into the system,. A combination of ICP and RIE power is used ($750W$ and $100W$ respectively), at a pressure of $10mTorr$ and a temperature of $30°C$, for 1 minute. Figure 3.6a shows a SEM micrograph of the etched mask: as the EBID masks were completely etched away the dots consist of silicon only, leading to a poor contrast in the secondary electron image. Figure 3.6b shows the same mask as in Figure 3.6a compared to the AFM 3D view, where the dots are more visible. The AFM height profile of the central horizontal row of dots, before and after etching, is shown in Figure 3.6c. We observe that this chemistry leads to a rough surface and provides a height ratio (after etching : before etching) of less than 2. The diameter of the dots remained constant, as observed from the SEM images. In this case, only the largest EBID dots could be retrieved after etching.

By inserting a dummy silicon sample in the plasma chamber, next to that with the EBID masks, it is possible to measure the etch rate of silicon. The same can be done in case of silicon oxide. The etch rate of the silicon oxide is measured to be approximately $2nm/min$, while that of silicon is approximately $46nm/min$. We conclude that the etch rate of the native silicon oxide is comparable or maybe even lower than that of the EBID deposits, causing complete etching of the mask before reaching the silicon substrate.

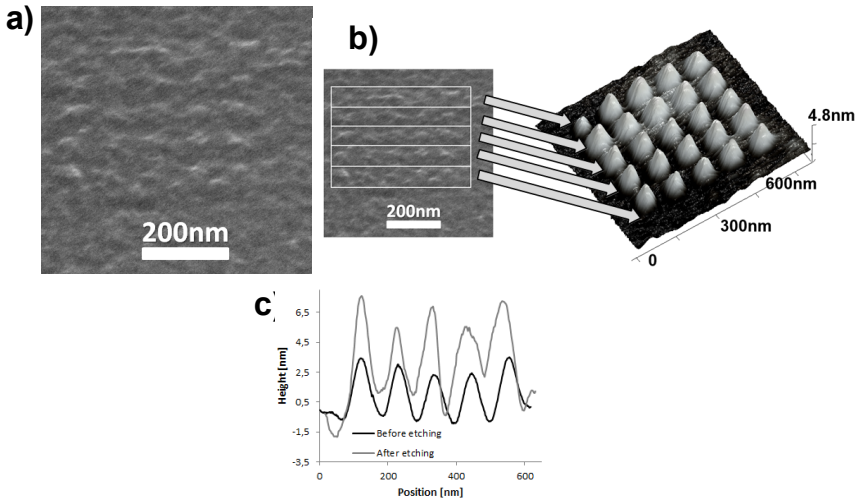

Figure 3.6: a) SEM micrograph of the array of dots A after etching (HBr chemistry). b) SEM micrograph and AFM 3D profile of the array of dots A after etching (HBr chemistry). c) The height profile measured with AFM of the horizontal central row of array A, before and after etching (HBr chemistry).

In case of pure chlorine chemistry, 50 sccm of Cl_2 is led into the chamber, together with backside cooling helium, at $10mTorr$ and $30°C$. When etching with Cl_2 for 1 minute, the surface of the sample became extremely granular, and the EBID dots too. The size of the dots, as estimated from the SEM images (Figure 3.7a), increased from $40nm$ to approximately $55nm$. As seen from the AFM profile (Figure 3.7b) the height ratio is approximately 3.5. Although this is an acceptable number, the granularity of the resulting mold will prevent the successful fabrication of single nanometer devices.

Figure 3.8a shows the result after etching with BCl_3/Cl_2 chemistry for 1

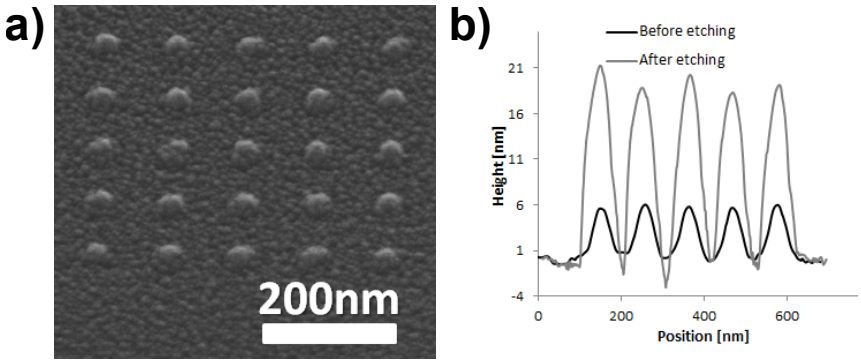

Figure 3.7: a) SEM micrograph of the array of dots A after etching (Cl_2 chemistry). b) The height profile measured with AFM of the central horizontal row of array A, before and after etching (Cl_2 chemistry).

minute. $50sccm$ of Cl_2 and $20sccm$ of BCl_3 are led into the chamber together with helium, at $10mTorr$ and $30°C$. In this case, the surface remained smooth, as shown in Figure 3.8a. However, some particles can be seen, close to the etched mask, as well as in other regions of the samples. The reason for that has not been established yet, but we think this might be caused by dirt in the etching chamber. The height ratio is approximately 2.5 (Figure 3.8b), while the diameter, as measured from the SEM image, increased from $40nm$ to approximately $50nm$. This could be caused by the halo deposited around the structures.

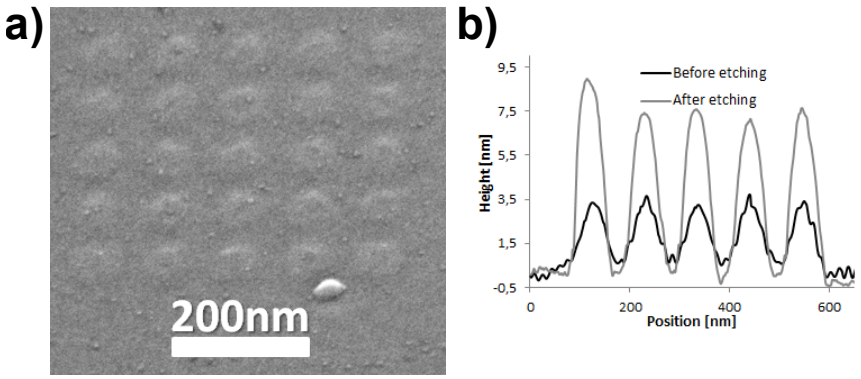

Figure 3.8: a) SEM micrograph of the array of dots A after etching (BCl_3/Cl_2 chemistry). b) The height profile measured with AFM of the central horizontal row of array A, before and after etching (BCl_3/Cl_2 chemistry).

Analysing the results, we observe good results in terms of height ratio for the Cl_2 etching process. Although, the resulting presence of the granularity must be avoided. The granularity may have been caused by the black spots on the silicon surface observed before etching and visible in Figure 3.2a. They could be resist residues from the lift-off process and cause the sample surface to become granular after the Cl_2 process. This might also explain the roughness of the surface resulting after the HBr etching process. To prevent this, the substrates for the $8-20nm$ EBID masks were carefully cleaned in an oxygen plasma before carrying out the etching step. We decided to repeat the hydrogen bromide and the chlorine recipes to verify whether the oxygen plasma cleaning improves the surface roughness. Because of the limited number of samples available, we decided to carry out a fluorine chemistry instead of BCl_3/Cl_2. Although known to be isotropic, fluorine etches silicon very fast and by adding other components, such as C_4F_8, a passivation wall can be formed, making the etch more anisotropic.

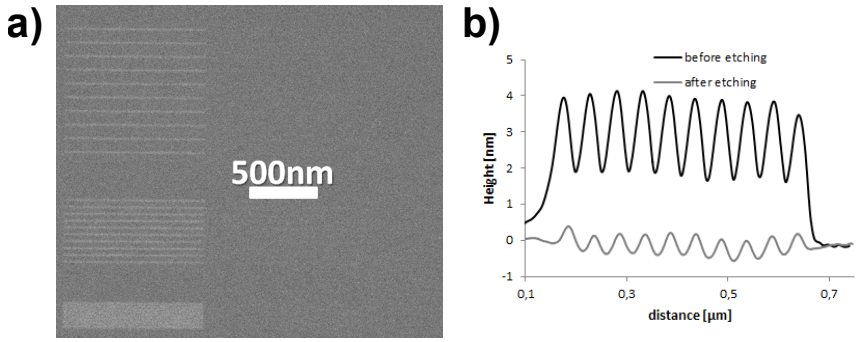

Figure 3.9: a) SEM micrograph of the EBID mask after etching (HBr chemistry). b) The integrated height profile measured with AFM of the $17nm$ lines with $50nm$ spacing, before and after etching (HBr chemistry).

HBr, Cl_2 and SF_6/C_4F_8 chemistries are then tested for the pattern transfer of the $8-20nm$ EBID masks. In case of the HBr chemistry, only the biggest set of lines is visible in both the SEM micrograph and the AFM image after the etching is performed. For these lines, of $17nm$ width and $5nm$ height, the EBID mask is preserved as it was thicker than the other deposits. In Figure 3.9a, the SEM micrograph shows the $17nm$ lines with spacing of $100nm$, $50nm$ and $20nm$. In figure 3.9b the integrated AFM profile of the $17nm$ lines with $50nm$ spacing shows that the height ratio is very low, approximately equal to $1/5$. In this

case, the etch rate of silicon is measured to be $50nm/min$ and that of silicon oxide is $1.8nm/min$. Although the etching rates are comparable to those of the $20-40nm$ mask experiments, the small height ratio might be caused by a thickening of the native silicon oxide layer during the plasma cleaning. If that is the case, the etch may remove the mask completely before breaking through the oxide layer, because of the slow etching rate of the silicon oxide. Further experiments were carried out to increase the etch rate of the silicon oxide by applying a higher bias voltage, however no improvements were observed. In case of the $17nm$ lines at $50nm$ spacing, the width decreased from $17nm$ to $12nm$ after etching, as estimated from the SEM images.

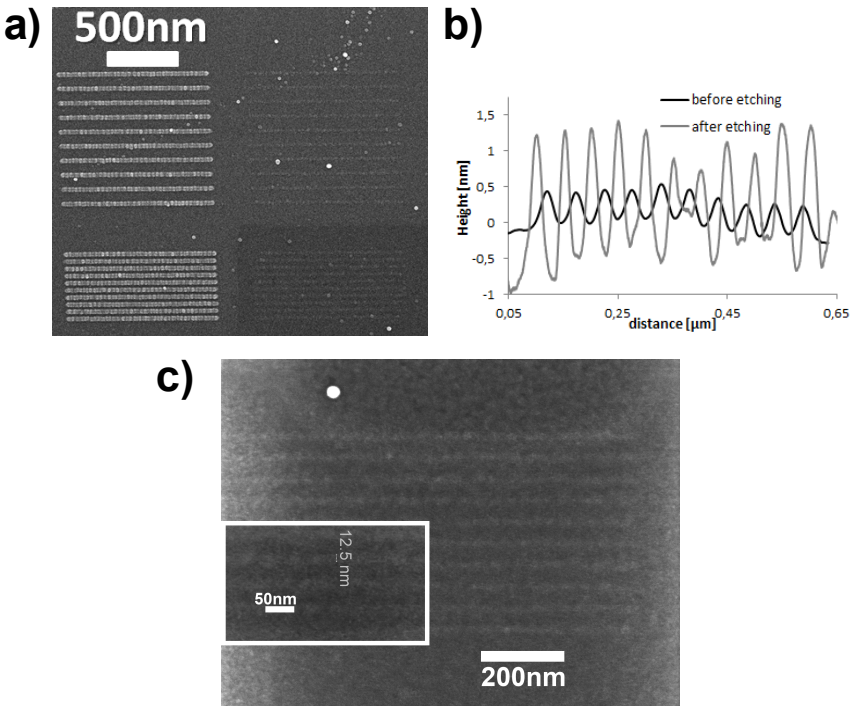

Figure 3.10: a) SEM micrograph of the EBID mask after etching (Cl_2 chemistry). b) The integrated height profile measured with AFM of the $5nm$ lines with $50nm$ spacing, before and after etching (Cl_2 chemistry). c) High resolution SEM micrograph showing the widening of the $8nm$ lines to $12.5nm$.

The sample surface, however, is quite smooth and the roughness observed in the case of the $20-40nm$ mask experiment did not occur. We therefore believe that the roughness caused by the HBr etching was caused by the photore-

sist residues on the silicon surface.

In case of pure chlorine etching, when using the same recipe as for the $20-40nm$ masks, the same granularity is observed, as shown in the SEM image of Figure 3.10a. All sets of lines were visible in both SEM and AFM graphs and the integrated AFM profile along the $8nm$ lines at $50nm$ spacing, depicted in Figure 3.10b, shows a height ratio of approximately 3.5. For these lines, the width increased from $8nm$ to $12.5nm$. Note that some particles close to the EBID deposit are seen in figure 3.5b, but they were also found in regions of the sample that have not been exposed to the electron beam while fabricating the etching mask.

Their origin has not been established yet, however we believe it can be caused by dirt in the etching chamber.

Lastly, fluorine etching chemistry is tested on a $8-20nm$ mask. In this test, $25sccm$ of SF_6 is mixed together with $50sccm$ of C_4F_8, at a pressure of $15mTorr$ and a controlled temperature of $15°C$, and at $1200W$ ICP and $30W$ RIE. The etch rate of Silicon in this condition is measured to be approximately equal to $160nm/min$, while that of the native oxide is $20nm/min$.

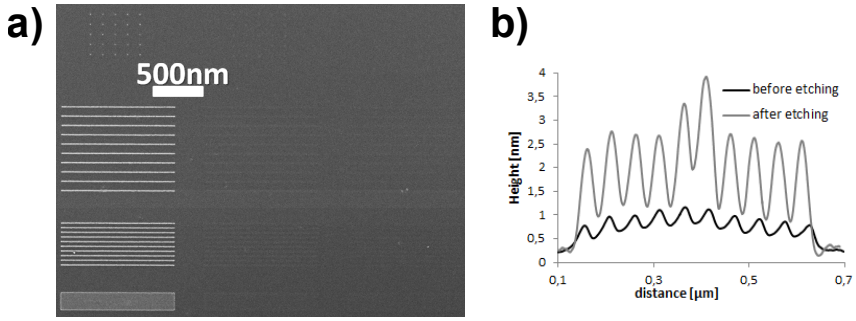

Figure 3.11: a) SEM micrograph of the EBID mask after etching (fluorine chemistry). b) The integrated height profile measured with AFM of the $8nm$ lines with $50nm$ spacing, before and after etching (fluorine chemistry).

The resulting lines appear to be smooth in the SEM micrograph, as depicted in Figure 3.11a. No granularity or roughness is encountered and the height ratio calculated from the integrated AFM line profile in figure 3.11b is approximately 5. The graph in figure 3.11b depicts the AFM integrated profile of the $8nm$ lines at $50nm$ spacing. The bump located in the fourth and fifth line corresponds to the presence of a particle accidentally deposited on top of these lines. For these

lines the width increased from 7.4nm to 14.3nm approximately, as shown in Figure 3.12a and Figure 3.12b. The contrast of the SEM micrograph in Figure 3.12b is extremely poor as the EBID mask has been completely removed during the etching process. The secondary electron image therefore only shows topographical contrast and no material contrast. This makes the measurement of the line width rather difficult.

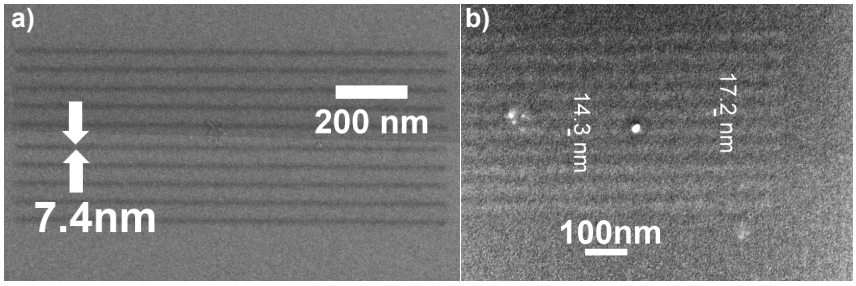

Figure 3.12: a) SEM micrograph of the EBID mask, zoom-in of the region of the 8nm lines at 50nm spacing, before etching (fluorine chemistry). b) SEM micrograph of the EBID mask; a zoom-in of the region of the 8nm lines at 100nm spacing, after etching (fluorine chemistry).

The sets of 17nm lines emit more secondary electrons than the others, as shown in Figure 3.11a, meaning the EBID mask was thick enough to remain. Figure 3.13a shows the high resolution SEM micrograph of the 17nm lines at 50nm spacing after etching. The width of the lines is measured to be 9.8nm, suggesting that the line width decreased. This could also be concluded from Figure 3.13b, that shows the integrated line profile of the secondary electron intensity emitted by the 17nm set of lines with 50nm spacing before and after etching. However, the AFM profile in Figure 3.13c reveals a broadening of the lines after etching, and a height ratio of about 8. This broadening, though, could be partly caused by the finite size of the AFM tip. Our conclusion is that it is not so obvious what a good criterion is for line width determination from SE-images.

3.2.3 Summary and Conclusion

EBID is a direct write lithography technique, that can be used to pattern high resolution structures, with sizes in the $sub-10nm$ range. Pattern transfer into silicon using masks made by EBID is a method that can potentially be used to fabricate stamps for Nano Imprint Lithography as it provides an aspect ratio en-

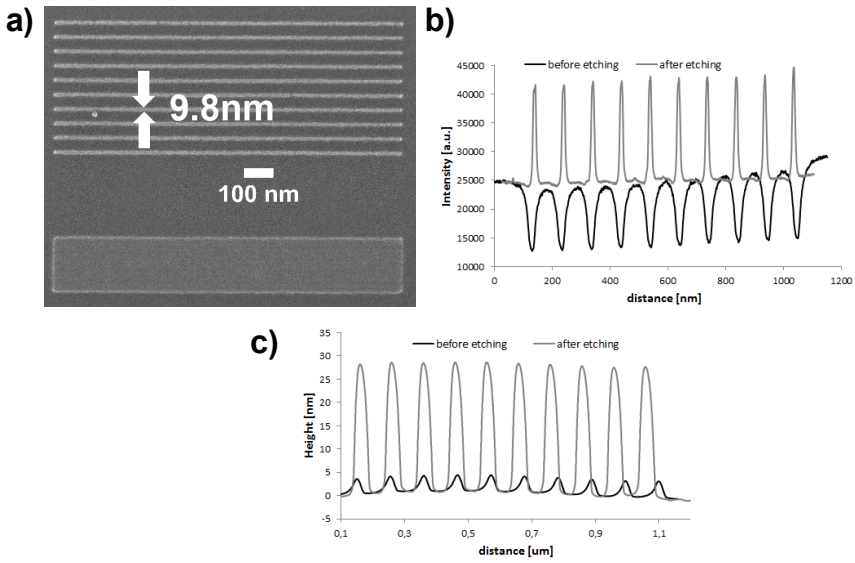

Figure 3.13: a) SEM micrograph of the EBID mask, zoom-in of the region of the $17nm$ lines at $50nm$ spacing, after etching (fluorine chemistry). b) Integrated secondary electron intensity of the $17nm$ lines at $50nm$ spacing, before and after etching (fluorine chemistry). c) AFM integrated profile of the $17nm$ lines at $50nm$ spacing, before and after etching (fluorine chemistry).

hancement compared to the aspect ratio of the EBID masks. Initial experiments were carried out using $20-40nm$ EBID masks, containing dots and lines, to demonstrate the possibility of using EBID masks for nano-patterning into underlying silicon. In this case, etching chemistries based on hydrogen bromide (HBr), chlorine (Cl_2) and boron trichloride (BCl_3) were chosen for their affinity in anisotropically etching silicon when using carbon-based masks. When etching with HBr chemistry, the EBID masks are transferred into underlying silicon with a height ratio, i.e. the ratio of the height of the structures before etching and after etching, of approximately 2, while the diameter of the dots remained constant. The roughness of the surface observed after the HBr etching might be caused by some residuals of photoresist, used for the fabrication of the samples. Chlorine etching leads to a height ratio of approximately 3.5 and the size of the dots increased from $40nm$ to $55nm$. However, in this case we observed a surface granularity, that was shown not to be caused by the photoresist residuals. BCl_3 mixed with pure chlorine provides a height ratio of approximately 2.5,while the size of the dots increased from $40nm$ to $50nm$. When using this chemistry, no surface roughening occurs. Further experiments were carried out with even smaller EBID masks to demonstrate the pattern transfer

of $sub-10nm$ structures. For this purpose, EBID masks consisting of lines with sizes varying from $17nm$ to $8nm$ were fabricated. In order to avoid the roughening and the granularity of the etched samples, the EBID masks were further cleaned in an oxygen plasma. This indeed led to smooth surfaces after HBr chemistry. The height ratio is now smaller than 1/5 probably because of the thickening of the native oxide layer as a result of the plasma cleaning. Because the etch rate of the silicon oxide using the hydrogen bromide chemistry is low compared to that of the EBID deposits, it is not possible to break through the oxidelayer without removing the mask. In case of pure chlorine etching, the height ratio remained approximately 3.5, as in the case of the $20-40nm$ masks, and the lines widened from $8nm$ to $12.5nm$. However, the granularity can still be observed on the sample surface as well as on the lines themselves, meaning that this is an inherent effect of the Cl_2 etch. Very good results are obtained with the fluorine based etching, in terms of height ratio and surface smoothness. In case of the $8nm$ lines, the height ratio is approximately 8 and the width increased from $7.4nm$ to $14.3nm$. However, because the mask was completely removed during the etching, the lines are made of only silicon, causing a very poor contrast in the secondary electron image. The $17nm$ EBID lines, being also thicker than the $8nm$ lines, were not completely etched away and the resulting lines have a width that is measured to be $9.8nm$. In summary: we have demonstrated that the pattern transfer of $7.4nm$ wide lines into silicon, using chlorine and fluorine chemistries, resulted in slightly broader lines of $14.3nm$ width.

3.2.4 Remarks on the line width measurement

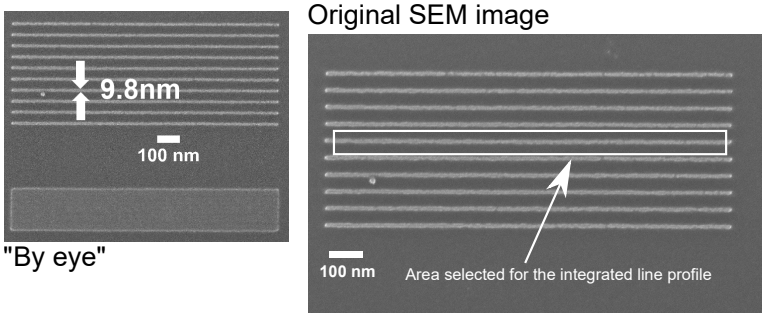

Figure 3.14: On the left, SEM image of the $9.8nm$ line as shown in figure 3.13a. On the right, the same image with an highlight on the line and the area where the integrated line profile was extracted.

The measurement of the line width is not trivial. In Chapter 2, we presented the measurement of lines with M-shaped profiles and analyzed three methods for the definition of the line profile. In this chapter, all measurements were performed "by eye", where the images were loaded into the ImageJ program and analyzed by manually dragging a measurement line. However, this method is very user-dependent and suffers from how the user distinguishes the "line" from the "background". In this section, we analyze the width of the lines shown in figure 3.13a, which have reported a width of $9.8nm$ (judgment "by eye"), using the inflection point method and the definition of FWHM and FW50 from the line profile integrated over the entire length of the line itself, as shown in figure 3.14. In this figure, we report the SEM image of the $9.8nm$ line, where we highlight the line that is analyzed and the area over which the integrated profile is extracted. As shown in figure 3.15, in the inflection point method, the derivative of the integrated line profile is calculated and the width is defined as the distance between the first peak and the subsequent minimum. The width measured with this method is equal to $12.9nm$. Following, the FWHM and the FW50, calculated via a simple Matlab script, report widths of $13.8nm$ and $14.72nm$. Those values are slightly bigger than the $9.8nm$ that was determined "by eye".

The estimation of the line width "by eye" is $3nm$ less than what is measured with the inflection point method, inducing and error of approximately 30%. We conclude that it is difficult to determine a "real" line width value, as there are many definitions and many techniques to measure the line width, all suffering from inaccuracies. The best approach is therefore to chose a line width measurement throughout the experiments and compare measurements derived from the same method.

3.3 Pattern transfer into ITO

3.3.1 Plasma etching of ITO using photoresist mask

Electron Beam Induced Deposition (EBID) will be used by us to fabricate stamps for Nano-imprint Lithography (NIL). Step and repeat NIL requires UV transparent stamps that can be made by EBID in two ways. By direct deposition of transparent features on top of the NIL stamp, or by transferring EBID fabricated patterns into the stamp material. We chose to aim at the latter and have studied the transfer of such nano-patterns into an underlying substrate using plasma etching. As transparent material, a glass substrate covered with ITO (indium-tin-oxide) can be used. Experiments were performed on a Plasmalab

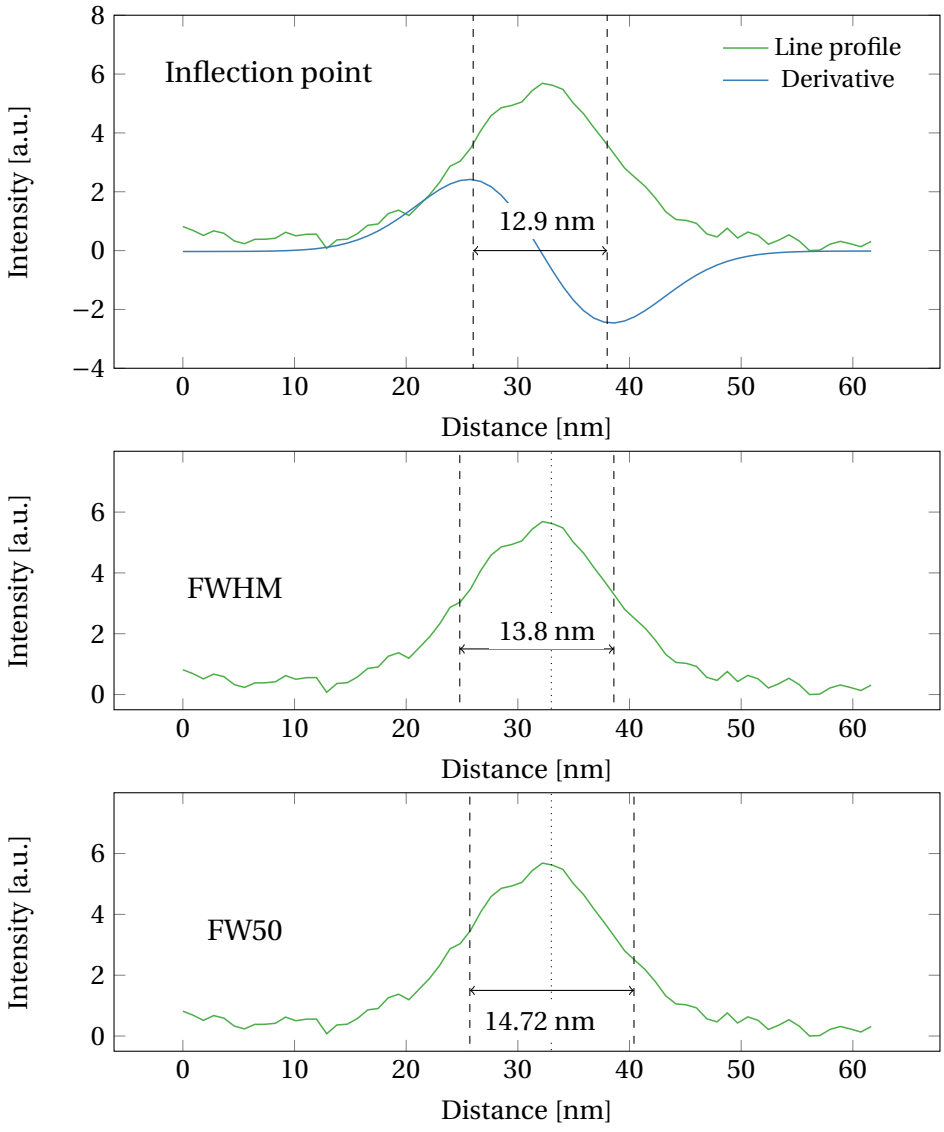

Figure 3.15: Width measurement of the line in figure 3.13a using the inflection point method and the definition of FWHM and FW50. The width of the line is measured to be 12.9nm, 13.8nm and 14.72nm, whereas "by eye" if was determined to be 9.8nm.

system133 etcher at and in cooperation with Oxford Instrument Plasma Technology (OIPT).

First, the etching recipe for ITO needs to be developed. For the process set up, we used ITO coated Si samples covered with a $1.4\mu m$ thick layer of AZ5214E photoresist (PR). We assume the resist to be comparable to EBID deposits patterned with the platinum precursor ($MeCpPtMe_3$) as both consist mostly out of carbon. The pattern in this resist consisted of trenches that can easily be measured with the metrology equipment available at OIPT, i.e. a high end scanning electron microscope and a profilometer. The long term goal is to find an etching recipe, by which $sub-10nm$ EBID deposits are transferred into underlying ITO, forming a NIL mask. Because $sub-10nm$ EBID deposits are also very shallow, in the order of few nanometers, the etching recipe must provide a high selectivity (at least higher than 5), in addition to low undercut and anisotropy.

Results of plasma etching of ITO using a CH_4/H_2 gas mixture are already reported in literature [113]. By using this chemistry, H_2 will reduce oxygen in the ITO film and CH_3 species will volatilize the metals (indium and tin). Initial experiments were performed by choosing a reactive ion etching (RIE) in combination with inductively coupled plasma (ICP) etching. Figure 3.16a shows the trend of the selectivity, which is defined as the ratio between etch rate of ITO and that of the PR masking material, as well as the ITO etch rate for different RIE power values. In this case the ICP power is kept constant at $1000W$. At $100W$ RIE, selectivity seems to be maximal. At these settings, the etch rate is $50nm/min$ and the selectivity equals approximately 2. For our purpose the etch rate value is acceptable, but the selectivity is not.

To improve the selectivity, which can be achieved by reducing the mask etch rate, the ICP power source has been switched off and RIE plasma etching has been carried out. Figure 3.16b shows the trend of selectivity of ITO with respect to PR and the ITO etch rate for different RIE power (ICP source off). In this case a negative selectivity appears due to the fact that polymer is deposited on top of the PR, while the ITO is still being etched. The etch rates are lower than those of the ICP plasmas, but still suitable for transferring EBID masks for NIL stamps fabrication. However, we noticed that CH_4/H_2 based etch chemistry yields rough surface morphologies. This can be caused by polymers deposited on the etched surface or insufficient chemical etching of the ITO. Polymers may grow not only perpendicular to the sample surface, but rather in any direction,

thereby reducing the lateral dimensional control of the EBID masks, which may be effectively widened by this effect.

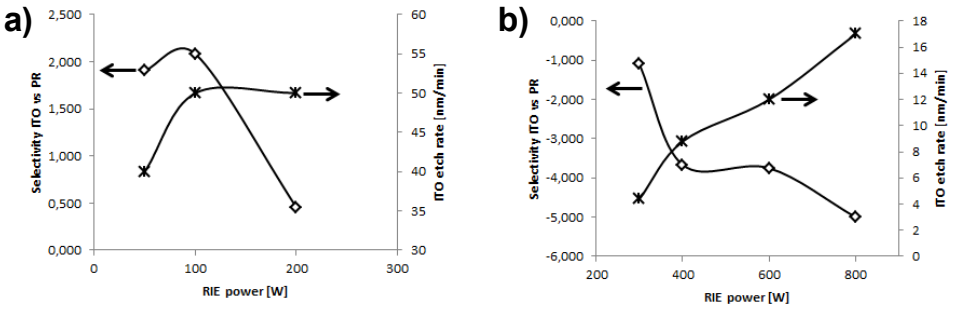

Figure 3.16: Selectivity of ITO with respect to PR AZ5214E and corresponding ITO etch rate in CH_4/H_2 plasma etching: ICP + RIE (a) and RIE only (b).

In order to reduce the polymerisation, and to prevent the resist thickness from growing or shrinking, we tried to add Argon to the gas mixture. In fact, Argon increases the ionic bombardment of the sample surface which may reduce the observed surface roughness by boosting the chemical reactions and sputtering the protrusions on the surface, as shown in literature [114]. Furthermore, Ar will also sputter the polymers that are deposited on top of the PR, which may reduce the loss of lateral dimensional control. The amount of polymerisation depends also on the CH_4/H_2 ratio. The smaller the amount of CH_4 in the plasma, the lower the polymerisation rate.

To investigate this, we added $30 sccm$ of Ar to the CH_4 and H_2 gas mixture. We chose to keep the Ar flow constant as we think that the CH_4/H_2 ratio is more significant in determining the polymerisation rate. Furthermore, a high Ar concentration might damage the EBID masks. Figure 3.17 shows the trend of the selectivity of ITO with respect to PR and the etch rate of ITO for different H_2 flows. In this case the total pressure is kept constant at $35 mTorr$ and the temperature at $20°C$. It is seen that the selectivity is negative due to polymer deposition on top of the PR. By decreasing the pressure to $25 mTorr$ the selectivity was found to strongly increase. The ITO etch ratio was $16.4 nm/min$ and the PR was not etched, and no polymer deposition occurred. This result is very promising: by further decreasing the pressure we expect that the etch rate of the PR increases, showing a positive selectivity. This has not been tried yet, because of time limitations, but will be studied later.

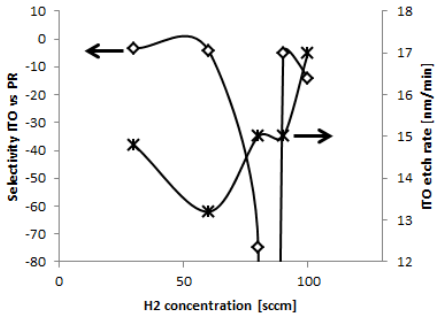

Figure 3.17: Selectivity of ITO with respect to PR AZ5214E and corresponding ITO etch rate in $CH_4/H_2/Ar$ plasma etching (RIE).

To prevent the formation of polymers, a BCl_3/Cl_2 chemistry has also been studied, taking into consideration the results presented in literature [115]. In this case, Cl reacts with both In and Sn, forming $InCl_x$ and $SnCl_x$, which are volatile at high temperature. By increasing the concentration of Cl_2, the etch rate should increase due to more available reactive Cl radicals in the plasma. However, by further increasing the concentration of Cl_2, the etch rate decreases because the concentration of BCl_3 ions and the ion energy are too low. By adding a small amount of CF_4, the etching rate can be enhanced due to a more efficient breaking of metal-oxygen bonds in ITO by CF_4. However Cl and F chemistries are known to attack PR quite efficiently, which may limit the selectivity. Table 3.3 shows the resulting selectivity between ITO and PR by varying the concentration of BCl_3, Cl_2 and CF_4 in the plasma. The RIE power and the ICP power are kept constant to $100W$ and $1000W$ respectively, while the pressure was set to be $10mTorr$ and the temperature 20 deg C. A selectivity of 0.28 is achieved with a $12sccm$ BCl_3 flow and the etch rate for the ITO is $18nm/min$. If the RIE power is set to $300W$, $20sccm$ BCl_3 flow (pressure $60mTorr$, temperature 20 deg C) shows a similar selectivity of 0.27, though the etching rate of ITO dropped down to $12nm/min$.

3.3.2 Pattern transfer into ITO using etch masks made by EBID

In order to gain some experience in pattern transfer, we first carried out experiments using silicon substrates covered by $100nm$ ITO. Structures consisting of sets of lines were patterned by EBID using the platinum precursor ($MeCpPtMe_3$)

BCl_3 $[sccm]$	Cl_2 $[sccm]$	CF_4 $[sccm]$	**RIE** $[W]$	**ICP** $[W]$	**ITO etching rate** $[nm/min]$	**Selectivity**
12	12	0	100	1000	17	0.09
12	0	0	100	1000	18	0.28
20	0	0	300	1000	12	0.27
12	0	6	100	1000	27	0.17
28	0	5	100	1000	20	0.20

Table 3.3: ITO etching rate and selectivity of ITO with respect to PR AZ5214E in $BCl_3/Cl_2/CF_4$ plasma etching.

in the FEI Nova Nano Lab 650 scanning electron microscope, equipped with a gas injection system. The etching experiments were performed on a Plasmalab system133 etcher at and in cooperation with Oxford Instrument Plasma Technology (OIPT). Two different batches of samples were patterned using the platinum precursor ($MeCpPtMe_3$). One batch consists of silicon chips, with a navigation pattern made by etching silicon to obtain black silicon. The other batch of samples consists of silicon chips covered by a $15nm$ layer of molybdenum on top of a $100nm$ ITO layer. Circular holes were opened in the Mo layer as a navigation pattern: in these circles the EBID deposits were patterned. Figures 3.18a and 3.18b show the patterns that were deposited in each circle. In order to have a chance to inspect one of the deposits with the profilometer available in OIPT, a line has been patterned to be approximately $10\mu m$ long and $500nm$ wide (circle a in Figure 3.18a). Series of smaller EBID lines, having either Gaussian profiles or long tail profiles (Figure 3.18b), have also been patterned (circles b, c, d and e), as shown in Figure 3.18a. The FWHM of these lines are approximately $30nm$ (circle b), $35nm$ (circle c), $17nm$ (circle d) and $22nm$ (circle e).

In literature it has been demonstrated that ITO can be etched using CH_4/H_2 chemistry [113] [114]. Firstly, the performance of different CH_4/H_2 etching recipes has been evaluated by varying the composition of the gas mixture, the pressure of the chamber and the power of RIE and ICP generators. This was done by using Silicon samples, on top of which $100nm$ of ITO has been deposited by sputtering. The resulting ITO deposition appeared to be extremely rough, which is an unwanted situation in case of nano-pattern transfer of $sub-10nm$ EBID masks. We decided to carry out the experiments in OIPT with these

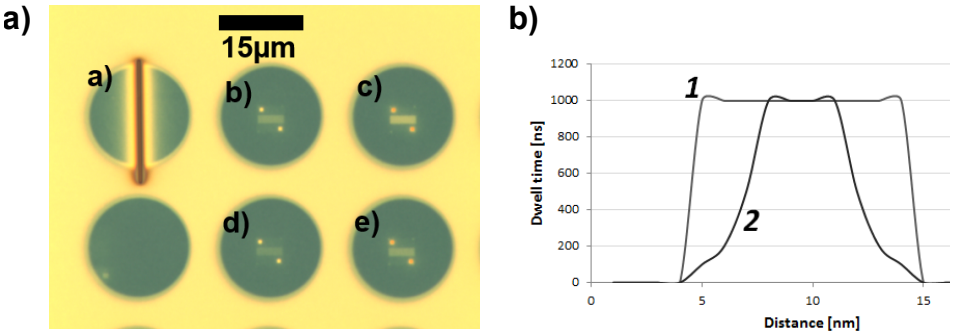

Figure 3.18: a) Optical image of the EBID deposits patterned on the $100nm$ layer of ITO (blue circles), on top of silicon. The yellow area around the circles corresponds to the molybdenum layer, which forms the navigation pattern. *Circle a*: EBID line of approximately $20\mu m$ length and $500nm$ width, which serves as a visible EBID pattern in the profilometer. Two sets of line series have been patterned with different line profiles. b) Profile 1 is defined to have a Gaussian profile (10 pixel wide, each of them patterned with $1\mu s$ dwell time, pixel size = $1nm$); profile 2 is defined to be patterned with $200ns$ dwell time at the edges of the lines and $1\mu s$ at the centre of the lines, leading to a long tails profile. Circle b+c in (a): Series of EBID lines with profile 1 (circle b: passes:10; circle c: passes:20). Circle d+e in (a): Series of EBID lines with profile 2 (circle d: passes: 10; circle e: passes: 20).

wafers anyway because of limited amount of time left. Our next goal is to improve the deposition parameters of ITO in order to get smoother films or switch to another conductive UV-transparent layer. The ITO layer was then partially covered by $1.5\mu m$ photoresist (AZ5214E), such that it was possible to easily calculate the etching rate of ITO and the selectivity of ITO with respect to PR. This has shown that the best recipe consists of a gas mixture of $7.5sccm$ of CH_4 and $60sccm$ of H_2, using only $800W$ RIE power source ($0W$ ICP), at $35mTorr$ pressure and $20\deg C$. This recipe is first tested on a black Si/Si chip. After 5 minutes of etching, the colour of the sample changed meaning that a polymer layer has been deposited. Profilometer measurements confirmed the deposition of a $50nm$ layer of polymer on top of silicon. Assuming that the same amount of polymer was deposited on top of the EBID line as well, then the EBID line etch rate is measured to be approximately $8nm/min$. However, we noticed that the polymer layer can be easily removed by performing Oxygen plasma cleaning. Therefore, we decided to repeat the same recipe but varying the etching time (3, 5 and 7 minutes). The idea would be to confirm the height of the deposited polymer by AFM analysis before cleaning them.

Figures 3.19a and 3.19b show the SEM image of a chip etched with the above mentioned chemistry for 5 minutes. It is clearly visible that polymers have been

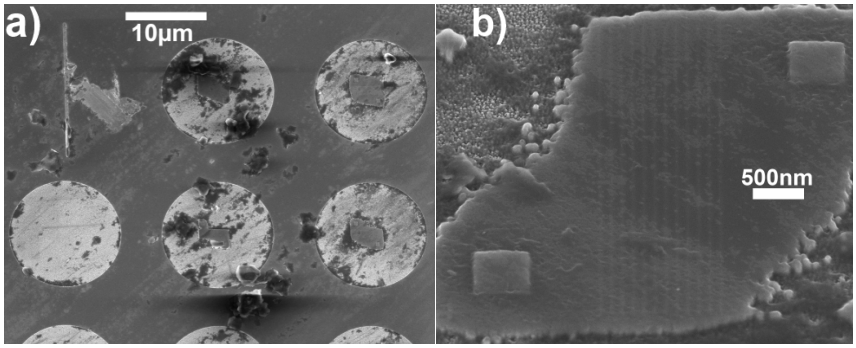

Figure 3.19: a) SEM overview of the EBID deposits after etching (800W RIE plasma with 7.5$sccm$ CH_4 and 60$sccm$ H_2 gas mixture, at 20°C and 35$mTorr$, etching time 5 minutes). b) Zoomed in image (tilted 45°) of one of the sets of lines (circle e).

deposited everywhere on top of the sample. In particular, a uniform thick layer of polymer has been deposited close to the EBID structures. We think this is because in that region there is already a thin Carbon layer, deposited during the EBID patterning by backscatter electrons. The amount of polymerisation depends also on the CH_4/H_2 ratio. By decreasing the concentration of CH_4 in the gas mixture from 7.5$sccm$ to 5$sccm$ we indeed confirmed (by etching a Si/ITO/Mo chip with EBID patterns) that the amount of polymer deposited is less, as shown in Figures 3.20a and 3.20b. Further AFM analysis will give more information on the difference in height of the two sheets of polymer.

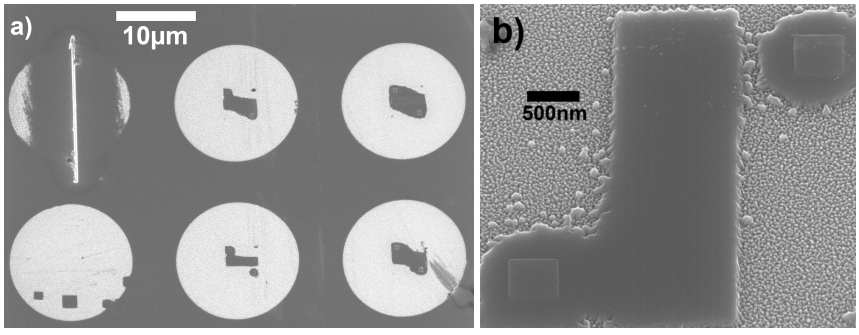

Figure 3.20: a) SEM overview of the EBID deposits after etching (800W RIE plasma with 5$sccm$ CH_4 and 60$sccm$ H_2 gas mixture, at 20°C and 35$mTorr$, etching time 5 minutes). b) Zoomed in image (tilted 45°) of one of the sets of lines (circle d).

In order to reduce the polymerisation, and to prevent the resist thickness from growing or shrinking, we tried to add Argon to the gas mixture [114]. In this case, previous results have shown that a good gas mixture is $5sccm$ CH_4, $80sccm$ H_2 and $30sccm$ Ar, using a $800W$ RIE plasma, at $20°C$. Different runs were performed on Si/ITO/Mo chips with EBID patterns and the pressure was changed for each run. Results are depicted in figure 3.21: in the high pressure ($35mTorr$ - $20mTorr$) regime, polymer has been deposited on top of the chips. This is concluded from the observation that the sum of the original thicknesses of the ITO and the Mo layers is lower than the one after etching. On the other hand, in the low pressure ($5mTorr$) regime the ITO etch rate is very low. We think that the best regime to work in is between $8.5mTorr$ and $12.5mTorr$. Three runs were then performed at $12.5mTorr$, $10mTorr$ and $8.5mTorr$, as depicted in figures 3.22a, 3.22b, 3.23a, 3.23b, 3.24a and 3.24b. In the case of $12.5mTorr$, a polymer layer is still deposited in the region surrounding the contact pad. The polymer sheet becomes thinner and thinner when the pressure decreases. However, it cannot be avoided completely. Figure 3.24b shows clearly the roughness of the ITO layer. For $sub-10nm$ devices this is catastrophic.

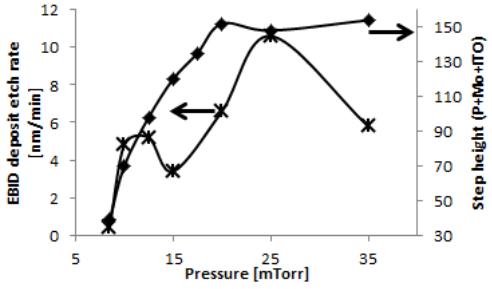

Figure 3.21: EBID etch rate in CH_4/H_2/Ar plasma etching (RIE only) and the step height of the polymer layer, molybdenum layer and ITO.

To prevent the formation of polymers, a BCl_3/Cl_2 chemistry has also been studied, taking into consideration the results presented in literature [115]. Although the resulting selectivity does not meet the requirements of transferring EBID masks into underlying ITO for NIL stamps fabrication, we think that further improvements of the recipe might enhance the selectivity. Strong efforts in improving the BCl_3/Cl_2 chemistry are worthy since this recipe prevents the formation of polymers. We decided to carry out this recipe on a Si/Black Si wafer to check the behaviour of the EBID deposits under this condition. We selected a

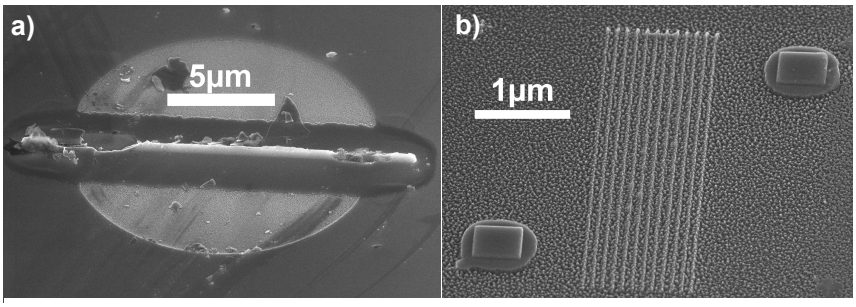

Figure 3.22: a) SEM image (tilted 45°) of the EBID line in circle a etched with $CH_4/H_2/Ar$ chemistry at $12.5 mTorr$. b) EBID lines in Circle c (image tilted 45°).

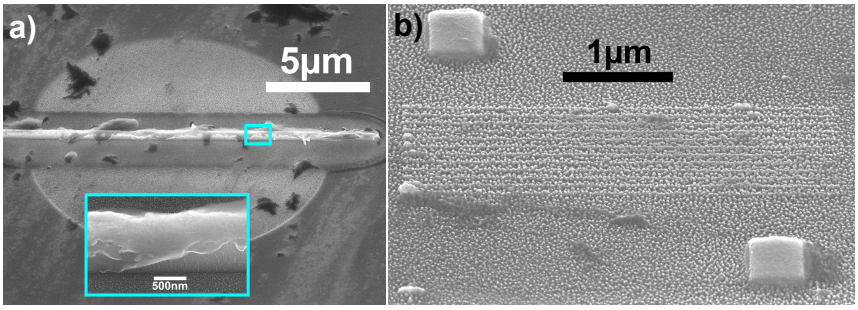

Figure 3.23: a) SEM image (tilted 45°) of the EBID line in circle a etched with $CH_4/H_2/Ar$ chemistry at $10 mTorr$ and zoomed in image of the thin polymer sheet deposited on top of the line. b) EBID lines in Circle e (tilted 45°).

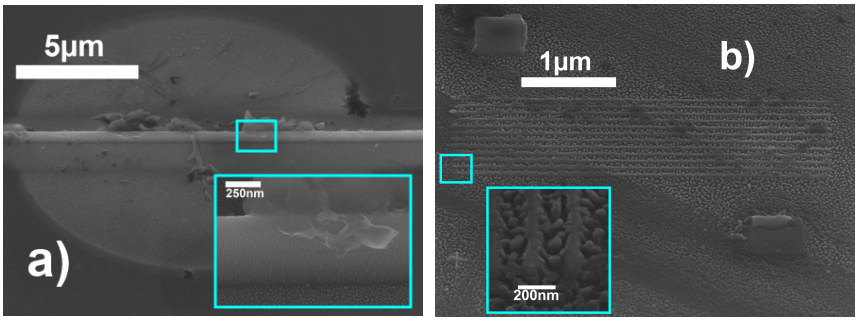

Figure 3.24: a) SEM image of the EBID line in circle a) etched with $CH_4/H_2/Ar$ chemistry at $8.5 mTorr$ and zoomed in image of the thin polymer layer deposited on top of the line. b) EBID lines in Circle c with a zoomed in image of the lines profile, taken by rotating the sample over 90°.

gas mixture of $28 sccm$ of BCl_3, $0 sccm$ of Cl_2 and $5 sccm$ of CF_4, at $10 mTorr$ and $20 \deg C$. We could measure the thickness of the silicon that has been etched by just gluing a strip of tape close to where the EBID deposits were patterned. The difference in height between the etched silicon and the protected silicon is $120 nm$. The profilometer cross-section of the EBID line in Figure 3.25a and 3.25b, shows that the height of the EBID line is approximately equal to $309 nm$ before etching and $130 nm$ after etching (etching time in this case is 1 minute). Hence the total height of the EBID line that has been etched is approximately $10 nm$. Therefore, the EBID etch rate using this recipe is $10 nm/min$. Previous experiments have shown that the ITO etch rate in this chemistry is $20 nm/min$. Hence, with this recipe we can achieve a selectivity of 2, preventing polymer to be deposited.

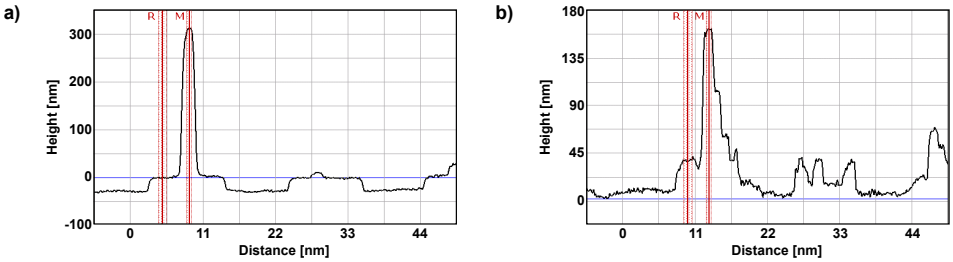

Figure 3.25: a) Profilometer cross-section of the EBID line in circle a before etching. b) Profilometer cross-section of the EBID line in circle a etched with the $BCl_3/Cl_2/CF_4$ chemistry. In this case, the EBID line lies on top of silicon.

We are now interested in studying further recipes for improving the selectivity by using either the CH_4 or the BCl_3 chemistry. The advantage of the first, is that a fast ITO etch rate can be achieved, however we need to prevent the polymer deposition. The advantage of the latter is that no polymer is deposited, but the selectivity seems to be too low for our purposes. We also need to improve the deposition of ITO to reduce the surface roughness or we could switch to other UV-transparent and conducting materials, such as TiN-based films, which is discussed in the next section.

3.4 Pattern transfer into TiN

ITO is a suitable UV-transparent and conductive material that can be used for the fabrication of NIL stamps. However, the granularity of ITO that results from

the method of deposition of ITO itself is not compatible with the size of structures that need to be deposited. Although it is possible to adjust the deposition parameters, the obtained surface might not be smooth enough.
Instead of ITO, a thin layer of TiN can be deposited by Atomic Layer Deposition (ALD), leading to an atomically smooth surface. Moreover, TiN is conductive as well as transparent for UV-light. Figure 3.26 shows the transmittance of a Pyrex wafer covered by $10nm$ of TiN when exposed to light of wavelength varying from $300nm$ to $650nm$. In the UV-light range, around $365nm$, the transmittance is approximately 60%.

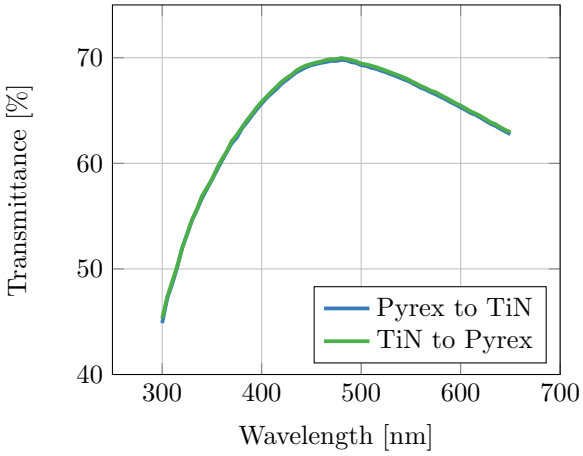

Figure 3.26: Transmittance of a $10nm$ layer of TiN deposited by atomic layer deposition (ALD) on top of a Pyrex wafer.

The idea is to deposit EBID structures on a wafer covered with silicon dioxide and TiN on top. The structures are then transferred into silicon dioxide, which has a lower roughness than ITO. The mask residual that may stick on top of the structures will be UV-transparent and therefore will not influence the NIL process. The goal of these experiments is to test the selectivity of TiN versus SiO_2. The sample used in these experiments is a silicon wafer covered with a thick SiO_2 and TiN, which resembles a Pyrex wafer covered with TiN that is used in a real case.

First experiments were carried out in order to find an optimal chemistry to etch TiN. In order to do so, we decided to use a sample covered with TiN and use SiO_2 as hard mask. To test ICP etching recipes for TiN, a silicon wafer is covered with:

- 450nm of SiO_2, thermally deposited
- 40nm TiN, deposited with ALD
- 70nm of SiO_2, deposited via CVD

Via optical lithography, the first layer of SiO_2 (CVD) is opened up, as shown in figure 3.27.

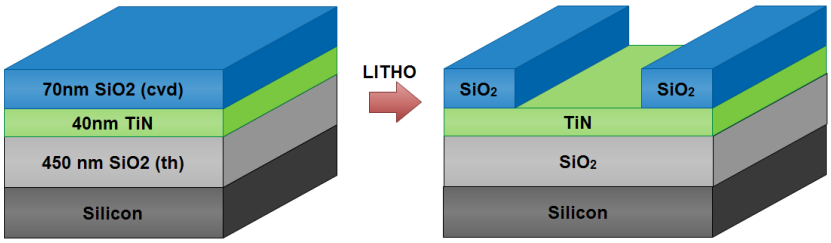

Figure 3.27: On the left, the SiO_2 (CVD)/TiN(ALD)/SiO_2(th) tri-layer on a silicon wafer used for testing the etch recipe for TiN. On the right, after the lithography step the top SiO_2 is opened up.

We first partially covered the surface of the sample with tape (in orange) and subsequently used fluorine chemistry (SF_6 13.5$sccm$ for 1.5 minutes) to etch the TiN as well as the CVD-deposited SiO_2. In this step, the TiN is completely etched away s well as a thin layer of the underlying SiO_2, which was thermally deposited, as shown in figure 3.28.

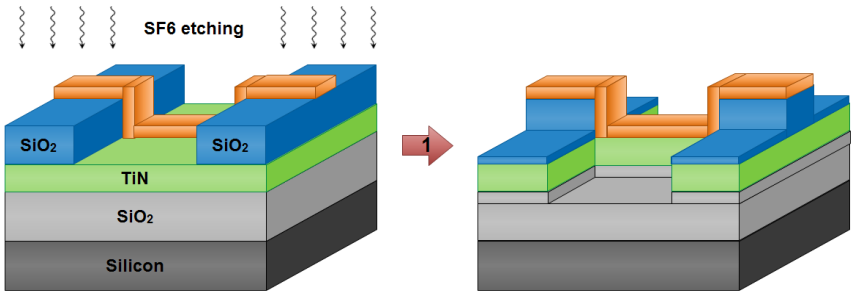

Figure 3.28: First fluorine etch to completely remove the TiN and open the underlying thermally deposited SiO_2 layer.(The structure in orange is the tape)

We then covered another area of the etched surface with a second piece of tape (in orange as depicted in figure 3.28). After that, a second etch run is carried out using the CH_4/C_4F_8/He chemistry for one minute, to completely

remove the remaining top SiO_2 (deposited by CVD) and TiN layer, that served as a mask in the first etching step, as shown in figure 3.29.

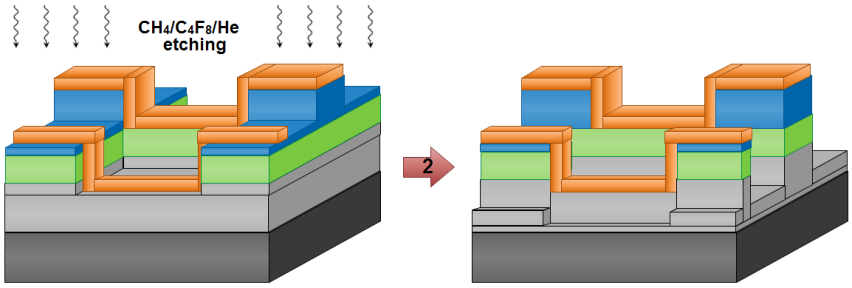

Figure 3.29: Second etching step using the CH_4/C_4F_8/He chemistry to completely remove the remaining SiO_2(CVD)/TiN layer. (The structure in orange is the tape)

By measuring the steps between each etched layer, as shown in figure 3.30, it is possible to retrieve the selectivities of the two etching processes:

- $Selectivity(TiN/SiO_2)_{1^{st}etching} = (40nm/min)/(32nm/min) = 1.25$
- $Selectivity(SiO_2/TiN)_{2^{nd}etching} = (232nm/min)/(40nm/min) = 5.8$

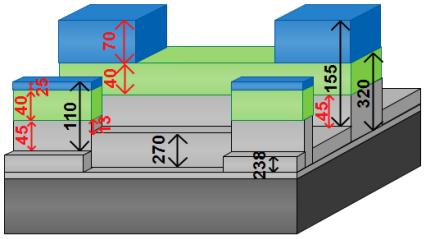

Figure 3.30: Measures of all etched steps that serve to retrieve the selectivity for the two etching processes. Values in black are measured values with a typical uncertainty of $3-5nm$. Values in red are derived from the measured data.

In these experiments we measured the etching rate of TiN and its selectivity towards silicon oxide hard masks. This seems a promising approach to fabricate UV-transparent stamps using EBID-defined masks patterned on TiN covered Pyrex wafers. The aspect ratio of the EBID structures can be enhanced by etching into the underlying TiN layer by optimizing these etching recipes.

We also considered an additional initial step, meant to increase the height of the very shallow EBID lines. This can be done by first patterning the shallow lines with EBID, ideally just one monolayer of Pt (so-called seed layer). Later, by means of ALD (Atomic Layer Deposition), single atomic layers of Pt can be selectively deposited on top of the existing seed layer of Pt. Mackus et al. [116] first introduced this technique, that is capable of achieving the fabrication of high Pt purity nanostructures with higher resolution than the area selective ALD-methods and higher throughput than EBID.

Figures 3.31a and 3.31b show a set of lines and an array of dots made by first depositing a thin EBID layer and subsequent deposition of Pt using ALD. Though the concentration of the Pt can be increased considerably [116], the shape of the lines and dots appear to be granular. Future work can be done on the optimization of the ALD parameters in order to get more control over the shape of the resulting structure.

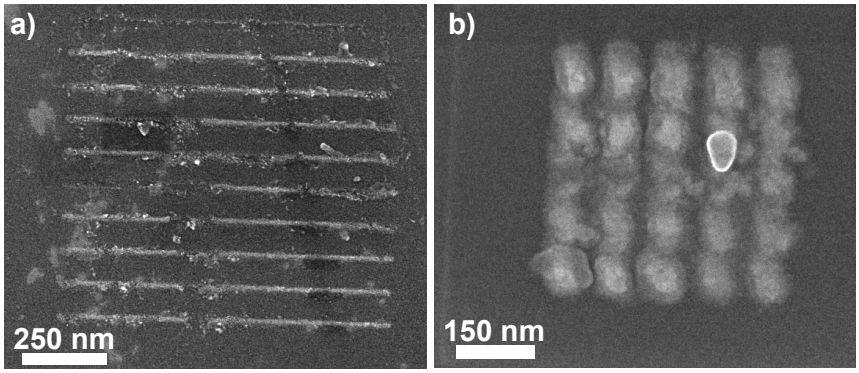

Figure 3.31: a) Set of 10 Pt lines deposited by EBID and subsequent ALD. b) Array of 5x5 Pt dots deposited by EBID and subsequent ALD

3.5 Conclusions

We have worked on the pattern transfer of nanostructures made by EBID into underlying layers. This process will, on one side, enhance the aspect ratio of the $sub-20nm$ EBID structures, that are typically very shallow. Secondly, if the EBID mask is completely etched away, the resulting structure will in principle have the shape of the mask, with enhanced aspect ratio and with the desired composition. As a first step, we carried out experiments on the pattern transfer of EBID nanostructures into the underlying silicon layer using hydro-

gen bromide, chlorine, boron trichloride and fluorine chemistries. Very good results were obtained with the fluorine chemistry, where lines with $sub-15nm$ width, were transferred into the underlying silicon layer with an aspect ratio of 8. Because the final goal is the fabrication of stamps for nano imprint lithography (NIL), that need to have a good transmittance for UV light, we decided to perform further experiments on the pattern transfer of EBID structures into underlying transparent layers. Moreover, to successfully pattern single-digit nanometre structures, the underlying layer must be conductive. Given these requirements, the first material candidate that we investigated was ITO. Though first results show good performance of EBID structures as etching masks, the roughness of ITO prevents single-digit nanometre structures to be successfully patterned. A possible follow up study is the investigation of the deposition of smoother ITO layers combined with the optimization of the etching process. We decided instead to carry out experiments using TiN as underlying layer. In fact, TiN can be deposited by ALD, which provides atomically flat surfaces and is conductive. We foresee that TiN is a good candidate for the fabrication of NIL stamps using masks made by EBID, where the aspect ratio is enhanced by a pattern transfer step. We have worked on the development of a process flow for the nano-pattern transfer of EBID structures in an underlying TiN layer, which is deposited on top of a silicon wafer. In particular, we focused on the pattern transfer of small EBID lines ($sub-8nm$ range). Because they are really thin (less than $1nm$ height), they do not work as a good mask for the subsequent etching process.

3.6 Pattern transfer into thin membranes

The pattern transfer on the single nanometer scale is challenging in two ways. First to develop recipes to successfully etch such delicate fine structures, and second, to image them properly to judge the result. To improve on the latter it was decided to carry out pattern transfer experiments using TEM membranes as a substrate. In this way, the deposited and etched structures can be imaged using a high beam energy transmission electron microscope (TEM). These experiments were carried out in collaboration with Oxford Instruments Plasma Technology (OIPT) and EPFL, both partners of the Single Nanometer Manufacturing for beyond CMOS devices (SNM) project.

Because we had already experience with pattern transfer into silicon, it was decided to cover $20nm$ thick SiN membranes with $20nm$ of Si, by means of sputtering. Subsequently Pt/C lines were written on top of the silicon layer, us-

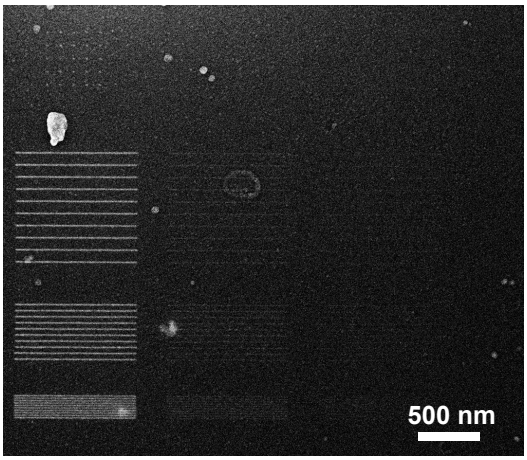

Figure 3.32: SEM image with enhanced digital brightness/contrast of Pt/C structures deposited by EBID on thin membrane consisting of a bottom layer of $20nm$ SiN and a top layer of $20nm$ sputtered Si (Sample 1). The patterning was done at $19kV$, $39pA$, and single pass writing mode.

ing EBID in our FEI NovaNanoLab 650 SEM, at $19kV$, $39pA$ beam current, in immersion mode. Two samples were fabricated following this recipe, sample 1 and sample 2. Figure 3.32 shows the patterned structure on sample 1. The contrast in the SEM image is very poor, leading to a very difficult judgment of the line widths. These samples were then inspected at EPFL in a STEM instrument using High Angle Annular Dark Field (HAADF) imaging at $80keV$. The schematic of the sample and measurement set up is presented in figure 3.33. The high angle annular dark field (HAADF) detector is used for the detection of the scattered electrons and the intensity of each pixel is proportional to the atomic number Z of the sample material. The schematics shows the imaging set up before (a) and after etching (b). The background around the deposited structures consists of the SiN membrane covered with a layer of silicon, that is thinned after etching, giving therefore different contrast in the STEM image.

Figure 3.34 shows the overview HAADF image of the deposited lines on the left and zoomed-in images of areas A, B and C on the right. The contrast in HAADF imaging is much higher than that of SEM imaging, shown previously in figure 3.32. The Pt lines result to be brighter than the Si/SiN background. Moreover, the deposition method of silicon leads to a granular surface, that is visible in the zoomed-images of areas B and C of figure 3.34.

Thanks to the HAADF images, a more accurate estimation of the line width can be done. Figure 3.35 shows the analyzed areas 1, 2 and 3 as previously defined in figure 3.34. The lines patterned in these areas are designed to have

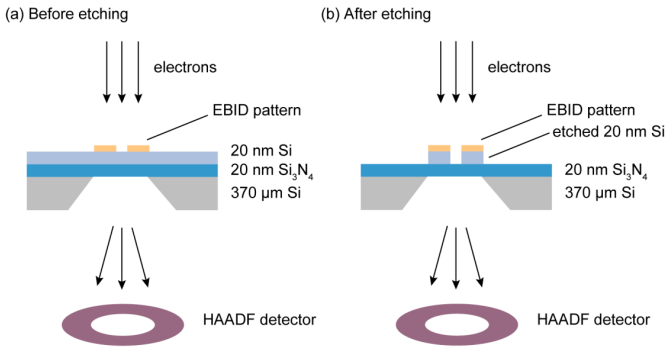

Figure 3.33: Schematic of the experimental setup. High energy electrons pass through the membrane on which EBID patterns are written (a) before and (b) after etching. Depending on the atomic number of elements electrons are inelastically scattered and detected by the high angle annular dark field (HAADF) detector. [Courtesy of D. Ovchinnikov]

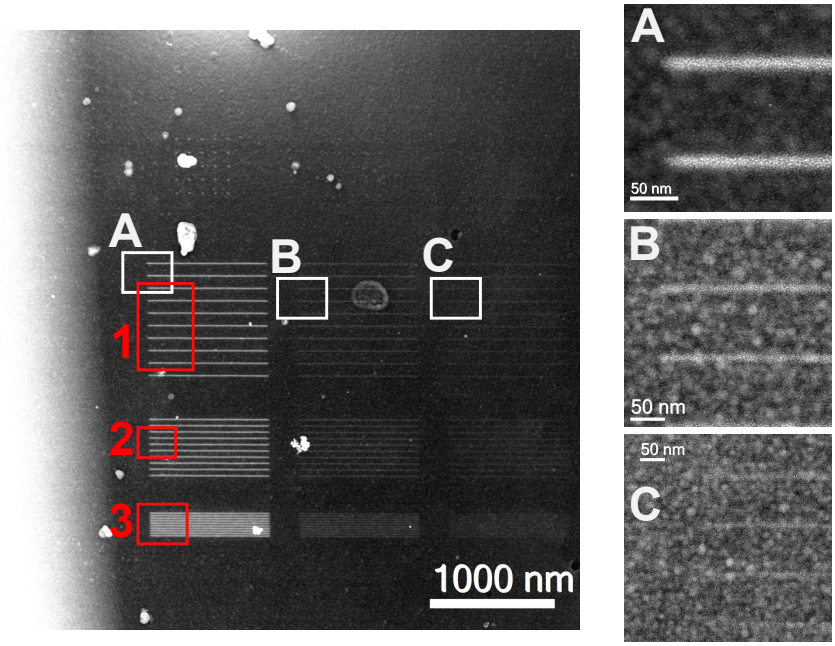

Figure 3.34: STEM HAADF overview image of the EBID patterns on the thin membrane substrate (left), and zoomed-in TEM images of the areas A, B and C, highlighted in the image on the left (Sample 1).

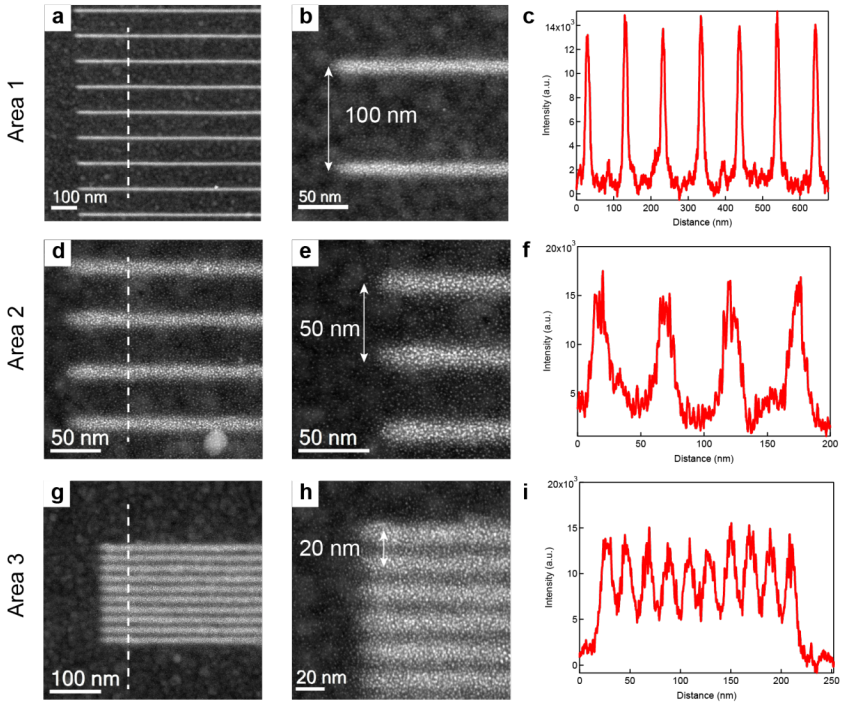

Figure 3.35: HAADF image of the EBID pattern and zoomed-in images of areas 1, 2 and 3 (Sample 1). Line profiles measured from the HAADF images at different magnification of Area 1 (a-c), Area 2 (d-f), Area 3 (g-i) are shown. Distance between the lines is extracted from plots of the HAADF intensity across the dashed line cut (a, d, g) and plotted as a function of distance in graphs c, f and i, respectively.

$100nm$, $50nm$ and $20nm$ spacing respectively and the same width of $10nm$. From the high resolution STEM images, the intensity profiles of the lines are extracted, from which the distance between the intensity maxima and the width of the lines are measured. The width of the lines is measured using the full width at half maximum value (FWHM). Table 3.4 shows the measured line spacing and line width for areas 1, 2 and 3. The line spacing is $101.5nm$, $52nm$ and $20.2nm$ respectively, which is in agreement with the designed geometry. The line width is $17.2nm$, $18.8nm$ and $18.4nm$ respectively for areas 1, 2 and 3.

Area	**Spacing [nm]**	**Line width [FWHM with gaussian fit]**
Area 1	101.5 ± 1.9	17.2 ± 1
Area 2	52.0 ± 0.5	18.8 ± 3.4
Area 3	20.2 ± 1.3	18.4 ± 4.1

Table 3.4: Line separation and line width measurement for areas 1, 2 and 3, measured from the HAADF STEM images in figure 3.35 (Sample 1).

From the zoomed-in images of figure 3.35b, 3.35e and 3.35h, we notice that the EBID lines consist of clusters of small and bright particles. Moreover, the same bright particles are also dispersed around the EBID lines themselves, forming a so-called halo. The lines with only $20nm$ spacing have barely some trenches in between because of the overlapping of the halo of neighbouring lines, as also confirmed by the line profile in figure 3.35i. We therefore expect that the etching of the underlying silicon layer will be stopped by the material deposited between these lines.

3.6.1 EDX analysis on the EBID structures

The zoomed-in images of the EBID structures in figure 3.34 and 3.35 reveal that the lines consist of small Pt grains, that have typical dimensions of several nm (particle size analysis is limited due to the contrast of the STEM images) and are located not only on the written lines, but also on the substrate around the EBID lines, where their density is relatively low. In order to have a more complete analysis, EDX is performed on this sample by EPFL. Energy-dispersive X-ray spectroscopy (EDX) is a broadly used technique that provides information on the elemental composition of structures from the detection of the characteristic X-ray emitted from the sample when interacting with the in-

cident beam [117]. While HAADF images provide only information on the intensity variation between structures made of different material, EDX allows to analyze the elemental composition. It is of fundamental interest to understand the composition of the Pt/C deposits prior to the etching step in order to study the most suitable etching recipe. A representative region was chosen, namely area 1, and the EDX spectrum was acquired for every scanned pixel in order to obtain an elemental composition map. Figure 3.36 shows the HAADF image of the selected region (*a*) and the EDX spectral map of carbon (*b*) and platinum (*c*). Though carbon is present in the EBID lines in a large percentage, it is here noticeable that there is a uniform C layer also around the EBID patterned region, that is possibly caused by contamination during SEM and STEM imaging. Platinum is concentrated on the EBID lines, but some granules are also visible around the lines.

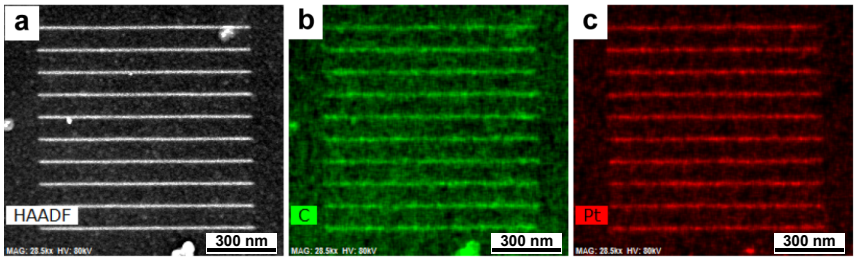

Figure 3.36: EBID patterns (Sample 1): lines $\approx 20nm$ wide with $\approx 100nm$ spacing before etching. (a) HAADF STEM image of patterned area with lines visible as brighter regions. (b) EDX map of C distribution. (c) EDX map of Pt distribution. (a), (b) and (c) images are acquired simultaneously.

3.6.2 Results and discussion

After the STEM inspection at EPFL, samples 1 and 2 were etched at OIPT using Atomic Layer Etching (ALE) with a Cl_2/Ar mixture. ALE using plasma is an etching process where a combination of gas dosing and ion bombardment removes material from a sample layer by layer. Cooke et al. demonstrated in a study the etching of silicon by ALE using the chlorine/argon recipe [118]. The main advantage of this technique is the potential to remove single atomic layers with low damage. Two samples were etched using the following recipes:

- **Sample 1**: $16s$ Ar pre-clean + 25 cycles of Cl_2/Ar ALE, where the etch depth on an OIPT reference sample of amorphous Si is $\approx 17nm$.

- **Sample 2**: $16s$ Ar pre-clean + 20 cycles of Cl_2/Ar ALE, where the etch depth on an OIPT reference sample of amorphous Si is $\approx 12-13nm$.

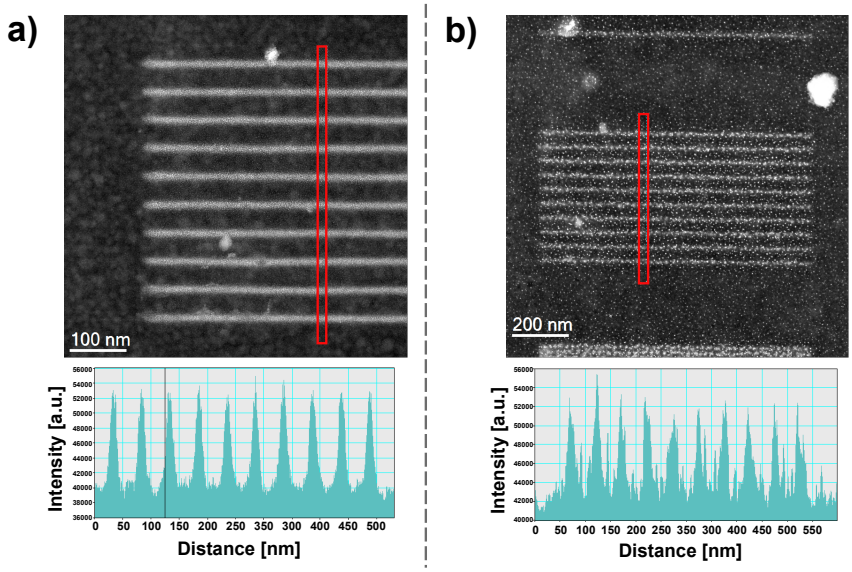

Figure 3.37: HAADF image of sample 1 taken at $80keV$ of line patterns defined by EBID masks, before (a) and after (b) a Cl_2/Ar ALE etching process. Below the images, the intensity profiles integrated over the rectangular areas indicated are shown.

Standard HAADF STEM imaging was performed again at EPFL after the samples were etched. Figures 3.37a and 3.37b show the $80keV$ HAADF images taken before and after etching for sample 1, including integrated intensity profiles obtained from the areas indicated by the rectangles. The intensity ratio before and after etching was measured and the layer thickness information was calculated, taking a linear relation into account. It is concluded that 40% (namely $8nm$) of silicon was removed. This is smaller than estimated for the same process on the a-Si calibration sample at Oxford Instruments, namely $\approx 17nm$. This is only an estimation concluded from the change in the detected HAADF signal before and after the etching, without considering all the possible parameters of influence, such as the detector electronics settings. Moreover, the presence of Pt grains that lay on the sample surface provides an additional contribution to the STEM intensity, thus increasing the total contrast, causing an underestimation of the etched silicon thickness. We therefore conclude that scanning probe techniques such as AFM are necessary for more reliable thick-

ness measurements.

From figure 3.37b, it can be observed that the Pt grains are found over a much larger area than where the deposition took place and were not visible in the STEM images taken before the etching process. It is unknown whether this is caused by the etching process, or the $80keV$ imaging or a combination of both.

The HAADF images before and after etching of sample 2 are shown in figures 3.38a and 3.38b. We noticed that the height of the EBID lines seems to have shrunk after the etching, making this not a suitable recipe. Moreover, much less platinum particles are found around the EBID lines, compared to sample 1 in figure 3.37. Therefore, we conclude that this type of etching, that is a cyclical process of gas dosing and ion bombardment, may cause damage to the EBID lines, leaving debris of platinum clusters around the patterned features.

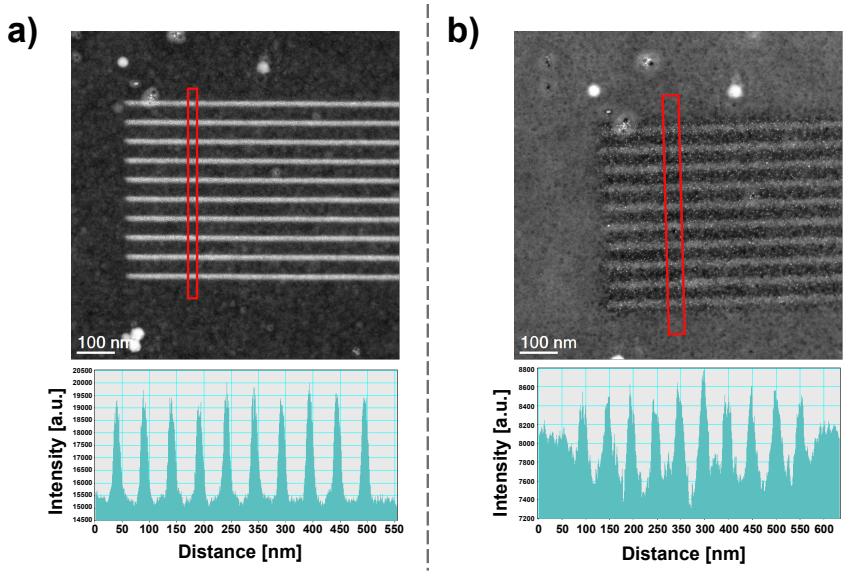

Figure 3.38: HAADF image of sample 2 taken at $80keV$ of line patterns defined by EBID masks, before (a) and after (b) a Cl_2/Ar ALE process. Below the images the intensity profiles integrated over the rectangular areas indicated are shown.

We performed EDX on sample 1 after etching to confirm that the composition of the bright particles is platinum. Figure 3.39 shows on the top row the HAADF image (left) of a region in sample 1 and the EDX maps for silicon (mid-

dle) and platinum (right) taken simultaneously. On the bottom, the zoomed-in HAADF image and the Pt map of the same areas, where some reference particles are highlighted. The EDX maps clearly show that the spread grains in between the lines are indeed platinum.

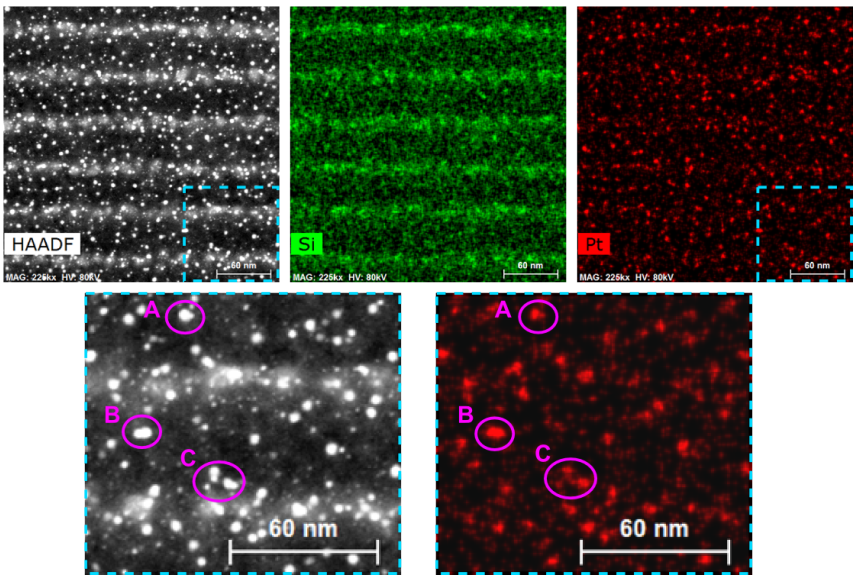

Figure 3.39: In the top row, HAADF image of sample 1 and EDX maps of the same region for Si (middle) and Pt (right). In the bottom line, zoomed-in images of the HAADF micrograph and the platinum EDX map of the same area, where Pt grains are highlighted.

3.7 Conclusions

When patterning $sub-10nm$ structures with electron beam induced deposition, the aspect ratio that is achieved is usually less than 1. A way to increase the height of the structure, while preserving the width, is to transfer it into an underlying layer, using an etching process, where the EBID deposit acts as a mask. We successfully demonstrated the pattern transfer of EBID structures in underlying silicon, using fluorine chemistry, which leads to an increase in height of a factor of 8. These samples can be used as masters for a subsequent UV-NIL step, meaning that a UV-transparent replica of the EBID-samples has to be made before the imprinting.
However, if we want to use EBID structures directly as NIL stamp, we need to

use transparent substrates. We considered the option to deposit an ITO layer, that provides a transparent and conductive surface, on top of glass. In this case, the best recipe for the pattern transfer of EBID structures in underlying ITO is based on BCl_3. However, the main disadvantage of this option is the roughness of ITO, that is not compatible with the size of the structures that we want to deposit.

Another option is to use TiN instead of ITO. Like ITO, TiN is conductive and has been demonstrated to be acceptably transparent in the UV-range. Moreover, TiN can be deposited by ALD and therefore results in very flat surfaces. We carried out experiments where we studied the selectivity of TiN towards silicon oxide and vice versa, from which we concluded that this is a promising approach for the fabrication of NIL stamps by EBID.

Etching experiments are finally carried out also on thin membrane samples using $sub-10nm$ EBID structures as mask. Such samples can be imaged in high acceleration voltage STEMs, leading to high resolution images from which it is easier to judge the dimensions of the patterned structures. HAADF-STEM images also reveal that the EBID lines consists of Pt particles, which can also be found in the areas surrounding the deposited structures, forming the so-called halo. The presence of platinum grains was confirmed by EDX analysis performed in the high acceleration voltage STEM. Despite the fact that the contrast in HAADF-STEM images is proportional to the mass thickness, the etch rate of the EBID lines and that of the silicon is not trivial to estimate. As for future experiments, AFM analysis prior to and after the etching process is required in order to accurately measure the selectivity of the etching.

4

EBID stamps for Nano Imprint Lithography

Religion is a culture of faith; science is a culture of doubt.

Richard P. Feynman

4.1 Introduction

The nanotechnology industry is putting efforts in demonstrating the fabrication of devices in the $sub-10nm$ range. Typically, the technologies that are used are optical lithography, where extreme ultra violet lithography (EUVL) is the leading patterning technology, and electron beam lithography (EBL). EUVL, that has been developed since the 1980s, makes use of photons of $13.5nm$ wavelength for patterning. Because of the short wavelength of these photons, they are absorbed easily, so the entire EUVL scanner must be kept under vacuum. To achieve high volume manufacturing with EUVL, progress and improvements have been done not only on the sources and the optics of EUVL scanners, but

also on contamination control, mask handling and resist [119]. In EUVL, the resolution is limited by the wavelength of light and thoughput can be increased by for instance employing high power light sources. On the other hand, EBL may ultimately have its greatest impact because of the increasing attention in the manufacturing industry on the number of components that can be fabricated in a chip [120]. In EBL, resolution is not limited by the resolution of the electron optical systems, but rather by the resolution of the resist and the subsequent fabrication process [121] [122] [18]. EBL has however disadvantages in terms of throughput, which can be overcome by integrating into one system, technologies like SCALPEL, developed by the Bell Laboratories (Scattering with Angular Limitation in Projection Electron-beam Lithography), PREVAIL, developed by IBM (Projection Reduction Exposure with Variable Axis Immersion Lenses) and multi-column systems [123].

Among these techniques, nanoimprint lithography (NIL) emerges as a low cost and high throughput patterning technique that is suitable for large area and large volume manufacturing. In this chapter, nanoimprint lithography is used in an attempt to fabricate structures in the $sub-10nm$ range. In nanoimprint lithography, a stamp is pressed on top of a sample coated with a polymer, or NIL resist. The template on the stamp is impressed into the sample resist and transferred into the metallic layer underneath the resist by pattern transfer. For this process, UV-transparent stamps are required to allow the resist to cure while the stamp is pressed on top of it. The fine structures, with sizes in the nanometre scale, can be patterned using Electron Beam Induced Deposition (EBID). The main advantage of using EBID for the fabrication of NIL stamps is that it is a direct write technique and it does not require any electron beam sensitive resist nor post-patterning steps. EBID can be easily performed in a scanning electron microscope (SEM) equipped with a gas injection system (GIS).

In this chapter, the fabrication of NIL stamps by EBID is thoroughly discussed. Experiments were conducted in collaboration with the EVG group, leader in supplying NIL instruments and partner in the Single Nanometer Manufacturing for beyond CMOS device (SNM) project. NIL requires stamps to be UV-transparent, therefore substrates made out of Pyrex or glass can be employed. Because EBID requires conductive substrates to pattern high-resolution structures, the Pyrex (or glass) samples need to be coated with a conductive and UV-transparent layer. The materials considered in this set of experiments are

TiN, chromium and molybdenum, that are all sufficiently transparent at the UV wavelength when deposited as thin films, with thickness less than $10nm$. Reference measurements of the NIL masters made by EBID and the imprinted wafers were performed by the Dutch institute of metrology (VSL), also participating in the SNM project.

4.2 State of the art of nano imprint lithography

Nano Imprint Lithography (NIL) is a high resolution and high throughput patterning technique, that makes use of a template stamp to be imprinted on a sample. Figure 4.1 shows the schematics of nano imprint lithography. A substrate is covered by a ductile resist and a sample with pre-patterned features, called NIL stamp, is positioned on top of the substrate. Usually, the NIL stamp consists of a quartz plate covered with a mold, on which the features are patterned. The stamp is pressed on the resist, that will be deformed according to the shape of the stamp. The resist is then hardened in a curing process. The stamp is released and positioned in another location of the substrate where the same process is repeated. We can distinguish two NIL processes based on the way the resist is cured: *thermal NIL*, that is based on the compression of a thin thermoplastic film, and *UV-NIL*, where the resist is liquid at room temperature. In the first case, the resist is cured at elevated pressure and temperature. In UV-NIL, the stamp is pressed at low pressure, to allow the liquid to fill the gaps of the stamp. Then, the resist is hardened by UV-exposure through the transparent stamp. This NIL method is used in the experiments described in this chapter, and can be referred to as Step and Repeat NIL (S-RNIL or S&R NIL) or Step and Flash NIL (S-FIL) [124].

The first published article on nano imprint lithography is dated 1995 and since then it had a more and more established position in research and in industry, as the low cost, high throughput and high resolution lithographic technique. NIL is low cost and it represents a valid alternative to electron beam lithography (EBL) or high-end photolithography (PL), that are costly and, in case of EBL, do not provide at the same time sufficiently high resolution and high throughput. NIL does not require complex optics nor sophisticated light sources nor electron optics systems, therefore NIL tools are generally less expensive than EBL and PL tools [125]. The NIL tools operate at atmospheric pressure and room temperature and use low-cost broadband mercury lamps for the UV source [126]. Because NIL relies on the mechanical deformation of the resist, it does not suffer from resolution limitation given by the diffraction

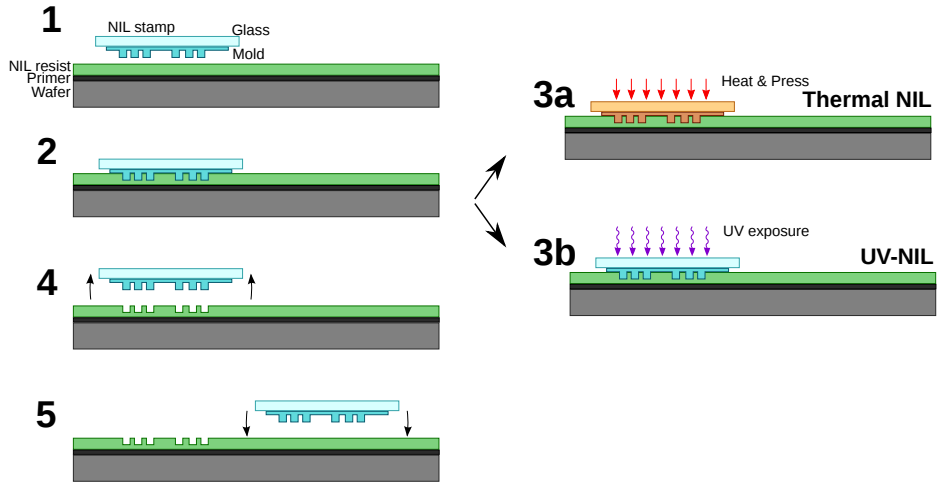

Figure 4.1: Schematics of nano imprint lithography. A NIL stamp, consisting of a glass handler and a mold with high resolution features, is brought in proximity of a silicon wafer covered with a NIL resist, with a layer of primer in between (1). The stamp is pressed on top of the sample (2) and the resist is cured, with either a Heat & Press process (3a) or a UV exposure (3b). The stamp is then released (4) and moved to a neighbouring location (5), where the entire process is then repeated.

of light or by the electron scattering, that are the main factors that limit the resolution in photolithography and in electron beam lithography. Instead, the resolution depends on the minimum size of the template feature [125]. Nanoimprint lithography can be of interest in the hard disk drive (HDD) industry and in the semiconductor industry, for example in device prototyping. In the field of memory products, where the requirements on high resolution are more stringent, NIL can become the preferred choice: because of the redundancy of the design of memory devices, they are also less vulnerable to defects [126].

Recently, nanoimprint was used in the fabrication of $200nm$ x $200nm$ cell area SRAM metal interconnects with $20nm$ half-pitch lines [127]. Nanoscale source-drain electrode pairs with continuous interconnects were also fabricated by thermal nanoimprint lithography [128], using a plastic substrate covered with silicon dioxide as stamp. In this case, the preferred choice of stamp material was Si/SiO_2, which has sufficient hardness and durability properties [129]. Nanowires are structures of interest in the field of photonics, electronics and life sciences. T. Martensson et al. demonstrated that the quality of arrays of nanowires fabricated using nanoimprint lithography is identical to those

fabricated by electron beam lithography [130]. More in general, nanoimprint lithography was demonstrated to be a suitable technique for the fabrication of integrated optical devices [131], grid polarizer [132], LEDs [133], photonic crystals [134] and plasmonic nanocavities [135].

Literature offers numerous review papers on nano imprint lithography [126] [124] [136] [129] [125]. H. Schift [124] addresses nano imprint lithography as a lithographic technique, giving an in-depth description of both the thermal-NIL and the UV-NIL processes. The author covers the NIL processes starting from the NIL resist materials and their mechanical properties, to an overview of different NIL machines. The paper from L. Guo [129] is an extensive review on nano imprint lithography, focusing especially on the fabrication of the NIL mold and the resist materials for both thermal-NIL and UV-NIL. More recently, E. Costner et al. [125] published a review paper on nanoimprint lithographic techniques, with a special focus on S-FIL (step and flash imprint lithography). Malloy et al. [126] describe the technological impact on industry, the performance of NIL in terms of resolution and throughput compared to other techniques and its intrinsic issues, mainly related to the defectivity.

The high resolution capabilities of NIL have already been demonstrated in many publications, where features in the $sub-20nm$ range can be resolved. Back in 1997, S.Y. Chou and P.R. Krauss experimentally demonstrated that the ultimate resolution of nanoimprint lithography could be in the $sub-15nm$ range, where the imprint process is repeatable and the stamp durable. They showed nanostructures imprinted into PMMA, including $10nm$ diameter holes and $15nm$ wide trenches, demonstrating uniformity over an area of $15mm$ by $18mm$ [137].

G.-Y. Jung et al. demonstrated the fabrication of high density lines at $17nm$ half pitch by nanoimprint lithography [138]. The NIL stamp with the $17nm$ features was fabricated by using the superlattice nanowire pattern transfer (SNAP) technique, where a superlattice, consisting of 300 layers of $34nm$ GaAs and $15nm$ AlGaAs, is used to produce 150 silicon nanowires on the stamp surface. The stamp is then pressed on the resist, which is cured by UV-light exposure. The resulting imprinted lines in the resist were transferred into an underlayer material. The substrate was covered with titanium and platinum by electron beam evaporation. The lift-off removed the under-layer, resulting in a sample with $17nm$ half pitch lines.

G. Calafiore et al. described a process flow to fabricate $sub-15nm$ lines,

that are also $sub-15nm$ thick at $50nm$ half pitch, using a multilayer lift-off process of features patterned by nanoimprint lithography [139]. The sample consists of a silicon wafer coated with PMMA, a silicon oxide layer, an adhesion promoter layer and the final NIL resist layer. First, the NIL resist is imprinted with a template containing gratings. Subsequent etching steps remove the NIL resist residual, the adhesion promoter layer and the silicon oxide layer. The PMMA is then opened up with an anisotropic etch using an oxygen plasma, followed by a metal deposition step, where chromium and gold are deposited by thermal evaporation. The smallest imprint that the author achieved is a $24nm$ pitch and $7nm$ wide gap grating, whereas the smallest metal line obtained was $14nm$ wide.

M.D. Austin et al. reported on the fabrication of lines with $5nm$ width and $14nm$ pitch using UV-nanoimprint at room temperature [140]. Also, they demonstrated that a 4 inch wafer was uniformly patterned in a single step. In this case, the stamp was fabricated by using a GaAs/AlGaAs superlattice. This process results in very dense $sub-50nm$ pitch features that can be manufactured over a large area, with very steep sidewalls and low defect and linewidth variation.

Single digit nanofabrication by nanoimprint lithography is demonstrated also by C. Peroz et al. [141]. The stamp consists of a quartz template with dense lines patterned in HSQ, that is an electron beam resist. The trench width varies from $100nm$ to $8nm$, while the height is constant at $30nm$, in order to keep vertical sidewalls. The stamp is first covered by Al_2O_3 by atomic layer deposition (ALD) such that the width of the trench can be carefully controlled by the thickness of the deposited alumina. The stamp is then pressed onto the sample surface, that is covered by a UV-light curable resist. Lines with sizes down to $7.2nm$ where successfully imprinted and transferred into silicon, with aspect ratios higher than 5 and 10 for $sub-10nm$ and $sub-20nm$ features respectively.

The resolution of NIL can be pushed even further using non conventional lithography techniques for the fabrication of the master. F. Hua et al. demonstrated the resolution limit of nanoimprint using single wall nanotubes (SWNTs) [142]. The SWNTs with typical size in the range $1-4nm$ are grown by CVD on a SiO_2/Si sample. A mold was derived from the $SWNT/SiO_2/Si$ master and used in a nanoimprint process. The author demonstrates that a SWNT of height of $2.4nm$ was successfully imprinted three times, resulting in tubes of height $2.4nm$. TEM analysis demonstrated that the lateral dimension of the tube is approximately $3.2nm$. This experiments demonstrated that NIL is capable of high resolution.

Typically, stamps for nanoimprint lithography are fabricated by electron beam lithography (EBL) [141] [143] or using more sophisticated GaAs/AlGaAs superlattice pattern transfer techniques [138] [140]. Other works [144] [145] presented nanoimprint stamps fabricated by proton beam writing, where a proton beam with high energy, typically in the order of MeV, is focused onto the sample surface and irradiates the resist. The main advantage of using protons instead of electrons is that because of their mass (approximately 2000 times that of the electrons) they travel through the material in a straight path. The secondary electrons generated by the interaction of the proton primary beam with the target are confined to the narrow primary beam, limiting the proximity effect compared to that of electron beam lithography. Stamps for nanoimprint lithography can also be fabricated by using edge lithography [146] [147], that consists of depositing thin films of materials on the sidewall of pre-patterned features, usually by evaporation. Also focused ion beam (FIB) is used for the fabrication of NIL stamps [148]. FIB uses a focused ion beam to remove material from a sample surface and it is a direct write technique that does not require any resist.

On a large scale, electron beam lithography is the preferred technique for the fabrication of high resolution $sub-300nm$ features. EBL, however, is a slow process that involves the spin coating of a resist on the sample surface, post-exposure development, the deposition of a metal layer and the lift-off of the residual of the resist. We want to use another electron-beam based lithography technique, that is also high resolution as EBL, for the fabrication of nanoimprint stamps. We propose to use Electron Beam Induced Deposition (EBID), that is a direct write lithographic technique, that does not require any resist nor post-exposure processing. A focused electron beam is scanned onto a sample surface in presence of a precursor gas, that is let into the system through a gas injection system. The precursor gas reacts with the primary beam and can be dissociated into a volatile part, that is pumped out the system, and a non volatile part, that sticks onto the sample surface, forming the deposit. EBID is a high resolution lithography technique, with which it is possible to pattern lines with sizes down to $3nm$ [38].

Typically, quartz substrates are used as support for NIL stamps, and there is little experience on transparent and conductive stamps in literature. W.J. Dauksher verified the compatibility of using ITO-based substrates as imprint-

ing stamps, reaching a fidelity of $20nm$ isolated lines and semi-isolated features of $20nm$ width in $150nm$ spacing [149]. While researchers are focusing their attention in addressing limitations such as overlay and multilevel capabilities and throughput [150], requirements on width and depth control strictly depend on the applications. The main drive is the reproducibility between NIL stamp and imprinted features, that can be achieved by investigating novel resists and tweaking the NIL parameters. Also, as best of our knowledge, no evidence was found on using EBID for the fabrication of NIL stamps.

In this chapter we will address the fabrication of NIL stamps using electron beam induced deposition: the mentioned experiments were performed in a collaboration with the EVG group, participant of the SNM project. We used silicon wafers, pyrex wafers covered with TiN and glass masters provided by the EVG group as templates, on top of which we patterned structures by EBID. Reference measurements of the NIL masters made by EBID and the imprinted wafers were subsequently validated by the Dutch Institute of Metrology (VSL), along with standard measurements performed with SEM and AFM.

4.3 Definition of the experiment

4.3.1 Design of the process flow for the fabrication of NIL stamps

We propose to use EBID for the fabrication of $sub-20nm$ nanoimprint stamps. As described in chapter 3, when patterning high resolution features, the aspect ratio is very small. $8nm$ wide lines can be as thin as $1nm$ and it is very difficult to control the vertical growth, without increasing the width. A way to overcome this problem is to increase the aspect ratio of high resolution lines by etching. In chapter 3, we described the pattern transfer of EBID lines into an underlying metal layer by plasma-based etching. We described the progress of etching into silicon, ITO and TiN. By using this knowledge it is possible to design a process flow for the fabrication of NIL stamps by EBID, with a subsequent pattern transfer to enhance the aspect ratio of high resolution features. Figure 4.2 shows the fabrication process of NIL stamps. First, the high resolution features are patterned by EBID in a scanning electron microscope, equipped with a gas injection system (GIS), that is positioned close to the sample. The sample can be either a silicon wafer or a pyrex wafer. In the first case, this sample cannot be used directly as a stamp because it is not transparent. The pyrex wafer, on the other hand, needs to be coated with a transparent and conductive layer, to

avoid charging effects during patterning. As already explored in chapter 3, the choice for such coating material can be either ITO or TiN. In the case of a silicon wafer, a first NIL process is done to fabricate a replica of the silicon wafer: in this intermediate step, the silicon wafer with which the transparent replica is fabricated, becomes the NIL master. In this phase, the silicon wafer is the stamp and the imprinted sample is a glass covered with a polymer. The curing phase is done by exposing the imprinted sample to UV light. Once the NIL stamps are ready, they can be tested as stamps for nanoimprint.

Typically, quartz substrates are used as support for NIL stamps, and there is little experience on transparent and conductive stamps in literature. W.J. Dauksher verified the compatibility of using ITO-based substrates as imprinting stamps, reaching a fidelity of $20nm$ isolated lines and semi-isolated features of $20nm$ width in $150nm$ spacing [149]. Also, to the best of our knowledge, so far EBID is not mentioned in literature with regard to NIL stamps fabrication.

4.3.2 Experimental methods

In this set of experiments our goal is to demonstrate the fabrication of NIL stamps by electron beam induced deposition. The questions that we want to answer are: will EBID structures survive the imprinting process or will they detach from the substrate they were patterned on? Are EBID structures transparent enough to the UV light for the NIL resist to be cured? How small can an EBID structure be to be still successfully imprinted? Ultimately, we want to investigate if stamps made by EBID can be imprinted multiple times without losing fidelity in terms of height and lateral size of the structures.

Patterning and imaging

The EBID stamps are fabricated in an FEI Nova Nano Lab 650 SEM using the platinum precursor ($MeCpPtMe_3$). For the patterning, we used a beam with $19kV$ acceleration voltage and $19pA$ current. The stamps are then imaged in the same microscope and then sent to EVG, where they are first analyzed with an AFM and then imprinted into a silicon wafer covered with a resist. The imprints are then analyzed with the AFM and returned back to Delft. Inspection with an FEI XHR Verios 460L is performed on the imprinted wafers using low landing energy as the resist charges heavily under the electron beam. Some of the analyses are repeated by the dutch institute of metrology (VSL) to have reference measurements.

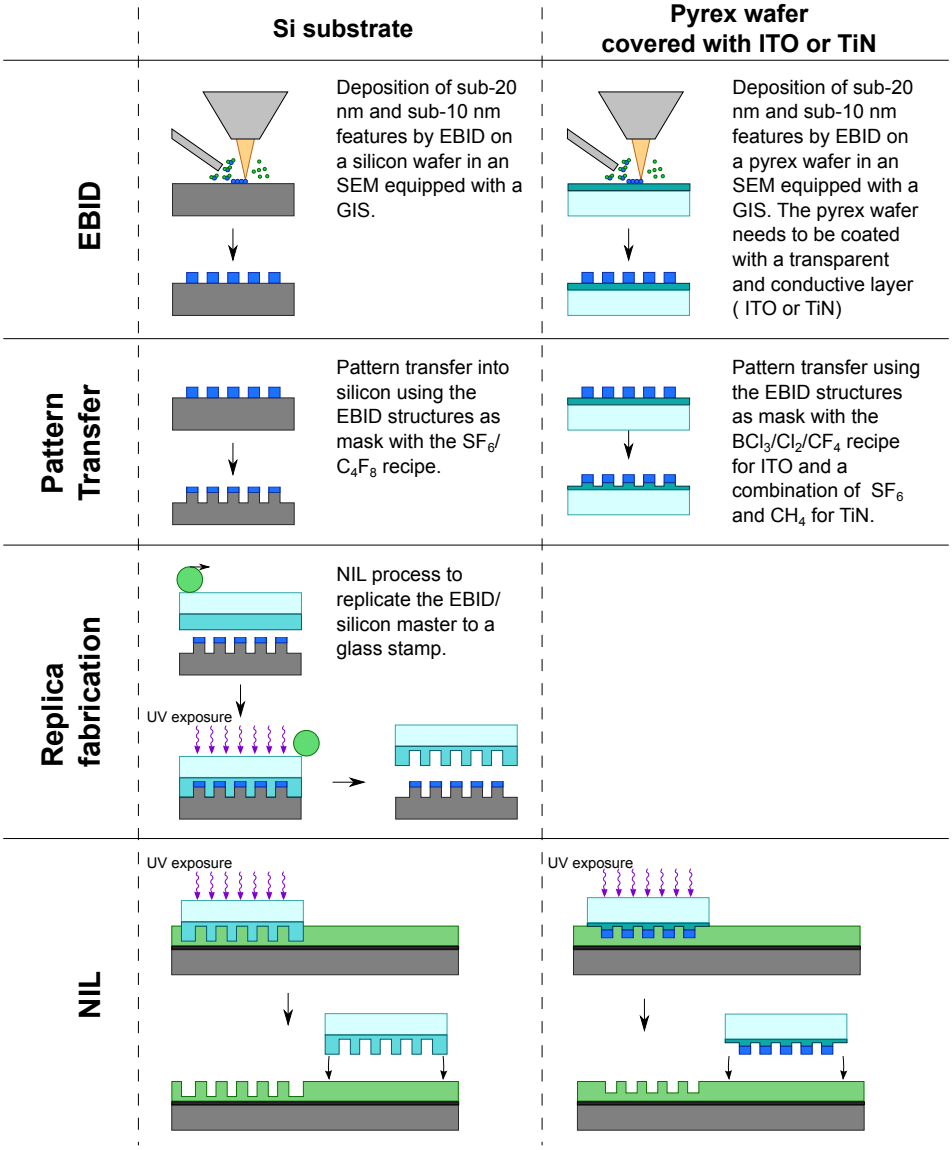

Figure 4.2: Process flow for the fabrication of nanoimprint stamps using electron beam induced deposition and a subsequent pattern transfer step, for enhancing the aspect ratio of high resolution features.

The substrate

We initially selected a Pyrex wafer covered with TiN, deposited with ALD, and subsequently diced to fit the NIL machine. However, it turned out that the wafer is too thin and cannot be clamped tightly in the NIL machine. We used then NIL glass stamps provided by EVG. To make them conductive, we deposited a thin layer of chromium on the first stamp and molybdenum on the second. Unfortunately, we could not deposit TiN because the NIL stamp was too big ($15x15cm$) to fit into the ALD machine.

The patterning template and the writing strategy

Figure 4.3a shows the patterned geometry and the patterning settings. 9 sets of lines with different width and spacing and three arrays of dots are patterned. The first array has dots of 12x12 pixels, while the second has 8x8 pixels and the third 5x5 pixels. All the arrays of dots are patterned with a dwell time of $100\mu s$. The lines are 1000 pixels long and have widths of 1 pixel, 2 pixels and 1 pixel for the first, the second and the third column of line sets respectively. The line sets are patterned with dwell times of $1ms$ (first column) and $100\mu s$ (second and third column). This geometry is patterned with a magnification of 31250× (small window), corresponding to a horizontal field of view of $4.096\mu m$, for which the size of a pixel is $1nm$. The line spacing, or pitch, is $100nm$ for the first row, $50nm$ for the second and $20nm$ for the bottom row and the pixel-to-pixel distance in each line is $1nm$. The entire template is patterned with 1000 passes. The entire geometry is patterned starting from the top left array of dots to the top right, and then the three sets of $100nm$ pitch lines (1A - 2A - 3A), followed by the $50nm$ pitch lines (1B - 2B - 3B) and the $10nm$ pitch lines (1C - 2C - 3C). This procedure defines 1 pass. More passes are implemented by following this procedure multiple times, in this case 1000. Four different fields are patterned, by changing the number of iterations, as shown in figure 4.3b: 10 (Field A), 5 (Field B), 2 (Field C) and 1 (Field D) iterations. The number of iterations defines how many times the 1000-passes template is repeated. Therefore, in case of 10 iterations, the pattern is repeated 10 (as the number of iterations) × 1000 (as the number of passes). Patterning fields A and B with 10 and 5 iterations respectively helps in navigating onto the sample surface as they are rather big. We tested the template D (1 iteration) on a silicon substrate. In this case, we patterned dots of $20nm$ (12x12 pixels), $13nm$ (8X8 pixels) and $7nm$ (5x5 pixels), and height $7nm$, $2.5nm$ and $1nm$. As for the lines, we expect a line width of $17nm$ (1 A-C), $10nm$ (2 A-C) and $6nm$ (3 A-C), with height of $5nm$, $2nm$ and $0.8nm$, as shown in figure 4.4. Field C, patterned with 2 iterations, will have slightly broader and slightly higher structures. We decided to pattern bigger

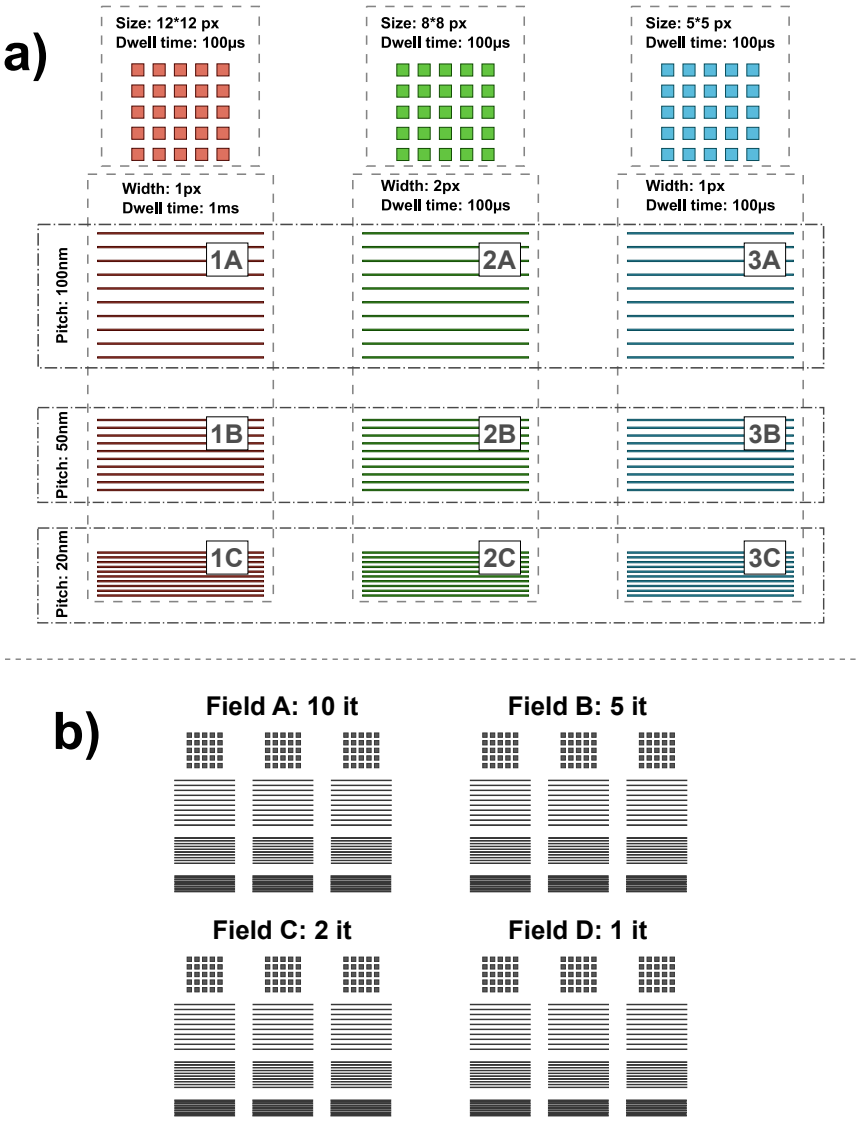

Figure 4.3: a) Template of the EBID structures, consisting of three arrays of 5x5 dots and 9 sets of lines of different widths and pitch and b) the four patterned fields with different iterations.

structures in case Field D did not survive the NIL process.

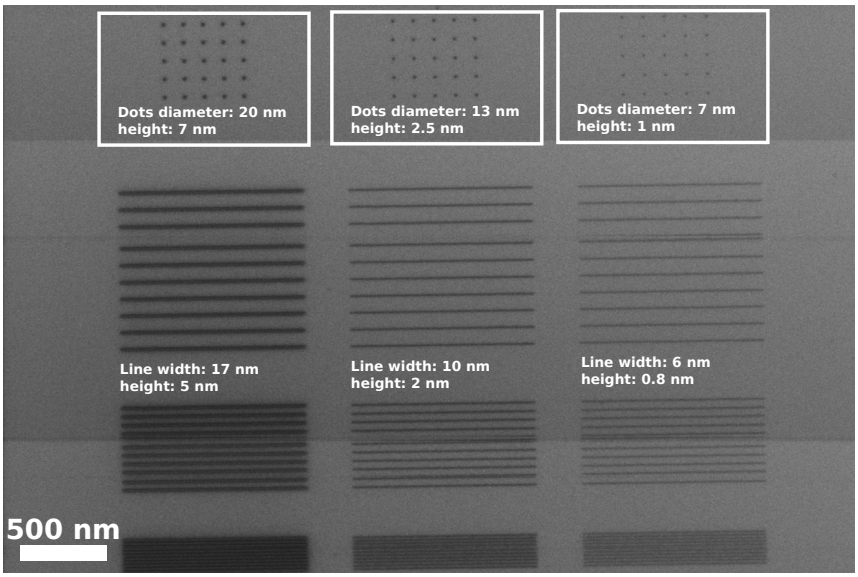

Figure 4.4: SEM image of the template in figure 4.3a, tested on a silicon substrate with 1000 passes and 1 iteration.

4.4 NIL using a replica of an EBID master - TiN on Pyrex

In Step & Repeat NIL (S&RNIL), stamps are made out of glass handlers, that are UV-transparent. In this experiment, a Pyrex wafer, that is a type of glass, was used. Because glass is non-conductive and charges under the electron beam, a UV transparent and conductive metal coating is necessary prior to depositing structures by means of EBID. A layer of TiN was deposited by atomic layer deposition (ALD), providing an atomically flat and UV transparent surface. The wafer is then diced to a square of size $65mm \times 65mm$, that can be fit in the NIL machine. As it turned out, however, the pyrex sample was not thick enough to be securely clamped in the NIL machine and therefore a replica of the EBID master needed to be fabricated.

Figure 4.5 shows the process flow of the first experiment. First, the stamp was fabricated using electron beam induced deposition in an FEI Nova Nano Lab 650 scanning electron microscope. We used a pyrex wafer covered with $10nm$ of TiN deposited with ALD. The structures were patterned at $19kV$ in spot 2 (equivalent to approximately $39pA$ current in the spot) in immersion mode using the platinum precursor. After that, a replica of the EBID master was

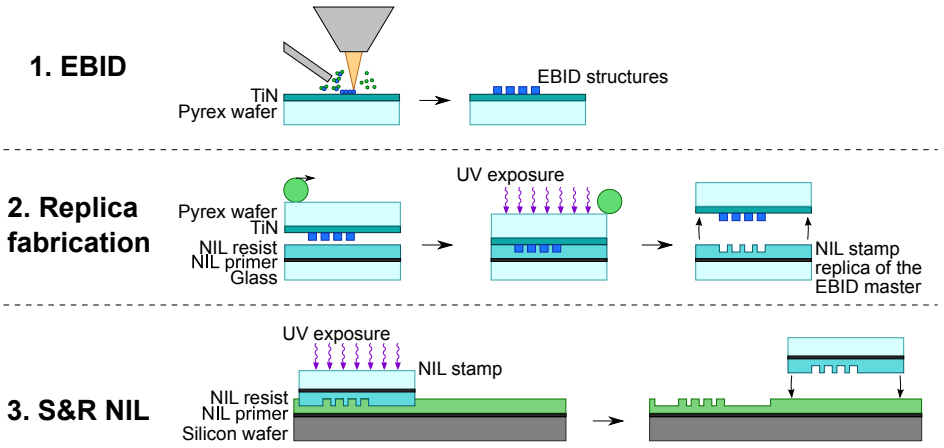

Figure 4.5: Process flow of the first experiment of fabricating NIL stamps by EBID. EBID structures were patterned on a pyrex wafer covered with TiN by EBID, in a scanning electron microscope (1). The sample features were replicated on a NIL master using the smart NIL process, where a roll moves across the EBID stamp placed on top of the NIL master, covered with NIL primer and resist. The stack is then exposed to UV light and the EBID stamp is released, leaving the negative impression of the EBID features on the resist (2). Lastly, the NIL stamp is impressed on top of a wafer covered with NIL resist and NIL primer, according to the S&RNIL flow depicted in figure 4.1 (3).

made in the EVG facility using the smart NIL process, which is done as follows. The EBID master is placed on top of the replica and pressed by means of a roll that moves across the pyrex wafer. When the roll has finished moving on top of the pyrex wafer, the sample is exposed to UV light. The EBID master is then released, after having imprinted the features in the replica. The replica is then used for the Step & Repeat NIL to imprint a silicon wafer covered with NIL resist. To ensure good attachment of the NIL resist to the substrate, a NIL primer layer is deposited in between. The primer layer increases the adhesion between the wafer and the imprinted structures. In fact, a strong force is needed to separate the template from the imprint and without the primer there is a high risk that the imprint will separate from the wafer and stick on the sample surface. The thickness of the primer is just a few nanometers, whereas the resist is approximately $400nm$ thick and both were spin coated on the entire sample. The replica is then pressed on the NIL resist, which is then exposed to the UV light. To cure the imprint, a light with wavelength of $320nm$ and $500nm$ is narrowed down from a broadband light source in the exposure unit. During the exposure, which takes only 60 seconds, a force of $1N$ is impressed on the replica.

Subsequently, the replica is released and moved to another location to repeat the imprint process. In total, 9 imprints have been done on a 8 inch wafer.

4.4.1 Fabrication of the EBID master

The glass wafer was cut to a square with lateral size of $65mm$. Because the region of interest where the EBID structures are patterned is very small compared to the actual size of the sample, a search geometry is patterned to guide to the location of the EBID patterns. Figure 4.6 shows the SEM image of the patterned search geometry, that was etched in the TiN layer by ion milling using a gallium Focused Ion Beam (FiB). The ion milling process was performed in the FEI Nova Nano Lab 650 dualbeam system, at $30kV$ and $26nA$ beam current. The searching geometry consists of 4 diagonal lines, starting from the corners of the TiN/Pyrex sample and are directed towards the centre of the sample, where the EBID structures are patterned. The region of interest is recognizable by 4 crosses of size $40\mu m$, milled in the TiN layer. Figure 4.6a shows the region of interest after the sample was cut, where some dust particles are visible.

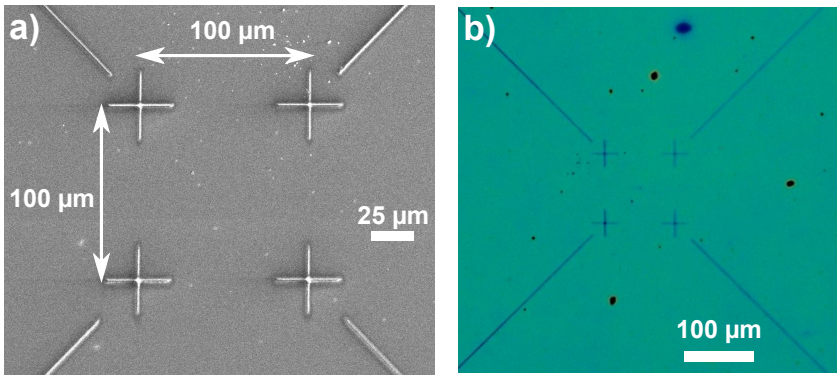

Figure 4.6: a) SEM micrograph of the search geometry, that defines the region of interest of size $100\mu m$ by $100\mu m$. The search geometry was patterned by ion milling. b) Optical image of the region of interest after cutting the TiN/pyrex wafer. The search geometry patterned by FIB is visible.

Before patterning the structures of the TiN/Pyrex wafer, the SEM chamber was thoroughly plasma-cleaned in order to remove any contamination. The Pyrex wafer was then tightly clamped to a heavy wafer handler, to limit mechanical vibrations. Prior the deposition, the SEM chamber was pumped

down for 30 minutes, until the pressure reached $1.62 \cdot 10^{-6} mbar$. First, the beam is focused on the patterned search geometry, where small features in the $sub-50nm$ range could be found. Then, the GIS was heated until reaching the temperature of $42°C$. Before starting the patterning of the structures, the flow is let stabilize for approximately 20 minutes. Fields A, B, C and D, previously defined in figure 4.3, were patterned in the middle of the search geometry of figure 4.6a, using a $19kV$ beam with $19pA$ beam current, at a working distance of $5.27mm$, equivalent to the eucentric height.

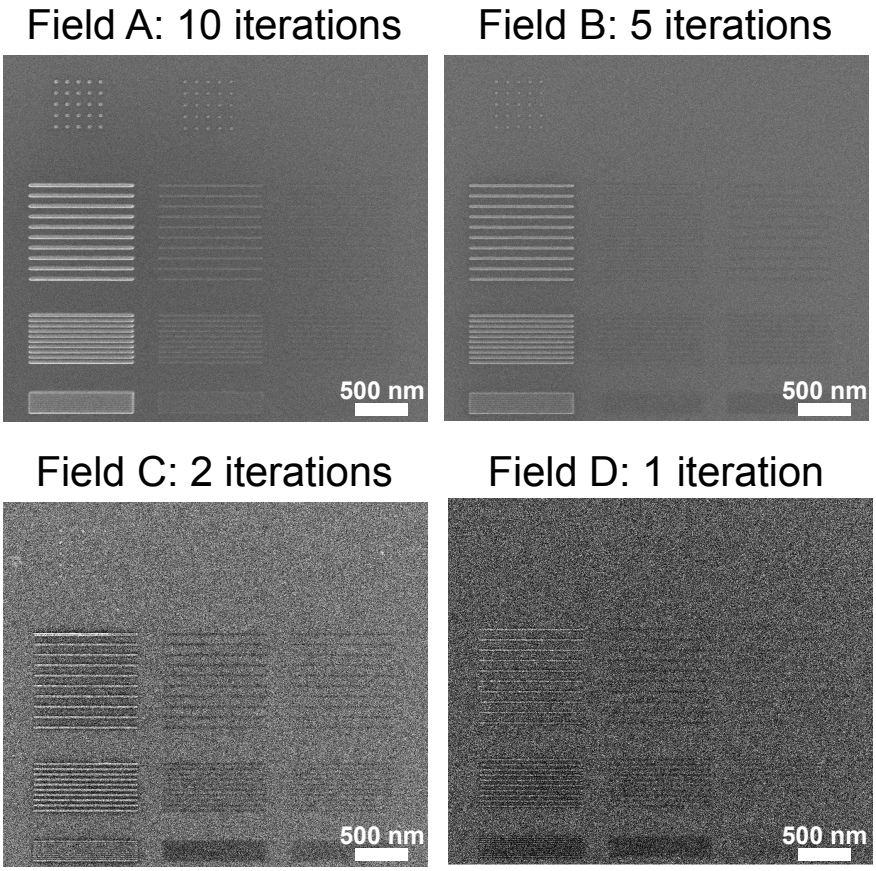

Figure 4.7: SEM micrographs of the EBID template patterned with 10, 5, 2 and 1 number of iterations on the TiN/pyrex wafer on the EBID master. The contrast of fields C and D was digitally enhanced.

Figure 4.7 shows the SEM micrograph of the four fields, that are patterned with 10, 5, 2 and 1 number of iterations. The images are taken at $19kV$ in spot 2

(approx $39pA$) in immersion mode with the through-the-lens secondary electron detector (TLD). The contrast of fields C and D is really poor because of the lines being very shallow. Measurement of the width of the lines on the EBID master and the comparison to the line width of the imprints will be discussed later.

4.4.2 Results

The EBID master could not be used directly as NIL stamp because the Pyrex was too thin to be clamped in the NIL machine. Following the work-flow presented in figure 4.5, a replica was made from the EBID master. The replica is used as NIL stamp to imprint a wafer covered with a few nm NIL primer (EVG Prim KR) layer and a $400nm$ thick resist layer (EVG NIL UV/SA). Figures 4.8 and 4.9 show the SEM micrographs of the 1st imprint and the 9th imprint, where the imprinted structures in the NIL resist are visible. The sample heavily charges under the electron beam, we therefore used the FEI Verios 460 SEM for inspection, which has higher resolution at low acceleration voltages than the FEI Nova Nano Lab 650. We used a $5kV$ landing energy beam, stage bias of $4kV$ and $100pA$ current. The EBID master, where the structures are standing out the surface, was replicated to fabricate the NIL stamp, where the negatives of the EBID structures can be found. Therefore, the EBID lines and dots became effectively indentations. The nine imprints, on the other hand, present the positive replica of the EBID structures as a consequence of imprinting the negative-NIL stamp.

In figure 4.8, SEM images of Field A and zoomed-in images of areas 1, 2 and 3 are shown. In area 1, we clearly notice that some of the lines are interrupted, whereas this is not observed on the other structures in the same field. If we compare this to figure 4.9, where a zoomed-in of area 1 on the 9th imprint is shown, we again see the same interruptions. We conclude that in this case the NIL stamp was damaged during the first NIL process. Unfortunately we did not receive the NIL stamp and this could not be verified. As for Field B, we notice again some damages on the imprinted lines. In the zoomed-in areas 4 and 5 interruptions are clearly visible, but are not reproduced on the ninth imprint, as shown in figure 4.9, zoomed-in imaged of areas 2 and 3, belonging to Field B. We conclude that in this case the damage was caused during the imprint. This was not an isolated case, however, as some damages can also be seen in the zoomed-in images 7 and 8 of figure 4.8 of Field C and are not replicated in the same areas of the ninth imprint (figure 4.9, areas 4 and 5).

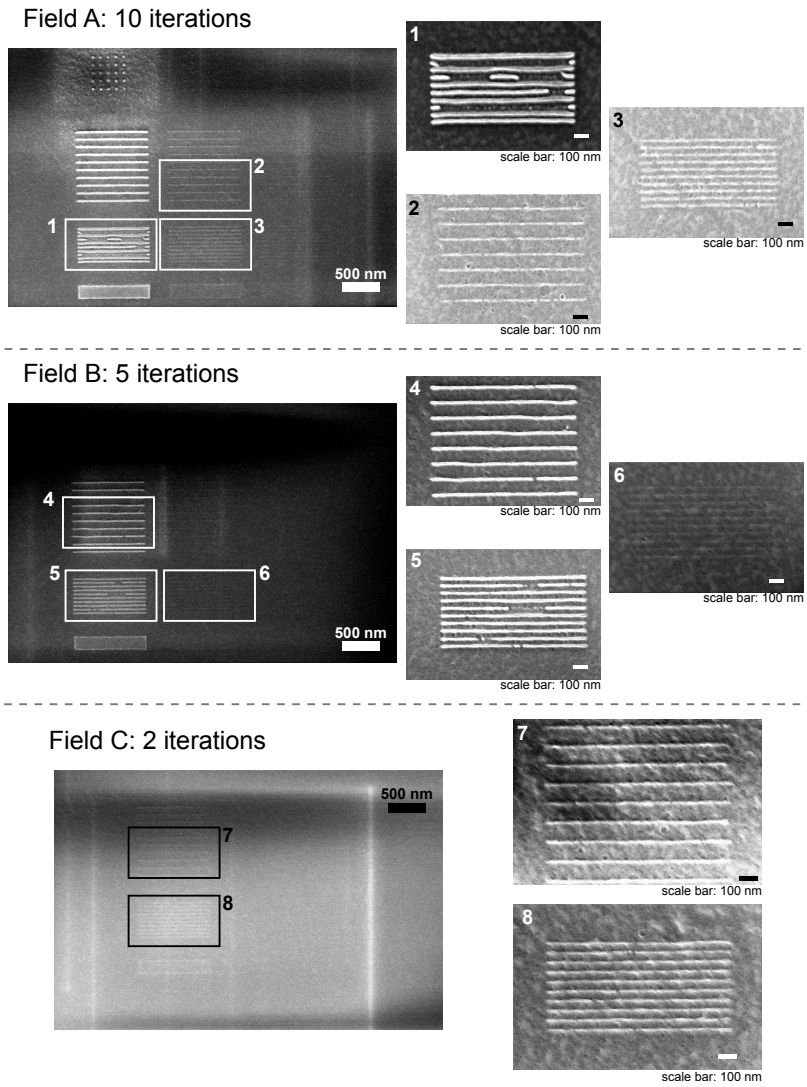

Figure 4.8: SEM micrographs of the 1st imprinted wafer, showing fields A (10 iterations), B (5 iterations) and C (2 iterations). Zoomed-in images of areas 1-8 are also shown. We observe some damages in the imprinted lines in areas 1, 4, 5, 7 and 8.

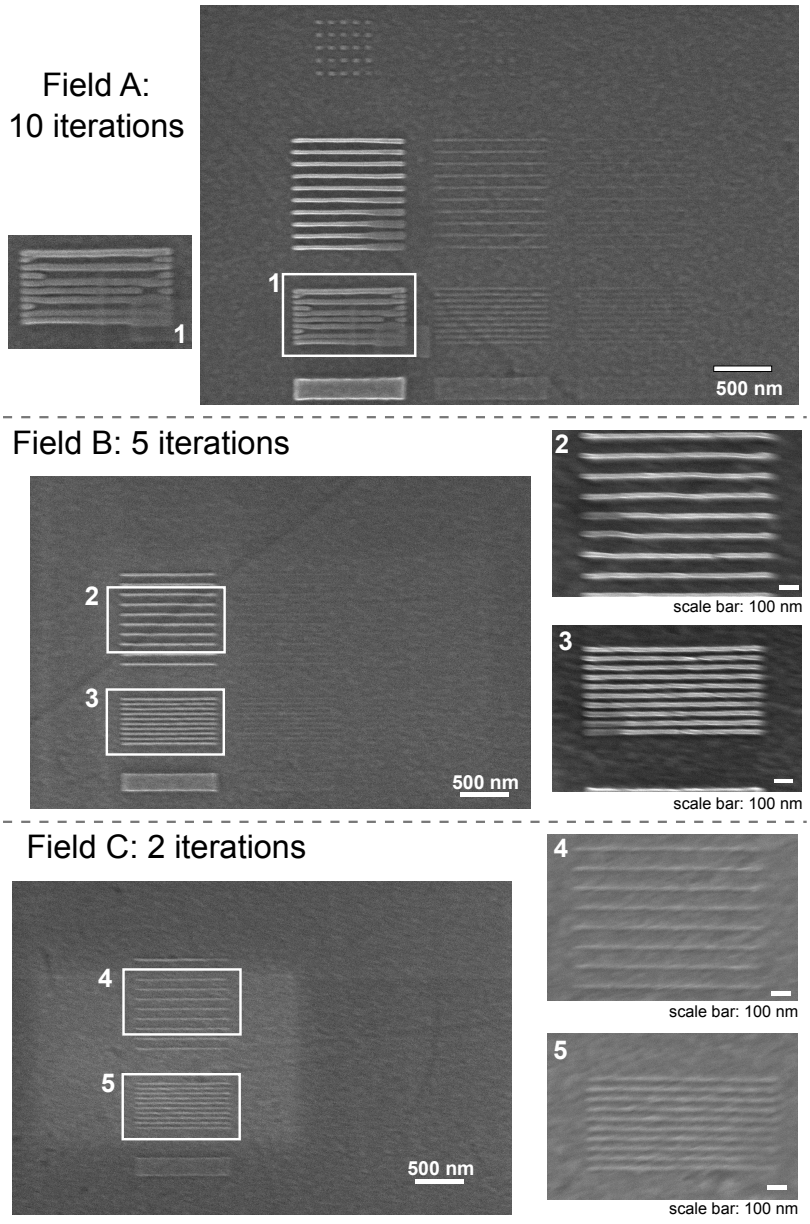

Figure 4.9: SEM micrographs of the 9th imprinted wafer, showing fields A (10 iterations), B (5 iterations) and C (2 iterations). The damages that we earlier saw in figure 4.8, area 1 are here again visible. We conclude that in this case the replica may be damaged. The other imprinted EBID lines do not show any damage, as those reported in figure 4.8 (areas 4, 5, 7 and 8). We conclude that in this case the first imprinting was faulty.

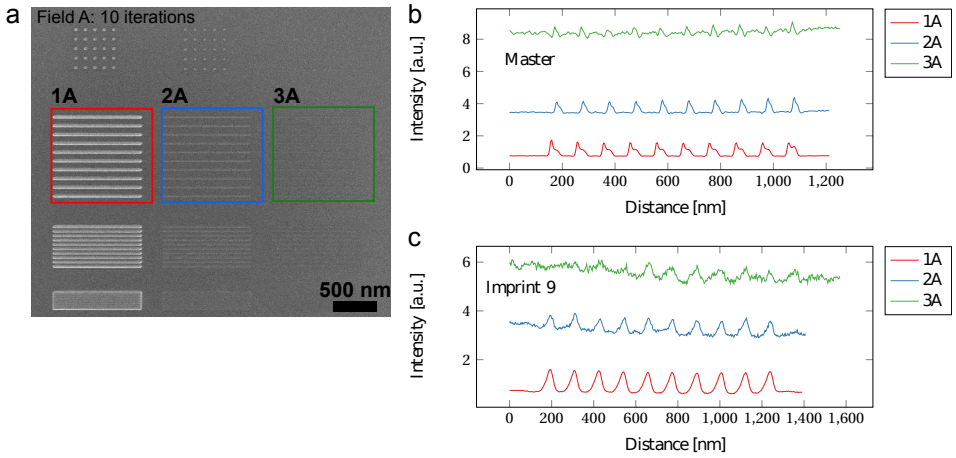

Figure 4.10: a) SEM image of Field A (1 iteration) of the master, showing areas 1A (theoretical width: $17nm$), 2A (theoretical width: $10nm$) and 3A (theoretical width: $6nm$), as described in figure 4.3a. b) and c) Integrated line profile over the entire length of the lines 1A, 2A and 3A in Field A (10 iterations) on the master and on the 9th imprint.

In figure 4.10a, we present the SEM micrograph of Field A (patterned with 10 iterations) of the EBID master, already shown in 4.7, where the sets of lines 1A (theoretical width: $17nm$), 2A (theoretical width: $10nm$) and 3A (theoretical width: $6nm$) - as described in figure 4.3a - are highlighted. Next, in figure 4.10b and 4.10c the integrated line profiles (over the entire length of the lines) of the master and the 9th imprinted wafer are shown, where the offset in the intensity was adjusted to fit the graph. We measured the line width at half maximum (FWHM) from the integrated line profiles. In case of the EBID master, the line profiles have a stair-case shape on the right of the peak. We nevertheless measured the width of the line profile at half the height of the peaks.

From the integrated line profiles of the EBID master, the first imprint and the 9th imprint, we measured the width of each of the 10 lines as the FWHM value. We then averaged the 10 measured line widths and calculated the 1σ (standard deviation). We plotted the resulting line width of Field A, B and C in figures 4.11. We noticed that typically the width of the lines decreases between the EBID master and the imprints. So, if we look at Field A, patterned with 10 iterations, the width of the line, initially of $\approx 54nm$ on the EBID master, decreases to $\approx 45nm$ and $\approx 32nm$ on the first and ninth imprint respectively. In this case, lines have shrunk by a factor of 17% in case of the first imprint and by a factor of 40.7% in case of the ninth imprint. The smallest line that could be

successfully imprinted for 9 times had a width of $\approx 23nm$ on the EBID master. In this case, however, the width increased to $\approx 29nm$ on the first imprint and to $\approx 31nm$ on the ninth imprint. The increase in line width could be an artifact introduced by the poor quality of the images on the NIL resist, where the lines are not well visible and the integrated line profile is noisy.

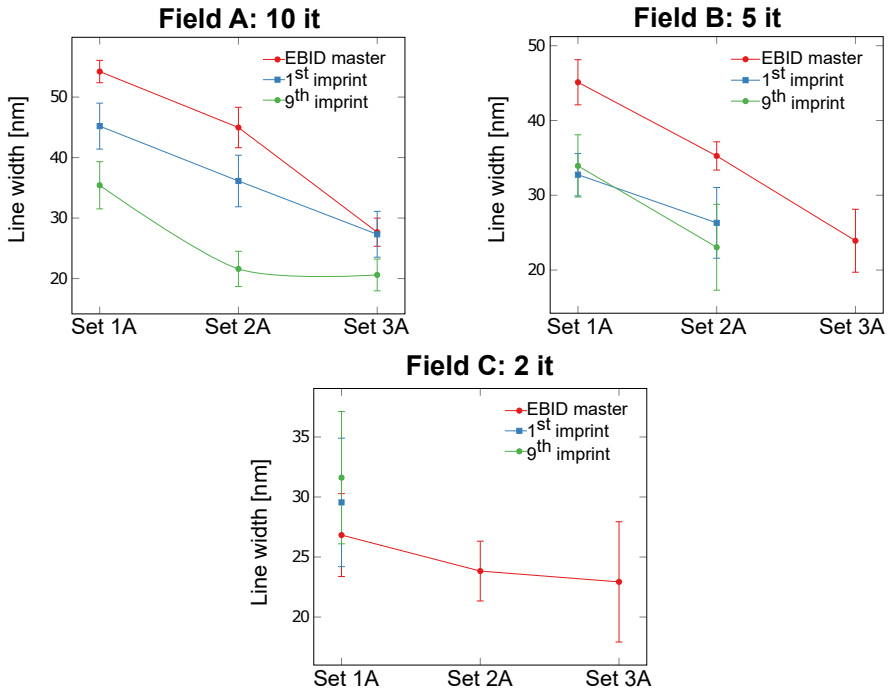

Figure 4.11: Results of the line width measurements, calculated from the integrated line profiles of Field A, B and C of the master, the first imprint and the ninth imprint.

Analysis with AFM on the EBID master, the replica and the first and the ninth imprints was performed in EVG. Thanks to this analysis, the height of the structures of the master, the replica and the imprints can be analyzed. Figure 4.12a shows an example line profile of the Field A (patterned with 10 iterations) and the set of lines 1A, as shown in figure 4.10. We noticed that in the AFM analysis the pitch of the line differs from sample to sample, probably due to drift or a poor calibration of the AFM. Also, as shown in figure 4.12b, the line width is broader than that measured from the SEM line profiles. The reason is that tip-deconvolution was not performed during this analysis.

Figure 4.13 shows the height of the lines from the master, the replica and the first and the ninth imprint, measured from the AFM analysis. For these mea-

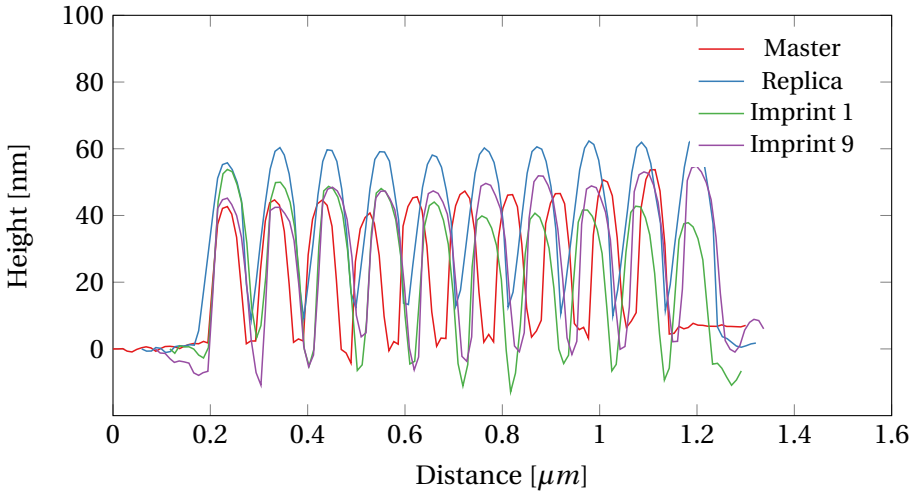

(a)

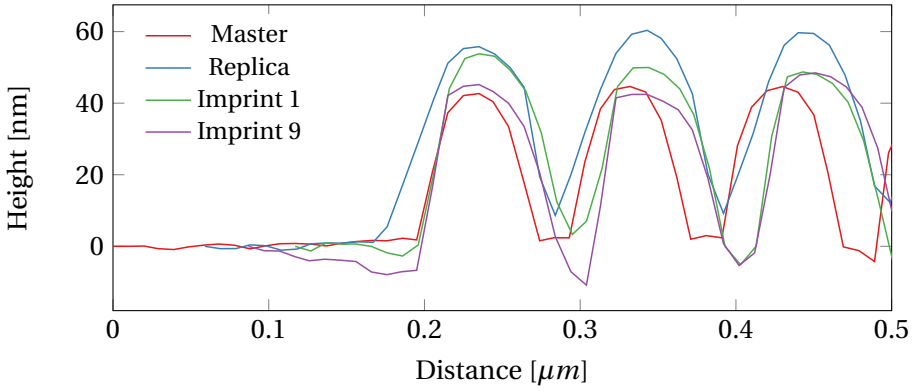

(b)

Figure 4.12: a) AFM line profiles of Field A (10 iteration) of the master, the replica, the first imprint and the ninth imprint of the 100nm pitch lines of box 1A from figure 4.3a. b) zoomed-in of the graph in a) showing the difference in height of the structures on the master, the replica and the imprinted chips.

surement, the integrated line profiles of the sets of lines 1A, 2A and 3A were analyzed. When looking at the height of the structures, the fidelity is higher than when measuring line widths. However, we noticed that the height of the structures on the master are smaller than the structures on the replica. We do not know the cause of this phenomenon, which may have occurred during the

process of replication.

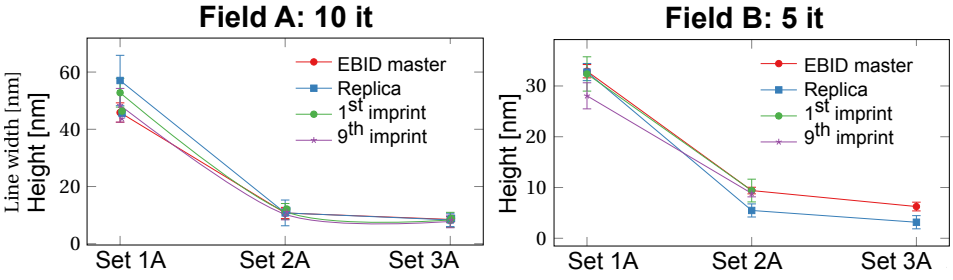

Figure 4.13: Results of the height measurements, calculated from the integrated line profiles of Field A and B of the master, the replica and the first imprint and the ninth imprint.

4.4.3 Discussion

In this section, we investigated the fabrication of an EBID master for nano imprint lithography, consisting of a Pyrex wafer covered with $10nm$ of TiN, deposited by ALD. We initially designed the experiment as if we could use the EBID master directly as NIL stamp, but because the Pyrex wafer was not thick enough, the master was replicated into the NIL stamp, which was then used to imprint nine locations on a silicon wafer covered with NIL resist. We patterned structures consisting of sets of lines and arrays of dots with a wide range of exposure times, that lead to lines of various sizes. While the biggest patterns served mainly as search features, the patterns deposited with lower exposure time served to characterize the NIL process. Still under the belief we could employ the EBID master directly as NIL stamp, we cut the wafer into a $65mm$ x $65mm$ square chip. Cutting the sample led to particles sputtered on the sample surface, but fortunately they did not cover the patterned structures. Once the replica was fabricated by Smart NIL, we used this stamp to imprint a wafer covered with a layer of NIL resist on top of a primer layer, that served as adhesion layer. We analyzed the line width and the height of the structures measured from SEM imaging and AFM inspection, respectively. More specifically, we investigated the sets of line 1A, 2A and 3A as previously defined in figure 4.3b for Fields A, B and C, patterned with 10, 5 and 2 iterations, respectively. The line width, measured as the FWHM, decreased considerably from the EBID master to the 9th imprint, up to a fraction of approximately 41%. As for the height of the structures, we analyzed the integrated profiles from the AFM inspection performed by EVG. We noticed that the pitch of the lines is not constant

throughout different AFM scans and we think the reason lies in the poor calibration of the AFM system. Despite the height decrease from the EBID master to the NIL stamp, as shown in figure 4.13 for field A, the line height remains constant, within the 1σ value, from the replica to the first and ninth imprints. To the best of our knowledge, this was the first attempt to imprint a wafer with a NIL stamp, fabricated with a Smart NIL process from an EBID master. Despite the fact that some fidelity is lost in the replica fabrication, the shape of the lines in terms of height is maintained during the nine imprints. As a next step, we wish to investigate the fabrication of NIL stamps directly by EBID to understand how the EBID structures react on the stress of being pressed on the NIL resist and released from it.

4.5 NIL using an EBID master - Cr on Glass

In section 4.4.3, the fabrication of a NIL master made by EBID was discussed. The NIL master consists of a Pyrex wafer covered with $10nm$ of TiN, on top of which sets of lines of different width and height were patterned by EBID. Initially, the experiment was designed to use the TiN/Pyrex wafer directly as NIL stamp. However, the thickness of the Pyrex wafer was not sufficient to tightly clamp it in the NIL machine. Therefore, a replica of the NIL master was fabricated using the Smart NIL process, shown in figure 4.5, step 2. The replica of the NIL master was used to imprint 9 locations on a single wafer using the S&RNIL technology. As resulted from this experiment, the fidelity in height was maintained for some of the patterns, as shown in figure 4.13. However from the SEM analysis some of the imprinted lines were observed to be damaged on both the first and the ninth imprint, suggesting that the replica was in fact damaged. Moreover, we also measured the line width from the integrated line profile of the SEM images, calculated using the FWHM definition. As a trend, the line width on the imprints has shrunk up to a factor of almost 41%.

Now that we have proven the possibility of producing NIL masters by EBID, we want to investigate the direct fabrication of NIL stamps by EBID. We asked EVG to provide standard NIL stamps, on top of which we could directly pattern the EBID structures. The NIL stamp, shown in figure 4.14 consists of large glass handle of $15cm \times 15cm$ in size with a thicker area in the middle of size $2.5cm \times 2.5cm$, called mesa, which is the area that will effectively be imprinted on the silicon wafer.

The stamp must be coated with an UV transparent metal layer, providing a conductive film. Unfortunately, TiN could not be deposited because the NIL stamp is too big to fit into the ALD machine. The choice of the coating metal is

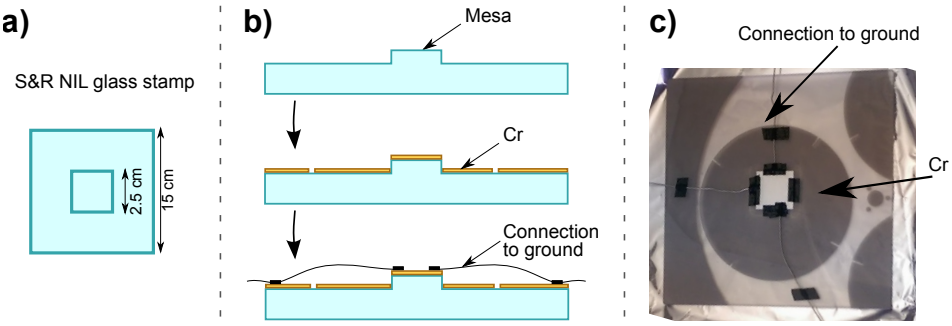

Figure 4.14: a) The NIL master consisting of a square glass plate of size $15cm \times 15cm$ with a thicker area in the middle of size $2.5cm \times 2.5cm$, called mesa, was provided by the EVG group. b) The NIL master was coated with a $10nm$ layer of chromium, that provides a smooth and conductive surface and wires were added to provide the electrical connection to ground. c) Picture of the NIL stamp covered with chromium (dark grey areas) with wired connections to ensure an electron path from the mesa to ground. The uncovered areas were in fact not exposed to the metal deposition because hidden behind the clamping system of the metal deposition machine.

limited to the range of available metals in a specific metal deposition machine where the NIL stamp fits. Within the range of available materials, chromium is a good candidate as a coating metal, as it provides a rather uniform metallic layer. Moreover, the transmittance of the chromium layer can be estimated for the UV-exposure wavelengths and for different layer thickness. Table 4.1 shows the transmittance of chromium as listed in the database [151]. A layer of $10nm$ of chromium offers at the same time a uniform conductive layer and an acceptable transmittance of 38% and 43% at wavelengths of $320nm$ and $500nm$. Therefore, as shown in figure 4.14b, we deposited the chromium layer on top of the NIL stamp. To provide electrical contact between the mesa and the lower part of the stamp, thus to ground via the stage, we connected the mesa to the lower chromium surface with wires, secured on the sample with carbon tape. Figure 4.14c, shows the chromium covered NIL stamp. The Cr covered parts show up in dark grey and the uncovered areas coincide with the clamping system of the metal deposition machine.

The process flow followed in this experiment is shown in figure 4.15. The NIL glass stamp is first covered with a $10nm$ layer of chromium, providing a sufficiently smooth conductive surface that has an acceptable transmittance at the UV-exposure wavelength (1). The structures are patterned using electron beam induced deposition (EBID) in an FEI Nova Nano Lab 650 SEM, equipped with a gas injection system, using the platinum precursor ($MeCpPtMe_3$). The

Wavelength	Cr thickness				
	$1nm$	$5nm$	$10nm$	$15nm$	$20nm$
$\lambda = 320nm$	0.90	0.61	0.38	0.23	0.19
$\lambda = 500nm$	0.92	0.66	0.43	0.28	0.14

Table 4.1: Transmittance of Chromium [151].

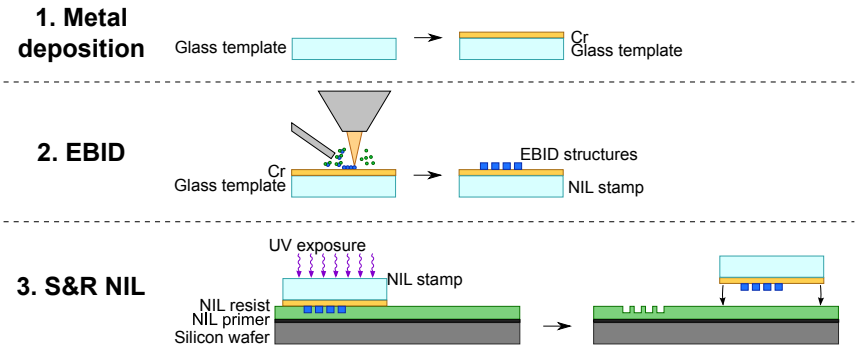

Figure 4.15: Process flow of the second NIL esperiment. A NIL glass template is covered with a chromium layer, providing a conductive surface (1). The structures are then patterned by EBID in a scanning electron microscope, using the platinum precursor (2). The NIL master with EBID structures is directly used as a stamp to imprint 9 times a silicon wafer covered with a NIL resist and a NIL primer, that acts as an adhesion layer (3).

NIL glass stamp, covered with the chromium layer and with the EBID structures is directly used in the S&RNIL process (3). The imprinted substrate consists of a silicon wafer, covered with a NIL resist and a NIL primer layer, providing good adhesion of the resist to the underlying silicon wafer. To cure the resist, a light with wavelength of $320nm$ and $500nm$ is narrowed down from a broadband light source in the exposure unit, as in the previous experiment. The NIL stamp with EBID structures is imprinted 9 times on different locations of the same silicon wafer.

4.5.1 Fabrication of the NIL stamp by EBID

Because the dimension of the mesa is rather large compared to the area where the EBID structures will be patterned, a search geometry was fabricated. A region of interest of size $100\mu m$ by $100\mu m$ is defined by four crosses milled away from the chromium layer using an ion beam, as shown in figure 4.16. The

search geometry was patterned in the FEI Nova Nano Lab 650 dual beam SEM, using a $30kV$ ion beam, with $26nA$ current. The crosses are then connected to the corners of the mesa by lines, that are also etched from the chromium layer by ion milling.

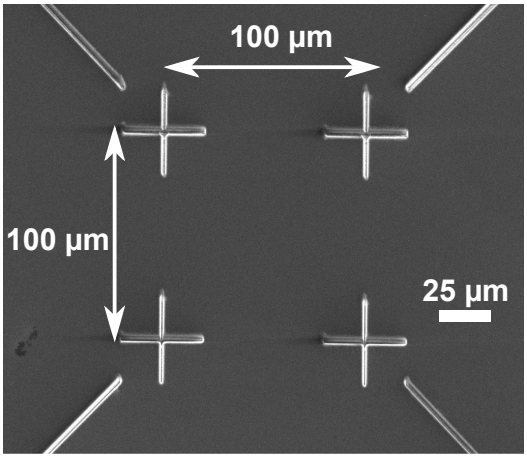

Figure 4.16: SEM micrograph of the region of interest and the search geometry, defined by four crosses etched from the chromium layer by ion milling in a focused ion beam (FIB) machine. The four crosses, that are $100\mu m$ from each other, are connected to the four corners of the mesa by lines that were also etched by FIB.

The structures are deposited using EBID in the FEI Nova Nano Lab 650 SEM, at $18kV$ and spot 1, that corresponds to a current of approximately $18pA$, in immersion mode. In the region of interest shown in figure 4.16, four different fields are patterned with 10, 5, 2 and 1 number of iterations. The writing strategy is the same as described in section 4.3.2 and the patterned geometry is that depicted in figure 4.3. The four patterned fields are shown in figure 4.17. Field A, patterned with 10 iterations, has large lines, whereas field D, patterned with lower dose, has the smallest features. The analysis of the line width based on these SEM images is presented in the next section. During the patterning, we noticed some charging effects possibly introduced by the natural growth of an oxide layer on the chromium film, which may have caused a broadening of the lines deposited by EBID.

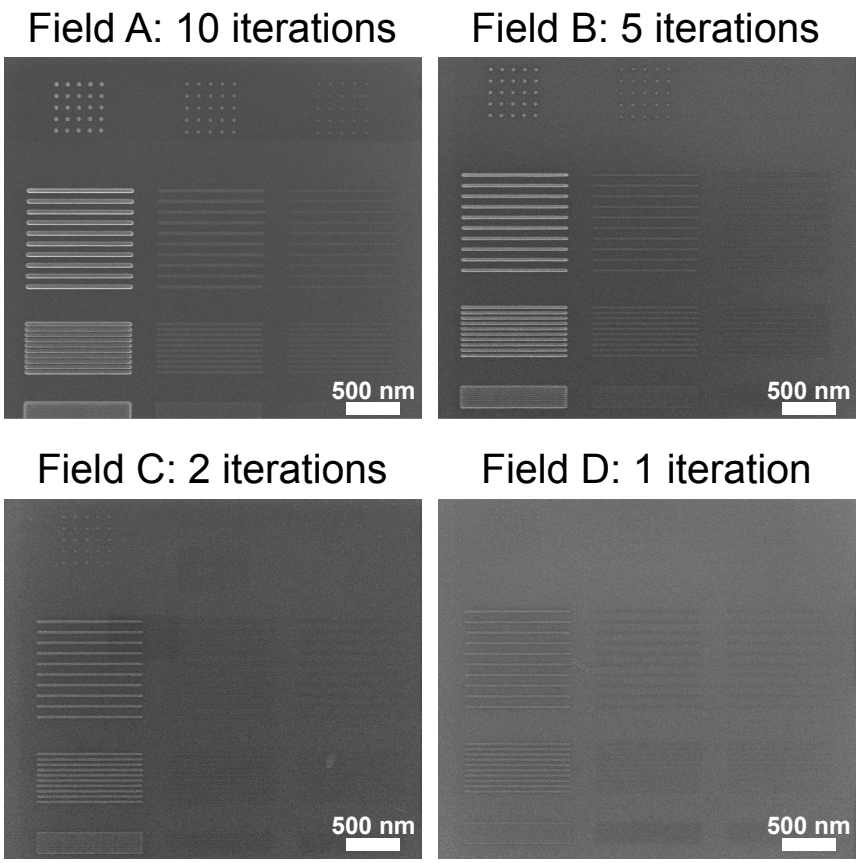

Figure 4.17: SEM micrographs of the NIL master before it was employed in NIL. The images show the fields A, B, C and D patterned with 10, 5, 2 and 1 iterations respectively.

4.5.2 Results

The NIL stamp with EBID features was imprinted 9 times on different locations on the silicon wafer covered with NIL resist at the EVG facility. The chromium layer was sufficiently transparent to the UV light, that cured the NIL resist during the NIL process. Figure 4.18 shows the SEM images of the NIL master of fields A, B, C and D after it was employed in the NIL process. Although some of the dots are damaged (for example the first array of dots in Field A), all the lines appear to be intact, demonstrating that the EBID structures adhere well to the chromium layer and survived all the nine imprinting steps. A dark halo appears in field D as well as in a small area of field B, for which the cause is unclear. We think it may be some residual of the NIL resist that got stuck on the EBID stamp.

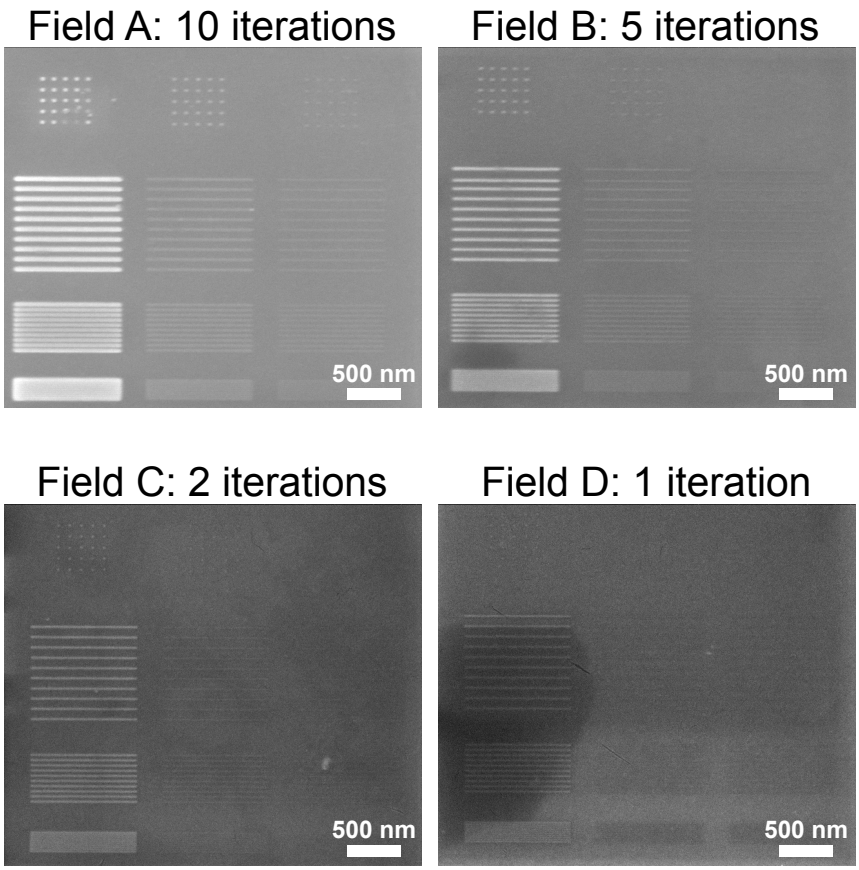

Figure 4.18: SEM micrographs of the NIL stamp, showing the four EBID templates, patterned with 10, 5, 2 and 1 iterations, after the NIL process.

Figure 4.19 shows an SEM image taken with the FEI Nova Nano Lab 650 of the region of interest inside the search geometry of the 9th imprint. The wafer is still covered with NIL resist: the crosses, that define the region of interest, are now sticking out the surface, while the patterned lines are now grooves in the resist layer. Because the sample is still covered with NIL resist it charges heavily. To image it, we used a $5kV$ beam and spot 3, which corresponds to a current of $98pA$.

We measured the line width of the EBID structures deposited on the NIL stamp before and after being used in the NIL process as well as that of the ninth imprint. In case of M-shaped line profiles, we used the method of the inflection point, where the derivative of the line profile is calculated and the line width is

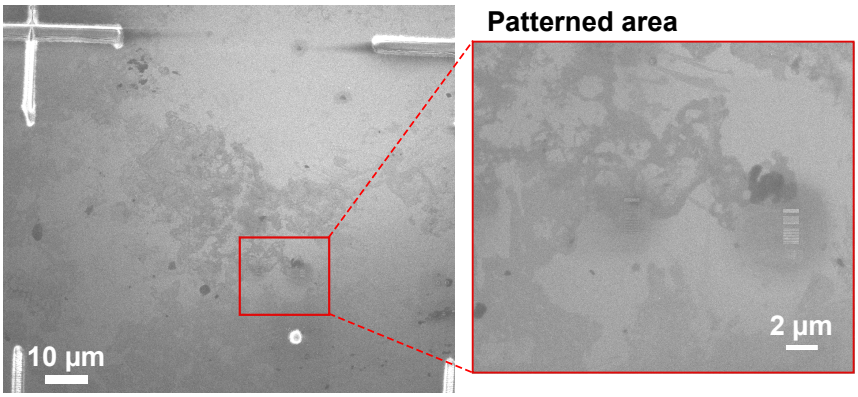

Figure 4.19: SEM micrographs of the 9th imprinted wafer, showing the region of interest and the milled crosses and a zoomed in image of the patterned area. Because the wafer is still covered with NIL resist, that is charging under the electron beam, imaging at low acceleration voltage ($5kV$) was necessary.

measured as the distance between the first peak and the second dip. If the line profile has a Gaussian shape, then we could measure the width as the full width at half maximum (FWHM). We performed ten measurements of the line width on the ten lines within one specific set, averaged them and calculated the 1σ value. Figure 4.20 shows the results of the line width measurements on the EBID stamp, before and after NIL and the ninth imprint, for fields A, B, C and D, patterned with 10, 5, 2 and 1 iterations respectively. Line sets described here as 1A, 1B and 1C follow the definition given in figure 4.3b. First of all, the line width on the EBID stamp does not correspond to the experimental results in figure 4.4, achieved using a silicon wafer. We believe that chromium may have oxidized and thus created a thin insulating layer on top of the substrate. This layer may have then caused charging effects, responsible for the broadening of the lines. We notice that the average values of the line width of the EBID stamp before and after being used in the NIL process has remained the same, given the 1σ margin. In general, we observe that the line width measured in the 9th imprint is smaller than that on the EBID stamp and in case of field C, set 1A, the width has reduced in size by a factor of 37.5%, from $38.53nm$ (EBID stamp before NIL) to $24.08nm$.

After the NIL process, the NIL stamp and the last imprint were imaged at VSL, the Dutch institute of metrology, using AFM. AFM images of the NIL master and the 9th imprint of the top left corner of field A are displayed in figure

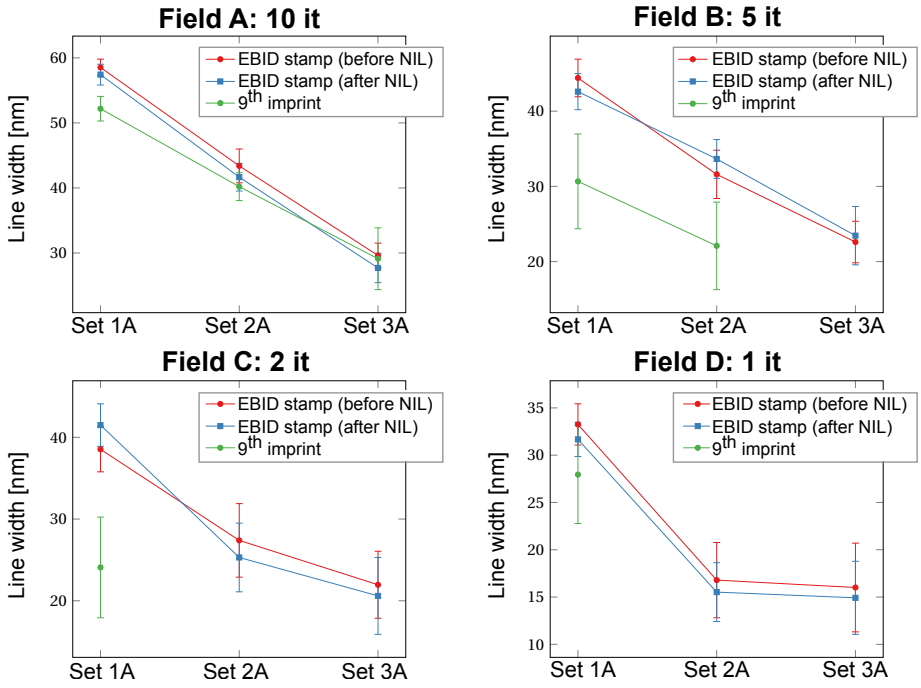

Figure 4.20: Results of the line width measurements, calculated from the integrated line profiles of Field A, B, C and D of the EBID stamp, before and after the NIL process and the ninth imprint.

4.21. From the 3D view of the AFM scan, it is clearly visible that the lines patterned on the NIL master are transferred as grooves in the resist of the 9th imprint.

We measured the height of the lines from the AFM profiles of the EBID stamp and the ninth imprint. The AFM profiles are integrated over the length of the lines. Figure 4.22 shows as example the integrated line profiles of the set of lines 1A of Field A of the EBID stamp (a) and of the ninth imprint (b). The lines on the EBID stamp stand out of the surface, whereas in the ninth imprint they are actually grooves in the polymer. In this case, the lines have a width of approximately 50nm and a height of 35nm. When imaging the imprint with the AFM, if the tip is not slender enough it may not touch the base of the grooves, leading therefore to an error in the measurement.

Figure 4.23 shows the measurement of the height of the lines of fields A, B, C and D of the EBID stamp (after NIL) and the ninth imprint. We notice that there is a shrinkage in height of the structures up to a fraction of 70% in case of set 1A in field D. The reason why the height of the structures of the imprint is always

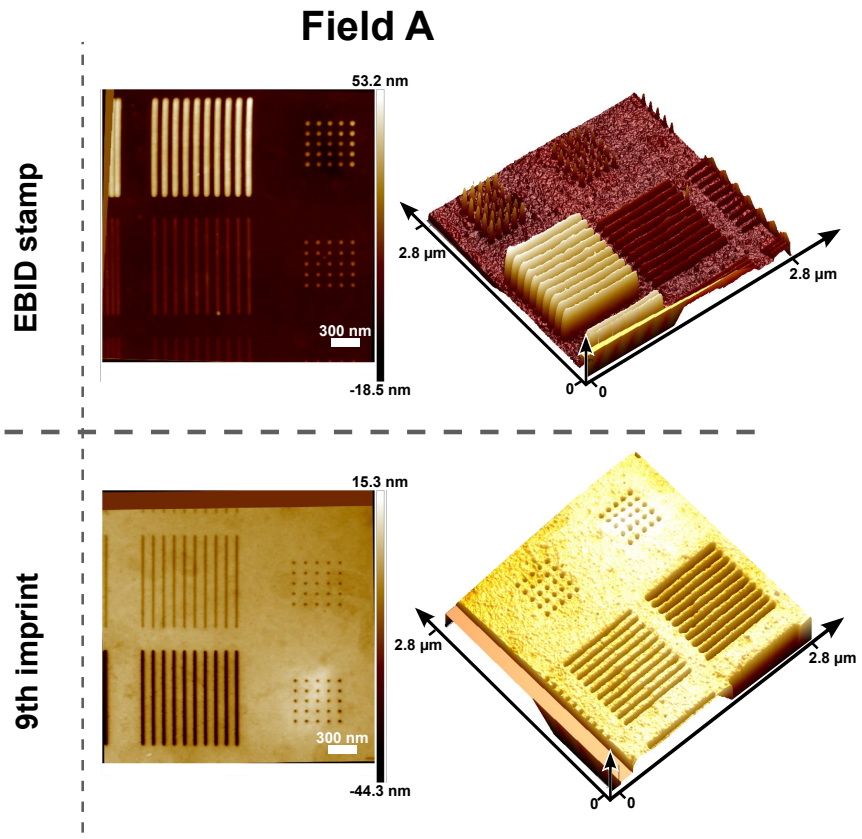

Figure 4.21: AFM 3D view of the EBID stamp and 9th imprint.

smaller than that of the stamp is that probably the stamp was not pushed into the resist enough. Also, we notice that the height of the structures on the EBID stamps differs to that measured on the silicon wafer in figure 4.4, especially for the set on lines 1A. We think that probably some NIL resist may got stuck on the stamp after the NIL exposure, altering the height of the structures.

4.5.3 Discussion

To the best of our knowledge, EBID stamps for nano imprint lithography were fabricated and tested by us for the first time. We used a NIL glass stamp, which we covered with a $10nm$ layer of chromium to provide a conductive metallic layer, but with sufficient transparency at the UV light wavelengths used in NIL. As for the previous experiment, four fields were patterned with different num-

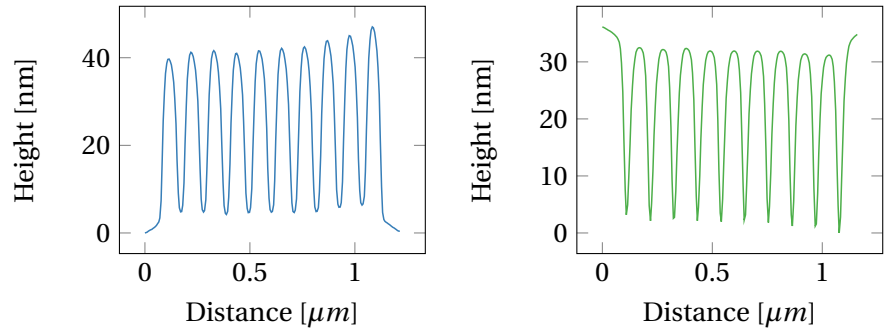

(a) (b)

Figure 4.22: AFM lines profiles of Field A on the stamp after NIL (a) and on the 9th imprint (b).

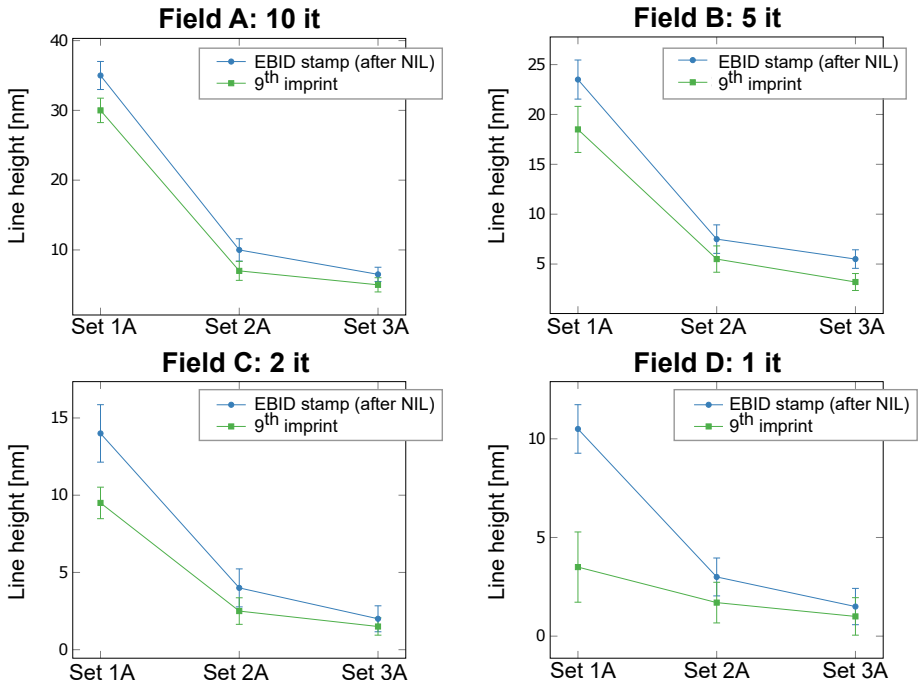

Figure 4.23: Results of the line height measurements, calculated from the integrated line profiles of Field A, B, C and D of the EBID stamp (after the NIL process) and the ninth imprint. The AFM inspection was performed at VSL.

bers of iterations, containing sets of lines and arrays of dots as explained in figure 4.3. The EBID stamp could be directly used to imprint a NIL resist on nine

locations of a silicon wafer. From the SEM inspection of the EBID stamp, we noticed some black shadows in some areas of field B and D, as shown in figure 4.18. We do not know the cause of this, but it may be attributed to the NIL resist remaining attached to some areas of the stamp when the stamp was released from the silicon wafer, after the NIL exposure. The imprinted fields on the ninth location could be imaged in the FEI Nova Nano Lab 650 using low acceleration voltage to avoid charging from the resist. While the line width measured from the EBID stamp before and after being used in the NIL process is maintained, the width of the imprinted lines is measured to be smaller. We think that maybe the stamp was not well pressed into the NIL resist, which could also explain why the height of the structures on the EBID master is always larger than that on the ninth imprint. The main achievement of this experiment is the demonstration that NIL stamp can be directly fabricated by using EBID. Also, the EBID structures not only survived nine sets of imprints, but also they seemed to be transparent enough to the UV light for curing the NIL resist. Because we noticed some charging effects possibly introduced by the natural oxide formed on the chromium layer that may have negatively influenced the EBID process, we decided to make a second attempt in the fabrication of NIL stamps by EBID using molybdenum as a conductive layer, replacing chromium. It is also possible that the charging was caused by a poor connection to ground, which was done using wires secured on the sample surface by carbon tape.

4.6 NIL using an EBID master - Mo on Glass

The results presented in section 4.5.3 show that, although the height of the structures loses fidelity, which may be caused by the stamp not being pressed completely into the NIL resist, the NIL process does not damage the EBID deposits. Moreover, the EBID deposits seem to be sufficiently transparent to the UV light, allowing the curing of the NIL resist. The goal of these experiments is to push the limits of resolution beyond the $10nm$ limit. Coating the NIL master with chromium leads to a smooth and transparent layer, that, however, was not conductive enough, leading to charging effects that may have influenced the EBID process. The reason for that may be that the chromium layer oxidizes forming a non conductive layer. For this reason, a third set of experiments was carried out with the aim of improving the conductivity of the NIL master coating layer and hence increasing the resolution of the EBID structures.

A second NIL stamp was provided by EVG. It is the same as that described in section 4.5.3: it is a glass stamp of $15cm \times 15cm$ with a thicker area in the

middle called mesa, which is $2.5cm \times 2.5cm$ in size, as shown in figure 4.24.

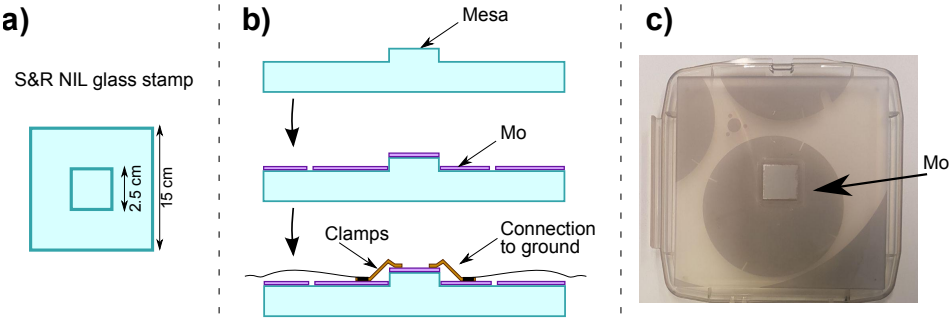

Figure 4.24: a) The NIL master consisting of a square glass plate of size $15cm \times 15cm$ with a thicker area in the middle of size $2.5cm \times 2.5cm$, called mesa, was provided by the EVG group. b) The NIL master was coated with a $10nm$ layer of molybdenum, that provides a smooth and conductive surface. c) Picture of the NIL stamp covered with molybdenum.

Because EBID requires a conductive surface to successfully pattern high resolution features, the deposition of a metal layer on the NIL stamp is a necessary step. With the same issue encountered in section 4.5.3, the range of materials available for the deposition of the metal layer is limited by the metal deposition machine used. A suitable material to replace the chromium coating is molybdenum. Molybdenum, as deposited by evaporation, forms a rather smooth layer and its natural oxide is also conductive. With a thickness of $10nm$, molybdenum still provides a transparency of 51% for a $667nm$ wavelength light, as shown in table 4.2.

Wavelength	Mo thickness				
	$1nm$	$5nm$	$10nm$	$15nm$	$20nm$
$\lambda = 667nm$	0.93	0.71	0.51	0.36	0.26

Table 4.2: Transmittance of molybdenum [151].

To provide an electron path, the mesa is clamped to wires that are connected to ground. The use of clamps instead of securing wires with carbon tape might provide this time a better electrical connection, hence limiting the charging effects. The picture in figure 4.24c shows the NIL glass plate covered with molybdenum. Also here, we can see the shadow of the clamping system of the metal deposition machine, that prevented some parts of the sample from

being covered with molybdenum.

Figure 4.25 shows the process flow of the third experiment, performed in collaboration with the EVG group. EVG provided the NIL glass template, that was later on coated at TUD with a $10nm$ film of molybdenum, deposited by evaporation (1). The EBID structures are patterned on the coated surface of the NIL stamp in a FEI Nova Nano Lab 650 SEM, using the platinum precursor (2). The NIL template with the EBID structures is used for S&RNIL, where it is imprinted nine times in the silicon wafer, covered with NIL resist (3).

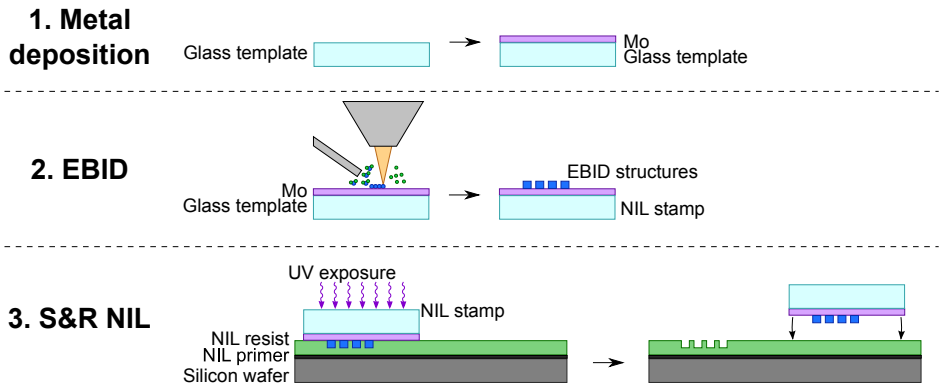

Figure 4.25: Process flow of the third experiment. The NIL glass template is covered with a layer of molybdenum (1), where the EBID structures are patterned using the platinum precursor (2). The NIL master with EBID features is used in a subsequent S&RNIL process to imprint nine times a NIL resist covered silicon wafer (3).

4.6.1 Fabrication of the second NIL stamp by EBID

Because the surface of the mesa is large compared to the patterned areas, as done previously in section 4.5.3, a searching geometry is etched in the molybdenum film by ion milling to allow the EBID patterns to be easily found. The fabrication of the searching geometry was performed in the FEI Nova Nano Lab 650 dual beam SEM, using the $30kV$ ion beam with $26nA$ current. Figure 4.26 shows the SEM micrograph of the patterned searching geometry. Contrary to what was done with the chromium/glass plate in section 4.5.3, the region of interest is not connected with milled lines towards the corners of the mesa. The clamps were positioned close to the electron microscope's polepiece and a large movement of the specimen would have caused a damage of the final

lens. Therefore, a large search geometry consisting of eight crosses and connecting lines, as shown in figure 4.26 was patterned. Inside the dashed square, the EBID structures will be deposited. The same template as shown in figure 4.3 was patterned with 10, 5 and 2 iterations, corresponding to fields A, B and C. The patterning was done in the FEI Nova Nano Lab 650 SEM, equipped with a gas injection system filled with platinum precursor.

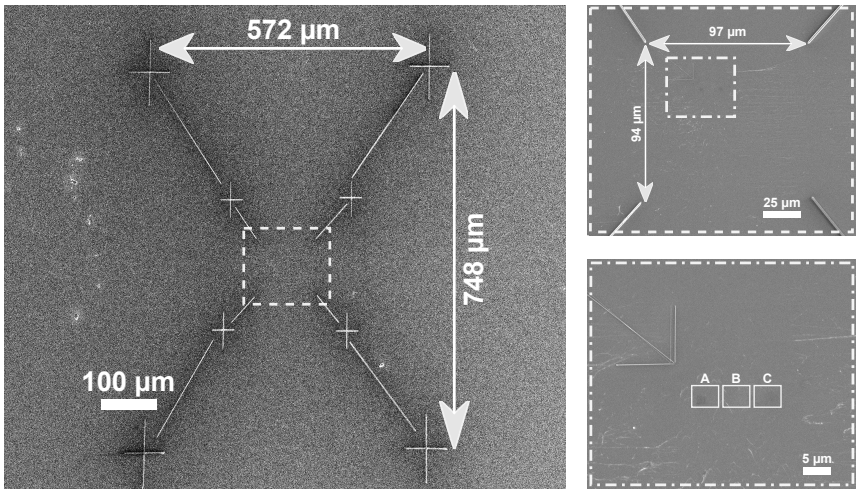

Figure 4.26: SEM micrograph of the search geometry for the molybdenum/glass plate (left) and zoomed in images of the region of interest where the three fields (A, B and C) of EBID structures were patterned, with 10, 5 and 2 iterations.

Figure 4.27 shows the SEM micrograph of the patterned EBID structures. Fields A, B and C are patterned with 10, 5 and 2 iterations, using a $19kV$ beam in spot 2, corresponding to a current of approximately $39pA$. A zoomed in image of a line in field C shows that the width is $8.1nm$. The sample surface has wrinkles that may be caused during the deposition of the molybdenum layer and will affect the quality of the imprinting process. However, the evaluation and the analysis can still be carried out on the lines that lay outside the wrinkles.

As visible in figure 4.27, the writing process of field A failed. The geometry seems to be patterned twice, with a little shift towards the bottom of the field of view. We suspect that there was a sudden and unexpected movement of the stage, that caused the geometry to be shifted during the patterning. For this

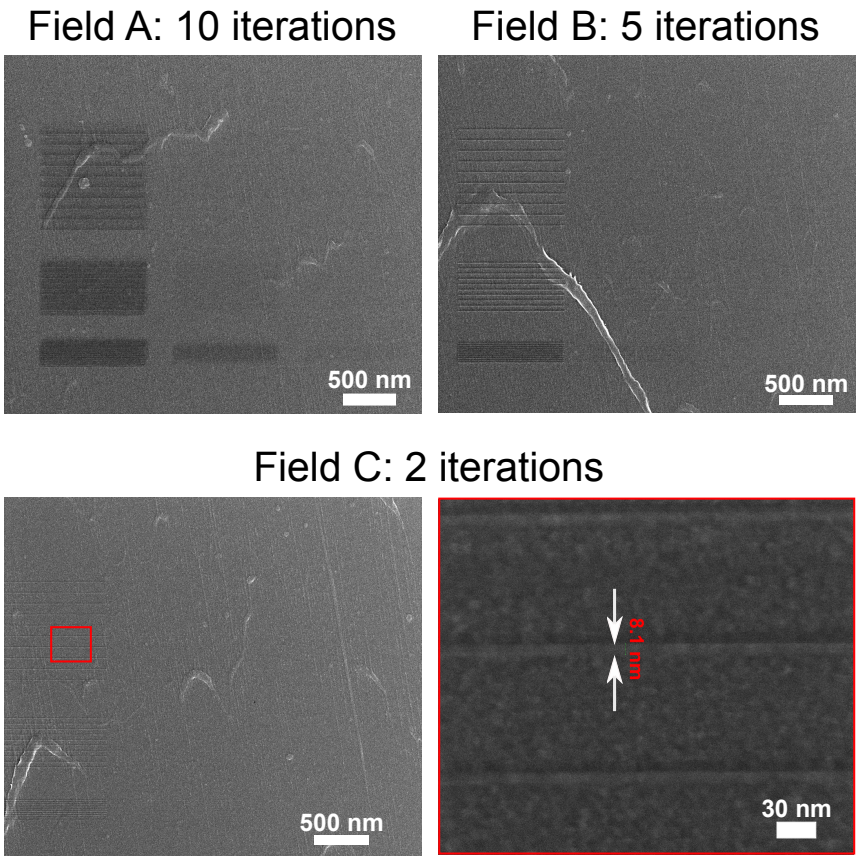

Figure 4.27: SEM micrograph of the fields A, B and C patterned with 10, 5 and 2 iterations, respectively, on the 10nm molybdenum film on the NIL glass plate and zoomed in image of an EBID line in field C showing a width of 8.1nm.

reason, we will not analyze this field. On the other hand, field B and C, patterned with 5 and 2 iterations respectively, were successful.

4.6.2 Results

The NIL master with EBID structures was used for S&RNIL, for nine subsequent imprints in a NIL resist spin coated on a silicon wafer. Figure 4.28 shows the SEM micrograph of the EBID stamp after it was used to imprint the nine locations on the silicon wafer. The wrinkles are still visible and more dirt particles can also be found in the area where the EBID structures were deposited. All the EBID lines survived the nine imprinting steps without showing any damage, as

shown in the bottom left SEM image of figure 4.27, where a small region of field C is shown.

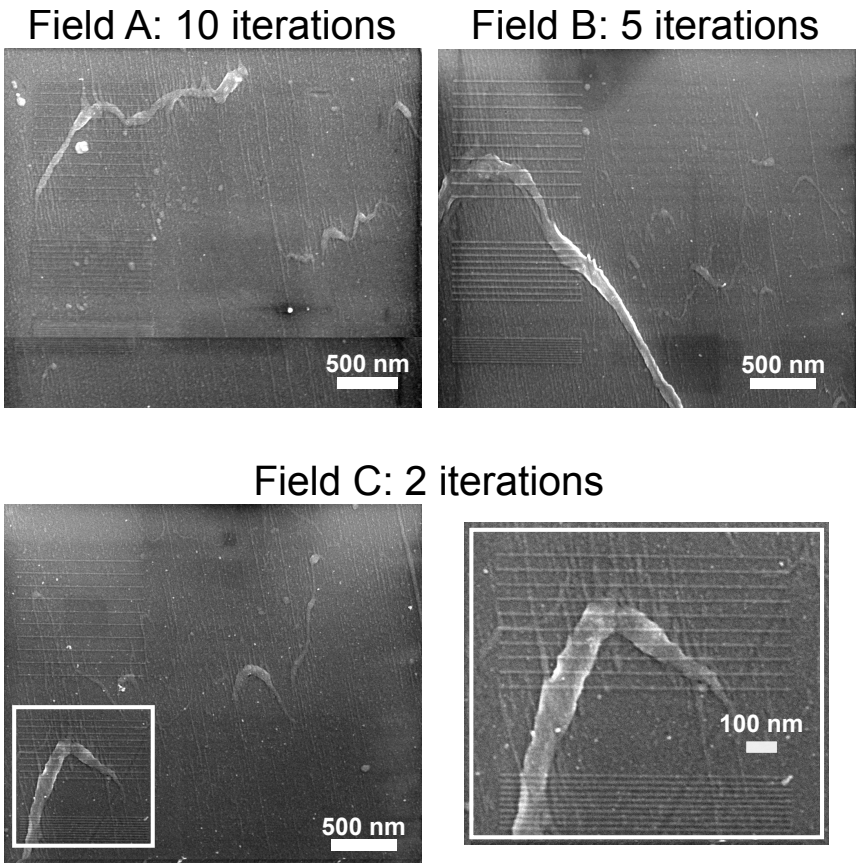

Figure 4.28: SEM micrographs of the EBID stamp covered with molybdenum, where fields A, B and C are shown. The sample has the same wrinkles that are visible in the EBID stamp before being used in the NIL process shown in image 4.27. On the bottom right, a zoomed image of field C, as highlighted in the SEM image. The EBID structures appear to be undamaged.

We could not image the ninth imprint in the SEM because of charging effects. Despite the low acceleration voltage and the low beam current used for imaging, we could not find the patterned locations. Therefore, we only analyzed the line width from the SEM images of the EBID stamp, before and after being used in the NIL process. The integrated profiles of the lines on the EBID stamp before and after NIL have very difficult shapes. An example is reported in figure 4.29. Here we report the integrated line profiles of the set of lines 1A

as defined in figure 4.3 for field B and field C, before (a) and after (b) NIL. While calculating the width with the inflection point method can be done in case of the line profiles in (a), it is more difficult in case of the profiles in (b) because of the bumps in the graphs. Because of that, we decided to measure the width of the lines "by eye" from the SEM images.

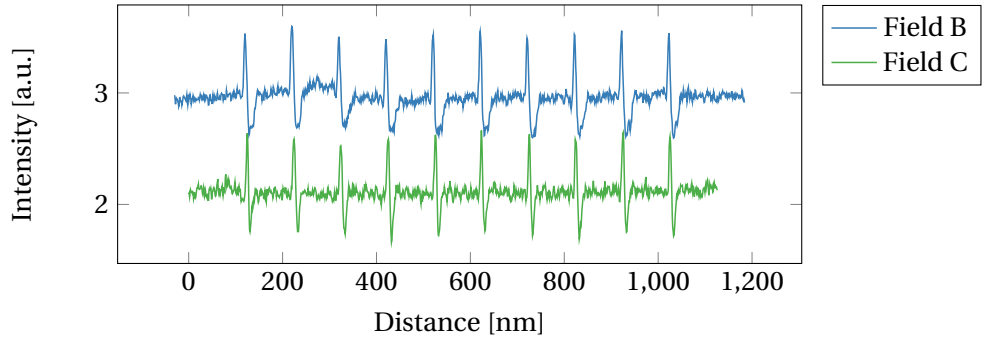

(a) EBID stamp - Before NIL

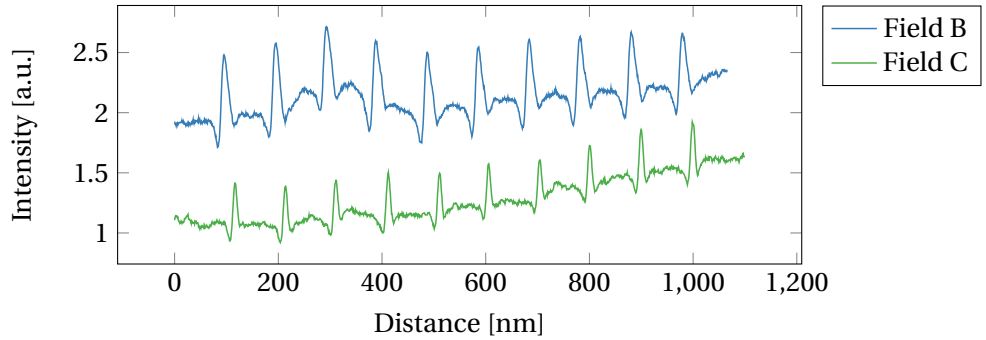

(b) EBID stamp - After NIL

Figure 4.29: SEM integrated line profiles of the EBID master before and after NIL. The line profiles are taken from fields B and C, on the set of lines 1A, as defined in figure 4.3b.

Figure 4.30 reports the measured width of the lines in fields B and C of the EBID stamp, before and after being used to imprint the wafer. We took ten measurements for each set of lines, averaged them and calculated the standard deviation 1σ. The smallest patterned line has a width of approximately $8nm$ and belongs to the set of lines 3A in field C. Considering the error in the measurement, we can state that the width of the lines on the EBID stamp did not change after the NIL process.

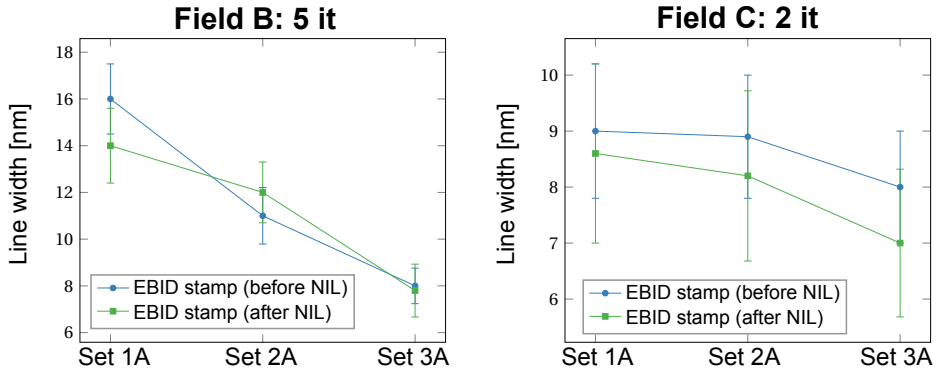

Figure 4.30: Results of the line width measurements, calculated "by eye" from the SEM images of Field B, and C of the EBID stamp, before and after the NIL process.

The NIL master and the nine imprinted wafers were then analyzed with the AFM at the Dutch institute of metrology (VSL). The AFM images of fields B and C of the NIL Master, the first and the ninth imprints are shown in figure 4.31. to measure the height, we retrieved the integrated line profile over part of the line width, without touching the wrinkles. The height of each line is then measured, the ten values are averaged and the standard deviation (1σ) is calculated.

Figure 4.32 shows the height of the lines in field B and C, for sets of lines 1A and 2A, on the EBID stamp and the first and ninth imprint. The height reduces rather considerably from the stamp to the ninth imprint. In case of field B, the average height of the lines in set 1A reduces from $6.63nm$ of the EBID stamp to $3.26nm$ (50.8% from the original height), whereas for the sets of lines 2A the height reduced by a factor of 57.7%, from $6.19nm$ to $2.55nm$. In this case, the line height of the nineth imprint is smaller than the first imprint, opposite of what we measure in field C, which is hard to explain. We think that the wrinkles may influence the fidelity of the imprints.

4.6.3 Discussion

In this last experiment, we used a NIL glass stamp to directly pattern the stamp by EBID, as done in section 4.5.3. Because in the second experiment we noticed that there was some charging effect that may have negatively contributed to the patterning of the structures, in this experiment we decided to change the coating material from chromium to molybdenum. Also, we changed the ground-

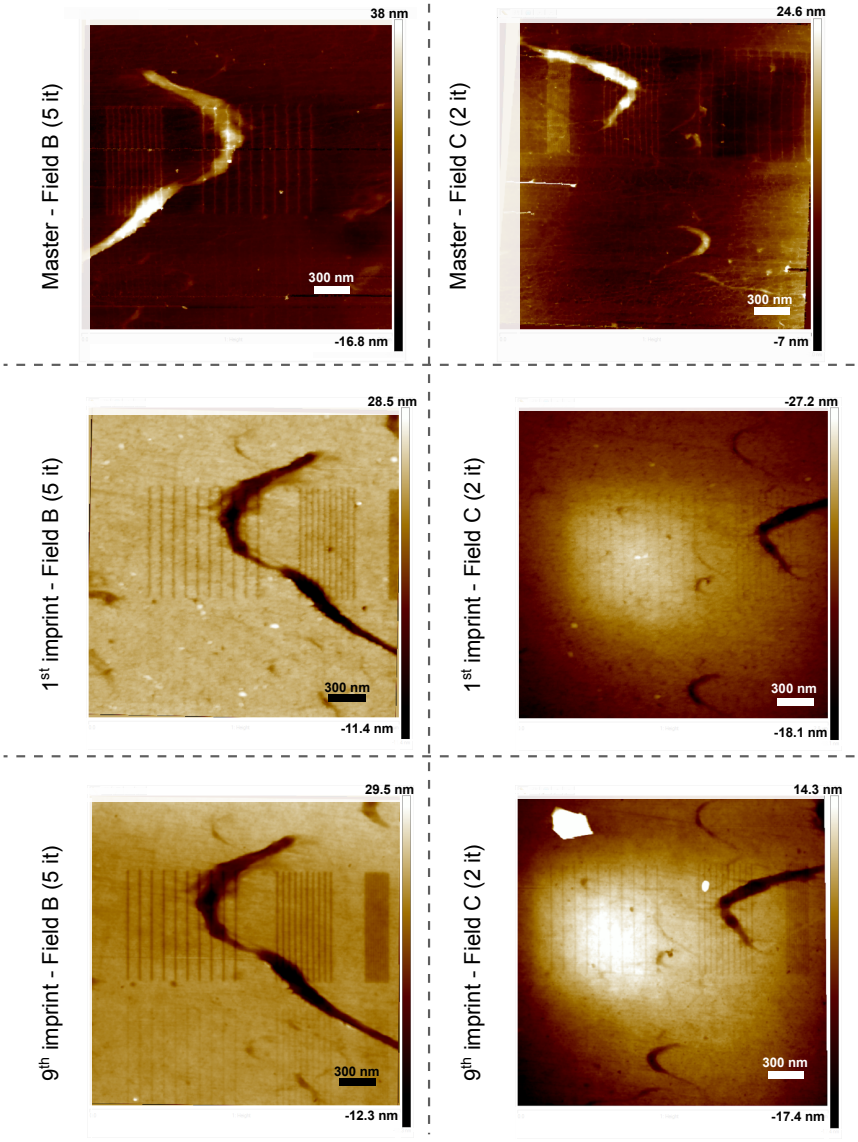

Figure 4.31: AFM images of fields B and C of the NIL Master, the first and the ninth imprinted wafers.

ing wire, that in the second experiment was made to stick on the sample surface with carbon tape, to a clamping system. While the patterning of the field with higher number of iterations (10) failed because of what we think a sudden

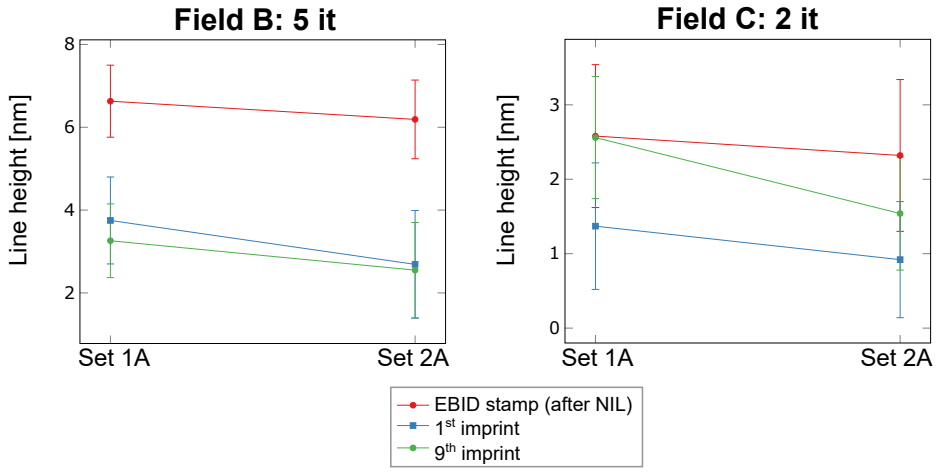

Figure 4.32: Results of the line height measurements, calculated from the AFM analysis performed at VSL of the EBID stamp (after NIL) and the first and the ninth imprint, for sets of line 1A and 2A.

small movement in the stage, the patterning of fields B and C was successful. We achieved our goal to fabricate an EBID stamp for nano imprint lithography where lines with width down to $\approx 8nm$ and height down to $\approx 2.3nm$ could be successfully imprinted on nine different locations of a silicon wafer, covered with NIL resist. The fidelity of the imprinting still needs some attention as from what we have measured, the height reduces by approximately 50% from the EBID stamp to the ninth imprint.

4.7 Conclusions

Experiments on different processes to fabricate NIL stamps using electron beam induced deposition were carried out in collaboration with the EVG group, leader in the supply of NIL machines and with the Dutch institute of metrology, VSL.

In the first experiment, EBID structures were patterned on a pyrex wafer covered with a $10nm$ layer of TiN. Despite originally planned to use this substrate directly as NIL stamp, the pirex wafer had to be replicated as it would not fit in the NIL machine. A NIL stamp was therefore fabricated with the Smart NIL technology from the EBID master and subsequently imprinted in nine locations on a wafer covered with NIL resist using the S&R NIL. From the SEM analysis, we observed that some of the lines on both the first and the ninth imprint were damaged, suggesting that the damages were actually present on

the NIL stamp. We measured that the line width drastically decreased from the EBID master to the last imprint, up to a factor of approximately 41%. On the other hand, the height remained constant from the master to the last imprint, within the 1σ value.

In a second stage, we investigated the fabrication of NIL stamps made directly by EBID. The EVG group provided a NIL glass templates that needed to be covered with a conductive and UV transparent metallic layer. We firstly decided to cover the NIL template with a layer of $10nm$ of chromium, having a transmittance higher than 38% in the wavelengths at which the NIL resist is cured. We patterned lines with width down to $16nm$ by EBID, that were successfully imprinted nine times into the NIL resist-covered silicon wafer. While the line width is in general maintained, apart from only one case where we measured a reduction of 37.5%, the height of the structures on the ninth imprint is always smaller than that on the EBID stamp, and it is reduced up to a factor of 70%. We think that the shrinkage of the structure height could be caused by the stamp not being completely pressed into the NIL resist during the imprint process. Because some charging was noticed during the patterning of the EBID stamp in the second experiment, we decided to change the coating material to molybdenum and to optimize the connection to ground of the mesa. With these precautions, we managed to pattern lines with width down to $8nm$ and height $2.3nm$, that were successfully imprinted on nine locations of a silicon wafer covered with NIL resist. As for the second experiments, also in this case we observed that the line width is in general maintained, while the height is reduced considerably, up to a factor of approximately 50%.

As a general remark, on one side the imaging of the imprints with the SEM was not trivial because of the sample being covered with polymer, that heavily charges under the electron beam. Despite the low acceleration voltage and low beam current, in the third experiments the structures could not even be found. In this case, an option would be to cover the imprint with a thin metal layer to prevent charging. However, even a thin $10nm$ layer of coating will permanently obscure the smallest features patterned with EBID. The analysis with AFM can be trivial when imaging the grooves made by the EBID stamp into the resist. If the aspect ratio is relatively high, however, it may occur that the AFM tip does not reach the bottom of the grooves.

As future work, we propose the study of the fidelity of the imprinted EBID structures, to investigate why the imprinted structures lose fidelity in terms of line height and not line width.

5

Multi Beam Scanning Electron Microscopes

If you could see the earth illuminated when you were in a place as dark as night, it would look to you more splendid than the moon.

Gallileo Gallilei

5.1 The 196 MBSEM

Electron Beam Induced Deposition (EBID) is a high resolution direct write lithography technique, that is capable of writing single nanometre patterns and it is suitable for the fabrication of high resolution NIL stamps. EBID is a serial writing technique and thus is limited by the low throughput. A way to overcome this limitation is by using scanning electron microscopes that deliver multiple beam-lets at the sample. In Delft, we are developing a Multi Beam Scanning Electron Microscope (MBSEM), shown in figure 5.1, that is intended to enhance the throughput by a factor of 196 [45] [46]. The Delft multi-beam SEM

is a single source and single column system, where the electron beam emitted by one single emitter is split by an aperture array. For the development of the multi-beam SEM, a commercially available FEI Nova Nano SEM 200 Scanning Electron Microscope (SEM) was used. The optical schematic of the FEI Nova Nano SEM 200 SEM is shown in figure 5.2a. Electrons are emitted from a Schottky (or thermal field emission) source. A first condenser lens, C1, images the source in a plane close to the Coulomb tube (CT), where beam shift and tilt coils can adjust the position of the electron beam exactly on the optical axis of the system. A second magnetic lens, C2, focuses the beam in a plane above the variable aperture (VA), that limits the current in the beam. A set of two magnetic lenses INT (INTermediate) and HR/UHR (High-Resolution/Ultra-High-Resolution) focuses the beam at the sample. The beam can be scanned over the sample by means of scan coils, located above the HR/UHR lens.

In such a configuration, one way of splitting the beam into multiple beams is by replacing the original source module with a multi electron beam source module. The multi beam source module consists of an aperture plate that splits the broad beam of a Schottky field emission gun (FEG) into sub-beams. Initially this was designed and developed by van Bruggen et al. for delivering 100 beamlets at the sample [152] [153], and the system was capable of single beam blanking [154]. The design was further optimized and simplified by Mohammadi-Gheidari et al. [45] [46] for delivering 196 beams.

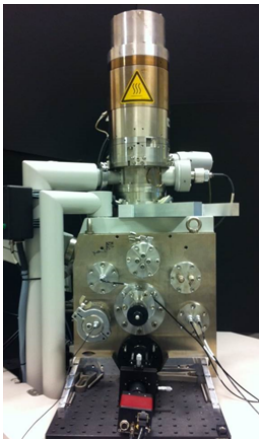

Figure 5.1: The Multi Beam Scanning Electron Microscope (MBSEM).

Figure 5.2b shows the optical schematic of a scanning electron microscope in our present multi-beam configuration.

The emission angle of the beam is bigger than in a standard SEM, but such that the brightness is still constant within the emission cone. An aperture lens array (ALA) splits the beam into an array of 14x14 beams and focuses each beamlet in the accelerator lens (Acc.) plane. The aperture lens effect is formed on the ALA by means of the E-2 electrode, while E-1 provides a zero strength lens (ZSL) that can correct for the field curvature. The accelerator lens, consisting of three macro-electrodes (Einzel lens), images the source in a plane above the C2 lens, in the Coulomb tube. The C2 lens creates a common crossover in the variable aperture plane, that is imaged in the UHR coma-free plane by the

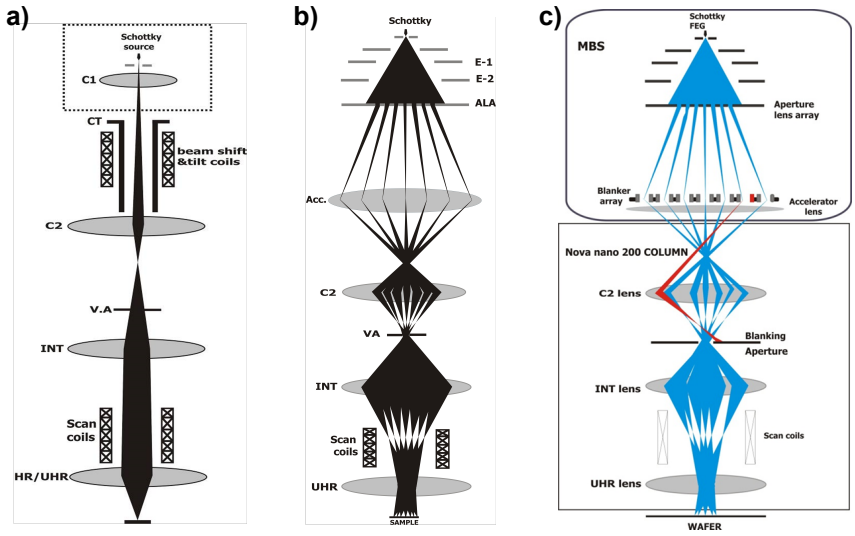

Figure 5.2: a) Optical schematic of a commercially available FEI Nova Nano SEM 200 Scanning Electron Microscope (SEM). b) Optical schematic of the Multi Beam SEM (MBSEM). c) Optical schematic of the Multi Beam SEM (MBSEM) including the blanking plate

INT lens. It is extremely important that all the beams have a common crossover in the coma free plane of the UHR lens. In this way, the off-axis aberrations of the UHR lens can be neglected and the contributions of the off-axis aberration of the other lenses will be demagnified by the objective lens (UHR). The magnification of the system can be changed by tuning the strength of the C2 lens.

In the present system, the logical location for the multi beam blanker array would be in the source module, as shown in figure 5.2c. However, in the source module unfriendly conditions, such as ultra-high vacuum and high tension, make the implementation of the blanker difficult. In fact, a large amount of feedthroughs (at high-voltage) would be needed to control each of the 196 deflectors. It would also lead to a highly-specialised, and costly, source module, which, from a commercial point of view, would be less attractive for applications.

To characterize this system by its optical properties the on-axis aberrations must be evaluated. On-axis aberrations include diffraction, spherical aberration and chromatic aberrations. Figure 5.3a [46] shows the variation of the total probe size and the on-axis contributions at the sample as a function of the half opening angle of the beam at the sample. The smallest achievable

probe size is $1.2nm$, corresponding to a half opening angle of $7.8mrad$. Figure 5.3b [46] shows the off-axis contributions to the probe at the sample of all lenses of the MBSEM, calculated for a half opening angle at the sample of $7.8mrad$, namely the case in which the on axis beam probe size is $1.2nm$. The relevant off-axis contribution is given by the INT lens, while those of the UHR are practically negligible because of the common crossover in the coma-free plane of the objective lens. With the Multi Beam Scanning Electron Microscope, high throughput Electron Beam Induced Deposition can be performed. Post et al [44] demonstrated the patterning of EBID dots using the Multi Beam SEM (MBSEM), shown in figure 5.3c [44]. These dots were deposited on top of a $W/Si_3N_4/W$ membrane using the $MeCpPtMe_3$ gas precursor, at $15kV$. The dots have a diameter of about $70nm$, and the average pitch is $436nm$ and the total field of 14x14 dots measures $5.7\mu mx5.7\mu m$.

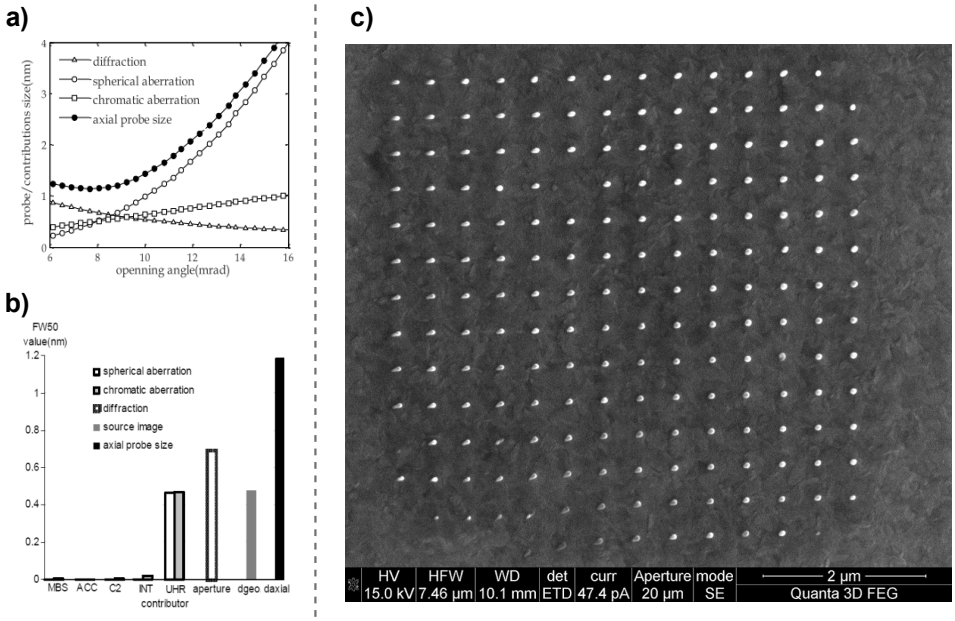

Figure 5.3: a) Variation of the total axial probe size and the on-axis aberration contributions to the probe as function of the beam half opening angle at the sample [46]. b) Off-axis contributions to the final probe of all lenses in the MBSEM [46]. c) Single-beam SEM image of an array of EBID dots deposited in the Multi Beam SEM (MBSEM) [44].

The 196-beam SEM can also be used for imaging large area samples. This is achieved by placing the sample on a fluorescent substrate, which converts electron into photons, and by adding an optical system below the substrate for the

detection of the transmitted photons. Such setup is shown in figure 5.4a [155]: the optical system, placed below the sample, is comprised of an objective lens which focuses the light coming from the fluorescent substrate into a camera. This way, Ren et al. demonstrated the potential of multi beam imaging of large area biological samples, as shown in figure 5.4b [155]. This SEM micrograph shows a 50μm field of view of a pancreatic tissue section placed on a YAG (yttrium aluminum garnet) screen.

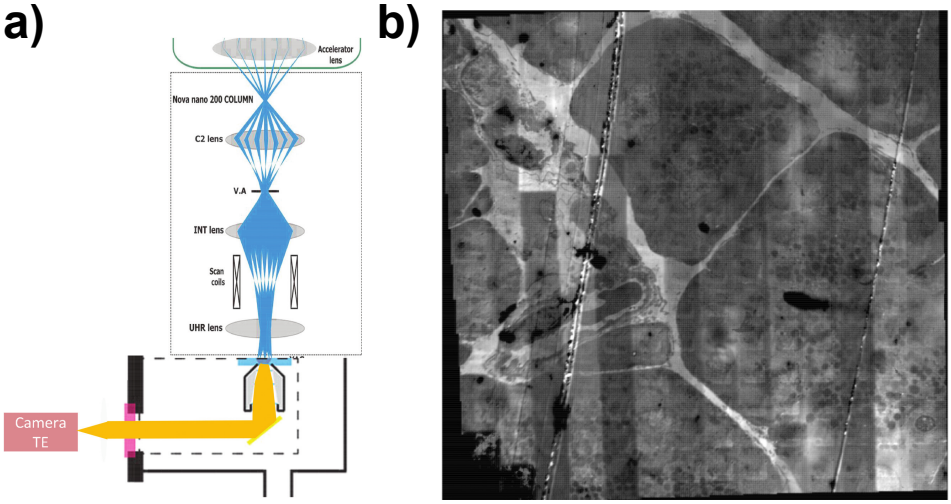

Figure 5.4: a) Schematic of the detection setup comprising of an optical system placed below the electron microscope [155]. b) Transmission image of a pancreatic tissue section, formed by stitching the 14 x 14 images formed simultaneously by the 196 multi beam SEM. The total field of view is 50μm [155].

5.2 Electronics control

The additional electrodes placed in the multi-beam source, shown in figure 5.2, allow the splitting of the beam into multi-beamlets. These electrodes are at high voltage and are controlled via a second FEG Gun System Control Unit (FGSU). An FGSU is a control unit that connects via a CANbus network the microscope PC to the electrodes, supplying the correct values of voltages and current. Typically, the FGSU controls the filament, the extractor, the suppressor and the C1 electrode that are located in the source module. With the extension of the electron source module to a multi-beam source module, a second FGSU is added to the network. The second FGSU is connected to a second PC, called support PC, via an I^2C network and controls the extra electrodes that are added

to the source module, namely E-1, E-2 and Acc. The objective is to integrate the electronics control of the second FGSU with the original microscope electronics control.

Originally, the microscope PC is connected to the FGSU and to the Vacuum System Control Unit via a CANbus network, as shown in figure 5.5a. The integration of the control electronics is provided by introducing a Support PC in the original CANbus network between the Microscope Server and the FGSU 01, as shown in figure 5.5b. In this way, two different CAN sub-networks are created, one is linked to the FGSU and the second to the Vacuum Control Unit. Because the support PC is placed in front of the original FGSU, the first FGSU does not interface directly with the CANbus network. The aim is for the Support PC to control also the second FGSU via I^2C bus.

The design of the new control network starts with understanding the CANbus control of the original FGSU. In order to do so, a monitoring test of the CANbus network is set up.

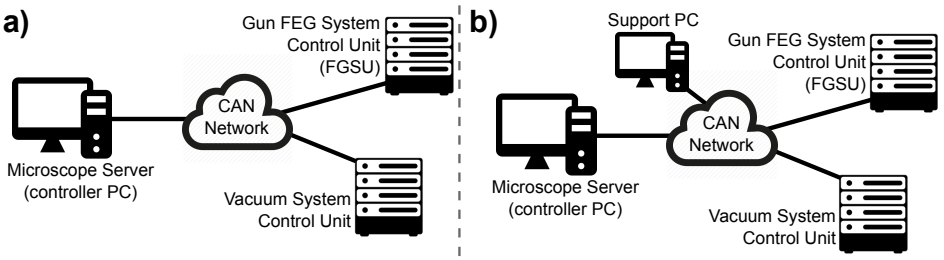

Figure 5.5: a) Schematics of the original control electronics. The microscope PC is connected to the Gun FEG system control unit (FGSU) and the vacuum system control unit via a CANbus network. b) The CANbus network configuration for the monitoring test. A support PC is connected to the CANbus network and runs a program that receives, stores and decodes the CANbus commands.

The monitoring of the CANbus network was performed by introducing the support PC in such a way that it can sniff the network without interfering, as shown in figure 5.5b. A Labview [156] program is running in the Support PC, that detects and stores all the CANbus frames, or commands, that are sent through the network. The monitoring program detects all the messages sent to both the original FGSU and the vacuum system. Figure 5.6 shows an example of received and stored CANbus frames. The messages have an ID (or identifier), which is a sequence of 8 bits that contain information about the addressed de-

vice. The Data field contains detailed information on the sent command, that can be the voltage of an electrode or the value of the filament current.

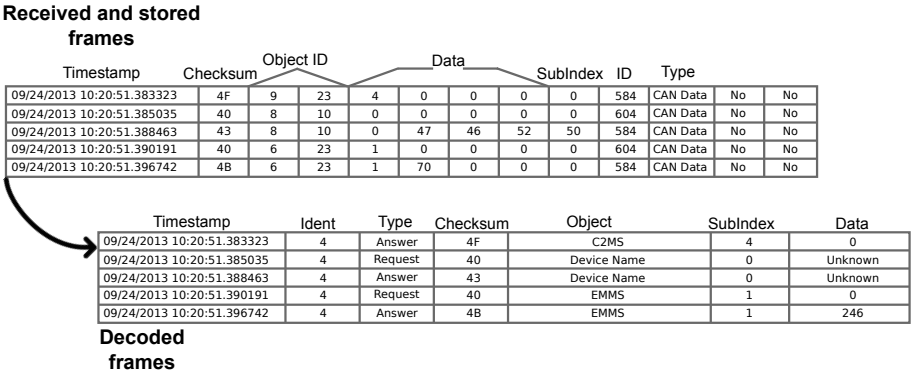

Figure 5.6: The received and stored frame configuration as they are sent to the monitoring program. The program decodes the frame using FEI documentation and generates the decoded frames.

The received messages are then decoded by the monitoring program. Decoding the CANbus frames is possible when the FEI documentation is available. In the decoding program, the received CAN frames are split into each fragment (time-stamp, identifier and payload). Decoding the CANbus frames means that it is possible to understand to which device the messages are addressed, for instance the FGSU or the vacuum control system, what the command is that is sent, for instance "Set suppressor voltage" and the corresponding value.

In a next step, the support PC is placed in front of the original FGSU, as shown in figure 5.7. In this configuration, the support PC is equipped with two CANbus ports, such that the CANbus network is divided into two subnetworks. A CopyFrame Labview program, that copies a frame arriving in one port to the other, is run on the support PC. This test verified that the speed of the frame processing of the Support PC is high enough not to generate timeup errors in the microscope PC.

The Support PC is here placed in front of the FGSU. The role of the Support PC is to just copy each frame it receives in one port and copy it to the other one. In figure 5.8 the set up for this experiment is shown. It is possible to create two separate networks because inside the PC two different ports have been in-

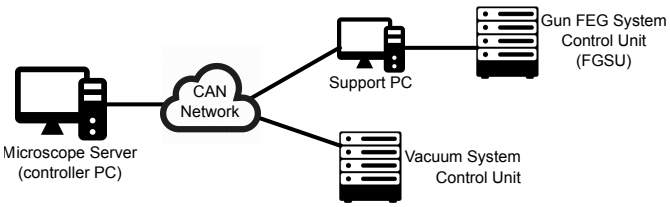

Figure 5.7: CANbus network configuration during the CopyFrame test. The support PC, that is equippend with two CANbus ports, is placed in front of the FGSU and runs the CopyFrame Labview program, that copies frames arriving in one port to the other.

stalled. Those two ports are not directly interfaced to each other and they both communicate to the Support PC mother board. This experiment is crucial. If the Support PC is not fast enough in terms of elaborating the frames and copy them to the other port, the timeout in the microscope server is not respected causing a "warning state". A warm reboot of the full system is then necessary.

The CopyFrame experiment was performed successfully, meaning that it is possible to place a computer in front of the FGSU that filters the commands sent from the microscope PC, without generating timeout errors. The integration of the second FGSU is done by connecting the Support PC to the FGSU through an I^2C network. Figure 5.8 shows the control schematics of the proposed solution.

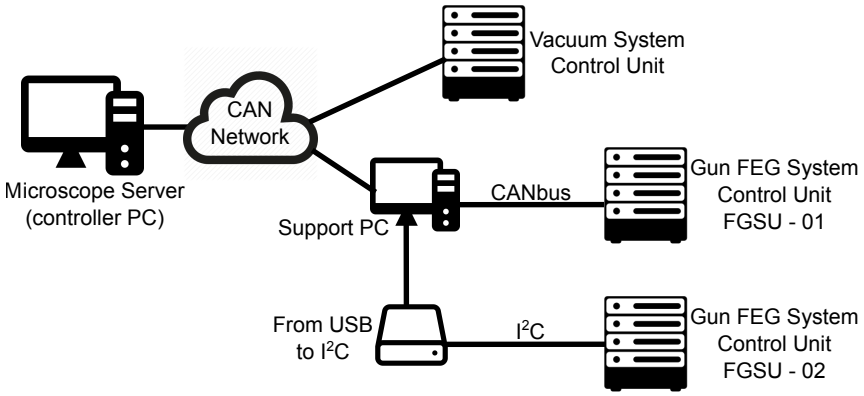

Figure 5.8: Schematics of the integration of the control electronics. The CANbus network is split into two through the Support PC, that is equipped with two CANbus ports. The Support PC is then connected to the second FGSU through a second I^2C network.

Figure 5.9 shows the user interface of the Labview program installed on the Support PC. The UI allows the user to set parameters like the emission current, the filament voltage, etc., that are sent to the original FGSU, as well as parameters like the voltages of the new electrodes, that are sent to the second FGSU, via the I^2C network. When commands are sent from the microscope PC directed to the original FGSU, the values are changed according to the user settings. When the microscope PC requires values from the FGSU, the Support PC is able to send back the values that the microscope PC is expecting.

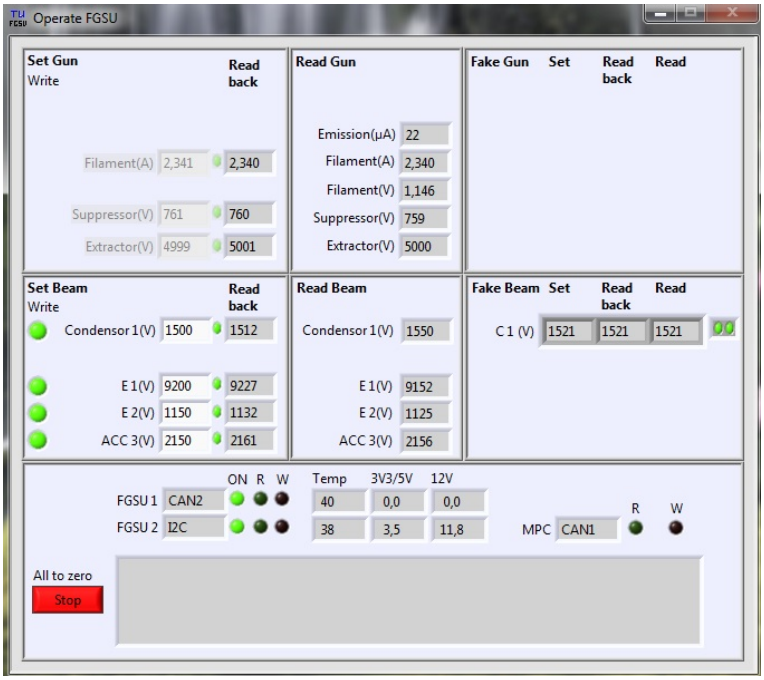

Figure 5.9: The user interface (UI) of the Labview program installed on the Support PC. The user can set parameters belonging to the original part of the electron source (like the filament voltage and current) as well as parameters belonging to the new stack of electrodes of the multi-beam source (like the voltages of E1 and E2)

5.3 Multi Beam EBID

In section 5.1, results on multi-beam EBID were presented. In this case, the dots have a diameter of about $70nm$, and the average pitch is $436nm$ and the total field of 14x14 dots measures $5.7\mu mx5.7\mu m$. It is our aim to improve the resolution of the features patterned by EBID in the 196 multi beam SEM.

The Multi-beam FEI Nova Nano SEM 200 is equipped with a SECOM Delmic door [4], which is an integrated solution for correlative light and electron microscopy, as shown in figure 5.10. The electron beam is scanned onto a sample surface, from which BSEs and SEs are emitted and collected by the detectors. The sample is placed on a piezo driven stage, which also hosts a light objective lens. If the sample is a scintillator, such as a YAG screen, light is produced after the material is hit by electrons. The light is then collected by the objective lens underneath the sample. An optical path guides the light into the CCD sensor of a camera, that can be placed outside the evacuated SEM chamber. In the multi-beam SEM, where standard imaging with ETD or TLD detectors is not trivial, the SECOM platform provides an easy and fast way to do transmission imaging. For the Multi Beam EBID experiments this platform is used with the ultimate goal of focusing the beams, which cannot be done with the standard SE-detectors. We used a YAG screen coated with a $10nm$ thick Al layer, that provides a conductive layer. On top of the Al layer, large areas at the center of the sample are patterned with W-dots and W-lines of different sizes, using EBL. These features provide 'knife' edges, i.e. sharp edges, that give a good contrast in transmission imaging, and help in judging the probe size of the focused beams. The microscope is further equipped with an FEI gas injection system (GIS), filled with the $MeCpPtMe_3$ precursor, that can be heated to $45°C$. The GIS consists of a reservoir, where the precursor is kept, and a needle, that can be placed in proximity to the sample surface and from which the Pt-based gas is led into the system.

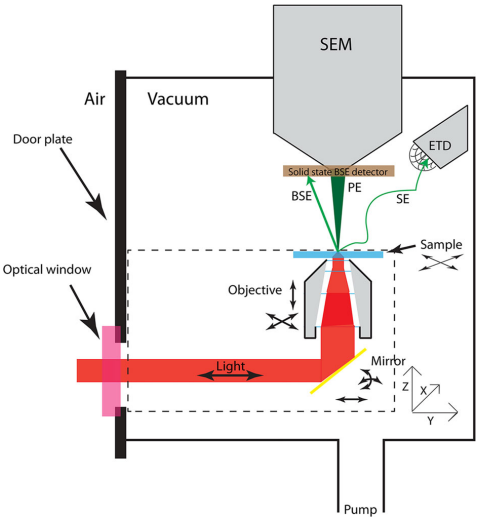

Figure 5.10: The schematics of the SECOM platform [157].

Unfortunately at the time of the experiments, there were a variety of problems with this set up. First, the precursor gas flow was limited. All apertures, except for the variable aperture, in the column were removed to enable multi-

beam SE-imaging. Also pumping apertures were taken out, such that extra precautions had to be taken when letting the gas flow into the chamber, because a large pressure increase in the chamber led to a higher pressure in the column, all the way up to the electron source, causing it to shut down.

Secondly, the handmade SECOM door is equipped with a piezo stage which is not accurate to control. For example, step sizes and the number of steps in a stage move were not consistent. Therefore, large area patterning with proper stitching was very difficult to perform.

Lastly, the Schottky source and Aperture Lens Array were at the end of their lifetime. Therefore, there was no current uniformity over the array of 14x14 beams. Also, the imaging resolution worsened because of a decreasing source brightness. Replacing the source is not as easy as in a standard single beam microscope. The source and the beam splitting optics are one unit, and after a source change the optics has to be cleaned and re-aligned with respect to the tip. We decided to continue with the experiments even though the quality of the source was not optimal and rather replace the tip in a later stage.

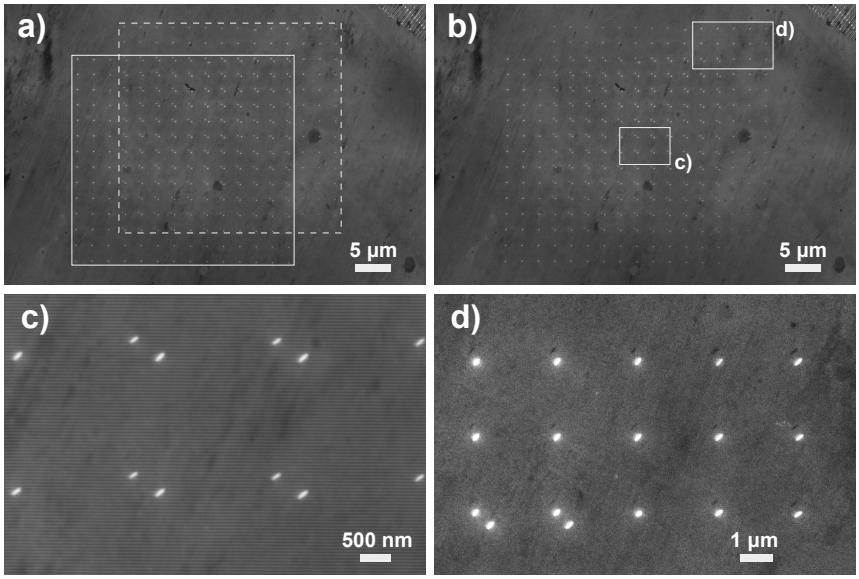

Figure 5.11: SEM image of two arrays of pillars of 196 EBID pillars. a) The two subsequent exposures where performed with a stage movement in between. The two exposures are highlighted with the continuous line box and the dashed line box. c) and d) show two zoomed-in images of two regions that are highlighted in b). the double dots that are here visible are originated from the two different subsequent exposures.

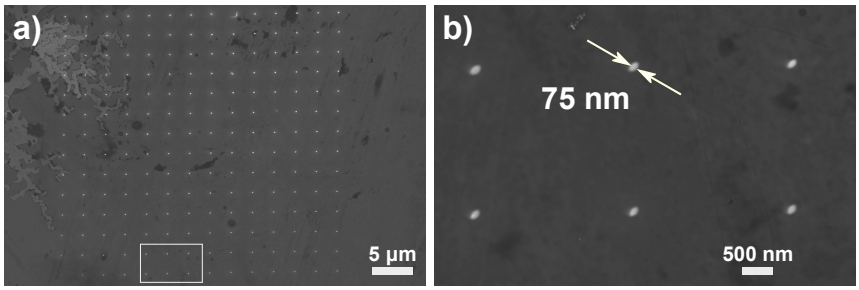

Figure 5.12: a) and b) SEM image of an array of pillars of 196 EBID pillars, showing pillars with size $75nm$.

The large area patterning, as described above, was difficult because of the problems encountered with the piezo stage controllers. First, the beams are focused by looking at the transmission optical image of the knife edge sample. Because of the poor quality of the source, the intensity of the 196 images is very different and the resolution is not optimal. Once the beams are focused, we blanked the beams and let the heated gas flow into the chamber until the pressure stabilized. We un-blanked the beams and exposed the first region in spot mode for approximately 5 seconds. After that, we blanked the beams again, moved the stage to another position and un-blanked the beams again, exposing that area for approximately the same amount of time. Figure 5.11 shows the SEM image of the two exposed arrays of 196 EBID pillars. This SEM image is taken afterwards in a single-beam FEI Verios 460 scanning electron microscope. The pitch between the beams is approximately $2\mu m$ and the diameter of the pillars is smaller than $100nm$. Unfortunately, the control of the piezo stage was so problematic that it was impossible to expose two consecutive regions, to demonstrate the large area patterning.

Figure 5.12 shows a zoomed in SEM image of some of the pillars deposited by EBID in the two subsequent patterning steps. The pillars have an elongated shape, where the smaller dimension is $75nm$. This deformation can be a consequence of a small spatial drift of the stage or is due to improper focusing.

In principle, it is possible to write connected nanowires by EBID in the multi-beam SEM. The idea is to align the scanning direction with the beam grid and adjust the scanning area of each beam to the pitch. This strategy is shown in figure 5.13: on the top, neighbouring beams are scanned such that the end of a scanline coincides with the start of the next one. The scan direction, as shown

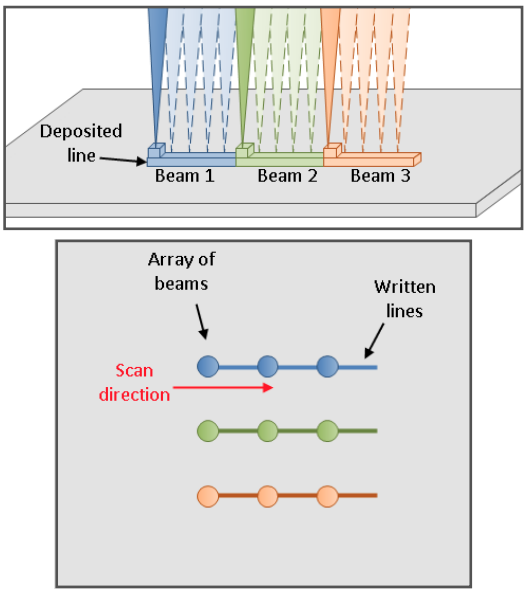

Figure 5.13: Schematics showing the writing strategy for the patterning of continuous lines.

in the image on the bottom of figure 5.13, is set to be along the grid.

Figures 5.14 and 5.15 show the resulting 'connected' nanowires. The lines have a width between $60nm$ and $80nm$, and the pitch is $1.8\mu m$. It is clear that the nanowires are not quite connected, because the scan direction was not exactly oriented parallel to a row of beams in the array of beams. Furthermore it is seen that the bright nanowires have actually lifted off the surface. This is a result of enhanced growth for those beams that contain more current than others in the very non-uniform current distribution within the array of beams. This problem will be solved after a source change and a change of the aperture lens array.

To aim for single nanometer structures the beams need to be better focused. In a number of experiments we tried to achieve that. But the electron source giving up on us and the limited sharpness of the knife edge structures on the YAG sample, posed a real challenge. Figures 5.16a and 5.16b show two arrays of pillars, with some of the smallest dots deposited. The exposure time was 5 sec, the pitch of the dots was $1.9\mu m$. In figure 5.16b a zoomed-in image is shown of some of the dots in figure 5.16a, while figure 5.16d is a zoomed image of figure 5.16c. The dots are seen to be elliptic, probably due to astigmatism and/or drift. The smallest size is $57nm$.

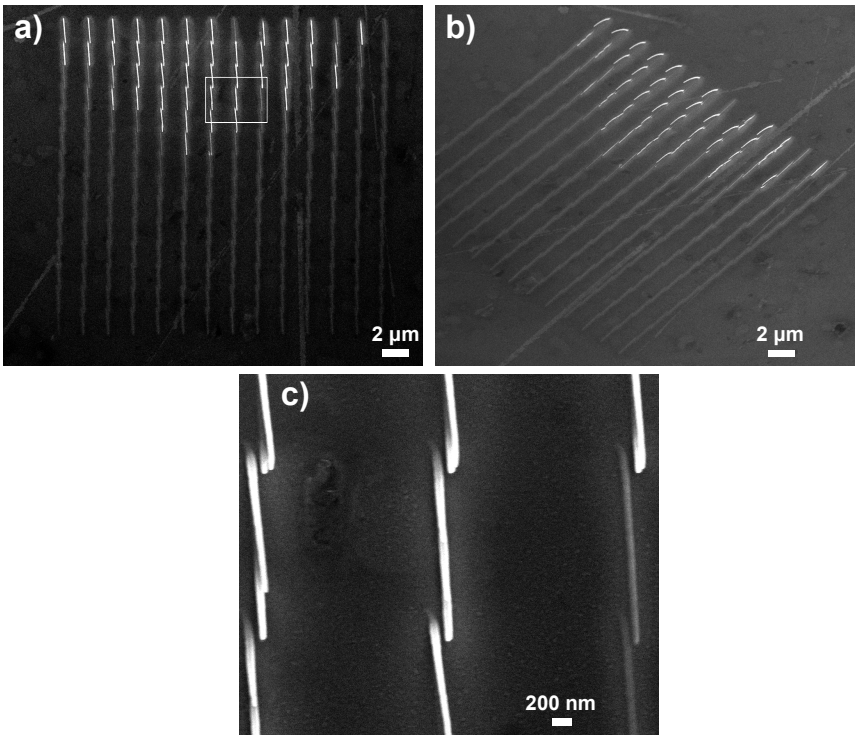

Figure 5.14: SEM image of the first set of 'connected' nanowires. a) Top view image, b) 45 deg rotation and tilt SEM image and c) zoomed in SEM image of the same 'connected' nanowires.

5.4 Conclusions

To increase the throughput of EBID, a multi beam SEM was developed in Delft to deliver 196 focused beams at the sample. The 196 multi-beam SEM is a single source and single column system, where the beams are split thanks to a multi-beam source module, that consists of an original Schottky FEG electron source equipped with additional electrodes and a beam splitting plate. The beam-lets are further focused at the sample thanks to the original electron optics of an FEI Nova Nano SEM 200. To control the multi-beam source module an additional FEG Gun Source Control Unit (FGSU) was added to the control network of the microscope, next to the original FGSU. In this chapter, the design and implementation of a second FGSU was described. The two FGSUs are controlled via two networks: the original FGSU is interfaced through a CANbus network, whereas the second FGSU uses an I^2C protocol. The integration was successfully implemented by running a Labview program on the Support PC

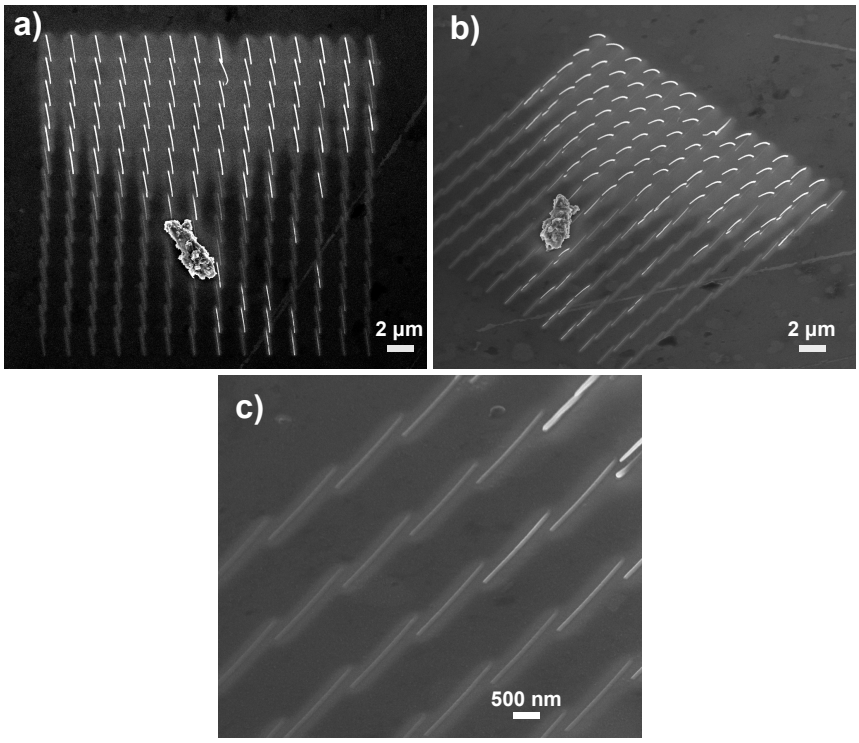

Figure 5.15: SEM image of the second set of 'connected' nanowires. a) Top view image, b) 45 deg rotation and tilt SEM image and c) zoomed in SEM image of the same 'connected' nanowires.

that allows the user to control the multi-beam source module. This program reads and eventually modifies the commands send to the FGSUs according to the user's wish.

In the second part of this chapter, the 196-beam SEM is used to demonstrate high throughput and large area patterning. The multi beam SEM was equipped with a gas injection system to allow deposition with EBID. Connecting nanowires were patterned by employing a writing strategy that takes into account the scan direction. Moreover, high resolution EBID pillars of minimum size of $57nm$ were patterned.

At the time of the experiments, several issues were encountered. First, the gas flow was on purpose limited in order to avoid gas flowing into the upper part of the electron column, which had no variable aperture to allow multi-

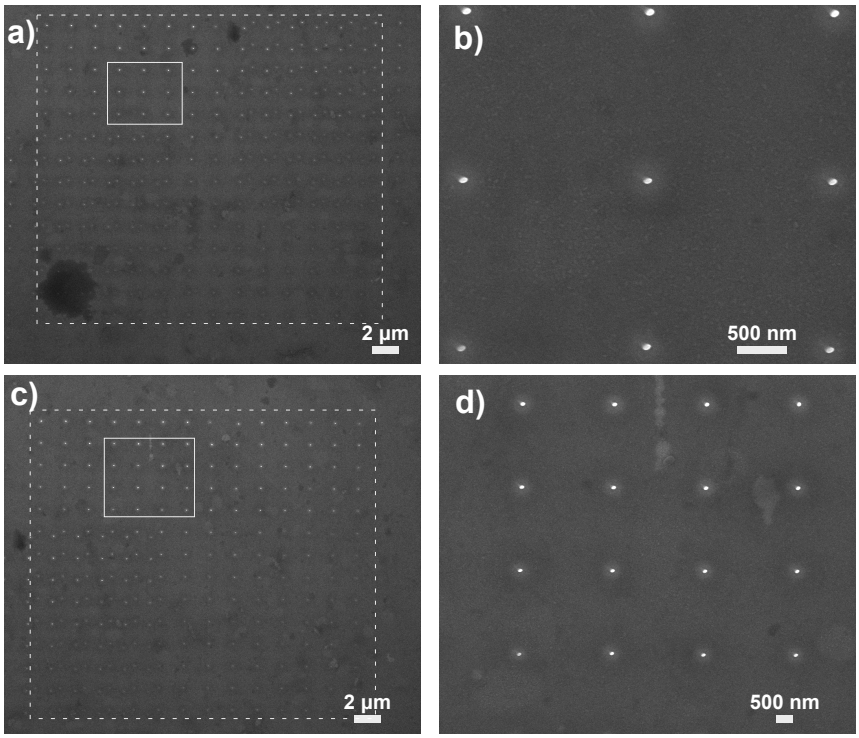

Figure 5.16: a) and c): SEM images of high resolution multi-beam EBID. showing two arrays of dots patterned in different locations. b) and d): Zoomed-in images of the box highlighted in a) and c). The smallest size is $57nm$.

beam imaging. Secondly, the movement of the piezo stage mounted on the SECOM platform was not accurate. And lastly, the system was at that time equipped with a source module at the end of its lifetime and thus with a non-uniform illumination. We expect that it is possible to demonstrate sub-20 nm structures patterned with multi beam EBID, once these issues are solved and we encourage further work to prove it. Moreover, the integration of a beam blanker that is capable of switching ON and OFF each beam individually is crucial for large area and high throughput patterning. However, the integration of a beam blanker is not trivial in the present system design. In the next chapter we will present and discuss a new concept of multi-beam splitting, where the individual blanking option can be more easily integrated.

6

Design of a Multi Beam Splitting and Blanking Unit

Non enim omnis error stultitia est dicenda.
We must not say that every mistake is a foolish one.

Cicero

6.1 Introduction

Multi-Beam scanning electron microscopes (MBSEM) are developed to match the need for high resolution and high throughput imaging and patterning. As briefly described in Chapter 5, A. Mohammadi-Gheidari has developed a Multi-Beam SEM that delivers 196 beams focused at the sample with an axial probe of $1.2nm$ with $26pA$ current. The beam is split into 196 beams in the source module and further accelerated into the Coulomb tube (CT). In this design, the original source module is replaced with a home-made source module, which consists of a Schottky source, an extractor, a suppressor, a set of three-electrodes, a

multi beam aperture array and an accelerator lens. The beams are then focused onto the sample surface by means of an intermediate lens and an objective lens and scanned over the sample surface thanks to the scan coils positioned in the lower part of the electron column. If a precursor gas is let into the SEM chamber, the dissociation of the gas molecules by the electron beam causes a deposition of material to occur on the sample surface that is being scanned (Electron Beam Induced Deposition). When using the 196 MBSEM, the throughput of this process is enhanced by a factor of 196. However, the beams are not controlled individually, the structures that all beams will deposit will have the same geometry. A way to control each beam independently is based on the use of a multi beam blanker. A blanker consists of two vertical plates positioned parallel to the beam trajectory with a voltage difference. This creates an electric field that deflects the beam from its original trajectory. When an aperture of a sufficiently large diameter is placed below the blanker, the beam can be stopped. If such a device is built for every single beamlet, a multi-beam blanker unit (MBU) is obtained. An MBU is designed and located in the electron optical system in such a way that each beamlet falls in between its dedicated blanker plates and, if a voltage difference between these plates is set, deviates from its original trajectory. A single aperture placed below the MBU serves as a beam stop, before it reaches the sample surface. This way, it is possible to select which beams are "active" and therefore will expose the sample in a certain position.

In the present multi-beam system, the logical location for the multi beam blanker array would be in the source module. In this case, the multi electron beam blanker can be integrated in a unit that first splits the beams and focuses them on the blanker plane, as demonstrated by Zhang and Van Bruggen [158] [159]. The schematic of this unit is shown in figure 6.1. The blanker array (BA) consists of many micro electrodes and controls the trajectory of each beamlet created by the current limiting aperture array (CLAA), situated above the BA. The aperture lens array (ALA) located below the BA has the function of creating a positive lens effect that focuses the beamlets further down in the column.

However, in the source module demanding conditions, such as ultra-high vacuum and high tension, make the implementation of the blanker difficult. In fact, a large amount of feedthroughs (at high-voltage) would be needed to control each of the 196 deflectors. It would also lead to a highly-specialised, and costly, source module, which, from a commercial point of view, would be less attractive for applications.

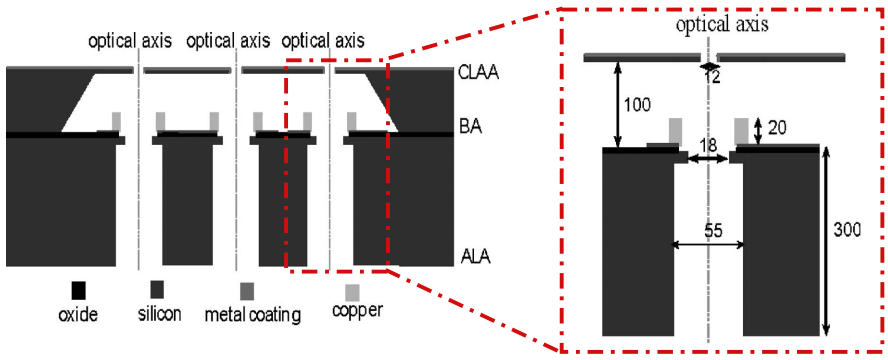

Figure 6.1: Schematics of the multi electron beam blanker array containing the current limiting aperture array (CLAA), the blanker array (BA) and the micro apertures lens array (ALA). Dimensions of the unit are in micrometer [154].

Because of the difficulties encountered in the past by other students, we began to wonder whether it would be possible to position the multi beam blanker unit somewhere else in the column in order to simplify the integration of the unit itself. The blanker unit can then be placed on a plane where all the beams are in focus but with a sufficiently large pitch that allows the positioning of the 14x14 array of deflectors. Obviously having the multi beam blanker unit and the splitting unit in different locations in the column would create enormous difficulties in the alignment of the two, especially considering the rotation in the beam trajectories introduced by magnetic lenses. A straightforward solution is then to rethink the design of the MBSEM in such way that the splitting and the blanking plates are built within the same unit to allow an easy alignment procedure.

6.2 Requirements for a Multi Beam Unit

Figure 6.2 shows the schematics of a single beam scanning electron microscope consisting of a set of condensor lenses, C1 and C2, an intermediate lens (INT) and an objective lens. The electron beam is generated in the source module above the C1 lens and it is focused down at the sample in a nanometre-sized probe. The distance between the lenses is fixed, while the position of the sample can be tuned. The distance between the objective lens and the sample is called working distance. To limit the beam current, a variable aperture plate is placed in between the C2 lens and the intermediate lens. This plate has aper-

tures of different sizes, varying from 20 μm for high resolution imaging to 1 mm, for elemental composition analysis. The blanker plate can be positioned below the variable aperture and is capable to switch on and off the beam by deflecting it onto a stop aperture, typically placed in the objective lens.

As discussed earlier, the easiest option in terms of alignment is to combine the multi-beam splitting and blanking devices into one unit. The location of this "Multi-Beam Unit" (MBU) should be easily accessible. In fact, we aim for *flexibility* and *versatility*, meaning that the changes to be made to a standard microscope do not have to be permanent and have to be easy to adapt to a variety of SEMs.

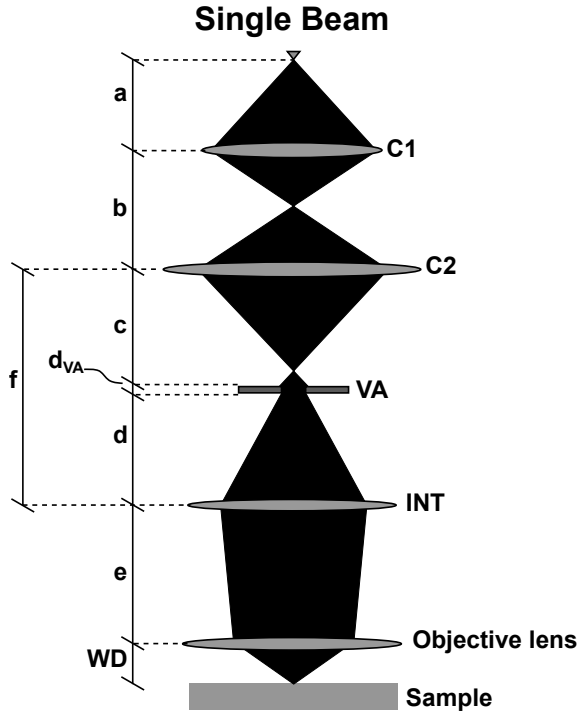

Figure 6.2: Optical schematics of an electron microscope in single beam mode.

From these considerations, two options follow. First, we considered to place the Multi Beam Unit under the pole piece, right above the sample, accessible from the microscope chamber. However, in this solution the optical system will not benefit from the strong de-magnification of the off-axis aberration

contributions by the objective lens as final lens. The second option is to place the Multi-Beam Unit inside the electron column via the Variable Aperture (VA) flange. This allows an easy design of the unit as the device is at ground potential and in relatively low vacuum, in the order or 10^{-6} mbar. Moreover, every microscope has a Variable Aperture stick to allow for different probe current, meaning that this solution could in principle be applied to all microscopes. Last but not least, it will be easy and straightforward to remove the Multi Beam Unit and replace it with the original VA stick, allowing for flexibility. The Multi Beam Unit consists of a **Micro Lens Array (MLA)**, that splits the primary beam and focuses each beamlet in the blanker plane, and a **blanker array**.

The requirements for the design of a new multi-beam unit can be summarized as follow:

- **Current per beam of** $\approx 50pA$. The current value must be a trade off between acceptable imaging signal from secondary electrons and low enough current to achieve a small probe size.
- **Total probe size of** $< 5nm$. To image and to pattern structures in the sub-10 nm range, a small probe size is required. The total probe size comprises also the contributions from on-axis and off-axis aberrations.
- **Number of beams: minimum 25**, in order to sufficiently improve the throughput.
- The unit consists of a beam splitter and a blanker array, that are pre-aligned in the device manufacturing process.
- The unit must fit the variable aperture port, which has a diameter of $1cm$. Within this space, the beam splitter and the blanker array must be placed.

From these requirements, three different types of optical geometries can be considered, as shown in figure 6.3. For all three options, the multi beam unit can be inserted in the optical path of the electron beam via the variable aperture port. The unit is placed at one end of a cylindrical support, inside of which electrical feedthroughs are envisioned. In all three cases, all the beamlets are focused in the objective lens, as also done in the 196 multi-beam SEM [160]. The reasons for doing so can be summarized as follows:

- Minimize the contribution of the off-axis aberrations of the objective lens
- De-magnify the off-axis contributions of the other lenses

- If the beams are focused in the coma-free plane, the contribution of coma from the final lens will be negligible.

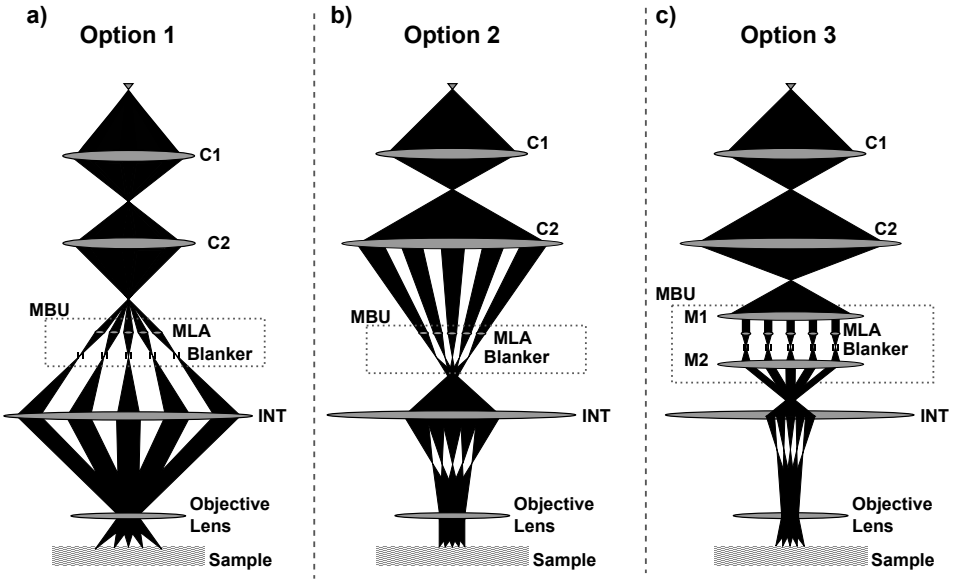

Figure 6.3: Three different optical configurations of the Multi-beam unit.

In the system of figure 6.3a, referred to as option 1, the source is imaged by the C1 and C2 lenses in a plane above the Multi beam unit, which is represented by the grey dashed line. The primary beam is split into beamlets by means of the Micro Lens Array (MLA) and focused in the blanker plane. All beamlets have a common crossover in the coma-free plane of the objective lens (UHR) and are focused in the sample plane. The system in 6.3b, referred to as option 2, differs from that in figure 6.3a by the strength of C2 lens. In this case, the source is imaged by the C2 lens in a plane beyond the multi-beam unit. The INT lens, then, is tuned such that all beamlets cross over in the coma-free plane of the UHR lens, creating a conjugate plane in between the INT and the UHR lens. The main disadvantage of these two solutions is given by the alignment of the MLA and the blanker plate. In fact, the apertures of the MLA and those of the blanker are not positioned at the same pitch, as the beamlets are travelling under angles away from the vertical through the multi beam unit. To overcome this limitation, a parallel beam configuration, shown in 6.3c, referred to as option 3, is also studied. In this case, inside the multi-beam unit, a macro lens M1, placed above the MLA, condenses the primary beam into a parallel beam.

The MLA apertures and the blanker apertures are now at the same pitch, allowing an easier alignment of the two plates. A second macro lens M2, placed beyond the blanker plate, makes all the beams cross over in a plane above the INT, which makes all beams cross over in the coma-free plane of the objective lens (UHR).

The evaluation of the three options is carried out by analyzing the following factors:

- Total probe size at the sample, given by the geometrical probe size and the contribution of the on-axis aberrations.
- Total number of beamlets, that is given by the illuminated area of the beam splitter plate and the aperture size.

Before studying the three options in detail, an introduction on first order optics and on-axis aberrations is here necessary.

6.3 First order optics

In electron optical systems, the **reduced brightness** is a quantity that expresses the current emitted from the tip per unit area and per solid angle. The reduced brightness remains constant throughout the system, despite the presence of beam current limiting apertures and lenses that may accelerate or decelerate the electrons. The reduced brightness B_r changes considerably for different types of sources and is given by equation 6.1, where dI is the current flowing through a surface dA within a solid angle $d\Omega$, with acceleration voltage V.

$$B_r = \frac{dI}{dA d\Omega V} \tag{6.1}$$

For a typical Schottky source, the reduced brightness B_r is equal to $5{\cdot}10^7 \frac{A}{m^2 sr V}$. The total current I_{tot} and the angular current density J_{tot} can then be calculated from the reduced brightness according to equations 6.2 and 6.3.

$$I_{tot} = B_r \cdot \alpha^2_{emission} d^2_{source} \frac{\pi}{4}^2 V_{acc} \tag{6.2}$$

$$J_\Omega = \frac{I_{tot}}{\pi \alpha^2_{emission}} \tag{6.3}$$

where $\alpha_{emission}$ is the opening angle of the beam emitted by the tip, d_{source} is the virtual source size, estimated to be 30 nm and V_{acc} is the acceleration voltage. If an emission cone angle of $120mrad$, for which the virtual source size of the Schottky emitters is constant [160] [161], is considered, in case of a $5kV$ beam voltage, the total emitted current I_{tot} is equal to approximately $2\mu A$ while the angular current density J_Ω is equal to $176.7\mu A/sr$. Effectively, the brightness defines the angular current density that has to illuminate the aperture in the MLA plane. This means that for a given acceleration voltage there is only one half opening angle beta that satisfies the requirement on the brightness to be equal to $5 \cdot 10^7 \frac{A}{m^2 sr V}$, as shown in figure 6.4. The angle β is calculated from equation 6.4.

$$\beta = \sqrt{\frac{I_{tot}}{B_r V_{acc} (\pi r_{MLA})^2}} \tag{6.4}$$

Where r_{MLA} is the radius of the aperture.

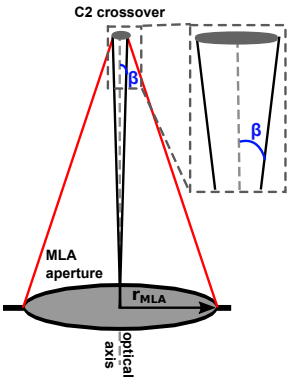

Figure 6.4: Condition on the illumination of the MLA aperture for which the reduced brightness has to be constant.

By varying the acceleration voltage and the size of the MLA aperture, beta varies as shown in graph 6.5. This means that for a certain probe size in the C2 crossover and for a certain aperture that needs to by illuminated by the beam, there is a certain distance between the C2 crossover and the aperture that fulfills equation 6.4.

6.3.1 On-axis aberrations

On-axis aberrations are effects that deteriorate the probe size in all charged particle optics instruments. These contributions are summed up to the *geometrical spot size*, meaning that the source, which has a non-infinite size, is

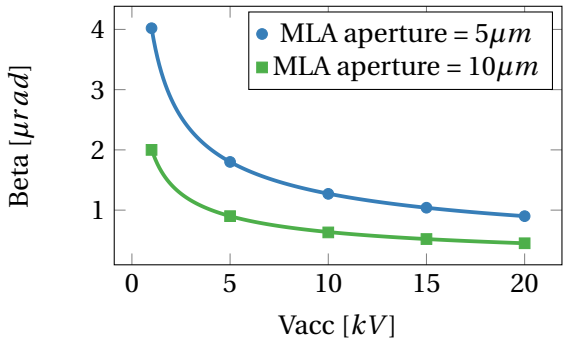

Figure 6.5: Half opening angle beta calculated for different beam acceleration voltages in case of an MLA aperture of 5μm and 10μm and for a current of 50 pA.

imaged in the image plane demagnified by a factor given by the strength of the lens. The on-axis aberrations include the *diffraction effect*, which is given by the wave properties of electrons, the *spherical* and *chromatic aberrations*, which depend on how far the electrons are travelling from the optical axis and on their energy spread. The FW50 (full width at 50%) geometrical spot size and the on-axis aberrations can be calculated as follows [162]

$$d_{geo} = d_{source} M \quad \text{[m]} \quad (6.5)$$

$$d_{diff} = 0.54 \frac{\lambda}{\alpha} = 0.54 \frac{1.266 \cdot 10^{-9}}{\sqrt{V}\alpha} \quad \text{[m]} \quad (6.6)$$

$$d_{sph} = 0.18 C_s \alpha^3 \quad \text{[m]} \quad (6.7)$$

$$d_{ch} = 0.6 C_c \frac{\delta U}{V} \alpha \quad \text{[m]} \quad (6.8)$$

The contributions to the total probe size are here calculated as the FW50 value. M is the magnification of the lens, λ the wavelength of the electrons, α is the half opening angle, V the acceleration voltage in $[V]$, C_s and C_c the spherical and chromatic aberration coefficients, δU the energy spread.

The total probe size is calculated by adding to the geometrical spot size d_{geo} the on-axis aberration contributions of diffraction d_{diff}, spherical aberration d_{sph} and chromatic aberration d_{ch}, as shown in equation 6.9.

$$d_{on-axis} = \left(\left(\left(d_{geo}^{1.3} + \left(\left(d_{diff}^{4} + d_{sph}^{4}\right)^{1/4}\right)^{1.3}\right)^{1/1.3}\right)^{2} + d_{ch}^{2}\right)^{1/2} \tag{6.9}$$

The total probe size is here calculated as the FW50 value using the Barth-Kruit equation [163].
In case of chromatic aberrations, the coefficient C_c can be approximated [162] as:

$$C_c = f \cdot (1 + M)^2 \tag{6.10}$$

In case of spherical aberrations, the coefficient can be approximated depending on the type of lens. Table 6.7 shows the estimated spherical aberration coefficients for all the lenses in the system [162]. In case of electrostatic lenses, such as C1, this is approximately equal to the ratio of the third power of its focal length f and the diameter of the lens aperture d to the second power. For a single electrode lens such as the MLA, the spherical aberration coefficient can be approximated as the ratio of the squared focal length f and the diameter of the aperture d. For magnetic lenses, such as C2, INT and UHR, the spherical aberration coefficient also depends on the pole piece gap S and on the pole piece diameter d, as shown in table 6.7 [162].

Lens	Type of Lens	Estimated C_s
C1 lens	Electrostatic	$C_s = \frac{f^3}{d^2}$
C2 lens	Magnetic	$C_s = \frac{0.24f^3}{s^2+0.45d^2}$
MLA	Single electrode	$C_s = \frac{f^2}{d}$
INT lens	Magnetic	$C_s = \frac{0.24f^3}{s^2+0.45d^2}$
UHR lens	Magnetic	$C_s = \frac{0.24f^3}{s^2+0.45d^2}$ (for $f >> d$)

Table 6.1: Estimated equations for the spherical aberration coefficients [164] [162].

6.4 Considerations on Coulomb Interactions

Stochastic Coulomb interactions play an important role in the design of an electron optics system characterized by high brightness as they worsen their performance. Coulomb interactions occur when particles of the same charge

are traveling close together on an optical path, disturbing each other. In our case, the electrons, that are negatively charged, are repelling each other and thus changing their path in the electron beam, resulting in a probe enlargement as well as in an energy spread.

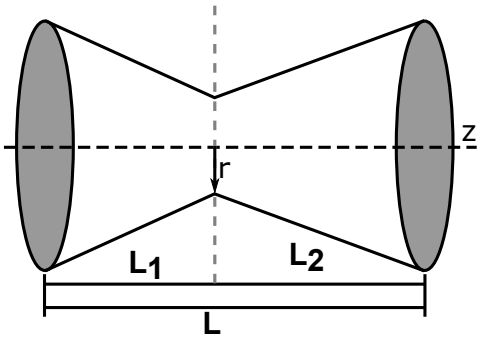

Figure 6.6: Definition of lengths in an electron optics segment for the calculation of the statistical Coulomb interactions. L is the distance between two lenses and L_1 and L_2 are respectively the image distance of the first lens and the object distance of the second lens [165].

Coulomb interactions are divided into two groups: trajectory displacement and the Boersch effect, or energy spread. Both effects can be approximated with analytical equations that refer to an optical segment as that represented in figure 6.6 [165]. When a beam is focused in a spot, L is the distance between two optical lenses and L_1 and L_2 are respectively the image distance of the first lens and the object distance of the second lens. In such a schematic, another variable S_c can be defined as the ratio between $L1$ and L, as shown in equation 6.11. S_c can vary only in the range between 0 and 1 and S_c is equal to 0 for a diverging beam and equal to 1 for a converging beam.

$$S_c = \frac{L_1}{L} \tag{6.11}$$

In such a system the stochastic Coulomb interactions can be estimated with an analytical expression, given by equation 6.12 [165]. This equation calculates the total FW50 probe size as interpolation of the FW50 probe sizes in different regimes, that are the Gaussian regime, the Holtzmark regime and the pencil beam regime. An electron optical system falls into one of these regimes according to the beam current or the beam voltage. Typically, in an electron microscope, the regimes encountered are the Holtzmark regime or the pencil beam regime. The FW50 probe size of these regimes are calculated according to equations 6.13, 6.14 and 6.15 [165].

$$FW50_{td} = \left(\left[\left(\frac{1}{FW50_G} \right)^6 + \left(\frac{1}{FW50_H} \right)^6 \right]^{\frac{1}{7}} + \left(\frac{1}{FW50_{PB}} \right)^{\frac{6}{7}} \right)^{\frac{-7}{6}} \tag{6.12}$$

$$FW50_G = 0.158 \frac{m^{1/4} e^{1/12}}{\epsilon_0^{5/6}} \cdot \left[\frac{1.27 S_c^{6/5} - 0.0025}{\left(1 + \frac{2e^{4/9}}{(2\pi\epsilon_0)^{4/9} \alpha_0^{4/3} V^{4/9} L^{4/9}} \right)^{1/2}} + \frac{0.95 - S_c}{1 + \frac{4e^{1/3}}{(2\pi\epsilon_0)^{1/3} \alpha_0 V^{1/3} L^{1/3}}} \right] \cdot \frac{I^{1/2} L^{2/3}}{\alpha_0 V^{13/12}} \tag{6.13}$$

$$FW50_H = 0.172 \frac{m^{1/3}}{\epsilon_0} \cdot \left[S_c^{2/3} + (1 - S_c)^{2/3} \right] \cdot \frac{I^{2/3} L^{2/3}}{V^{4/3} \alpha_0^{4/3}} \tag{6.14}$$

$$FW50_{PB} = 0.145 \frac{m^{3/2}}{e^{7/2} \epsilon_0} \cdot \left[S_c^3 + (1 - S_c)^3 \right] \cdot \frac{I^3 L^3 \alpha_0}{V^{5/2}} \tag{6.15}$$

Where m and e are the mass and the charge of an electron, I and V the current and the acceleration voltage of the beam, α_0 the half opening angle and ϵ_0 the dielectric constant.

Similarly to the trajectory displacement, also the Boersch effect, or the energy spread, can be approximated with an analytical expression, shown in equation 6.16 [165]. This equation calculates the total energy spread as interpolation of that resulting from the four different regimes: Gaussian, Holtzmark, Lorentzian and pencilbeam. The contributions to the energy spread for these regimes are expressed in equations 6.17, 6.18, 6.19 and 6.20 [165].

$$\frac{E}{\Delta E_{FW50}} = \left[\left(\frac{E}{\Delta E_{FW50_G}} \right)^4 + \left(\frac{E}{\Delta E_{FW50_H}} \right)^4 + \left(\frac{E}{\Delta E_{FW50_L}} \right)^4 + \left(\frac{E}{\Delta E_{FW50_{PB}}} \right)^4 \right]^{\frac{1}{4}} \tag{6.16}$$

$$\frac{\Delta E_{FW50_G}}{E} = 0.802 \frac{m^{1/4}}{\epsilon_0^{1/2} e^{1/4}} \frac{I^{1/2}}{V^{3/4}} \tag{6.17}$$

$$\frac{\Delta E_{FW50_H}}{E} = 0.891 \frac{m^{1/3}}{\epsilon_0} \frac{I^{2/3}}{r_c^{1/3} \alpha_0 V^{4/3}} \tag{6.18}$$

$$\frac{\Delta E_{FW50_L}}{E} = 1.41 \frac{m^{1/2}}{\epsilon_0 e^{1/2}} \frac{I}{\alpha_0 V^{3/2}} \tag{6.19}$$

$$\frac{\Delta E_{FW50_{PB}}}{E} = 0.642 \frac{m}{\epsilon_0 e^2} \frac{I^2 L}{V^2} \tag{6.20}$$

Where r_c is the minimum radius of the beam in the crossover.

Influence of stochastic Coulomb interactions

Figure 6.7 shows how the source angular current density varies with emission angle [166], namely the half opening angle from which the electrons are emitted from the tip in the source module, for different extractor voltages. If we consider an extractor voltage of $5kV$, which is the extractor voltage used in Schottky sources, then we can consider a half opening angle of $30mrad$ as still "safe".

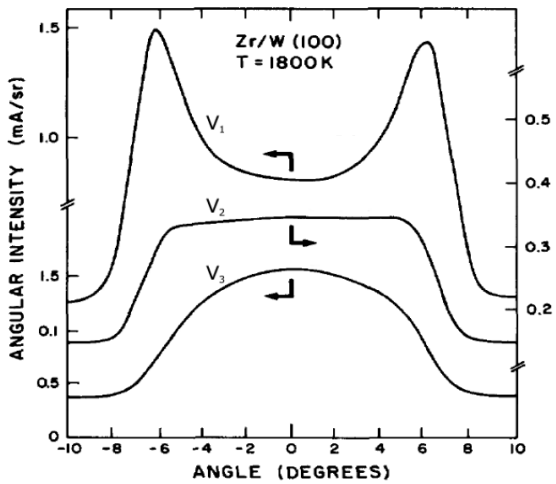

Figure 6.7: Measured angular intensity of a Schottky electron source with a tip radius of $0.8\mu m$ for different extractor voltages, where V1>V2>V3 and V1 = 4600V [166].

For increasing emission angles, the total current increases with the second power of the angle, as shown in equation 6.2. When the current increases also the contribution of the Coulomb interactions increases, compromising the performance of the system. In this section, the contributions of trajectory displacement and energy spread from the source down to the variable aperture port are analyzed, following equations 6.12 to 6.20. Figure 6.8 shows the segments used for the estimation of Coulomb interactions in the electron optical system from the source to the variable aperture. This study aims at understanding how the interaction between electrons affects the probe size and the energy spread by varying the emission angle at the source.

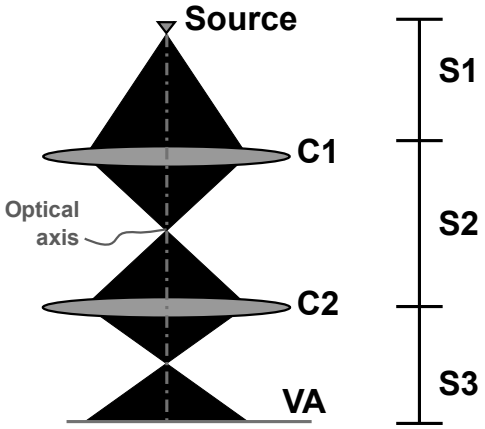

Figure 6.8: Schematics of upper part of the electron column of a scanning electron microscope, comprising the source and the C1 and C2 lenses. S1, S2 and S3 are the segments into which the system is devided for the calculations of the Coulomb interactions.

Figure 6.9 shows the Coulomb interactions calculated in segment S1, i.e. from the source to the C1 lens. In these graphs, the four regimes are highlighted: pencil beam, Holtzmark and Gaussian for the trajectory displacement (TD), Lorentzian for the energy spread (or Boersch effect, BE). In orange is the interpolation of all the regimes, calculated according to equations 6.12 and 6.16. In trajectory displacement, up to an emission angle of approximately $15mrad$, the dominant regime is pencil beam, while for larger angles the Holtzmark prevails. In case of the energy spread, the dominant regime for larger emission angles is the Lorentzian regime. With an emission angle of $60mrad$, the contribution to the probe size is approximately $4.3nm$, but exponentially decreases for small angles. For an opening angle of $4mrad$, the total trajectory displacement is less than $0.01nm$. The energy spread, on the other hand, is larger than $175meV$ when the opening angle is $60mrad$, but decreases to $0.2meV$ for an emission angle of $4mrad$.

Figure 6.10 shows the trajectory displacement and the Boersch effect for the

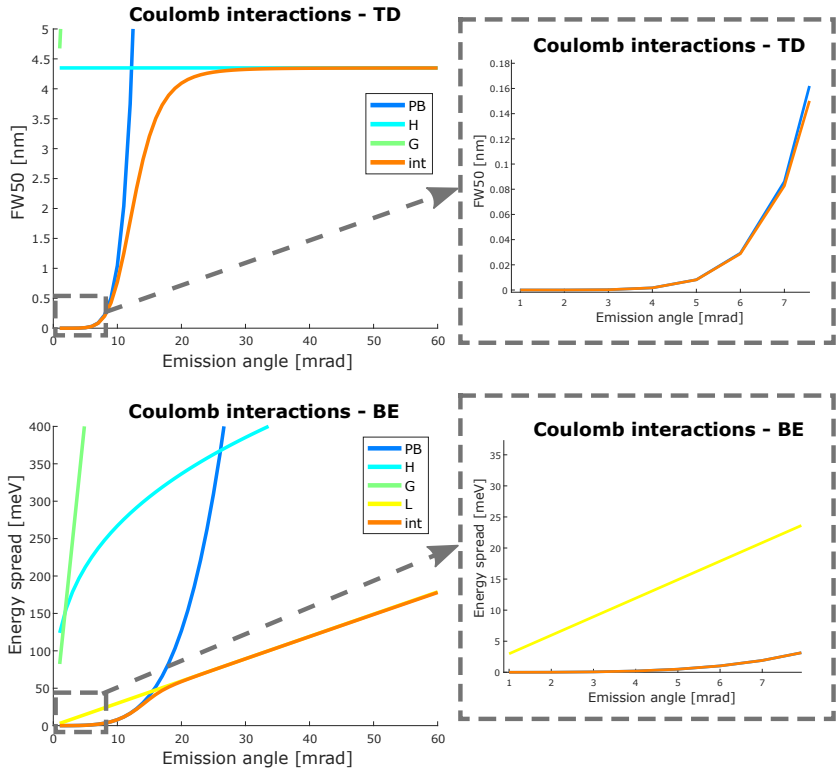

Figure 6.9: Stochastic Coulomb interactions in segment S1: the trajectory displacement (TD) and the Boersch effect (BE) are here shown as function of the emission angle. In case of TD, the Gaussian (G), Pencil Beam (PB) and Holtzmark (H) regimes are presented, together with the interpolation (int), calculated according to equation 6.12. For BE, the Gaussian, Pencil Beam, Holtzmark, Lorentzian (L) regimes and their interpolation are shown. The interpolation is calculated using equation 6.16.

segments S1, S2 and S3. The larger contribution comes from the S2 segment, where the trajectory displacement is larger than $500nm$ for an emission angle of $60mrad$. All the contributions are smaller than $5nm$ for an emission angle of $4mrad$. Similarly, the energy spread becomes acceptable for an angle smaller than $4mrad$, where the three contributions are smaller than $60meV$.

Because of the Coulomb interactions being large for large emission angle and to prevent these effects to limit the performance of the multi-beam system, an emission angle of $4mrad$ is accepted. In practice, the rest of the cone can be blocked in the source by adding an aperture before the C1 lens. If an aperture is added at $3.75mm$ distance from the tip, the diameter of such an aperture is

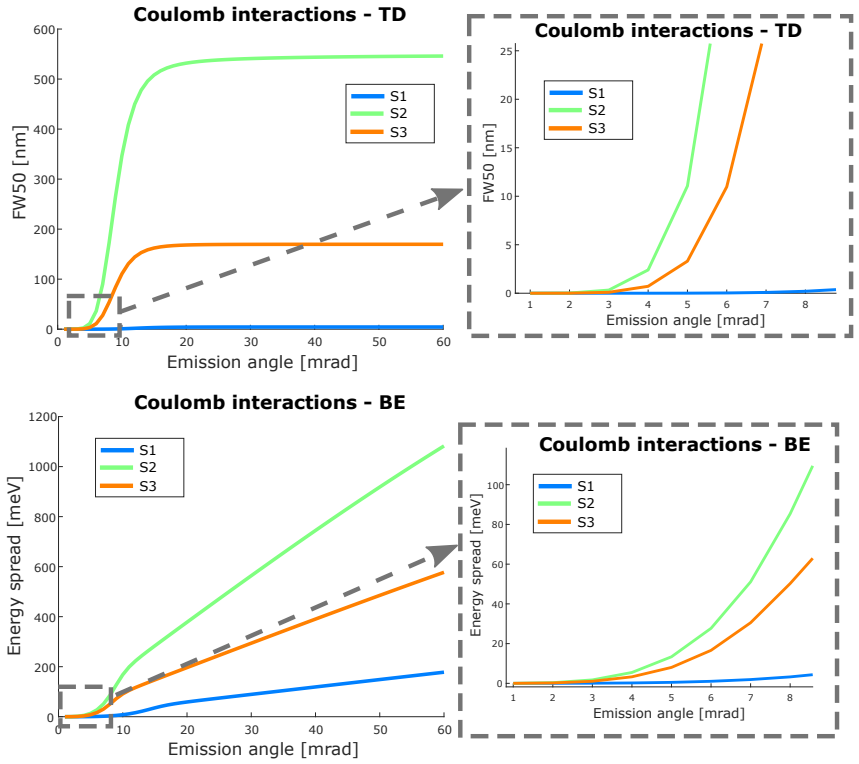

Figure 6.10: Stochastic Coulomb interactions in segment S1, S2 and S3: the trajectory displacement (TD) and the Boersch effect (BE) are here shown as function of the emission angle.

$30\mu m$ In this case, the total emitted current is approximately $8.8nA$.

6.5 Analysis of the three options

Figure 6.11 shows the on-axis performance of the three options calculated from the equations for the on-axis aberrations and total probe size described in section 6.3. In this case, the contributions to the final probe size of all lenses were calculated considering the following assumptions:

- Acceleration voltage: $5kV$
- MLA aperture: $15\mu m$
- Working distance (applicable for graph 6.11a): $3mm$
- Probe current at sample: $50pA$

- Position of the MLA w.r.t. upper edge of the variable port: $3mm$
- Distance between MLA and blanker: $4mm$

The blanker is not taken into account for this initial calculation, however the position of the blanker determines the image position of the MLA lens.
In figure 6.11a, the total probe size for different acceleration voltages is shown. In this case, for low acceleration voltages option 3 performs better, achieving for $1kV$ a total probe size of $5.2nm$. At higher acceleration voltages, from $5kV$, the difference is negligible. Also, for voltages higher than $5kV$, all solutions report an on-axis probe smaller than $5nm$. In figure 6.11b, the probe size as function of the working distance is shown. In this case, option 3 has better on-axis performance especially for small WD. For this calculation, option 1 and 2 perform equally.

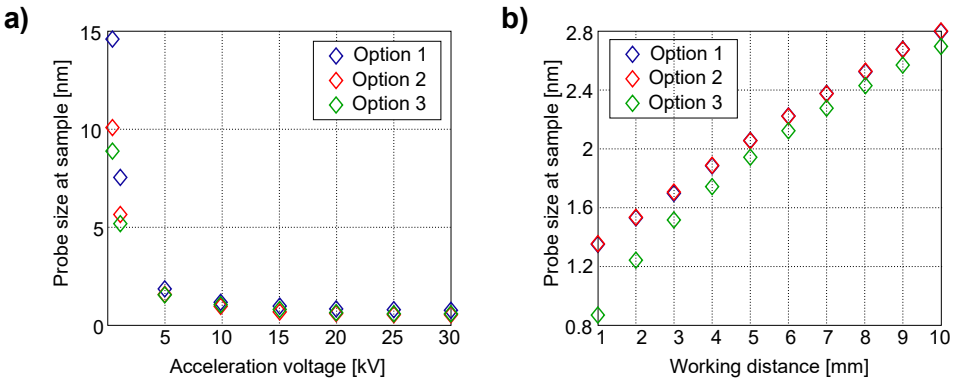

Figure 6.11: Total probe size as function of the beam acceleration voltage (a) and the working distance (b) for the three options depicted in figure 6.3.

The number of apertures that the MLA can host, or the number of beamlets that the beam can be split into, depends on the *illuminated* area on the MLA plate, or the size of the beam at this location. It also depends on the aperture size and on the pitch between apertures on the MLA. Because of the requirement on the beta that needs to be fulfilled, as described in equation 6.4, the illuminated area on the MLA depends on the size of the aperture and by increasing the aperture diameter the geometrical spot size at the sample increases. To understand how many beamlets each solution can provide, calculations have been done with the following settings:

- MLA diameter: $10\mu m$

- Working distance: $3mm$
- Acceleration voltage: $5kV$
- Distance MLA-blanker: $4mm$

Figure 6.12 shows the schematics of the MLA for option 1, 2 and 3. In such a configuration, for option 1, the total beam size at the MLA is approximately $133\mu m$ in diameter. Considering that each aperture in the MLA has a diameter of $10\mu m$ and assuming a pitch of $15\mu m$, the total beam can be split into 49 beams. Figure 6.12 shows the top view of the MLA as well as the top view of the blanker plate. The outer circle refers to the total beam and the white inner one to the apertures of the MLA and the blanker. The pitch between beams is chosen such that there is enough space for the wiring of the blanking electrodes. The main disadvantage of this solution is that the MLA apertures and the blankers are not on the same axis, apart from the central beam. This may introduce severe issues when aligning the plates to each other. To overcome this limitation, it is necessary to put markers outside the region of interest to make the alignment possible. In case of option 2, the illuminated area has the same size as option 1 and therefore a maximum of 49 apertures can be located within the illuminated area with a pitch of $15\mu m$. As in Option 1, also for option 2 only the central apertures are on the same axis, making the alignment of the two plates more challenging. In case of option 3, the size of the total beam at the MLA is approximately $66\mu m$. Figure 6.12 shows the top view of the MLA and blanker plate. In this case, all the apertures are exactly on the same vertical axis, providing a much easier aligning procedure. However, the main limitation of this option is the limited amount of beams delivered at the sample because of the limited size of the illuminated area.

6.5.1 Can we increase the number of beams even further?

When compared to the present Multi Beam SEM, the disadvantages of the mentioned solutions is that the number of beams is less than 196 and each beam carries more current. While the existing MBSEM delivers 196 beams, with the three options that we are studying, the number of beams is 49 or 9. So far, we have calculated the electron optics design of such multi beam units without allowing for changes made to the electron column of commercially available SEMs. Moreover, we do accept a smaller emission angle to prevent the Coulomb interactions to worsen the system, as described in section 6.4.

Figure 6.13a shows how the number of beams increases with the emission angle for both option 1 and 2. By allowing more current, the number of beams

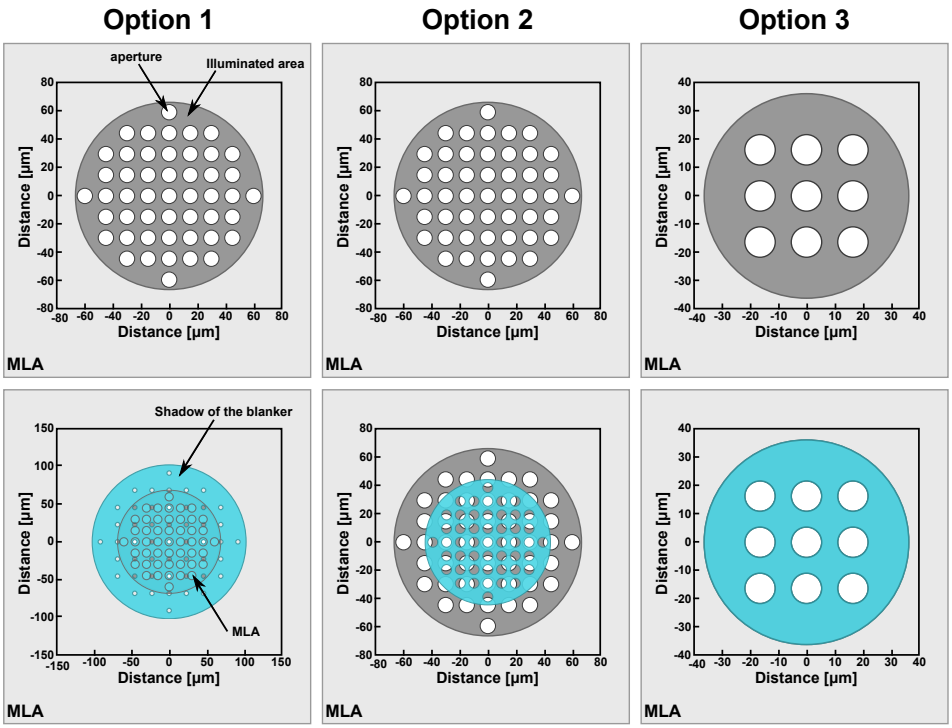

Figure 6.12: On top, schematics of the MLA apertures for option 1, 2 and 3. For options 1 and 2, 49 apertures can fit the illuminated area, in option 3 there is space for only 9 apertures. On the bottom, schematics of the blanker apertures overlapping the MLA plate. In case of option 1, the pitch between apertures is larger, whereas for option 2 is smaller. In case of option 3, the pitch between apertures on the blanker is the same as on the MLA.

increases considerably. However, this also means that the Coulomb interactions and the off-axis aberrations will become more of an issue. When an emission angle of $8mrad$ is chosen, i.e. twice the current value, it is possible to obtain 233 beams in option 1 and 2. In these cases, in fact, the radius of the illuminated area on the MLA is $66\mu m$ for an emission angle of $4mrad$ and becomes $133\mu m$ at $8mrad$. At $30mrad$, the illuminated area on the MLA is $500\mu m$ in diameter, giving space for more than 3000 apertures of $5\mu m$ at a pitch of $7.5\mu m$. Also in the case of option 3 the number of beams increases rapidly with the emission angle, as depicted in figure 6.13b. For an emission angle of $8mrad$, the number of beams becomes 49. In order to be comparable with our current Multi-Beam SEM, the emission angle has to be set to $15mrad$, corresponding to 193 beams.

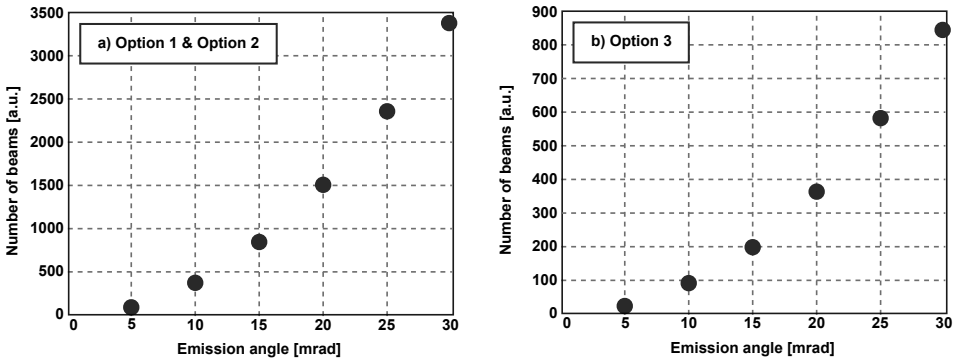

Figure 6.13: Number of beams for different emission angles, in case of options 1 and 2 (a) and 3 (b).

6.5.2 Final considerations and conclusions

The analysis of three possible designs of the Multi Beam Unit was presented in this section. The main difference is the direction in which the beams are travelling in the Multi Beam Blanker Unit. In practice, only the design of the blanker plate differs among the three solutions, having blanker apertures located at different pitch.

Main advantages and disadvantages of these three options are listed in table 6.2. Options 1 and 2 offer more beams than option 3 (for the same emission angle), but at the cost of having the apertures on the blanker plate on a different pitch than on the MLA. In option 1, the pitch between apertures on the blanker is larger than on the MLA, leaving more space for the wiring connecting to the deflectors. The main disadvantage for Option 1 may be the large off-axis aberrations from the INT lens, where the beams are travelling far away from the optical axis. If these aberrations turn out to be too large, it may be necessary to add a macro lens at the bottom of the stack, below the blanker, to condense the beamlets in a smaller beam. The main disadvantage for option 2, on the other hand, is the limited space between the apertures in the blanker plate. To have enough space for the wiring, the pitch on the MLA must increase, and consequently the number of apertures will decrease. In option 3 the beamlets are travelling parallel in between the MLA and the blanker and therefore the pitch between apertures in the two plates is identical. This ensures an easier alignment procedure when fabricating the MBU. Moreover, the size of the beam at the INT lens is small and therefore the contribution to the final probe size from off-axis aberrations is smaller than for option 1 and 2. The biggest limitation for option 3 is the limited number of beams. Moreover, because two

extra macro electrodes are needed, it may be necessary to split the device into two parts, one being placed at the variable aperture location and the second at the standard blanker location, positioned below the variable aperture. This will of course create extra challenges for the alignment of the system and of the two parts between each other.

	Advantages	**Disadvantages**
Option 1	Number of beams More space for connecting the blanker electrodes to the outside world	Off-axis aberrations Beam travelling diagonally: difficulties in aligning the MLA plate and the blanker plate. It can be solved with markers outside the ROI A second unit might be needed if a macro lens has to be inserted for limiting the off axis aberrations
Option 2	Number of beams	No space for contacts for the blanker electrodes on the blanker plate Off-axis aberrations Beam travelling diagonally: difficulties in aligning the MLA plate and the blanker plate. It can be solved with markers outside the ROI
Option 3	Small off-axis aberrations Easy alignment of MLA plate and blanker plate	Limited number of beams A second unit in the blanker aperture is necessary as the whole stack of plates will not fit the VA aperture.

Table 6.2: Overview of advantages and disadvantages of the three options.

We can conclude that Option 2 is less likely to be chosen, as it can deliver the same amount of beams as Option 1 with the big limitation of not having enough space for the wiring of the blanker electrodes. We might prefer Op-

tion 1 because, although an extra macro lens may be needed to limit the off-axis aberrations, it provides the largest amount of beams at the sample without changing the extractor aperture in the source module. Regarding the number of beams, considerably more beamlets can be obtained when choosing a larger emission angle, at the cost of loss of resolution given by Coulomb interactions.

6.6 Optimization of the MBU final design

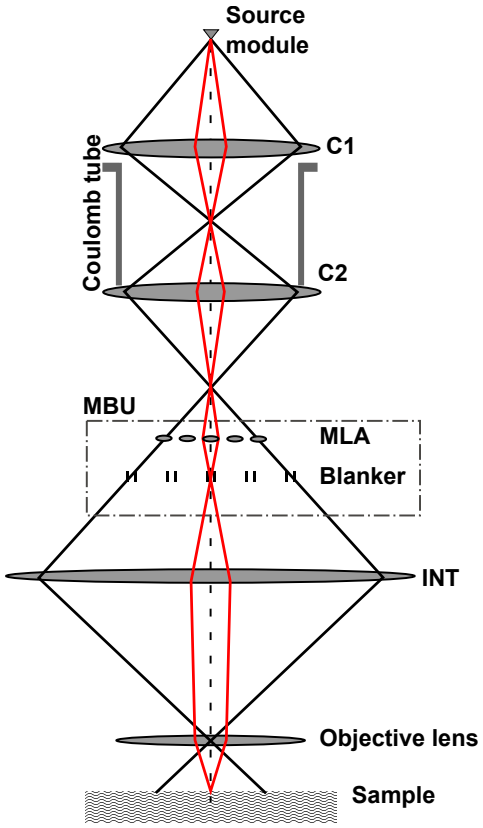

Figure 6.14: Electron optics schematic of an SEM with the developed multi beam unit inserted in the variable aperture port. The red trajectory is the central beam that is focused at the sample. The black trajectory is the path of the off-axis beams, that have a common crossover in the final objective lens.

Figure 6.14 shows the beam trajectories throughout the optical column of the FEI Nova Nano Lab 650: the black rays refer to the trajectories of the outermost beams, while the red beam represents the central beam. The source module consists of elements that extract the beam, limit its current and focus it into a crossover thanks to a condenser lens C1. After that, the beam travels through the Coulomb tube (CT), in which the so-called beam shift and tilt coils allow the alignment of the beam into the optical axis of the following set of lenses.

Below the Coulomb tube, a magnetic lens C2 creates a crossover, right above the current limiting aperture, or variable aperture. The beam is then focused at the sample by an intermediate (INT) and an objective lens. In order to scan the beam on the sample, the scan coils placed in between the intermediate and the objective lens deflect the beam in the X and Y directions. When the multi beam unit is used, the MLA splits and focuses the beams in the multi blanker plane. Furthermore, the beams are focused together in the coma free plane of the final lens by the INT lens. As consequence, the INT also focuses the single beamlets in a plane beyond the sample plane. The common crossover in the objective lens is a requirement for avoiding the off-axis aberrations contributions of the objective lens itself, in particular the coma. The strongest demagnification is given by the objective lens, that focuses each beam onto the sample surface. When one of the deflectors in the multi-blanker plate is switched on, the beam will be stopped onto an aperture to be placed in the objective lens. Eventually, the multi beam unit can also host a single beam aperture, such that it is possible to switch between single-beam and multi-beam mode by retracting the stick, using the variable aperture positioning mechanism.

The design of the multi-beam splitting and blanking unit is limited by the constraints that the system introduces. First, it has to fit the variable aperture port, which is $10mm$ in size. Within such space, the MLA, the electrodes that cause the lens effect on the MLA and the blanker plate need to be placed. Hence the design of the unit starts from the constraint of the position of the multi-aperture lens array, which needs to be placed roughly in the middle of the aperture port, to allow three electrodes to be placed above the MLA and the blanker plate to be placed below the MLA.

The optimization of the design is done by analyzing the on-axis aberrations and the total probe size at the sample. The parameters that can be fine tuned are the acceleration voltage, the MLA aperture diameter, the working distance, the position of the blanker, the position of the MLA in the variable aperture port and the sample current.

6.6.1 Optimization and fine tuning of the parameters

The optimization of the MBU design is carried out by analyzing the total probe size at the sample and fine tuning some parameters. The parameters that can be tuned are:

- Acceleration voltage
- Diameter of the MLA aperture
- Working distance
- Position of the blanker, or the distance between the MLA and the blanker
- MLA position, or the distance between the upper edge of the variable aperture port and the MLA plate (VA-MLA)
- Sample current

Figure 6.15 shows how the total probe size at the sample varies by fine tuning the crucial parameters listed above. This analysis was performed using the configuration shown in table 6.3. So, when the acceleration voltage is changed, for instance, as in the top left graph of figure 6.15, all the parameters are kept constant apart from the voltage, that is varied from 1 V to 30 V.

Parameter	Value
Current per beam	$50pA$
VA-MLA	$3mm$
Acceleration voltage	$5kV$
MLA aperture	$15\mu m$
Distance MLA - blanker	$4mm$
Working distance	$3mm$

Table 6.3: Configuration of the MBU for which the fine tuning of the parameters is performed.

For higher acceleration voltages the probe size decreases exponentially and at $5kV$ it is equal to approximately $2nm$. For higher acceleration voltages, a stronger electric field above the MLA is needed to focus the beamlet into the blanker plane. Back-of-the-envelope calculations estimate an electric field of $10kV/mm$ to focus a $5kV$ beam in the configuration under analysis. Decreasing the size of the MLA aperture contributes positively to the reduction in the probe size, which reaches its minimum at $5\mu m$ diameter. Apertures smaller than this value are not considered because they are too challenging to be fabricated. Decreasing the working distance also reduces the final probe size: a value of $3mm$ is a reasonable choice to obtain a sufficiently small probe size

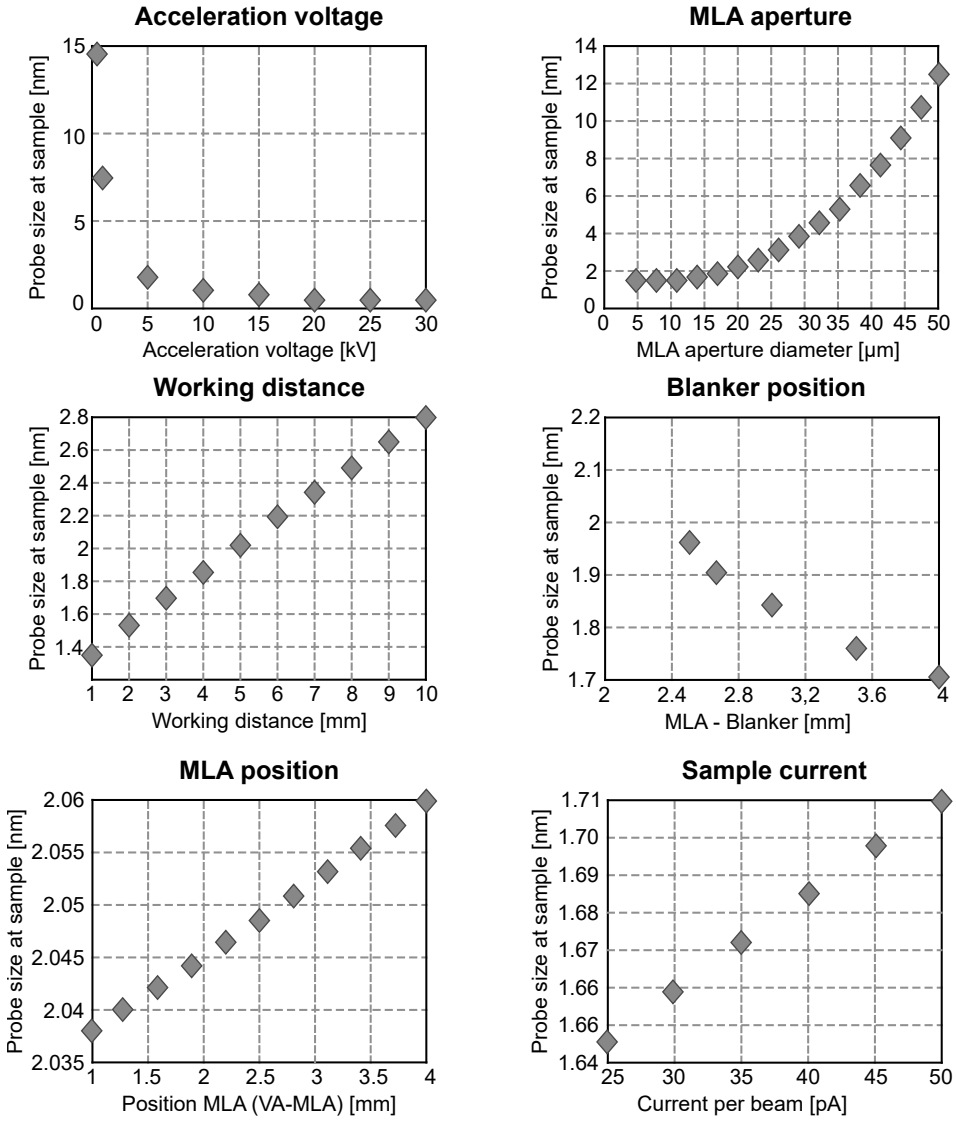

Figure 6.15: Total probe size variation when tuning the key parameters: acceleration voltage, MLA aperture diameter, working distance, blanker position, MLA location from the variable aperture and the beam current.

and being physically able to place a sample that close to the final lens. When the distance between the MLA and the blanker increases, the probe size at the sample decreases. A distance of $4mm$ ensures that the entire module, that also

consists of a set of macro electrodes above the MLA to create the lens effect, can fit the variable aperture port. When the MLA is shifted away from the top side of the variable aperture port, keeping constant the distance between the MLA and the blanker, the probe size increases. Placing the MLA at $4mm$ means that there is enough space for three macro electrodes of thickness $0.5mm$ and three spacers of $0.5mm$. The three macro electrodes could serve as decelerating the beam, creating the lens effect on the MLA and to correct for the field curvature. Lastly, if the sample current decreases, then the probe size at the sample also decreases. Because the main application of this unit is patterning, a higher beam current such as $50pA$ is preferable. Hence, the optimal parameters in table 6.4 are set based on these considerations. The only degree of freedom left in the design of the unit is the opening angle at the sample, that can be tuned by moving the C1 and C2 crossover. This will be discussed in the next section.

Parameter	Value
Current per beam	$50pA$
VA-MLA	$4mm$
Acceleration voltage	$5kV$
MLA aperture	$5\mu m$
Distance MLA - blanker	$4mm$
Working distance	$3mm$
Blanker position	$4mm$

Table 6.4: Optimized settings of the MBU final design.

6.6.2 On-axis performance

With the optimized settings analyzed in paragraph 6.6.1, an analysis of the on-axis performance of the system is performed. For each lens of the system the on-axis aberrations are calculated and demagnified to the sample. Then, the final probe size as the sum of all contributions is calculated. Figure 6.16 shows the total contributions of the on-axis aberrations at the sample: the contributions of all lenses have been summed up in the following way. The geometrical spot size is calculated by multiplying the magnification of all lenses in the system:

$$M_{tot} = M_{C1} \cdot M_{C2} \cdot M_{MLA} \cdot M_{INT} \cdot M_{UHR} \tag{6.21}$$

The d_{source} that is considered here is that of the typical Schottky source, namely approximately 30 nm. The diffraction spot size d_{diff} only depends on the opening angle at the sample and the wavelength of the incoming electron beam, namely the acceleration voltage.

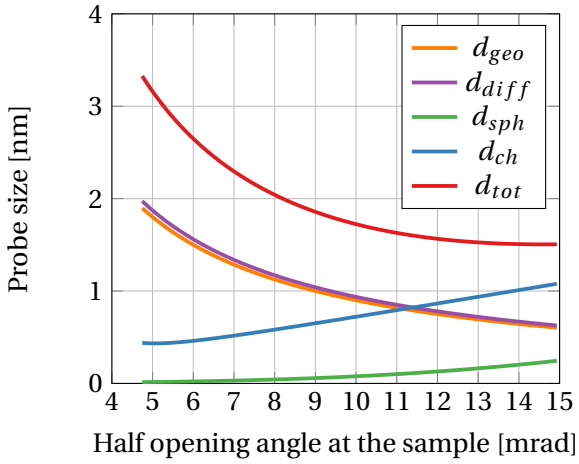

Figure 6.16: Contributions to the probe size at the sample given by the geometrical spot size, the diffraction, the spherical and chromatic aberrations and the total probe size, calculated with equation 6.9, for all lenses.

Figure 6.16 shows the contributions to the probe size and the total probe size, calculated as function of the half opening angle of the central beam at the sample. This was calculated for a FEI Nova Nano Lab 650 column, with the parameters listed in table 6.5.

Parameter	Value
Current per beam	$50pA$
Total probe size	$< 5nm$
Acceleration voltage	$5kV$
MLA aperture	$5\mu m$
Distance MLA - blanker	$4mm$
Working distance	$3mm$

Table 6.5: Parameters for which the contributions to the probe size at the sample and the total probe size are calculated.

Changing the half opening angle at the sample is effectively achieved by changing the strength of the C2 lens, namely the position of the C2 crossover. Because the distance between the MLA and the blanker plate is physically fixed, also the image position of the MLA is fixed. This means that the half opening angle of the beam focused in the blanker plane is fixed.

However, because of the common crossover in the final lens, a stronger C2 lens constrains the INT lens to be weaker. In fact, with a stronger C2 lens, the C2 crossover will be closer to the C2 lens. To image the C2 crossover in the final lens, a weaker INT lens is required. At the same time, a weaker INT lens provides a larger beam size in the final lens, hence a bigger half opening angle at the sample.

If the C2 lens is very strong and the image position is very close to the lens, the INT becomes so weak that its focal length becomes larger than the distance between the blanker and the INT lens, namely the object distance of the INT lens, which will make the INT lens a negative lens. However, a magnetic lens cannot be negative, hence these values cannot be considered. This is the reason why the half opening angle at the sample has a maximum value.

In this case, for the parameters listed in table 6.5, the maximum half opening angle at the sample is approximately $15mrad$. On the other hand, the lower limit of the half opening angle is given by the position of the C2 crossover when it is set to the height of the MBU shielding. The lower the C2 crossover, the smaller the pitch at the blanker, and hence little space is left for wiring. The graph in figure 6.16 shows that in the range 4 to $15mrad$ the total probe size decreases, with a minimum of $1.5nm$ at $14.59mrad$. For small opening angles, the probe size is limited by the geometrical spot size and d_{diff}, while for larger opening angles the chromatic aberrations are dominant.

The probe size depends on the working distance. The higher the sample, the stronger the final lens, the bigger the half opening angle and the smaller the probe size. Figure 6.17 shows how the probe size changes when the working distance is changed. For each value of the working distance, the position of the C2 crossover, hence the half opening angle at the sample, is varied in order to calculate the minimum probe size achievable. In figure 6.17 also the opening angle for which the minimum probe size is calculated is shown. By increasing the working distance, the minimum probe size is found for increased strength of the C2 lens, hence decreased image distance of that lens. In this case, the size of the central beam in the final lens will increase, however the change in working distance is larger and the total effect gives a reduction in half opening

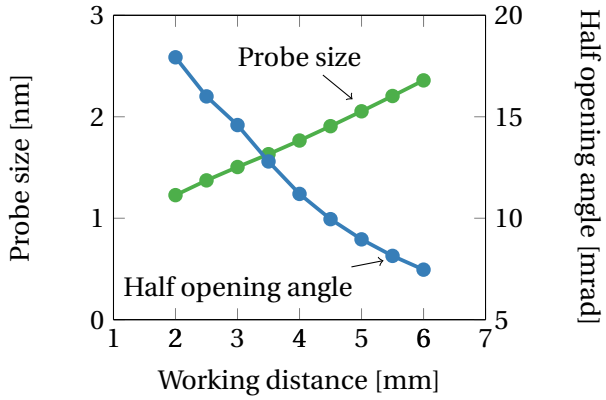

Figure 6.17: Total probe size and half opening angle of the central beam at the sample calculated for different working distance. The total probe size is calculated by summing up all the on axis aberration contributions of all lenses according to equation 6.9.

angle, hence a bigger total spot size.

Figure 6.18 shows the probe current delivered by the central beam for different spot sizes, in case of a $5kV$ beam, with $3mm$ working distance. In this case, the position of the C2 crossover remains constant, meaning that the strength of the INT lens is unchanged because the INT must image the C2 crossover in the coma-free plane of the final lens. In order to increase the current per beam, the illuminated area on the MLA surface needs to be smaller. This is achieved by decreasing the strength of the C1 lens, which is effectively translated into a larger C2 image distance. The beam size in the C2 lens will be therefore smaller, hence a smaller illuminated area at the MLA. Increasing the current this way means increasing the probe size, as depicted in figure 6.18.

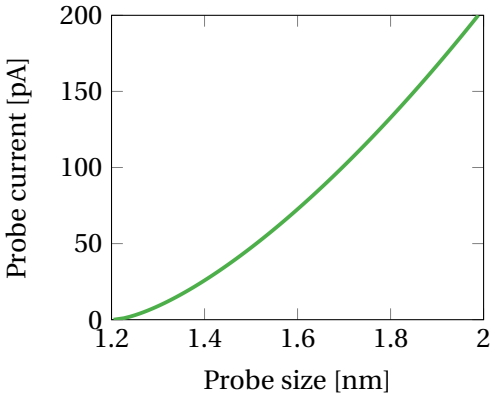

Figure 6.18: Probe current and probe size at the sample. For the same optical geometry, the requirement on the current per beam is changed, from 0 to 200pA, and for each case the total probe size is calculated.

6.7 Final geometry

The analysis of the on-axis aberrations described in section 6.6.2 refers to an optimized configuration, with the parameters listed in table 6.6.

Parameter	Value
MLA aperture	5μm
Distance MLA - blanker	4mm
Working distance	3mm

Table 6.6: Optimized parameters for which the contributions to the probe size at the sample and the total probe size are calculated.

Figure 6.19 shows a cross-section of the Multi Beam Blanker Unit. The outer metal case, which in reality has a circular shape, is grounded and acts as a shield. It also prevents the stack of electrodes to get damaged accidentally. Internally, a stack of three macro electrodes are placed above the MLA and the blanker. The Dec electrode decelerates the beam, E1 provides the zero strength lens to correct for possible field curvature, and E2 creates the lens effect on the MLA. The MLA is positioned 4mm above the blanker.

From the optimized settings discussed in section 6.6.2 for achieving the smallest on axis probe size at the sample, the illuminated area at the MLA is 66μm. It is possible to place the 5μm apertures in any desirable way, on a

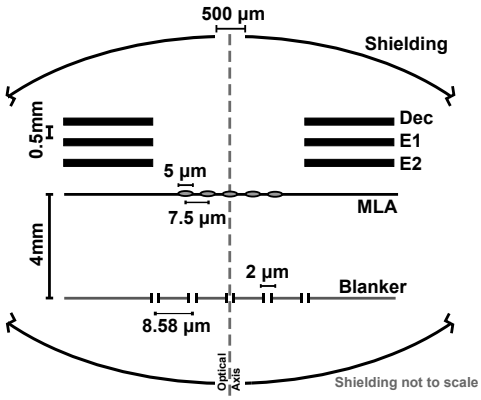

Figure 6.19: Cross-section of the Multi Beam Blanker Unit. The MBU comprises three macro electrodes, i.e. Dec, E1 and E2, the MLA and the blanker. The stack of electrodes is protected by a shielding case at ground potential.

concentric construction or in a hexagonal geometry. We decided to opt for a square array of apertures to allow better stitching. Also, the distance between apertures has to be sufficiently large such that at the blanker plate the spacing is enough to host the wiring. In our design, the MLA has apertures of $5\mu m$ in diameter at a pitch of $7.5\mu m$. This means that at the blanker plane, the pitch becomes $8.58\mu m$. The size of the aperture at the blanker plate is not of importance, as the beams are in that point focussed: as for this point in the design process, apertures of $2\mu m$ are chosen to be of a reasonable dimension. Having set the MLA aperture size and the pitch, and knowing the illuminated area at the MLA, the total number of beamlets in which the single beam is split is an array of 5x5, or 25 beams.

6.7.1 Off-axis performance

When dealing with multi-beam systems, off-axis aberrations are of importance as they deeply affect the performance of the system. Off-axis aberrations are caused by the charged-particle beams that are travelling far from the optical axis, and the outermost beam is the one that is most affected.

Figure 6.20a shows an off-axis beam travelling through a lens, which focuses it on the image plane on the right. The off-axis beam is described by the off-axis object position $h(i, j)$, which is the distance between the optical axis and the object, the half opening angle α and the position where the beam crosses the optical axis, or also called the aperture position, Z_a. Figure 6.20b

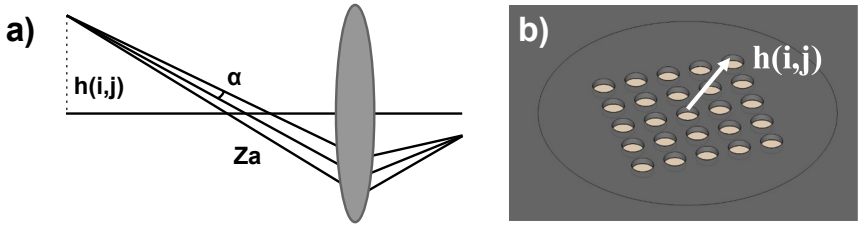

Figure 6.20: a) An off-axis beam travelling through a lens is characterized by the height of the object $h(i,j)$, the half opening angle α and the position where it crosses the optical axis, namely the aperture position, Z_a. b) Definition of the height of a beam for a lens when calculating the off-axis aberrations.

shows the outermost beam position on the MLA plate, which is the beam on one of the corners of the 5x5 array of apertures. The off-axis aberration contributions consist of *astigmatism, field curvature, coma* and *chromatic magnification error*. These can be calculated according to equations 6.22, 6.23, 6.24 and 6.25 [45]. Once these contributions are calculated, it is possible to sum them up as shown in equation 6.26.

$$\frac{d_{AS}(i,j)}{M} = \sqrt{2}h(i,j)^2\alpha\sqrt{C_a^2 + c_a^2} \tag{6.22}$$

$$\frac{d_{FC}(i,j)}{M} = \sqrt{2}h(i,j)^2\alpha|D_a + C_a| \tag{6.23}$$

$$\frac{d_{CO}(i,j)}{M} = h(i,j)\alpha^2\sqrt{F_a^2 + f_a^2} \tag{6.24}$$

$$\frac{d_{CM}(i,j)}{M} = h(i,j)\frac{\Delta E_{50}}{U}\sqrt{C_{Da}^2 + C_{\Theta a}^2} \tag{6.25}$$

$$d_{off-axis}(i,j) = \sqrt{d_{AS}(i,j)^2 + d_{FC}(i,j)^2 + d_{CO}(i,j)^2 + d_{CM}(i,j)^2} \tag{6.26}$$

$$d_{tot}(i,j) = \sqrt{d_{off-axis}(i,j)^2 + d_{on-axis}^2} \tag{6.27}$$

Where α is the half opening angle of the beam, M the magnification of the lens shown in figure 6.20a. h is the height of the beam on the MLA, as depicted

in figure 6.20b. C_a, c_a, D_a, F_a, f_a, C_{Da} and $C_{\Theta a}$ are the off-axis aberration coefficients for astigmatism, field curvature, coma and chromatic aberrations. These coefficients are calculated by simulating the actual lenses with a finite element simulation package EOD [167].

With the optical system designed in section 6.6, only the INT lens and UHR lens contribute to the off-axis probe size. As a matter of fact, the object position of the beams travelling in the C1 lens and C2 lens is on the optical axis, hence $h(i, j) = 0$. The off-axis aberrations coefficients are calculated by simulating the INT lens and the UHR lens with the EOD simulation program.

Figure 6.21 shows the off-axis contributions to the probe size of the combination of the INT lens and UHR lens and the total off-axis probe size resulting from equation 6.26 as function of the half opening angle of the beamlet at the sample. The outermost beam is considered, namely the beam on the corner of the 5x5 array. The total off-axis probe size decreases significantly with the half opening angle. The half opening angle on the object side is constant because of the fixed geometry of the multi beam unit. However, to increase the half opening angle at the sample, the image position of the C2 lens is decreased, meaning closer to the lens. In order to have a system in which each beamlet delivers $50pA$ of current, the C1 lens needs to be weaker: this way the illuminated area at the MLA plate will be constant. The pitch between the beams will then change at the blanker plate: as the half opening angle of the beams at the sample increases, the pitch at the blanker decreases exponentially. Therefore, the height of the outermost beam, namely its distance to the optical axis decreases, resulting in smaller off-axis aberration contributions.

Figure 6.22 shows the off-axis aberration contributions of the combination of the INT and UHR lenses and the total off-axis probe size calculated from equation 6.26 for different working distances. In this case, however, the pitch between the beamlets decreases and becomes constant for a working distance of $3.5mm$, which explains why the total off-axis probe size decreases for small working distance. However, when the working distance increases the magnification of the virtual lens consisting of the sum effects of the INT lens and the UHR lens increases. This explains why the field curvature increases with large working distance and therefore the trend of the total off-axis probe size.

Figure 6.23 shows the total on-axis probe size and the total off-axis probe size for different working distance values. The total probe size is then calcu-

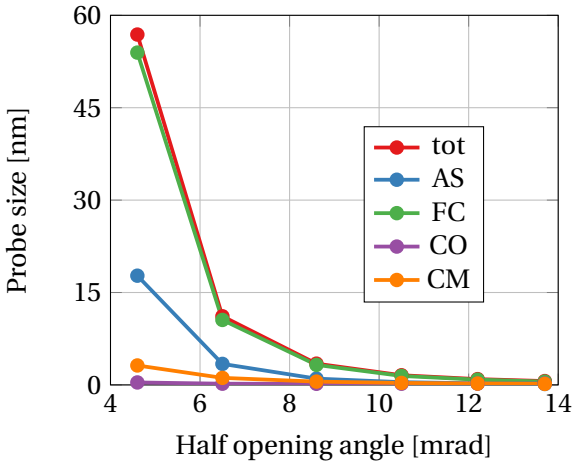

Figure 6.21: Off-axis aberration contributions to the probe size of the combination of the INT and UHR lenses calculated at the image side, namely at the sample and total off-axis probe size resulting from equation 6.26 for different half opening angle of the beam at the sample.

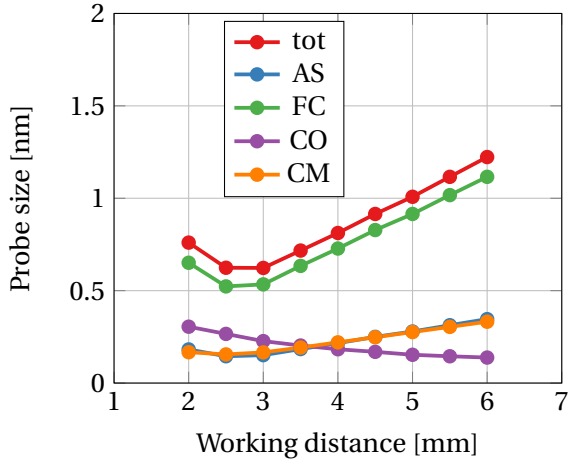

Figure 6.22: Off-axis contributions to the probe size of the combination of the INT and UHR lenses and total off-axis probe size resulting from equation 6.26. The trend of the total probe side has a minimum around $3mm$ working distance as a consequence of a decreasing pitch at the blanker for small values of working distance and an increasing magnification of the virtual lens, which is obtained by combining the effect of INT and UHR.

lated as the root sum squared of the on-axis and off-axis total probe sizes. The smaller the working distance, the smaller the total probe size. If the initial set-

tings are considered, with which the working distance was set to $3mm$, the total off-axis size is $0.7nm$, that are summed to the on-axis probe size, that is equal to $1.5nm$, resulting in a total probe size of the outermost beam of $1.6nm$.

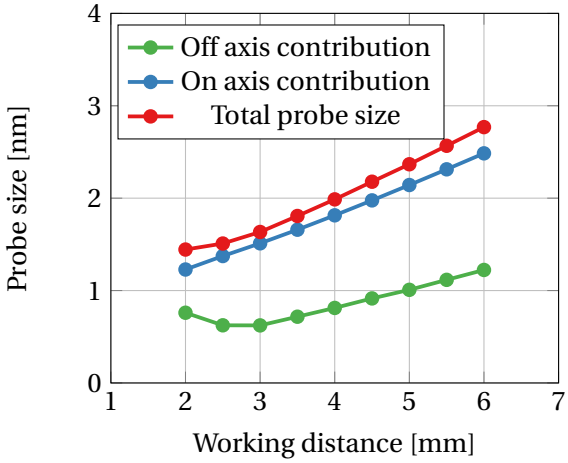

Figure 6.23: Off-axis total probe size of the outermost beam in the 5x5 MBU, on-axis total probe size and the total probe size as the root sum squared of the first two.

6.8 Simulations with EOD

The multi beam unit is simulated using the program EOD. The geometry of the MBU in EOD is schematically shown in figure 6.24. The MBU consists of two plates at each side of the unit at ground potential, the shielding in dark blue. Three sets of electrodes with a hole of radius $300\mu m$ are placed above the beam splitting plate (MLA). The first electrode, depicted in orange in figure 6.24, decelerates the beam and is therefore called *Dec*. The second electrode *E1* shapes the beam to minimize the effect of field curvature for all lenses in the column. This electrode is shown as the cyrillian plate in figure 6.24. The last electrode *E2*, which is the green plate, provides the lens effect on the MLA and its voltage is calculated via EOD in order to focus the beam in the blanker plane. The MLA is the red plate and has a central hole of $5\mu m$ in diameter. In order to have a focus plane on the blanker plate (in z = -250.9 mm) for an object positioned in the C2 crossover (in z = 282 mm), the voltages listed in table 6.7 need to be applied to the electrodes.

Figure 6.25 shows the beam potential in the multi beam unit. The beam en-

Electrode	Voltage
Shielding	$0V$
Dec	$-1.5kV$
E1	$1kV$
E2	$4.846kV$
MLA	$0V$

Table 6.7: Parameters for which the contributions to the probe size at the sample and the total probe size are calculated.

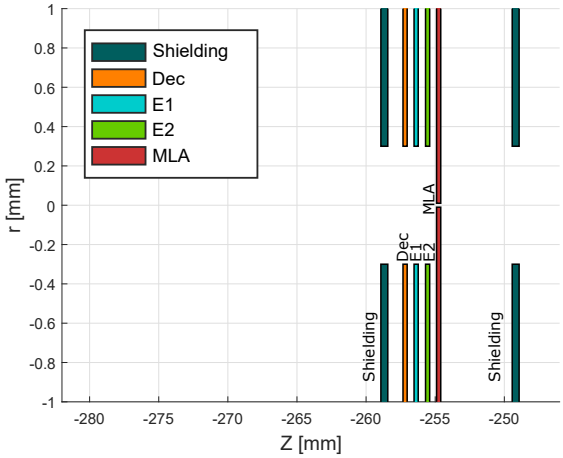

Figure 6.24: Schematics of the MBU as set in EOD. The dark blue plates represent the shielding, that is at ground potential. From the left, the Dec, the E1 and E2 macro electrodes, and the MLA.

ters the unit with an acceleration voltage of $5kV$ and is decelerated by the Dec lens to approximately $3.5kV$. The beam is further accelerated by E1 and E2 to approximately $9.5kV$. The beam is focused on the blanker plane by means of the lens effect on the MLA aperture.

Figure 6.26 shows the ray tracing of the on-axis beam at $5kV$, from the C2 crossover to beyond the MBU unit. When the beam is under the influence of the Dec lens, it starts diverging, because Dec is a negative lens. The combined positive lenses of E1 and E2 make the beam converging to the blanker plane. Figure 6.27 shows the five off-axis beams traveling from the C2 crossover to beyond the MLA unit.

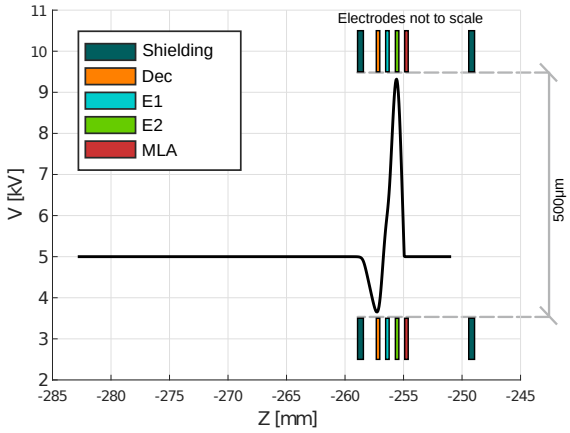

Figure 6.25: Acceleration voltage of the beam when entering the MBU. The initial value of the beam energy is $5kV$, the beam is then decelerated by the Dec lens and subsequently accelerated by E1 and E2, to be focused on the blanker plane.

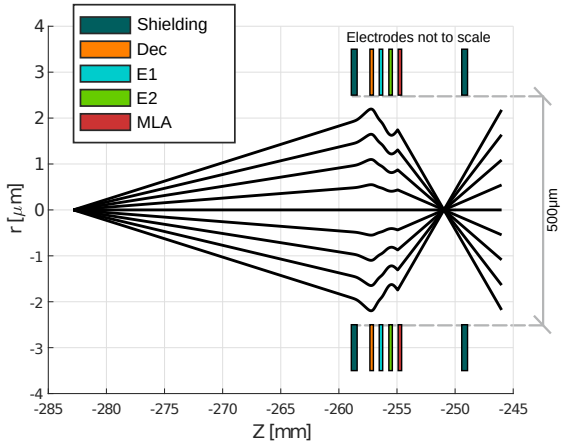

Figure 6.26: Electron ray tracing of a $5kV$ beam from the C2 crossover into the MBU. The size of the ray-traced trajectories is adjusted to the size of the graph.

6.9 Field Curvature

The Field Curvature is an off-axis aberration that derives from the fact that the electric or magnetic field is non uniform along the r-axis, which is the perpen-

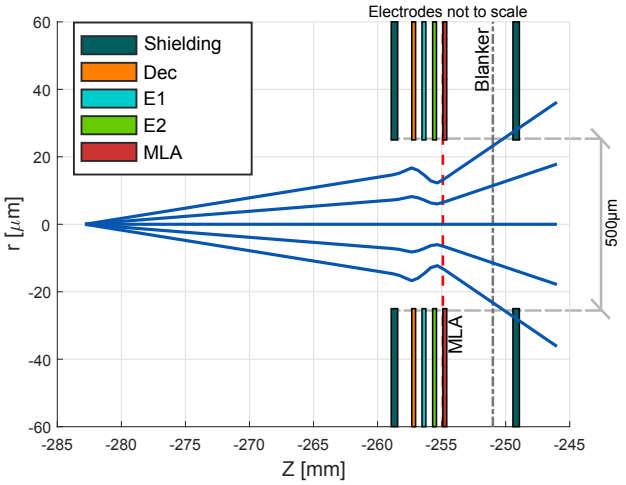

Figure 6.27: Electron ray tracing of the $5kV$ beams from the C2 crossover into the MBU. The size of ray tracing is adjusted to the size of the graph.

dicular axis to the optical axis. This means that beams that are travelling more off-axis will have a smaller image distance. In case of the MLA in the 5x5 multi beam unit, the field curvature rises when the electric field given by the electrode E2 is non uniform above the MLA plane. Therefore the strength of the lenses increases with the distance of the lens to the optical axis. The lens effect of the central aperture will be effectively weaker than the lens effect of the outermost lens. The designed multi beam unit (MBU) is simulated with the electron optics simulation program EOD. The geometry of the macro electrodes, the multi beam aperture array (MLA) and the shielding can be inserted in an input file and the electric field can be calculated, given the potential on each electrode, as described in section 6.8.

For the field curvature, we are mainly interested in the axial field E_z, which is the electric field component parallel to the optical axis, as function of the perpendicular axis r, which represents the height on the MLA plate. Figure 6.28 shows the simulated z-component of the electric field as function of the height on the MLA plate, on a plane $60\mu m$ above the MLA plate itself. The z-component of the electric field is weaker at position 0, which is the optical axis, and increases for increasing distances. From the electric field it is possible to approximately calculate the focal length of the MLA lens, according to equation 6.28, which is shown in figure 6.29.

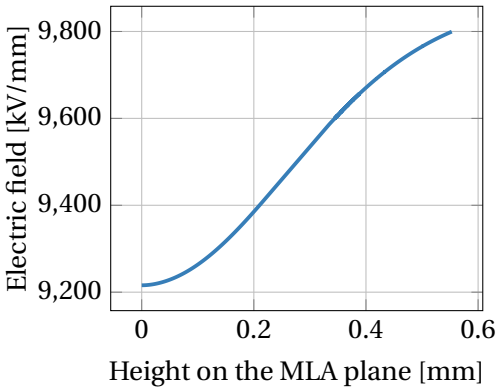

Figure 6.28: Z component of the electric field, where z is the optical axis, as function of the height on the MLA plane, calculated on a plane $60\mu m$ above the MLA plane itself. The electric field is calculated by using the simulation program EOD.

$$f_{MLA} = \frac{4U_a}{E_z} \tag{6.28}$$

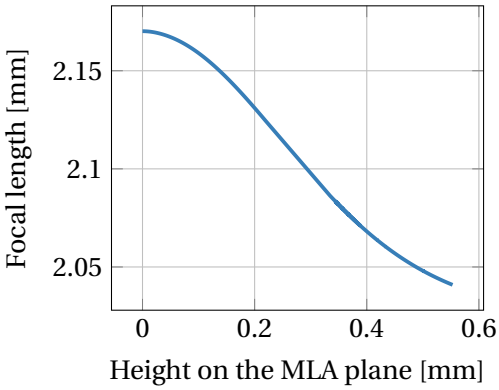

Figure 6.29: Focal length of the MLA calculated from the electric field in figure 6.28 using equation (6.28), for U_a equal to $5kV$.

In our case, we will have an array of 5x5 beams, the aperture array diameter is $5\mu m$, with a pitch of $7.5\mu m$. The centre of the outermost aperture is then positioned approximately $21.2\mu m$ from the centre, which means that we are interested in the axial electric field only in the range from the optical axis to approximately $25\mu m$ from the optical axis. From the focal length, equation 6.29 gives the image position of the MLA lenses, which is shown in figure 6.30.

$$i_{MLA} = \frac{1}{\frac{1}{f_{MLA}} - \frac{1}{o_{MLA}}} \tag{6.29}$$

Where o_{MLA} is the distance between $C2_{Crossover}$ and the MLA.

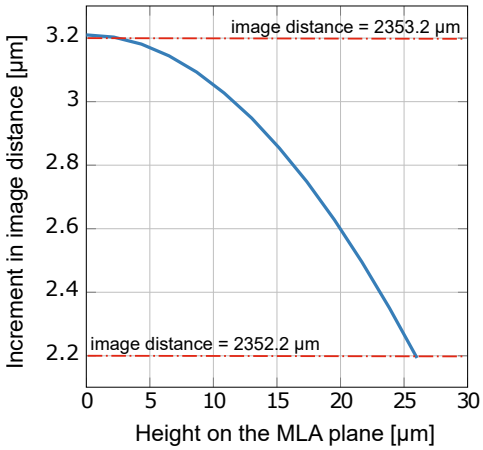

Figure 6.30: Image distance of the MLA calculated from the focal length of the MLA lens in figure 6.29, using equation (6.29). The scale of the y axis is in μm and shows the increment in the image distance, which is approximately $1\mu m$. The image distance at the center of the MLA plane is $2353.2\mu m$ and it decreases to $2352.2\mu m$ at a height of $26\mu m$ from the center of the MLA plane.

Once the image distance of the MLA lens for different heights on the MLA plane is known, it is possible to calculate the image position of the UHR lens, that derives from the field curvature on the MLA plane. The image position of the MLA is the object position of the INT lens, which allows to calculate the image position of this lens, which is the object position of the objective lens. Finally, the image position of the objective lens can be calculated. Figure 6.31 shows the UHR image distance difference at the sample, simply calculated with equation 6.30. Effectively, the effect of the field curvature at the MLA is very small at the sample, as the image difference is in the order of a few nanometers.

$$\delta i_{UHR} = i_{UHR}(r) - i_{UHR}(0) \tag{6.30}$$

Figure 6.32 shows the contribution to the probe size in nm of the field curvature on the MLA plane, demagnified at the sample by the INT and UHR lenses. The contribution can be considered very small and negligible.

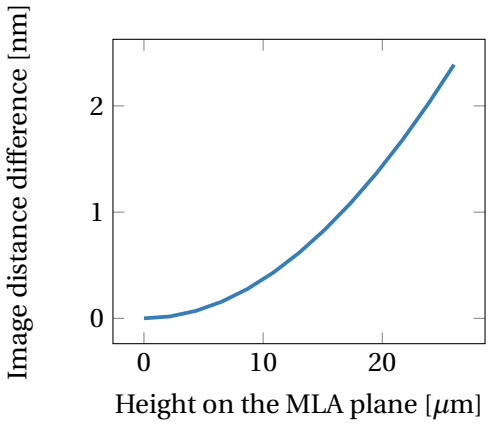

Figure 6.31: Image distance of the UHR lens affected by the field curvature on the MLA plate for different height on the MLA plate.

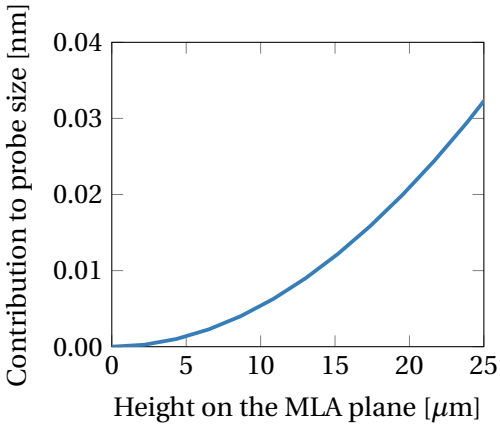

Figure 6.32: Contribution to the probe size given by the field curvature on the MLA plane, calculated at the sample, after being demagnified by the INT and UHR lenses.

Figure 6.33 shows the contribution to the probe size of the field curvature introduced by the combined INT and UHR lenses for different height on the MLA plane. These lenses are first simulated with the EOD program in order to estimate the field curvature coefficients D_a and C_a. The contribution to the probe size is calculated using equation 6.31, considering as height of the object the actual height of the beams in the blanker plane. This contribution is also rather small and negligible.

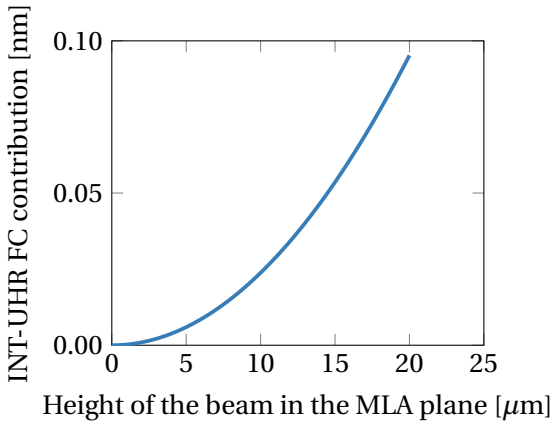

Figure 6.33: Contribution to the probe size given by the field curvature in the combined INT and UHR lenses. The field curvature coefficients is estimated using the simulation program EOD and further elaborated.

$$\frac{d_{FC}(i,j)}{M} = \sqrt{2}h(i,j)^2\alpha|D_a + C_a| \tag{6.31}$$

In conclusion, the effect of the field curvature on the total probe size is very small. The field curvature can be fine tuned with the combination of E1 and E2 lenses. Because the effect is small and the correction non necessary, E1 can be taken out of the design. To create the zero-strength effect, where the off-axis beams are not deflected to avoid chromatic deflection errors, the Dec and E2 electrodes can be fine tuned.

6.10 Coulomb interactions

Using equations 6.12 to 6.20, it is possible to calculate the stochastic Coulomb interactions of the multi beam SEM. First, the optical system needs to be divided into segments, as shown in figure 6.34. The first segment $S1$ is the source, while $S2$ comprises the optical path between C1 and C2 lenses and $S3$ between C2 lens and the MLA. From beyond the MLA down to the sample, the beam is split into 25 beams, that are travelling together, overlapping in most of the path. In this part of the microscope, the above-mentioned formulas cannot be used. In order to get an approximation of the Coulomb interactions also in this part of the column, a pessimistic simplification of the system is done by assuming that instead of 25 beams partially overlapping from the MLA to the sample, there is

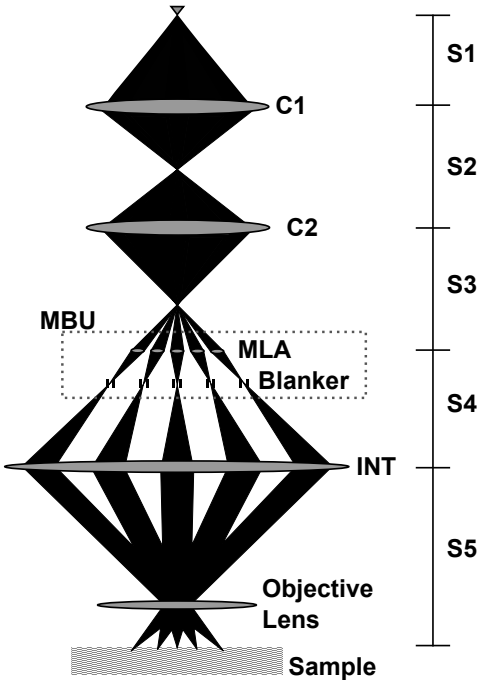

Figure 6.34: The optical column is divided into five segments for which the statistical Coulomb interactions are calculated.

only one beam delivering 25 times the current delivered by one beamlet. This is of course a pessimistic approximation, as the real current density will be lower than what is here considered. By calculating the trajectory displacement for all segments and for all regimes, the result is that the dominant regime is the pencil beam regime, for all segments.

Figure 6.35 shows the contribution to the probe size of the trajectory displacement of each lens, demagnified at the sample. This means that for each segment the FW50 radius given by the pencil beam equation 6.15 is further multiplied by the total magnification of the lenses below that segment. Segments S2 and S3 have a sharp change in slope. This is explained by the presence of a beam current limiting aperture below the Coulomb tube with diameter 250 μm, that cuts the beam for half opening angles at the sample smaller than approximately $7.5 mrad$. If the aperture would be removed, the contributions from S2 and S3 would exponentially decrease with the half opening angle at the sample. For half opening angles smaller than $7.5 mrad$, the dominant regime is still pencil beam and the trajectory displacement decreases because the half opening angles of the beam after C1 and C2 lenses decreases. The biggest con-

tribution comes from the last segment, namely that consisting of the INT and UHR lens, because it is not demagnified by any lens before reaching the sample.

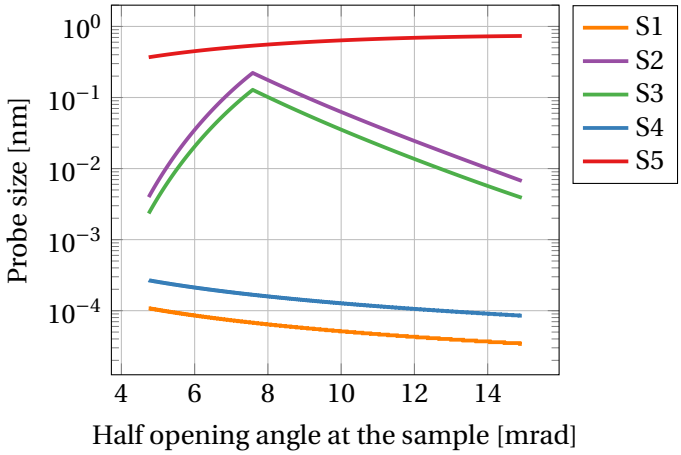

Figure 6.35: Probe size contribution due to trajectory displacement.

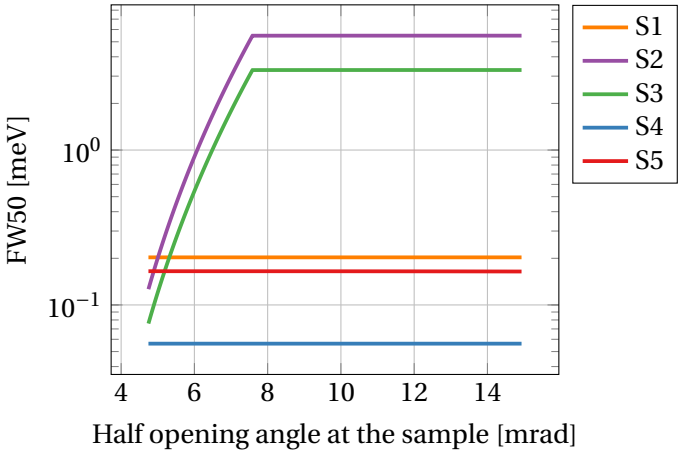

Figure 6.36: The Full-width containing 50% of the energy distribution due to the Boersch effect.

Nevertheless, the total FW50 probe contribution at the sample is smaller than $1nm$. Figure 6.36 shows the energy spread calculated for each segment. Here we can notice that the graphs of $S2$ and $S3$ are not constant after a half opening angle of approximately $7.5mrad$, which is caused by the cut-off of the

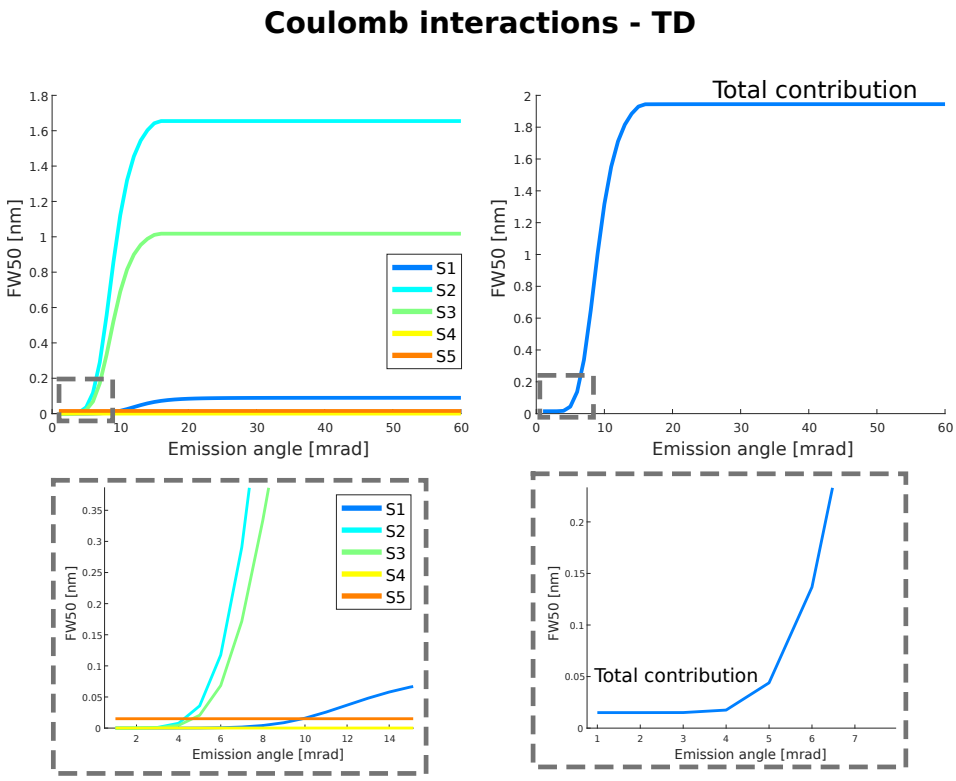

Figure 6.37: Trajectory displacement of the 5 segments described in figure 6.34 (right) and total contribution calculated with the root mean square method.

current at the C2 aperture. When the beam is cut, for both S2 and S3 segments the total allowed current increases with the half opening angle at the sample, and, because pencil beam is the dominant regime, the energy spread goes with the second power of the current. After $7.5 mrad$, the beam is not cut by the aperture anymore and the energy spread becomes constant because the allowed current then is constant. The contribution to the energy spread from segment S4 and S5, where the dominant regime is pencil beam, is constant because the current of the beam is kept constant. Moreover, $S4$ and $S5$ are not influenced by this cut-off because the total current in the central beam is forced to be 25 times the required current at the sample ($50 pA$) for each half opening angle. The energy spread caused by the Boersch effect is really small and will not negatively influence the performance of the system.

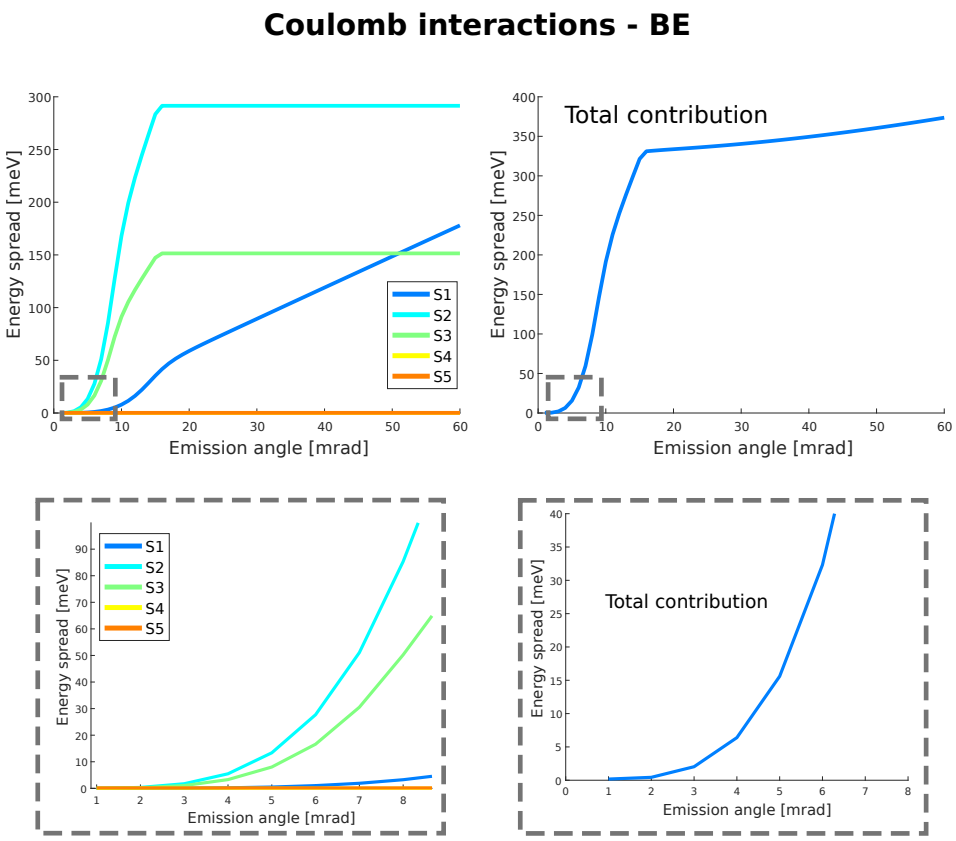

Figure 6.38: Energy spread of the 5 segments described in figure 6.34 (right) and total contribution calculated with the root mean square method.

The number of beams can be increased if a larger emission angle is chosen, at the cost of decreased system performance due to Coulomb interactions, as described in section 6.4. For this system, where the emission angle is kept at $4mrad$, the effects of trajectory displacement and Boersch effect are negligible. Figures 6.37 and 6.38 show the trajectory displacement (TD) and the energy spread (BE) for the optimized system, where the half opening angle at the sample is approximately $14mrad$, calculated for different emission angles, from $1mrad$ up to $60mrad$. The TD contributions are de-magnified to the sample and the total contributions shown in figures 6.37 and 6.38 are calculated with the root mean square method. The main contributors are segments S2 and S3 for both TD and BE and for an emission angle of $20mrad$ the TD becomes $2nm$, while the BE is approximately $400meV$.

6.11 Blanker design

The idea behind a new design of a multi-beam SEM is to integrate a blanker array, which allows individual blanking of every beam in the system. Because in the present 196 multi-beam SEM the only reasonable place to position the blanker is in the source, it was never possible to have it integrated, because of the challenge to fit all the 197 feedthroughs (196 driving signal plus the ground) in the nasty environment in the source module, where the beam splitting optics is located, that is at high tension and high vacuum. Mainly for this reason, a new design of beam splitting and blanking optics started. In the new concept of a multi beam unit (MBU) the blanker plate is located $4mm$ below the multi beam aperture lens array (MLA), which is placed below a stack of three macro electrodes, as shown in figure 6.39. The size of the apertures on the MLA is $5\mu m$ and the pitch is $7.5\mu m$. The pitch at the blanker becomes $8.58\mu m$ in order to have the minimum axial probe size at the sample, for $5kV$ beamlets each delivering $50pA$ at the sample, with $3mm$ working distance. To achieve this, the C2 crossover needs to be located at approximately $53mm$ from the C2 lens, which is translated into a half opening angle of $14.59mrad$ at the sample.

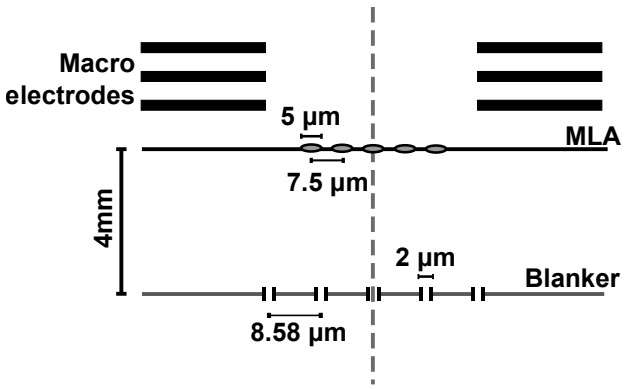

Figure 6.39: Schematics of the multi beam unit, consisting of a set of three macro electrodes, a multi beam aperture lens array (MLA) and a blanker plate. The aperture size at the MLA is $5\mu m$, while the pitch is $7.5\mu m$. At the blanker the pitch is fixed to $8.58\mu m$, because of the fixed position of the C2 crossover, providing at the sample the minimum probe size.

In order to blank a beam, the blanker unit needs to be activated by sending a signal to a deflector, which will create an electric field that will deflect the beam. The beam can be stopped, for instance, on a beam stop aperture located in the final objective lens. This is an easy accessible location and the aperture

can be easily mounted on the pole piece of any microscope. Such a geometry is shown in figure 6.40, where the red beam represents the deflected beam that is stopped onto the beam stop aperture. In such configuration, the deflecting angle at the blanker needs to be sufficiently big to get the beam stopped on a relatively large aperture, that is easy to mount and to align in the microscope.

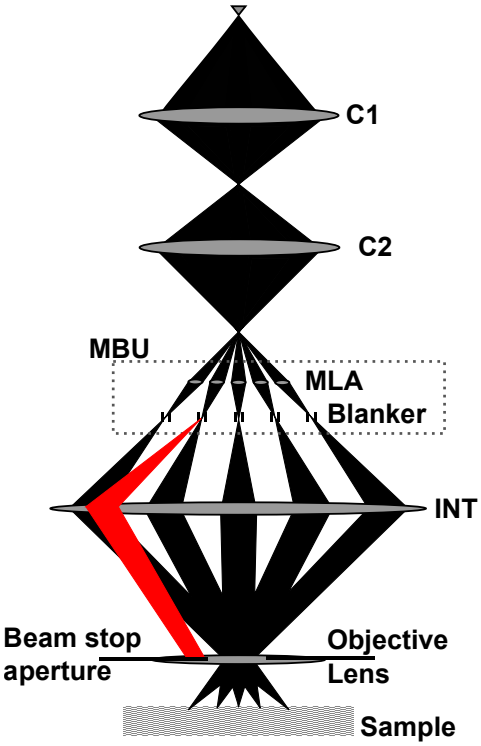

Figure 6.40: Electron optics schematic of an SEM with the developed multi beam unit inserted in the variable aperture port. The red trajectory is one of the beamlets that gets deflected by the blanker and stops at the aperture in the objective lens. The black trajectory is the path of the other beams, that have a common crossover in the final objective lens.

The blankers are at a pitch of $8.58\mu m$, which is very small. In such limited space, the two deflecting electrodes need to be positioned and their wiring as well. Figure 6.41a shows the case in which the separation between the blanking electrodes is $2\mu m$, with $2\mu m$ wide electrodes: here there is only $2.58\mu m$ left for the wiring. This issue can be solved by designing multi-layer wiring, with a sufficiently thick oxide layer in between to avoid breakdowns.

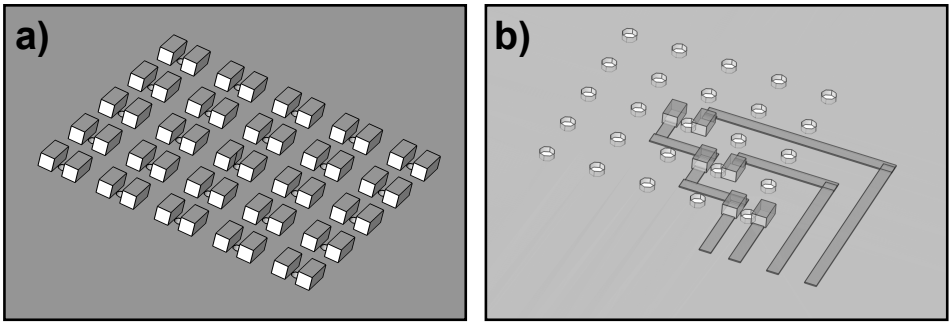

Figure 6.41: a) 3D image of the proposed blanker array, where only the deflecting electrodes are visible. The connecting wires can be designed one on top of the other because of the limited inter-space. b) 3D image of the simulated blankers. Only the central beam and the two positioned diagonally from the central one will be deflected. Outside the blanker array, there is a macro blanker for the deflection of all beams, such that effectively the micro blanker that is switched on will bring back that beam on the sample.

So, ideally we would like to have an array of 5x5 deflectors. To avoid the control electronics of 25 deflectors, and for a proof of concept experiment, however, we decided to adopt a much easier configuration, that is more feasible to fabricate. The blanker array will only integrate 3 deflecting pairs of electrodes, one on the central beam and two on the diagonally positioned beams, as shown in figure 6.41b. This way, the number of connecting wires will be much less, only 4, considering the 3 driving signals and the common ground. In order to simplify the design even more, the grounding electrodes are all connected together to the same ground feedthrough. Now that the requirements are less strict, spacing between the electrodes can be slightly bigger, $2.5\mu m$. This will make the fabrication process much easier. Having only three blankers means that we can switch-off only three beams, while the others are focused on the sample. For practical reasons, a macro blanker is positioned outside the blanker array, that will deflect all the beams and all the beams will be stopped at the aperture. By switching on a micro blanker, it will be possible to bring back one beam at a time on the sample, and eventually measure its probe size and current. The macro blanker can be designed with a thin electrodes design, that uses the electric field fringes to deflect the beams [168]. The main reason to do so is because the height of such electrodes is then the same as that of the electrodes in the blanker array, shortening the fabrication process.

The blanker plate will be mounted on the bottom side of the rigid support that holds the MLA and the three macro electrodes on the top. In order to avoid the device to be damaged during the stacking process, the blanker plate will be mounted upside down, meaning that the electrodes do not face the incoming beams. Figure 6.42 shows the schematics of the blanker plate: the blanker plate is mounted upside down and the incoming beams will only see the backside of the plate. Figure 6.42a also shows in green the macro electrodes and in yellow the micro electrodes, that are positioned only around three beamlets.

The macro and micro deflectors can be switched on individually. Figure 6.42b shows on the left the case in which the macro deflector is switched on, deflecting all the beams, while on the right the case in which only one of the micro deflectors is switched on, and therefore only that beam is deflected. The idea is that we use the combination of the macro and micro electrodes to get only one beam down, as shown in figure 6.42c. All the beams are here deflected because the macro deflector is switched on, however the central beam is deflected back by the micro deflector, that generates effectively an electric field with opposite sign than the macro deflector.

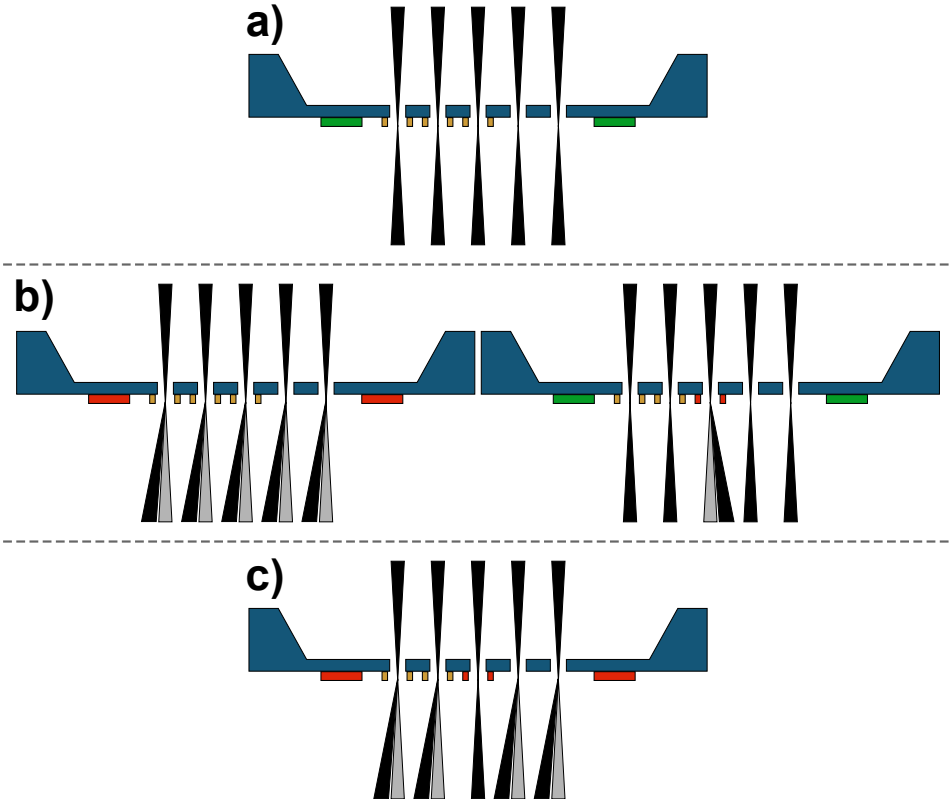

Figure 6.42: a) Schematics of the geometry of the blanker plate. The electrodes are located on the bottom side of the blanker plate. The macro electrodes are here depicted in green while the micro deflectors are depicted in orange. b) Schematics of the blanker array when the macro electrodes are switched on deflecting all the beams to the left and when one of the micro electrode is switched on, deflecting only one beam to the right. c) Schematics of the blanker when the macro electrode and one of the micro electrodes are switched on. In this case all the beams are deflected by the macro blanker and one is pushed back on its original trajectory by its micro blanker.

6.11.1 Simulation of the blanker in COMSOL

The design of the blanker is simulated using the software COMSOL [169], where the *electrostatic* package is used for the calculation of the electric field generated by the deflecting electrodes and the *charged particle tracing* is used for the electron particle tracing. The 2D simulation package is used for the simulation of the macro blanker and the central micro blanker in the configuration shown in figure 6.43. The macro electrodes are positioned outside the array of blankers, with a spacing in between of $150\mu m$. Each electrode is $250\mu m$ wide and $2\mu m$ high. In this case, the beam is not deflected by the field in between the plates but by the fringes of the electric field that are located below the blanker plate. The central beam blanker consists of two electrodes, separated by $2.5\mu m$. Each electrode is $2\mu m$ high and $2\mu m$ wide.

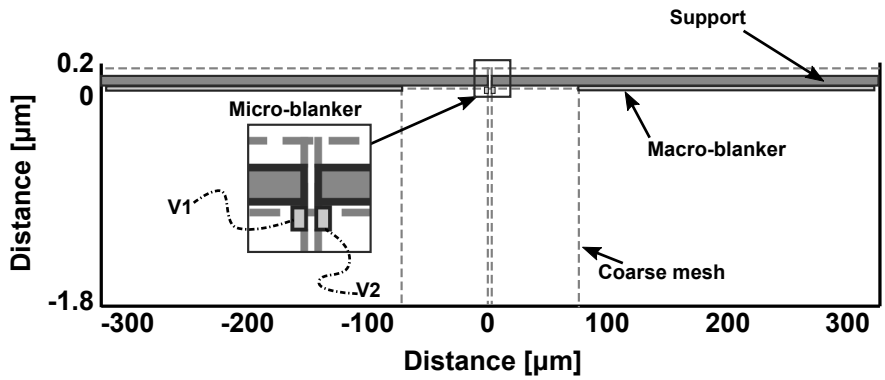

Figure 6.43: Simulated geometry of the macro blanker in combination with the micro blanker.

First, the electric field and the particle trajectory of the central beam micro blanker is tested, when a blanking voltage is applied to one of the electrodes. Figure 6.44 shows the trajectory of the beam particle for different deflecting voltages, ranging from $10V$ to $30V$ with a step of $5V$. The deflection angles and the deflection of the particle in the objective lens are calculated and are shown in figure 6.45.

In case of the macro blanker, it is possible to either apply symmetric voltages to both electrodes, for instance $+50V$ to one electrode and $-50V$ to the second, or ground one electrode and apply the blanking voltage only to the second electrode, for instance $+100V$. Effectively, the result should be the same. Figures 6.46 and 6.47 show respectively the central beam particle trajectory and

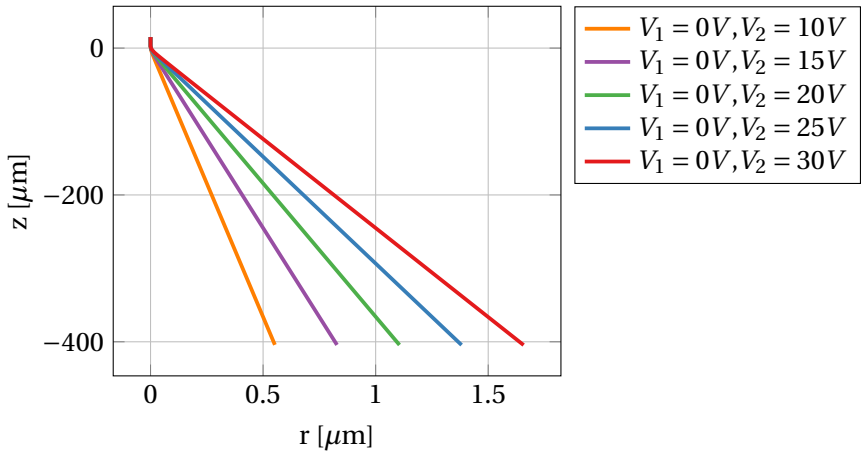

Figure 6.44: Particle trajectory of the central beam when its micro blanker is switched on with different voltages.

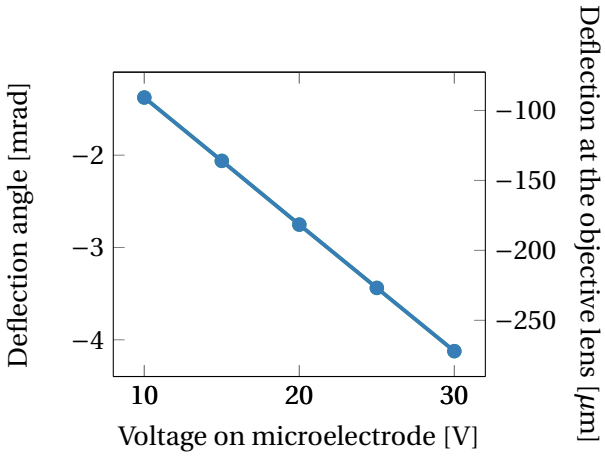

Figure 6.45: Deflection angle at the blanker and total deflection at the objective lens for different blanking voltages V2, while V1 is zero.

its deflection angle and the deflection at the objective lens for symmetric blanking voltages. The applied blanking voltages range in between $\pm 30V$ to $\pm 50V$, with a step of $5V$. The y-axis is the same as in figure 6.44 and it is noticeable that the deflection of the beams extends to a large spatial length.

Figure 6.48 and 6.49 show respectively the central beam trajectory and the

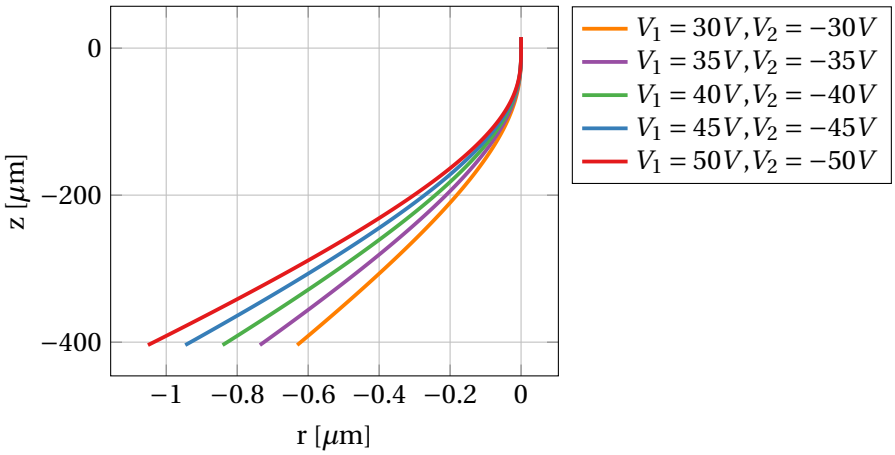

Figure 6.46: Particle trajectory of the central beam when the macro blanker is switched on with different blanking voltages.

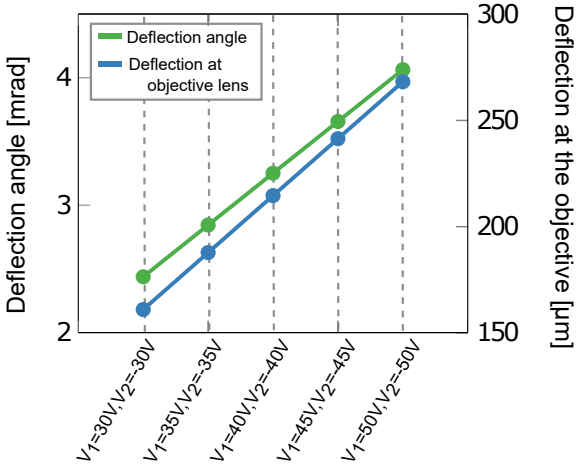

Figure 6.47: Deflection angle and total deflection at the objective lens of the central beam for different blanking voltages on the macro blanker.

deflection angle at the blanker plane and the deflection at the objective lens when an asymmetric field is applied. The blanking voltages range from $60V$ to $100V$, with a step of $10V$. Basically the two modes, namely the symmetric and asymmetric blanking voltages, provide the same deflection angle.

Once the macro blanker and the micro blanker are evaluated individually,

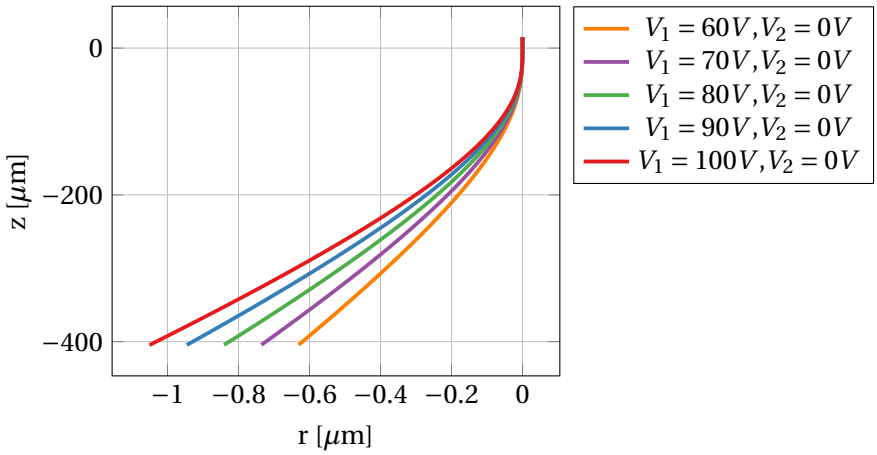

Figure 6.48: Particle trajectory of the central beam when the macro blanker is switched on with different blanking voltages.

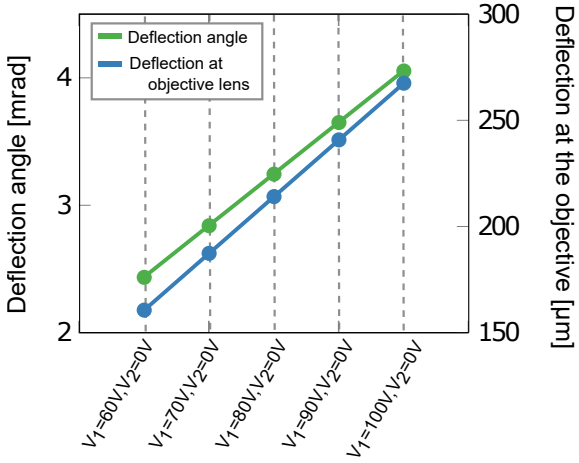

Figure 6.49: Deflection angle and total deflection at the objective lens of the central beam for different blanking voltages on the macro blanker.

it is possible to simulate the case in which both blankers are switched on simultaneously. Figures 6.50 and 6.51 show respectively the central beam particle trajectories when a blanking voltage of $\pm 40V$ and $\pm 50V$ is applied on the macro deflecting electrodes for different blanking voltages applied to the micro blanking electrodes. The effect of such simultaneous blanking is that the micro blanker effectively cancels the deflection caused by the macro deflector for that

particular beam, hence its deflection angle and the deflection at the objective lens should be both zero. Figure 6.52 shows the deflection angle for both macro electrode blanking voltages, for the considered micro blanker voltages. In case of $\pm 40V$ the deflection angle is zero when $30V$ is applied to the micro blanker. On the other hand, for $\pm 50V$ macro electrodes blanking voltage, the deflection angle is zero for a much higher voltage, in between $35V$ and $40V$. Having a larger macro electrodes blanking voltage allows a larger aperture size, that is easier to make and to install. However, in order to have a zero deflection angle for the central beam, a large field needs to be applied at the micro deflector, introducing possibly flashovers and other unwanted effects.

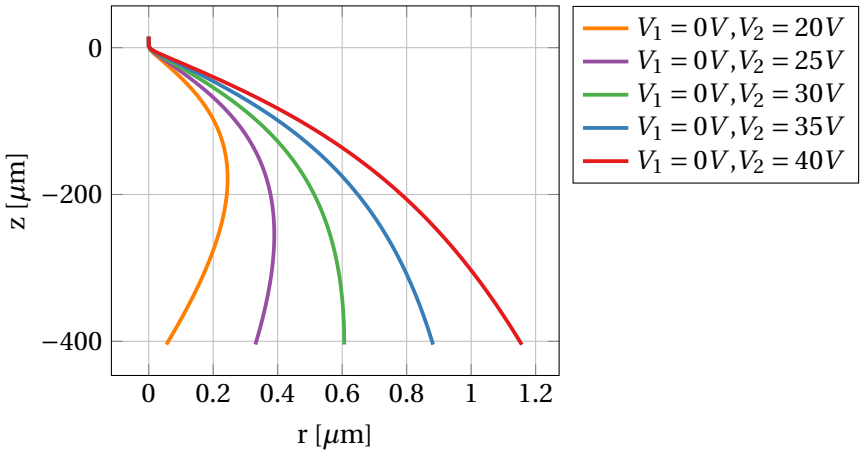

Figure 6.50: Particle trajectory of the central beam when the macro blanker is switched on at $\pm 40V$ with different micro electrode blanking voltages.

The COMSOL simulation of the micro electrodes and the macro electrodes proves that it is possible to blank all 25 beams and un-blank one beam back. This is done by activating both macro and micro deflectors with the correct voltages, to allow the un-blanked beam to travel to the sample without being stopped by the aperture in the final lens. A voltage of $\pm 50V$ is applied to the macro deflectors and a voltage of approximately $25V$ is applied to the micro deflectors. Because of the dimensions of the micro deflectors, the speed of the blanker is really low. This is however outside the final purpose of this device, that is designed for a proof of principle experiment.

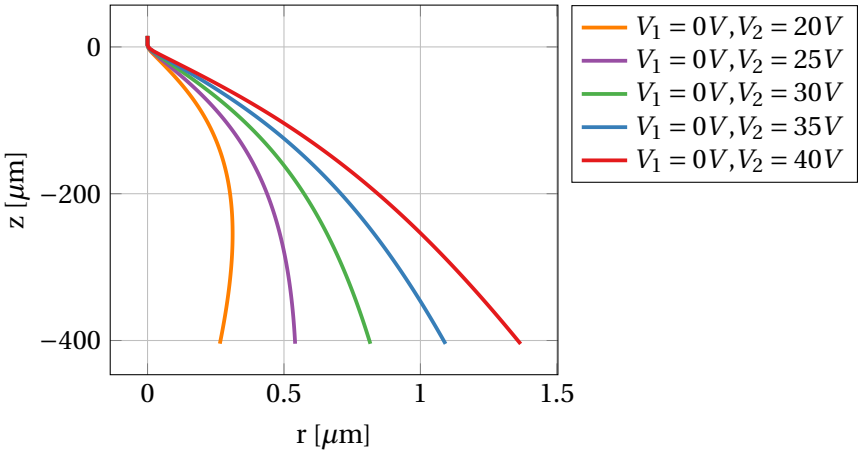

Figure 6.51: Particle trajectory of the central beam when the macro blanker is switched on at $\pm 50V$ with different micro electrode blanking voltages.

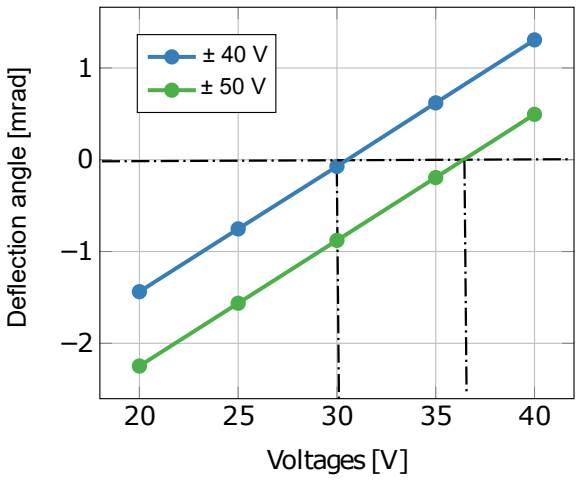

Figure 6.52: Deflection angle of the central beam when its micro blanker is switched on as well as the macro blanker, with $\pm 40V$ and $\pm 50V$.

6.11.2 Analysis of the crosstalk

When one of the deflectors is switched on, the neighbouring beams will be disturbed by that field and their path changes accordingly: this effect is called crosstalk. The crosstalk can be estimated by calculating the displacement of neighbouring beams when one of the micro deflectors is switched on. The trajectory of the beams can be simulated using the program COMSOL in 3D mode. An array of deflectors is built, as shown in figure 6.53. The array of blanker deflectors actually faces down, and therefore a convention on the numbering of beams is taken as shown on the left image of figure 6.53. The central beam is here considered to lie on the optical axis, at coordinates $x = 0\mu m$ and $y = 0\mu m$. The positions where the blanking electrodes are placed are:

- *Beam 13*, located at $x = 0\mu m$ and $y = 0\mu m$
- *Beam 17*, located at $x = -8.58\mu m$ and $y = -8.58\mu m$
- *Beam 21*, located at $x = -17.16\mu m$ and $y = -17.16\mu m$

The image on the right of figure 6.53 shows the numbering of the beams on the top view of the blanker plate, where the electrodes and the wiring are placed on the other face of the membrane. Each beam trajectory is simulated by tracing a test particle for each beam. The test particle has energy of $5kV$ and is released from the mesh border, that is $7.5\mu m$ above the membrane. The particles are traced for a total length of $15\mu m$, which is sufficient for calculating their deflection. The membrane is set to be at ground potential, as the common ground electrode. The blanking electrode voltages are on in case that the beam is to be blanked. We named V_1 the voltage on the electrode of beam 13, V_2 that of beam 17 and V_3 that of beam 21.

The crosstalk is calculated according to formula 6.32.

$$CT = \frac{\sqrt[2]{\Delta x_i^2 + \Delta y_i^2}}{\sqrt[2]{\Delta x_{ON}^2 + \Delta y_{ON}^2}} \cdot 100\% \tag{6.32}$$

Where Δx_i and Δy_i are the displacement in x and y of the neighbouring beam and Δx_{ON} and Δy_{ON} is the displacement of the blanked beam. The resulting crosstalks of the 25 beams when beam 13, 17 and 21 are switched on are shown respectively in figures 6.54, 6.55 and 6.56. When beam 13 is blanked,

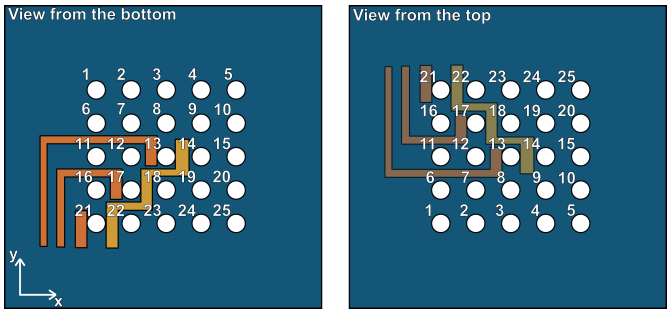

Figure 6.53: Numbering of the beams on the blanker array, bottom view on the left and top view on the right. The common light orange electrode is the ground electrode and the dark orange electrodes are the blanking electrodes of beams 13, 17 and 21.

the beams that are affected the most by the voltage on the deflector and on the wiring are beams 6, 7, 8, 11 and 12, namely the beams close to the connecting wire and the electrode itself. Also when beam 17 is blanked, the beams close to its blanking electrode are those that are more influenced by it and therefore have higher crosstalk, namely beams 11, 12 and 16. When beam 21 is blanked, only beam 16 has high crosstalk compared to other beams because of the effect of the close-by blanking electrode.

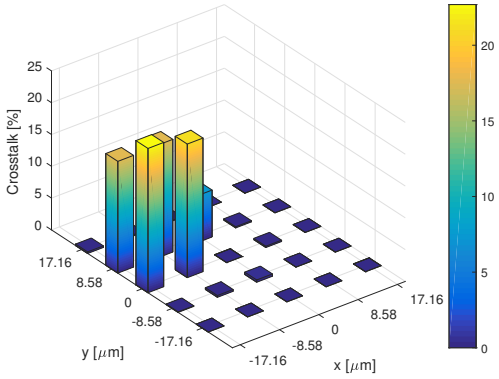

Figure 6.54: Crosstalk on neighbouring beams as effect of switching on the blanker electrode of beam 13.

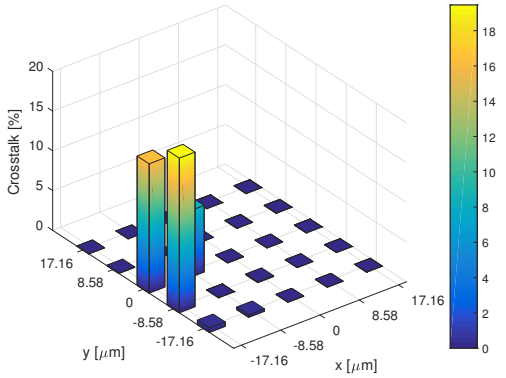

Figure 6.55: Crosstalk on neighbouring beams as effect of switching on the blanker electrode of beam 17.

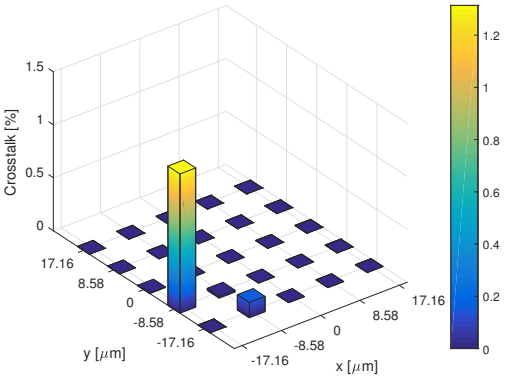

Figure 6.56: Crosstalk on neighbouring beams as effect of switching on the blanker electrode of beam 21.

Figure 6.57 shows the trajectory of the neighbouring particles that have higher crosstalk when beam 13, namely the central beam, is deflected. The direction of the deflection of the neighbouring beams is not, however, in the same direction as beam 13. This means that when the macro blanker deflects back beam 13 and blanks all the other beams, the neighbouring beams with high crosstalk will be effectively blanked.

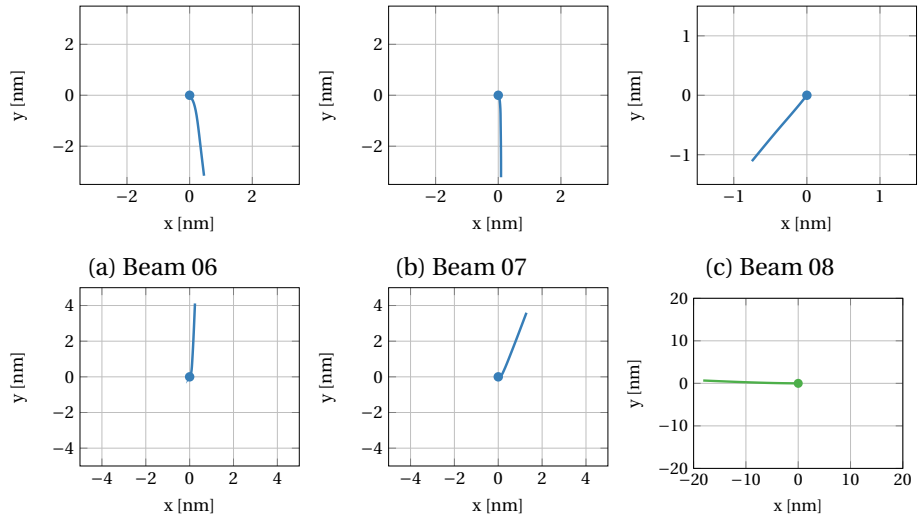

Figure 6.57: Beam trajectories when Beam 13 is switched on.

Figures 6.58 and 6.59 show the deflection of the neighbouring beams respectively when beams 17 and 21 are blanked. As for the case of beam 13 being deflected shown in figure 6.57, also in these cases when the beam is deflected the neighbouring beams will be also deflected, but not in the same direction. When the macro blanker is then switched on, beam 17 or 21 will be displaced back, nullifying the effect of the micro-blanker. The neighbouring beams, though affected by the crosstalk, will be deflected and stopped at the beam stop aperture anyway.

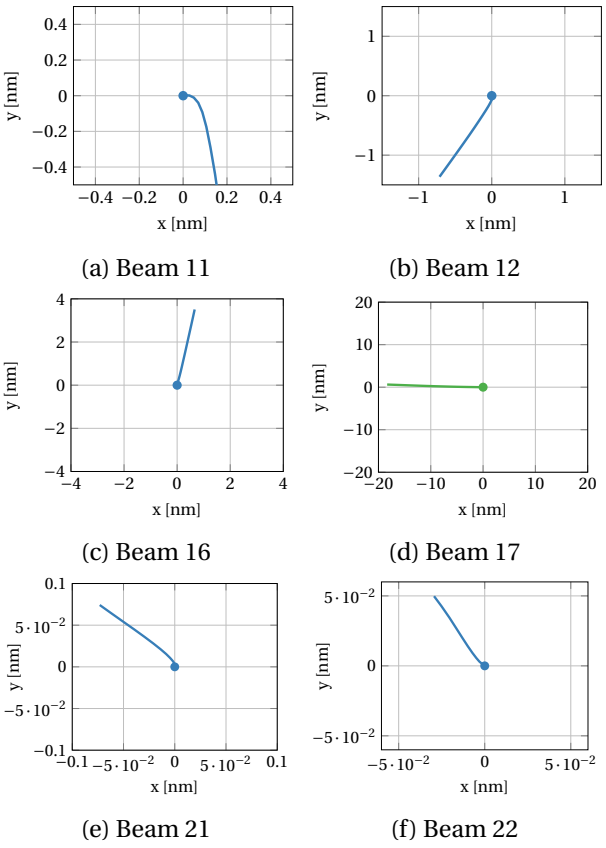

(a) Beam 11 (b) Beam 12

(c) Beam 16 (d) Beam 17

(e) Beam 21 (f) Beam 22

Figure 6.58: Beam trajectories when Beam 17 is switched on.

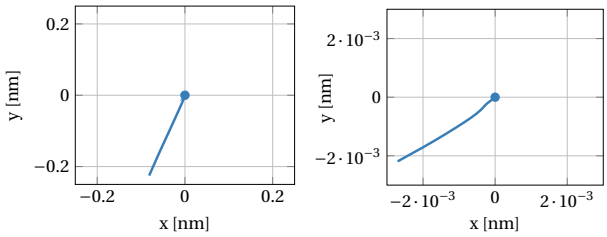

(a) Beam 16 (b) Beam 17

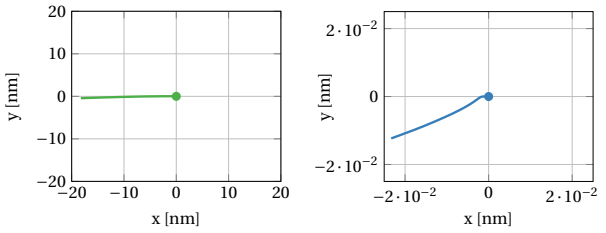

(c) Beam 21 (d) Beam 22

Figure 6.59: Beam trajectories when Beam 21 is switched on.

6.12 Summary and conclusions

In this chapter, the design of a multi beam splitting and blanking unit (MBU) is presented. The main function of the MBU is to turn a single-beam SEM into a multi-beam SEM, where the throughput in imaging and patterning is increased. The design of the MBU starts with setting requirements that the system must fulfill: a beam current of $50pA$, a total probe size smaller than $5nm$ and at least 25 beamlets must be generated. The requirements are dictated from the needs of patterning as well as imaging. The most suitable location where the MBU can be inserted in the microscope's column is via the variable aperture port: this position is favorable because of a lower vacuum level compared to that of the source and because it is at ground potential. This, however, sets a limit in the size of the entire unit, that must fit the $1cm$ port, commonly used for the variable aperture. The unit consists of a beam splitter (or multiple lens array, MLA) and a beam blanker array and depending on the direction the beamlets are traveling, three options can be distinguished. The beams can travel outwards and therefore the aperture pitch at the blanker is larger than that at the MLA or towards the optical axis and hence the aperture pitch at the blanker is smaller than the pitch at the MLA. Lastly, beams can also travel parallel to the optical axis, and therefore MLA and blanker array have the same

aperture pitch. The inclination of the beams depends on the location of the C2 crossover, while in the last case, the beams are made parallel by a macro electrode M1. The preferred situation is that where the beam are traveling outwards, as it offers a larger number of beams, although the different aperture pitch on the blanker and MLA may introduce challenges in the alignment between the two in the fabrication process. Moreover, the pitch at the blanker being larger, there will be more space for the fabrication of the deflector electrodes and the wiring.

Following this analysis is the optimization of the MBU design, where parameters like MLA aperture, distance between the MLA and the blanker and the working distance are tuned to achieve the smallest on axis probe, found to be approximately $1.5nm$. Moreover, the analysis of the off-axis performance, that are dominant over the on-axis aberrations, shows that at a working distance of $3mm$ the total off-axis contribution is minimum and is limited by the contribution of field curvature. The smallest total probe size for the outermost beam is $1.63nm$. Following, the analysis of the field curvature in the MBU reveals that the effects are negligible and thus the correction for field curvature is not needed. Stochastic Coulomb interactions occur when particle with the same charge are traveling close together and include trajectory displacement and energy spread, that worsen the performance of the electron optical system. It was estimated that these contributions to the final probe size are negligible because of the low total current density in the system.

Because of the need of having a configuration that is easier to fabricate, a simplified design of the blanker array was studied. The blanker array consists of three micro deflectors and two macro deflectors, which combined effects allow all the beams apart from one to be stopped on a stop aperture placed in the final lens. COMSOL was used to prove the functionality of this device. When a voltage of $\pm 50V$ is applied to the macro deflectors and a voltage of approximately $25V$ is applied to a pair of micro deflectors, all the beams can be stopped in the final aperture, while the activated beamlet is un-blanked and reaches the sample without any displacement. Finally the crosstalk was also simulated using the program COMSOL. By activating a blanker on the blanker array, the displacement of the neighboring beam is found to be negligible and the displaced beams will be further deflected by the macro-blanker and stopped at the aperture in the final lens.

The analysis performed in this section prove that it is possible to design a multi beam splitting and blanking unit, that can split a $5kV$ beam into 25 beamlets, each of which carry $50pA$ current, with an on-axis probe size of $1.5nm$. Following this study is the mechanical design and fabrication of the first MBU prototype.

From this chapter, the following conclusions can be drawn:

- It is possible to split the beam of a commercially available SEM by using a multi beam unit that can be fit in the variable aperture port.
- The number of beamlets that can be achieved strongly depends on the emission angle at the source. If a large emission angle is allowed, the number of beamlets increases exponentially. However, the stochastic Coulomb interactions, i.e. trajectory displacement and energy spread, start to affect the performance of the system drastically. An emission angle of $4mrad$ allows a "safe" operating condition, where the probe size of the sample is not limited by Coulomb interactions. For large area imaging, where the resolution is not a concern, a larger emission angle does not only allow for an increase of the number of apertures on the MLA, but also relaxes the strict requirements on the pitch at the blanker plane.
- In the MLA design described in this chapter, the inclination of the beamlets between the C2 and the INT lens must be constant because the MLA and the blanker are on fixed positions. The pitch between beams at the sample can be changed with the working distance.
- High acceleration voltages reduce the probe size at the sample, as the contribution from both on-axis aberrations and Coulomb interactions decrease. However, to be able to focus the beamlets from the MLA on the blanker plane requires a very strong field that will make the system vulnerable to electrical breakdowns.
- The field curvature introduced by the system is negligible and therefore a lens that corrects for it is not necessary.
- The proposed simplified design of a multi beam blanker allows for an easy-to-make prototype that is capable of delivering one beam at a time at the sample. In this configuration, the crosstalk between neighboring beams is negligible. This design of MBU can be used for probe size measurements.

Despite the achievements described in this chapter, some open research questions can still be addressed:

- What's the optimal emission angle at which the off-axis aberrations and the stochastic Coulomb interactions are sufficiently small, while keeping the total probe size at the sample smaller than $5nm$?
- If the emission angle is allowed to be slightly larger, how can the design of the blanker be improved?
- In the design of the MBU, the stack of electrodes is protected against damages by a shield, where a $500\mu m$ aperture lets the beam reach the MLA. What is the effect on the field from the shield that is kept at ground potential?
- Is there a possibility to easily change the pitch of the beamlets at the sample, avoiding to change the working distance? Can this be done by adding a macro-lens below the blanker without compromising the system performance?
- How does the shape of the apertures in the MLA contribute to the probe size? What happens if the apertures are not perfectly round as assumed in this chapter?

7

Mechanical design and fabrication process of the Multi Beam Unit

I'm a pessimist because of intelligence, but an optimist because of will.

Antonio Gramsci

7.1 Introduction

As thoroughly discussed in chapter 5, the present multi-beam SEM delivers 196 focused beams at the sample, in a $1.2nm$ on-axis probe with $26pA$ current and $15kV$ acceleration voltage. To achieve that, the standard Schottky source module is replaced with a multi beam source, that consists of 5 additional electrodes and a beam splitting unit. Figure 7.1 shows the electron optics schematic of the source module in the 196 multi beam SEM (left) and the mechanical drawing

(right). The multi beam source consists of two modules, the multi beam splitting unit, with two extra electrodes (E1 and E2) and the beam splitting plate (AA or aperture array) and the accelerator lens, created by the three electrode Einzel lens (Acc-1, Acc-2 and Acc-3). The main problem that this design has to face is the out-gassing of the elements and to maintain the high vacuum level, typically in the order of $10^{-9} mbar$. The main limitation of this microscope is the impossibility of blanking each beam individually, which is crucial for lithography. The most natural way to do that would be to integrate a blanker array plate in the source module, in the conjugate plane. However, this is a very challenging task, combining many electrical feedthroughs with the high voltage source environment. Therefore we propose a novel design of a Multi Beam SEM, where we aim for flexibility and versatility, namely the changes to be made to a standard microscope do not have to be permanent and will have to fit easily in a variety of SEMs.

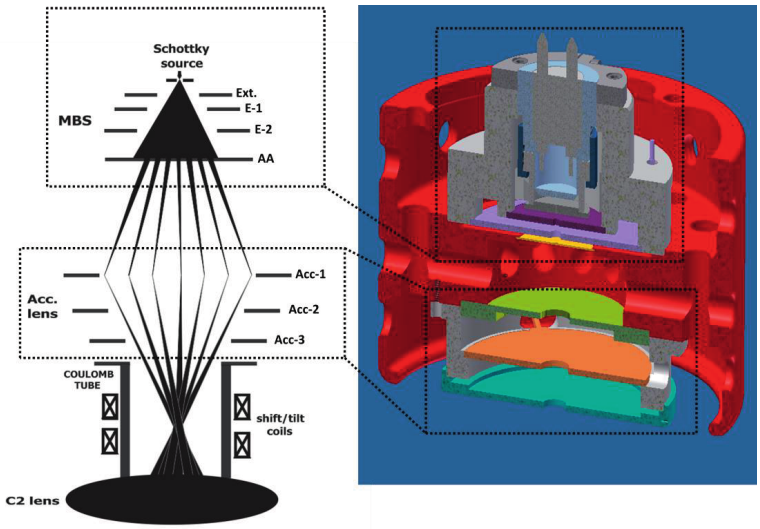

Figure 7.1: Electron optics schematic (left) and the mechanical design (right) of the source module of the 196 multi beam SEM [160].

In chapter 6, the design of the Multi Beam Unit (MBU) was thoroughly discussed. As shown in figure 7.2, the beam is split not in the source module, but around the middle of the column, and the intermediate lens and the objective lens will focus the beamlets to the sample surface. The minimum on axis probe size at the sample of a $5kV$ beam that is split into an array of 5x5 beams

is 1.5nm, carrying 50pA current. The MBU consists of three macro electrodes, that decelerate the beam, and a micro aperture lens array (MLA) that focuses the beams in a plane where the multi beam blanker array is placed. The MBU is positioned in the variable aperture port, and can be easily removed to bring the microscope back in the standard configuration. It is therefore a *flexible* and *versatile* solution and it can be adopted by microscopes of any brand, as all microscopes have a current limiting variable aperture port.

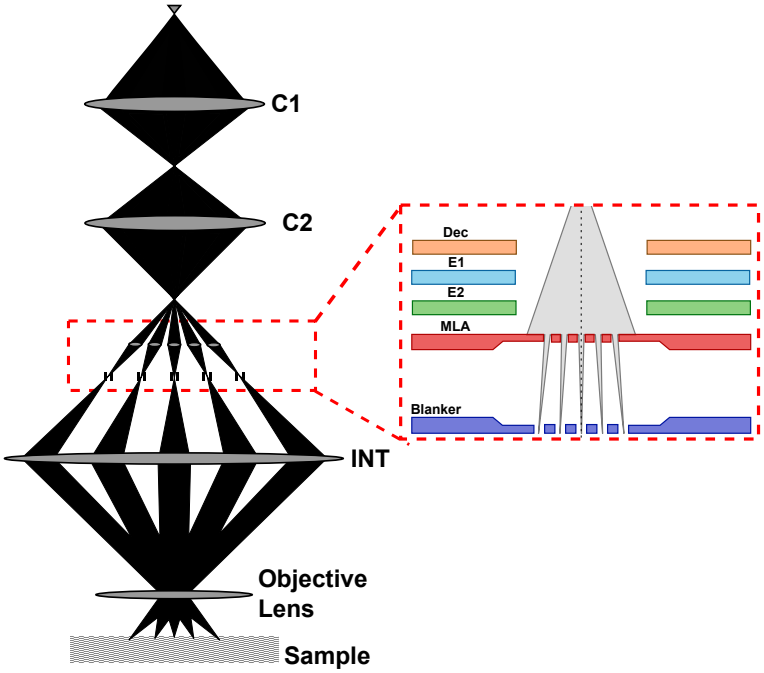

Figure 7.2: Electron optics schematic and the geometry of the multi beam unit, consisting of three macro-electrodes (Dec, E1 and E2), the beam splitter (MLA) and the blanker plate.

In this chapter, the mechanical design of the support and alignment mechanism are discussed. The set of macro-electrodes, the MLA and the blanker plate need to be mounted on a rigid support, that can be covered with a shielding that protects the stack from accidental collisions with other metallic parts. All the electrodes and the MLA need to be isolated from each other to prevent breakdown or leakage current. The support needs to be mounted on a stick that is inserted in the microscope column through a variable aperture port. The main limitation is the size of the port, that is only 10mm in diameter.

Within that space, the stack of electrodes, the blanker plate and the shield of the unit need to be designed. Moreover, the alignment mechanism needs to be designed such that the alignment of the unit with the optical axis is possible. Furthermore, the fabrication processes of the macro electrodes, the micro aperture lens array (MLA) and the blanker are described.

7.2 Requirements on the mechanical design

The MBU consists of a set of three macro electrodes, a micro lens aperture array (MLA) and a multi beam blanker array. Figure 7.3 shows the geometry of the MBU unit, including the shielding case at ground potential. Because the unit is inserted in the column of an electron microscope, it needs to be designed for a $10^{-6} mbar$ vacuum environment.

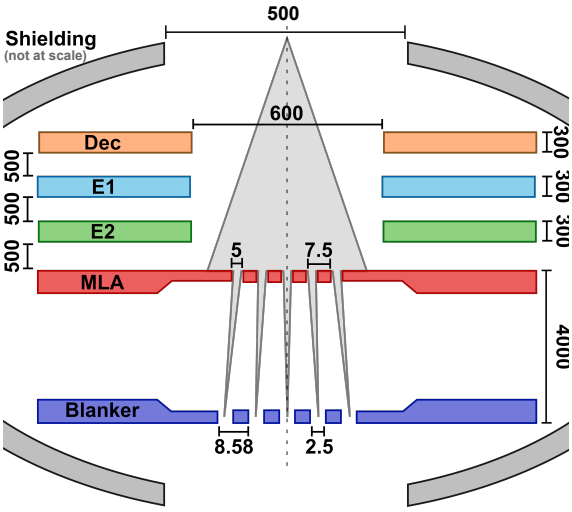

Figure 7.3: Geometry of the MBU, consisting of the Dec, E1 and E2 electrodes, each 300μm thick, that are separated from each other by insulating spacers of 500μm thickness and have an aperture size of 600μm in diameter. The MLA is positioned 500μm below E1 and has an array of 5-by-5 apertures of 5μm diameter, at a pitch of 7.5μm. The blanker array is positioned 4mm below the MLA, with apertures of 2.5μm diamter and 8.58μm pitch. The unit is protected by a shielding element, that is at ground potential. All the values in this figure are in μm. This is not a faithful schematics as the aspect ratios are modified to make the drawing understandable. For this reason, the shielding seems oval, while it is meant to be circular.

As shown in figure 7.3, the top electrode is *Dec*, which decelerates the elec-

Element	Voltage
Dec	$-1.5kV$
E1	$1kV$
E2	$4.5kV$
MLA	GND
Blanker	GND

Table 7.1: Required voltages on the electrodes in the multi beam unit.

tron beam. The Dec electrode is followed by two macro electrodes, *E1* and *E2*, that respectively compensate for the field curvature and create the lens effect on the *MLA*. The distance between each macro electrode and between E2 and the MLA is $500\mu m$, while the thickness of these electrodes is $300\mu m$, that of a standard silicon wafer. The macro electrodes have one hole with diameter of $600\mu m$, they are separated with insulating spacers and they need to be aligned with respect to each other. The MLA is made out of a silicon wafer, that is thinned in the middle to form a suspended membrane, to make it possible to etch an array of 5x5 holes with $5\mu m$ diameter at a pitch of $7.5\mu m$. This stack of macro electrodes and MLA is positioned $4mm$ above the blanker plate: the spacer between the MLA and the blanker can be made out of metal, as both the MLA and the blanker are grounded and no insulation is needed in between. The pitch at the blanker plate is $8.58\mu m$ and the distance between the blanking electrodes is $2.5\mu m$. The blanker plate is going to be mounted upside-down to facilitate the accommodation of the signal wiring. The device needs to be protected with a cylindrical shielding, that is also at ground potential. The voltages that need to be applied to each element are shown in table 7.1.

First, the entire unit has to fit the variable aperture port, which has a diameter of $10mm$. The outer diameter of the MBU, including the shielding case, has to be smaller than $10mm$ in total, considering that it needs room to be slid in the variable aperture port. The thickness of the case is set to be $0.5mm$, in order to be sufficiently robust to protect the unit against accidental collisions with the column body during insertion. The case has two holes with $1mm$ diameter that allows the beam to travel through without being cut.

Strict requirements are related to the spacers in between the macro electrodes. Figure 7.4 shows the ideal geometry of the insulating spacers. In be-

tween each electrode there are two glass plates, that have a hole centred with the optical axis, with radii of respectively r_1 and r_2. As a rule of thumb, r_1 should be equal to at least three times the radius of the macro electrode, therefore $r_1 = 900\mu m$. Each spacer sticks out the electrode by a distance of d_1 and d_2 and their thickness is respectively $t_1 = 300\mu m$ and $t_2 = 200\mu m$.

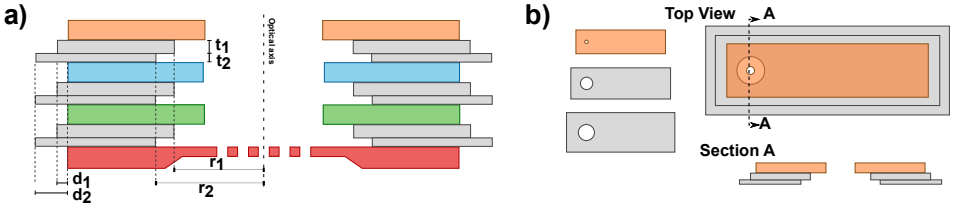

Figure 7.4: a) Ideal geometry of the insulating spacers in between each electrode in the MBU. Each spacer consists of two insulating glass plates that have a hole of radii r_1 and r_2 and thickness t_2 and t_2. This spacer configuration is preferred in order to prevent breakdown currents from one electrode to the other. b) Ideal geometry of the double-plate insulators below the Dec lens. On the left, the top view of the three elements: the Dec electrode in orange, and the two spacers. On the right, top view of the stack of electrode and spacers and cross-section along the perpendicular to the optical axis.

Figure 7.4 shows in better detail the geometry of the spacers: the top view of the single elements, the top view and the cross-section of the stack. The top electrode, shown as the orange plate in figure 7.4, is the Dec electrode and the other two plates are the insulating spacers in between Dec and E1. The size of the hole of the lower spacer is bigger than the top spacer and its outer dimensions are also larger. As shown in the top view, the electrode is smaller than the insulating spacers and the holes in the plates are all aligned with the optical axis. Section A in figure 7.4 shows the cross-section of the electrode and the spacers as specified in the top view. The extended electrodes effectively enlarge the path that electrons have to travel to go from the top electrode to the bottom one, preventing leakage currents.

Although this solution is ideal, we decided to opt for a configuration shown in figure 7.5, that is easier to accommodate in the shielding case. The length of the two insulating plates is smaller and does not reach the electron optical axis, as shown on the left of figure 7.5 and from the top view of the stack.

In order to have a device capable of turning a single beam microscope into a multi beam SEM and then easily back to single beam mode, the multi beam

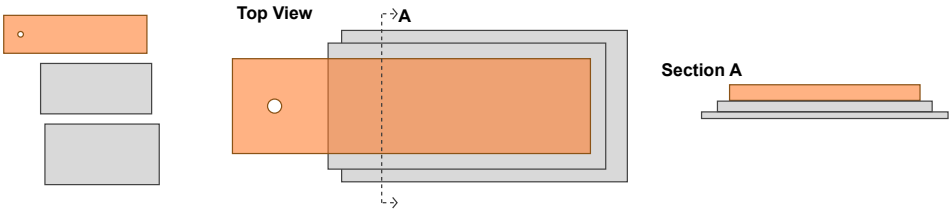

Figure 7.5: Adapted geometry of the spacers. In this case, the orange plate is the top plate in the stack, or the Dec electrode, while the grey plates are the insulating spacers between two electrodes. The length of the spacers is smaller compared to that of the ideal spacers: the edge of the spacers does not reach the apertures where the electron beam is travelling.

unit should also contain a single beam aperture. Figure 7.6 shows the top view of the MLA and of the shielding case, with the single beam (SB) and multi beam (MB) segments highlighted. The MLA has a single beam aperture of diameter $d_{SB} = 30\mu m$ on the left of the multi beam aperture lens array. The shielding case has two holes of $1mm$ diameter that allow the beam to go through. The one on the left is placed above the single beam current limiting aperture, while the one on the right is above the multi beam lens array. The distance between the single beam segment and the multi beam segment is $2.5mm$. A staircase like slit machined on the top part of the shielding case serves as alignment guide when inserting the support. It will be possible to image it in cross-over mode and insert the stick in the right direction.

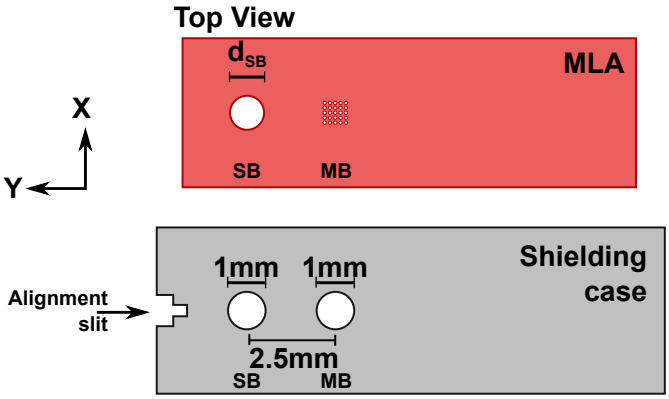

Figure 7.6: Top view of the MLA plate and of the shielding case. The MLA has a $30\mu m$ single beam current limiting aperture and next to it the multi beam lens array. The shielding has two large holes of $1mm$ in diameter for the single beam (SB) segment and for the multi beam segment (MB). The distance between the two segments is $2.5mm$.

The alignment of the stick to the electron beam is of importance when working in multi beam mode. We need therefore to be able to move the stick holding the lens stack along the X and Y axis, which define the plane perpendicular to the optical axis, as shown in figure 7.6. The stroke in the Y axis needs to be sufficient to align both the single beam aperture and the multi beam segment with the optical axis, covering a distance of $3.5mm$.The stroke in X can be smaller, depending on how accurately the aperture is centred with the optical axis when inserting the stick. For a fine adjustment, it is possible to use the gun shift and gun tilt coils that are positioned higher up in the column, thus aligning the beam to the multi beam unit. The rotation Ry and Rx around the X and Y axis are also essential to correct for misalignments.

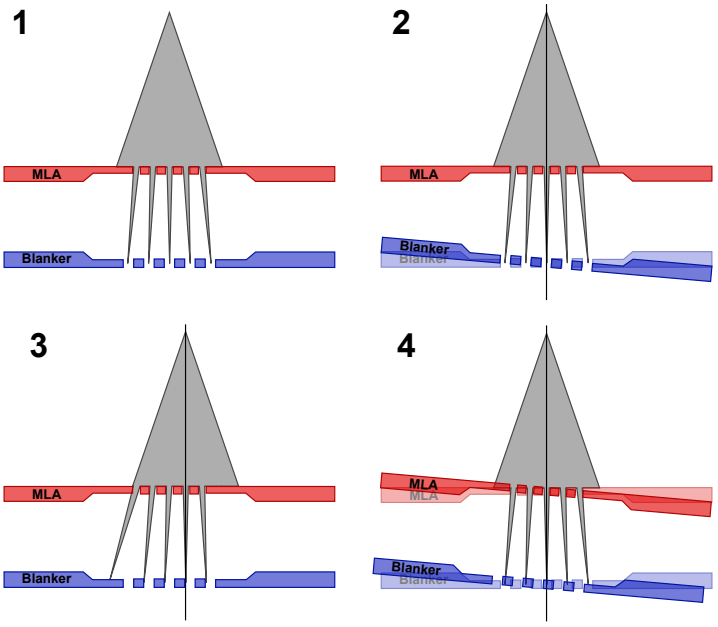

Figure 7.7: Consequences of the misalignments on the multi beam unit. Image 1 shows the ideal situation, where the MLA and the blanker plates are parallel and the stack is centred with the optical axis, without any rotation. Image 2 shows the case in which the MLA and the blanker plate are not parallel, while image 3 and image 4 report on misalignment in translation T_X and T_Y and in rotation R_X and R_Y respectively.

Figure 7.7 shows the translation and rotation misalignments that might occur: image 1 shows the ideal situation, where the MLA and the blanker plates are perpendicular to each other and perpendicular to the optical axis, that is well centred to the central aperture, allowing the diagonal beams to go through

the blanker plate array of holes. Image 2 in figure 7.7 shows the case when the MLA and the blanker plates are misaligned. In this case, when the two plates are well aligned to the optical axis with an accuracy of $1\mu m$, it is straightforward to calculate that the maximum tilt angle of the blanker plate that still allows the beam to go through the aperture is 30 deg. Image 3 shows a translation misalignment of the entire stack with respect to the optical axis. If the optical axis is not centred with the central aperture, then some of the beams will be cut off. This can be easily adjusted by either move the stack in X and Y or by using the gun shift and gun tilt coils. Finally, image 4 shows the effect of a rotational misalignment around Rx or Ry, where for a rotation larger than $0.3mrad$ the central beam will be stopped. To correct for this, fine alignment will be done with the gun tilt coils.

The MBU hosts three high voltage electrodes summarized in table 7.1 and ideally 25 low voltages of the blanking electrodes. It is necessary to wire bond the high voltage electrodes to a flex print PCB and from there to the outside world via high voltage MHV connectors. For the low voltage feedthroughs, a flex print PCB can also be used, combined with LEMO connectors. The flex print needs to be specifically designed for holding vacuum at a pressure of $10^{-6}mbar$ and such that there is no leaking current between the high voltage wires.

7.3 Mechanical design

The design of the multi beam support is shown in figures 7.8 and 7.9. It is a robust piece, that can be made out of titanium or bronze. On the top part, as shown in figure 7.8, the electrodes are stacked with glass spacers in between. In the dashed box the single beam and the multi beam segments are highlighted, as well as the alignment slit. The macro electrodes have different lengths on the connection side such that they stick out in a stair-case like structure, to ease the wire bonding to the flex printed PCB, that is also depicted in figure 7.8. Figure 7.9 shows the cross section, the front view and the bottom view of the support. Two flex printed PCBs are fixed to the MBU support using a UV-curable glue: one is fixed on the top surface of the support and will be connected to the high voltage macro electrodes, while the second is fixed on the bottom side of the support and will be connected to the low voltage pad on the blanker plate. They both have a horseshoe-shape end, that embraces the electrodes stack and the blanker plate. From the cross-section view, the stair-case like structure of the macro electrodes, that facilitates the wire bonding, is visible. The multi beam

and single beam segments are also highlighted here in the dashed boxes.

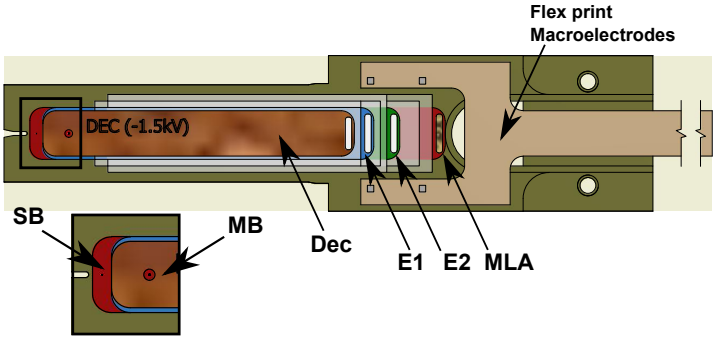

Figure 7.8: Top view of the designed support and highlighted in the box the single beam and multi beam segments. The electrodes are glued together with two glass spacers in between. A flex printed PCB is also glued on the right hand side of the support and has a horseshoe-like shape to allow wire bonding.

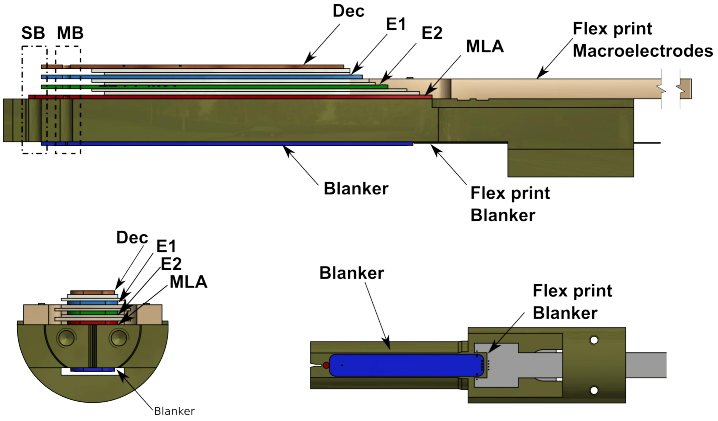

Figure 7.9: Cross-section, side view and bottom view of the support. The multi-beam and single-beam segments are highlighted with the dashed boxes. The single-beam aperture is implemented in the MLA plate, that is grounded. Two flex printed PCBs allow the wire bonding to the macro electrodes and to the blanker plate, thanks to their horseshoe-like shape and to the stair-case like structure of the macro electrodes.

Figure 7.10 shows the 3D view of the support holding the stack of electrodes and the flex printed PCB (a) and the shielding case mounted on the support (b). The support is further secured to the stick with two top screws and it is protected by the shielding case. The shielding case has two apertures on the

single beam segment and on the multi beam segment and an alignment slit at its very edge. The stick will be inserted through the alignment mechanism and the variable aperture port into the microscope column.

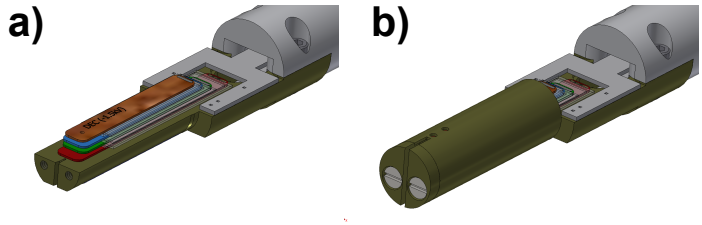

Figure 7.10: a) 3D view of the support, with the stack of macro electrodes and glass spacers, the flex printed PCB, mounted to the stick. b) 3D view of the shielding case mounted on the support, covering the stack of electrodes

Figure 7.11 shows the definition of the adopted coordinate system, represented in the 3D cross-section of the MBU support and alignment mechanism when the stick is inserted in the variable aperture column of the FEI Nova Nano Lab SEM. In the figure, the coordinate system is defined such that the Y axis is the axis along the stick, the X axis is the perpendicular axis laying in the horizontal plane, the Z axis is the optical axis. The pivot point P is the centre of rotation (or tilt) R_X and it is located on the port itself. The pivot point is that point that does not move when the rotation occurs and it is positioned in the port where the room for movements is limited.

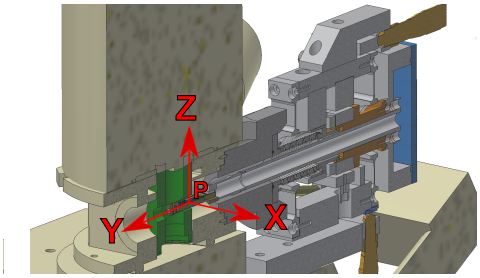

Figure 7.11: 3D view of vertical section of the MBU and its alignment mechanism when inserted in the column of an FEI Nova Nano Lab SEM, showing the definition of the axis X, Y and Z and the pivot point P, around which the rotation and tilt are centered.

Figure 7.12 shows how the translation in Y is implemented. The bottom

plate of this construction is attached to the fixed world, while the upper plates and the body that holds the stick can be moved from right to left, in the left image of figure 7.12, by means of a micrometer screw. The movement mechanism is better shown in the right image of figure 7.12, that is the result of a stress analysis, where the colorbar refers to the amount of displacement. The blue elements are attached to the fixed world and the red parts are those that are displaced the most. The body that holds the stick is connected to the fixed world by means of flexible elements, that allow the displacement of the body itself. The force is applied by the screw and is here depicted by the gold arrow. The maximum displacement of the body that holds the stick is approximately $\pm 2.5mm$.

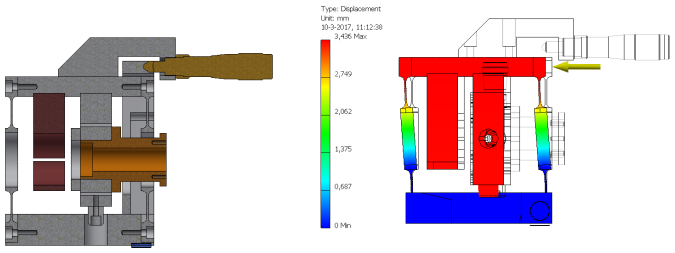

Figure 7.12: Construction that provides the translation along the Y axis. On the left, the cross-section of the mechanism shows the screw that can move the body that holds the stick, while the bottom plate is attached to the fixed world. On the right, the result of the stress analysis when a force is applied to the movable parts. The force is represented by the gold arrow, the blue parts are fixed and do not move while the red parts are those that move the most. The maximum displacement of the body holding the stick is approximately $\pm 2.5mm$.

The translation along the X axis is also provided by a micrometer screw that applies a force on the part that needs to be moved, as shown in figure 7.13. On the left, the top view of the mechanism that provides the movement along the X axis. On the right, the result of the stress analysis, where the colorbar represents the displacement of the mechanical parts. The force is applied laterally by means of a screw. The movement along the X axis is bigger in the parts colored in red and it is equal to approximately $\pm 0.5mm$. The movable parts are also here connected to the fixed world (in blue) by means of elastic elements. These elastic elements are in this case 4 rods, that from the top view are parallel to each other.

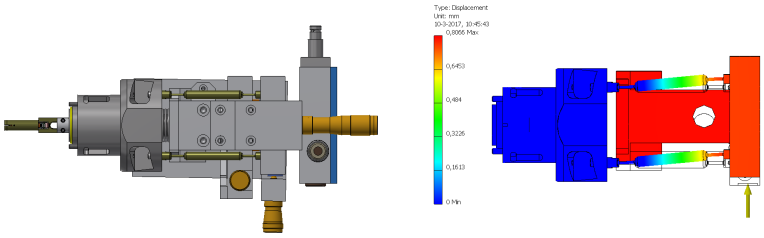

Figure 7.13: Machanism that provides the movement along the X axis. On the left, the top view of the mechanism and on the right the results of the stress analysis, where the colorbar refers to the displacement. The red parts are those that are displaced the most, up to a total of $\pm 0.5mm$.

The mechanism providing the rotation around the X axis is shown in figure 7.14. On the left, the side view of the mechanism, comprising the MBU stack covered with the shielding case, the cylinder fixed to the VA port, 2 of the 4 elastic elements pointing at the pivot point P of figure 7.9, the screw for the Y translation and the screw for the X rotation. By turning the bottom screw, a force is applied to the movable body, that is attached to the fixed world by means of four elastic rods pointing at the pivot point P. Effectively the translation is converted into a rotation around the X axis at the MBU location, with a small movement in Z. On the right, the results of the stress analysis, where the colorbar relates to the amount of displacement. The blue parts are fixed, while the red parts are displaced to a maximum of approximately $0.7mm$.

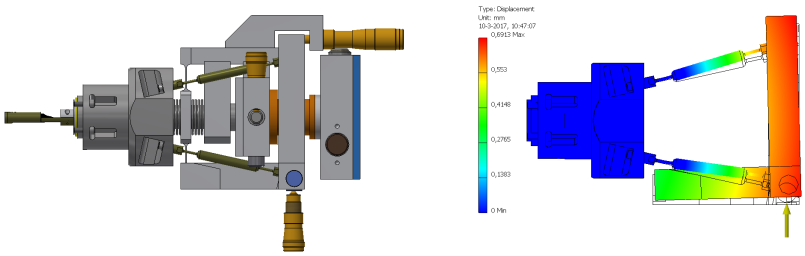

Figure 7.14: Implementation of the rotation around the X axis. On the left, side view of the alignment mechanism, with the MBU covered with the shielding case, the 4 alignment rods and the screws for the Y translation and the rotation around X. On the right, results of the stress analysis, when a force is applied from the screw to the body. The body rotates around the pivot point P of figure 7.9.

The rotation around the Y axis is implemented by applying a force via a screw to a ring plate, that will effectively rotate, and that is connected to the fixed world by means of two elastic rods. Figure 7.15 shows the mechanics that implements the rotation around Y. On the left, the front view of the mechanism, showing the screw, the ring and the two elastic elements. On the right, the results of the stress analysis, where the rotation of the ring and the displacement of the elastic rods is visible.

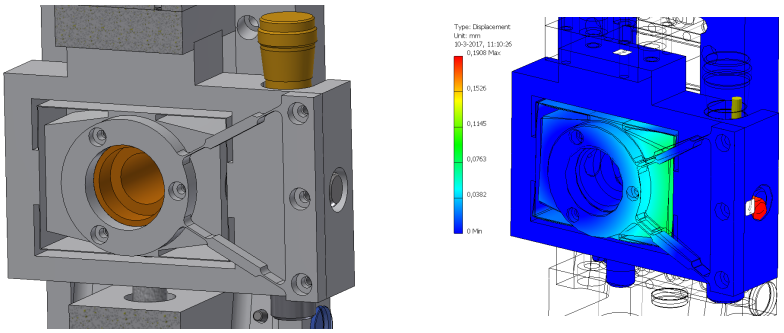

Figure 7.15: Part of the MBU alignment mechanism that implements the rotation around the Y axis. On the left, the side view of the mechanism, comprising the ring that rotates under the stress given by the screw and the two elastic elements by which it is connected to the fixed world. On the right, the results of the stress analysis when a force in applied by the screw and translated to a rotation of the ring.

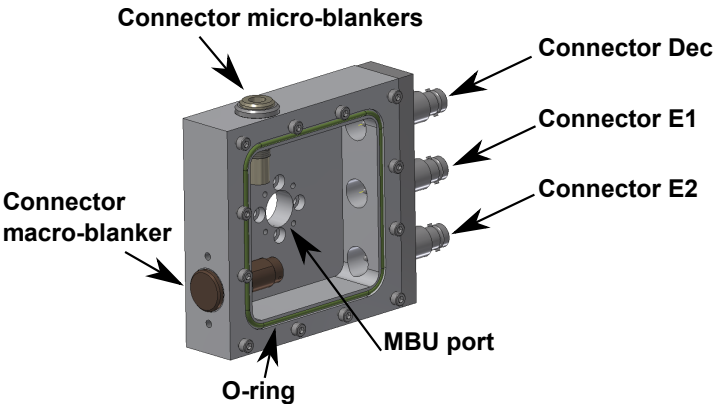

Figure 7.16: Design of the connector box, that comprises the MBU port, three high voltage MHV connectors and two low voltage feedthroughs. The O-ring and a lid provide vacuum in the small chamber.

The interface to the outside world is effectively the connector box, shown in figure 7.16. The connector box is mounted on the alignment mechanism and it has a port where the MBU stick can be slid in. The stick is fixed to the connector box by four screws placed around the circular port. Three high voltage connectors are located on the right hand side face, while two low voltage feedthrough LEMO connectors are located on the top and on the left hand side faces of the box. The connector box is sealed with a rectangular O-ring and closed with a lid, that holds the vacuum.

Figure 7.17 shows the 3D view of the designed mechanism, with the MBU unit covered with the shielding case. Some of the alignment screws are visible in this perspective, as well as some of the elastic rods. The image on the right of figure 7.17 shows the alignment construction when mounted on the FEI Nova Nano Lab SEM. Because the construction is quite heavy, it is supported by a plate on the top of the chamber.

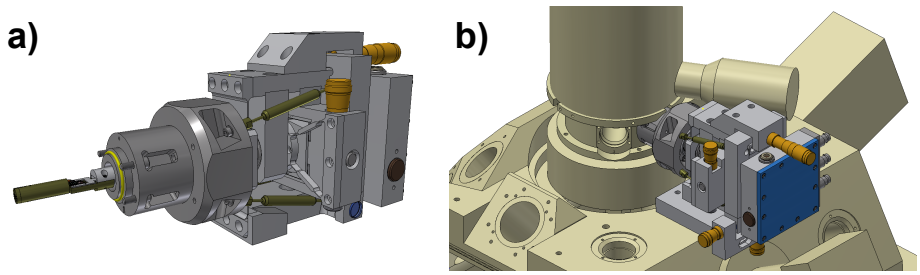

Figure 7.17: (a) 3D view of the designed alignment mechanism holding the support covered with the shielding case on the left of the device. (b) The entire alignment mechanism mounted on the Nova Nano Lab column.

7.4 Fabrication of the beam splitting unit

The MLA and the macro electrodes were fabricated using microfabrication techniques in the Kavli-nanofacility in Delft. A set of masks was designed for the lithography process for the fabrication of the macro electrodes and the MLA plate. Markers were included in the masks to facilitate alignment in the stacking process of the electrodes. The process steps of the MLA fabrication are sketched in figure 7.18.

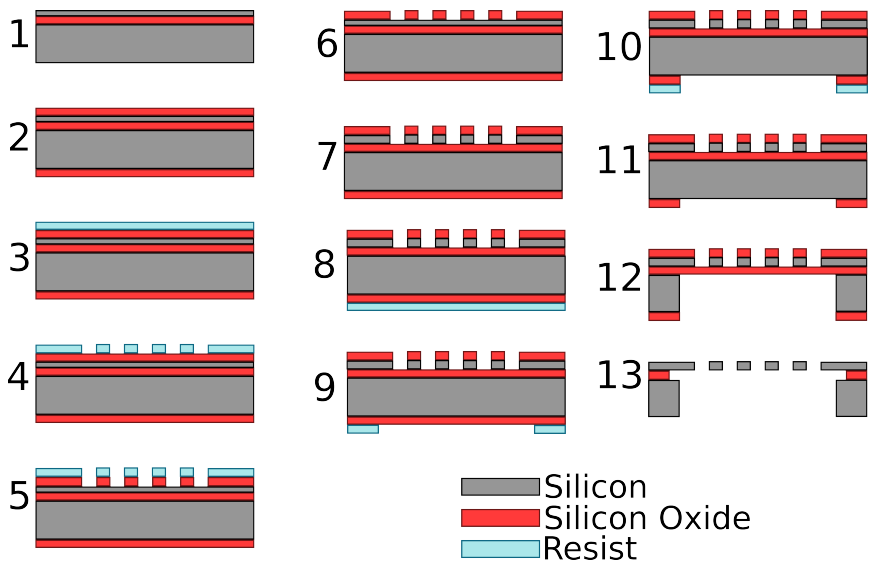

Figure 7.18: Schematic overview of the process steps in the fabrication of the Micro Lens Array (MLA).

1. The MLA was fabricated using a SOI wafer, i.e. Silicon on Insulator. The wafer has a $1\mu m$ oxide layer (BOX) buried below the upper $10\mu m$ silicon layer. The thickness of the handle is $300\mu m$.

2. Silicon oxide is deposited on both sides using PECVD. $1\mu m$ oxide is deposited on the device layer and $2.5\mu m$ oxide is deposited on the handle.

3. The top side of the wafer is coated with a $1.4\mu m$ SPR3012 positive photoresist in the EVG120.

4. The photoresist is exposed using optical lithography in the EVG420. The resist is then developed forming the 5x5 array of holes.

5. The top silicon oxide layer is opened up in the Drytek 384 Triode RIE dielectric etcher.

6. The photoresist is stripped away in the Tepla Plasma 300 O_2 asher.

7. The $10\mu m$ silicon device layer is opened up using a Bosch etch (SPTS Rapier) using the silicon dioxide as hardmask. The etching process is very selective and will stop on the buried oxide layer.

8. The backside of the wafer is covered with a $1.4\mu m$ SPR3012 positive photoresist in the EVG120.

9. The resist is exposed in the EVG420 and developed in the EVG120, forming the backside hole.

10. The backside silicon oxide is opened up by etching in the Drytek 384 Triode RIE dielectric etcher.

11. The photoresist is stripped away in the Tepla Plasma 300.

12. The silicon handle is etched using the silicon oxide as hardmask in a DRIE etcher (Bosch etcher SPTS Rapier).

13. The buried oxide layer is removed with BHF, leaving a thin Si membrane, with a thickness equal to that of the device layer.

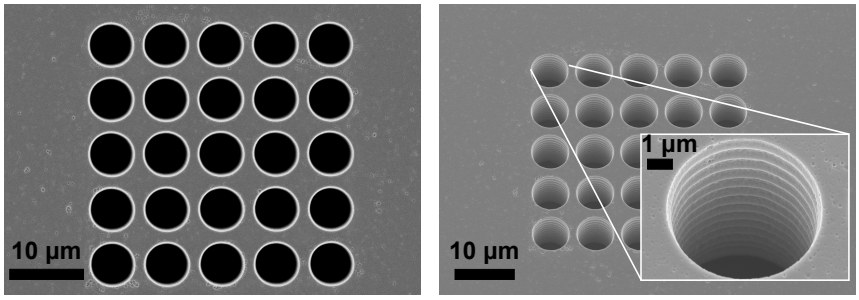

Figure 7.19: a) top view SEM micrograph of the MLA. b) Tilted SEM micrograph of the MLA, with a zoomed-in image of one of the apertures, where the trenches left by the Bosch etch are visible.

The device layer of the SOI wafer, used for the fabrication of the MLA, has a resistivity of $\sim 50\mu\Omega \cdot cm$, so no full metallization was needed. The macro-electrodes were made out of a $300\mu m$ thick SOI wafer. Only one end of the MLA electrode and the macro-electrodes was metallized with Al to enable wire bonding to nearby contact pads. An example of the MLA is shown in figure 7.19, while figure 7.20 shows a macro electrode.

7.5 Fabrication of the blanker array

The fabrication of the blanker plate was carried out in the TU Delft facility for microfabrication (Else Kooi Laboratory - EKL). Both the micro electrodes and

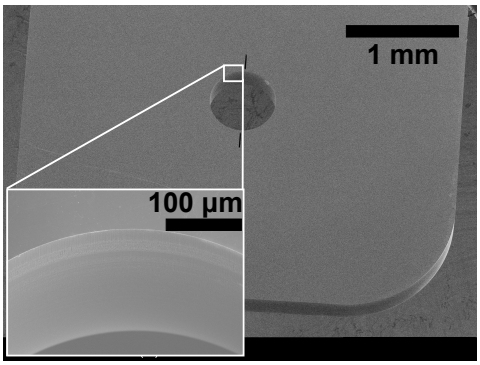

Figure 7.20: SEM micrograph of one of the macro electrodes, with a zoomed-in image of the $600\mu m$ aperture.

the macro electrodes are patterned within the same lithography step as they are designed to have the same height and can be made out of the same metal layer, that consists of AlSi (1% of Si). The blanker array plate will be mounted upside down, with the back side hole facing the incident electron beam. The fabrication process flow is shown in figure 7.21.

Three sequential lithographic steps are performed in order to fabricate the macro and micro electrodes (1-7), the array of 5 × 5 apertures (8-9) and the backside hole to create the suspended membrane (10-14). The alignment between the first two lithographic steps needs to be accurate, as the aperture array, with apertures at a pitch of $8.58\mu m$, needs to be positioned very precisely beneath the micro electrodes. A trick to weaken the alignment accuracy demands is to enlarge the size of the apertures, from the designed $2.5\mu m$, which is also the distance between the electrodes, to $4\mu m$. This way the aperture pattern overlaps with the electrodes pattern, allowing a misalignment of up to $750nm$ in any direction, which lays within the capabilities of the ASML wafer stepper that was used for the exposure.

1. The substrate used to fabricate the blanker is a silicon-on-insulator (SOI) wafer, with a device layer of $10\mu m$, a buried oxide layer (BOX) of $1\mu m$ thickness and a handle of $300\mu m$.

2. A $1\mu m$ layer of SiC is deposited by PECVD: this is the insulating layer that prevents shorts between electrodes through the device layer. Ini-

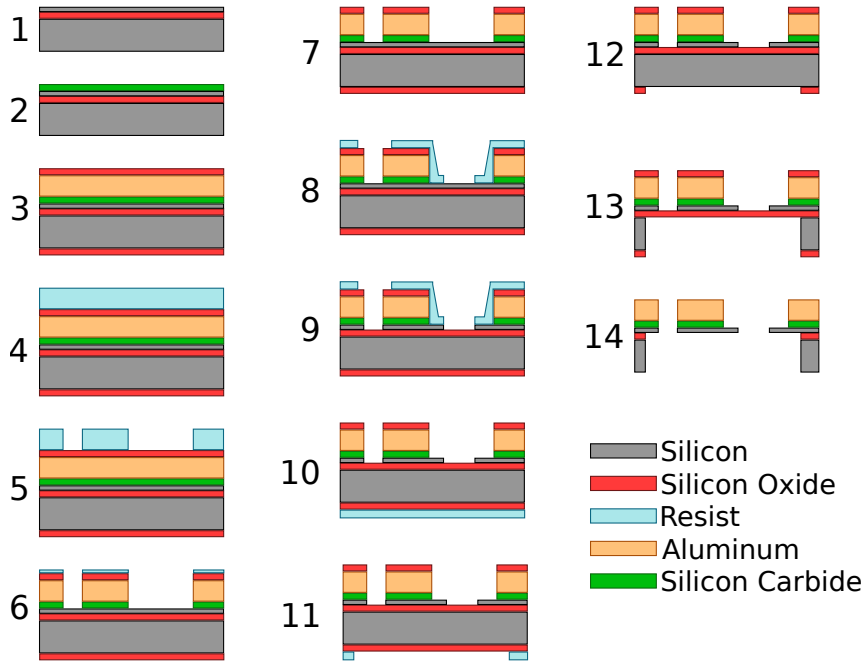

Figure 7.21: Schematic overview of the process steps in the fabrication of the blanker array, consisting of three lithographic steps for the patterning of the macro and micro electrodes (1-7), the 5x5 array of apertures (8-9) and the backside hole(10-14), forming the suspended membrane.

tially SiOx was used instead of SiC, but it turned out to be attacked too much by the last diectric removal step.

3. A layer of $2\mu m$ of AlSi (with 1% of Si) is deposited by sputtering: the wiring, the electrodes and contact pads are made out of this layer. The AlSi(1%) was chosen because of its immediate availability as a target in the machine that was used, while for pure Al there would be more waiting time. Moreover, for our purposes it would not matter to prefer one over the other. On top of the aluminum, a $500nm$ layer of silicon oxide was deposited by PECVD. This is a sacrificial layer that serves to protect the electrodes from the Bosch etch during etching of the handle. After that, a $2\mu m$ layer of silicon oxide is also deposited by PECVD on the backside of the wafer. This layer will be the hard mask used to pattern the backside hole.

4. The top side of the wafer is coated with $2.1\mu m$ SPR3012 positive photore-

sist. The thickness of the resist needs to be sufficient to handle the three etching steps, that pattern the silicon oxide, the AlSi and the carbide layers.

5. The photoresist is exposed in the ASML wafer stepper: first the macro and micro electrodes are exposed ($300 mJ/cm^2$), together with the alignment marks ($250 mJ/cm^2$), that will be used to align the other lithographic patterns. The photoresist is then developed in the EVG120.

6. Three etching steps are performed to pattern the top three layers. The $500 nm$ silicon oxide layer is etched in the Drytek 384 Triode RIE dielectric etcher, the $2 \mu m$ AlSi and the SiC are etched in a the Trikon Omega 201 ICP etcher.

7. The resist on the top side of the wafer is stripped in a Tepla Plasma 300 O_2 asher.

8. A coating of $2.1 \mu m$ SPR3012 positive photoresist is spinned on the frontside of the wafer in the EVG120. Because of the $3.5 \mu m$ topography of the metal and insulating layer etched in the previous steps, the resist will have a non-uniform thickness. Especially in the proximity of the micro electrodes. For this reason, the pattern is over-exposed with a dose of $500 mJ/cm^2$ to ensure that the pattern will be fully opened.

9. The silicon device layer is patterned by Bosch etching in an SPTS Rapier. This etch process is very selective and will stop on the buried silicon oxide layer.

10. The resist is stripped in the Tepla Plasma 300: now the frontside of the wafer is ready. The backside is coated with a $1.4 \mu m$ layer of SPR3012 resist.

11. The backside (or silicon-handle) is exposed with the ASML wafer stepper to form the backside hole.

12. The oxide layer is opened up by etching in the Drytek 384 Triode RIE etcher and the resist is stripped in the Tepla Plasma 300 O_2 asher.

13. The backside silicon layer is patterned with the SPTS Rapier Bosch etcher using the silicon oxide as a hardmask. The etching will stop on the buried silicon oxide layer. As a result, the depth of the apertures is determined by the device layer only and is therefore uniform within a micrometer.

14. The residual oxides, the backside hardmask, the frontside protective layer and the buried silicon oxide, are removed in an SPTS u-etch HF vapour etcher. The etching residues are rinsed out in a quick dump rinser and the wafer is spun-dry.

Figure 7.22 shows an SEM image of one of the fabricated blanker array plates: the left-hand image *a)*, shows the overview of the macro and micro electrodes, together with part of the wiring to the contact pads. Image *b)*, on the right, shows a zoom-in of the 5x5 array of apertures and the three micro electrodes, consisting of the common ground electrode and the three blanking electrodes. The deformation of some of the aperture holes is caused by the non-uniform resist thickness.

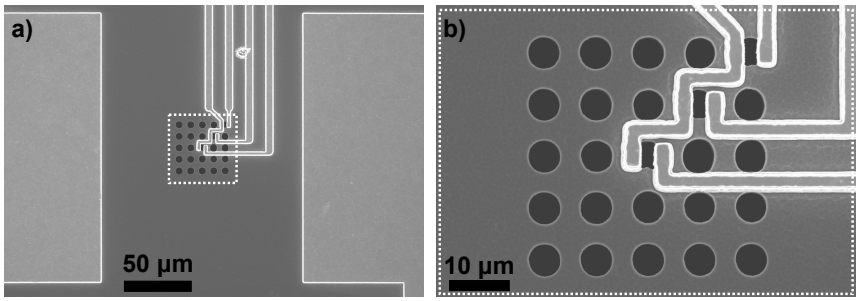

Figure 7.22: SEM micrograph of the macro and micro electrodes on the left, and a zoomed-in image of the 5x5 array of apertures with the three blankers.

Figure 7.23 shows the SEM micrographs of one of the micro deflectors: image *a* is a top view, while image *b* is rotated and tilted. Because the array of apertures is patterned after the electrodes and the wiring, the apertures that lay underneath the electrodes are deformed. From image *b* the AlSi layer and the insulating SiC layers are clearly distinguishable.

7.6 Assembly of the stack of electrodes

The assembly of the stack of electrodes is a challenging step in the device fabrication. To stack and align the macro-electrodes, the MLA and the blanker plate we used a specially developed alignment tool based on a 6-degrees of freedom PI-hexapod system [170]. This system has a proven alignment accuracy of $500nm$ [170]. The alignment tool is shown in figure 7.24 and it consists of a

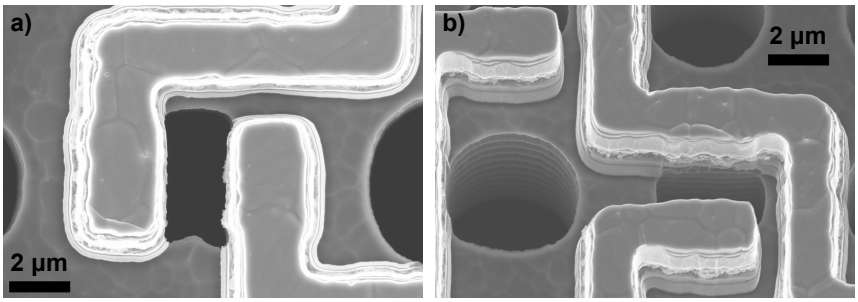

Figure 7.23: Top view SEM micrograph of one of the micro blankers on the left and the rotated and tilted view of the same area. The apertures close to the electrodes are deformed because of the non-uniform thickness of the applied photoresist.

6D stage that allows for translation along the x, y and z axes as well as rotation around these axes, a mounting fork, lower and upper element chucks, a z-stage, an optical detection system and granite mounting blocks. The alignment procedure to align two plates with alignment markers is performed as follows. The first plate is mounted and brought to the image plane of the objective lens and the optical image of the plate is taken and stored. The first element is then moved up to make room for the second plate with the insulating spacers to be positioned in the image plane of the objective lens. An image of the second plate is taken and stored. By comparing the two stored images of the two elements, it is possible to align the two elements by moving the second one with the 6D stage. Once the second element is in position, the first element is lowered and fixed with UV-curable glue.

When an actual stack is built, first the blanker is manually glued on the bottom of the support after which this assembly is placed in the hexapod alignment tool. The MLA is then first aligned with the blanker, and after that the macro electrodes follow. The macro electrodes are electrically insulated from each other by glass spacers. These spacers consist of two glass plates where one has greater lateral dimensions, forming a step in the cross-section. This step elongates the path between two adjacent electrodes, which reduces the risk of voltage breakdown and flashovers. All electrodes are fixed by gluing them together using UV-hardening glue. Figure 7.25 shows an SEM image of the beam splitting optics stack. The top three electrodes are the Dec, E1 and E2 electrodes and they are aligned with respect to the MLA plate, that is glued directly on the support.

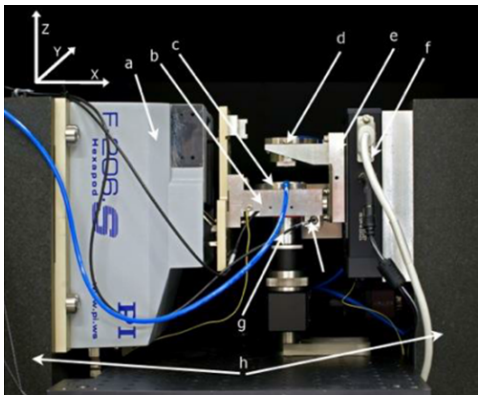

Figure 7.24: The 6D-alignment tool. *a)* the 6D-stage (PI F206 hexapod), *b)* 6D-stage mounting fork, *c)* lower element chuck, *d)* upper element chuck, *e)* z-stage mounting fork, *f)* z-stage (PI M605-1D), *g)* microscope objective, *h)* granite stage mounting blocks.

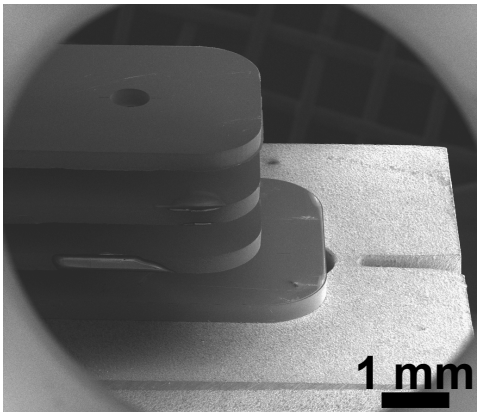

Figure 7.25: An SEM image of the beam splitting optics stack, consisting of 3 macro-electrodes (on top) and the MLA (bottom).

Figure 7.26a shows the assembled multi beam unit stack, the support, the shielding case and the flex print. The flex print is used to provide rigid electrical contacts close to the stack. The electrodes are connected to the pad on the flex print by means of wire bonding, using 30μm diameter wire. The bonding wires are depicted in figure 7.26b, that shows an SEM micrograph of the macro electrodes and the flex print.

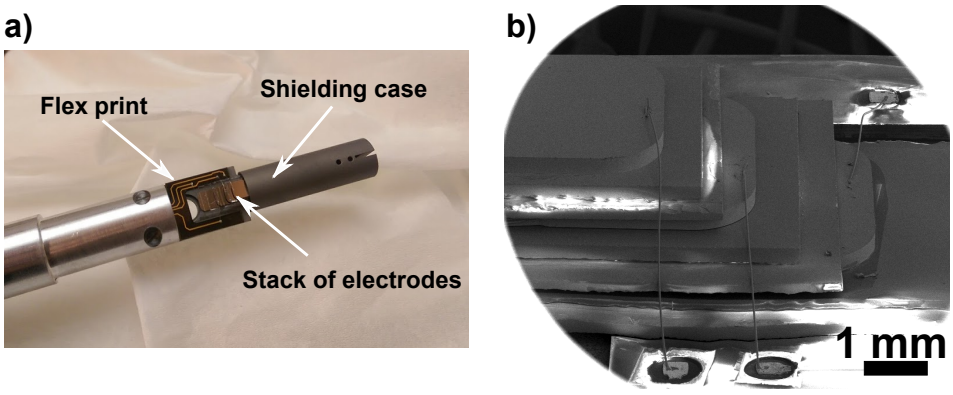

Figure 7.26: a) part of the flex print is seen next to the rear of the electrode stack. b) SEM image of the wire bonds between the electrode stack and the contact pads of the flex print.

7.7 Summary and conclusions

In this chapter, the mechanical design and the fabrication of the multi-beam unit are presented. The MBU consists of the beam splitter, the multi-beam blanker and the three macroelectrodes. Between the three macroelectrodes and the beam splitter, insulating spacers with $0.5mm$ thickness prevent discharge between the elements at high voltage. The MBU is mounted on a rigid support that can be inserted in the variable aperture port of the electron microscope. The support, that is covered with a ground shield, is connected to an alignment mechanism. This mechanism allows alignment of the unit in X, Y and Z and the correction for the rotation Rx and Ry. The stroke in X is as long as $2.5mm$ to be able to reach the single beam aperture on the splitter plate. The fabrication process of the MLA and the blanker plate is discussed in sections 7.4 and 7.5 and the assembly of the device is shown in 7.6.

8

Multi Beam Unit - Experimental results

The noblest pleasure is the joy of understanding.

Leonardo da Vinci

8.1 Introduction

The schematics in figure 8.1 show the optical design of a standard SEM (left) and an SEM with a multi beam unit (MBU) on the right. The designed multi beam SEM splits a $5kV$ beam into 25 beamlets that deliver $50pA$ current at the sample. In this system, the source is imaged by the C1 and C2 lenses in a plane above the Multi Beam Unit. The primary beam is split into beamlets by means of the MLA and focused in the blanker plane (or deflector array plane). All beamlets have a common crossover in the coma-free plane of the objective lens (UHR) and are focused in the sample plane. The MLA and the blanker plate need to be designed such that they fit in the Variable Aperture port, which

has a circular shape of $1cm$ in diameter. Moreover, to obtain the lens effect on the MLA and the possibility to compensate for field curvature of the outer beams, two electrodes need to be added above the MLA plate, *E1* and *E2*. The top macro electrode, called *Dec*, effectively decelerates the electron beam, before it is split and focused by the MLA. Because standard electron detectors cannot be used, we use a scintillator as sample, that converts the transmitted electrons into photons. We used a YAG (yttrium aluminium garnet) screen and we covered it with a $10nm$ Al layer, that provides a conductive surface that is sufficiently thin to let as many transmitted electrons hit the YAG screen as possible. An optical set up consisting of an objective lens and a CMOS camera is used to display the optical image, as shown in figure 8.1.

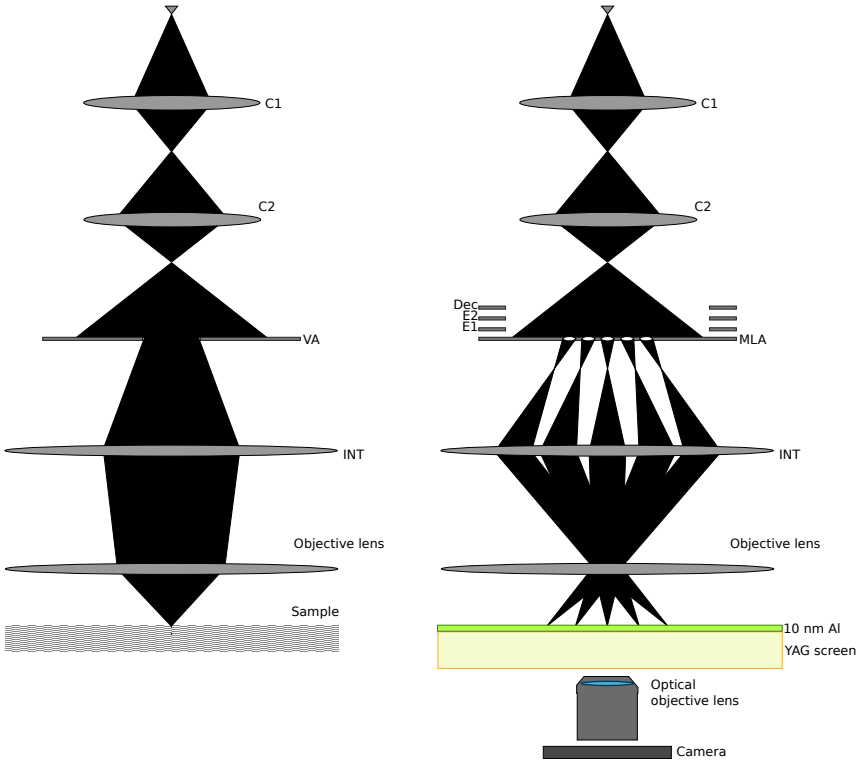

Figure 8.1: Electron optics schematic of a single beam SEM (left) and an SEM equipped with the multi beam unit (MBU).

To characterize this system by its optical properties, the on-axis aberrations were evaluated in chapter 6. On-axis aberrations include diffraction, spherical

aberration and chromatic aberrations. The smallest achievable probe size delivering $50pA$ at the sample is $1.5nm$, corresponding to a half opening angle of $14.59mrad$. The pitch at the wafer is $0.4\mu m$. Off axis aberrations are also evaluated. The contributions to the probe size are astigmatism, field curvature, coma and chromatic aberrations. The minimum probe size of the outermost beam, obtained at $14mrad$ half opening angle, is approximately $1.6nm$. Also Coulomb Interactions are evaluated: the trajectory displacement remains below $1nm$, and the Boersch effect (the energy spread) stays within $10meV$. Therefore the statistical Coulomb interactions do not pose a problem.

In chapter 7, the mechanical design of the MBU is discussed. The chip stack will contain the multi-beam splitting array as well as a conventional single aperture, to allow for single beam operation. The entire chip stack must then be enclosed into a grounded cylindrical shielding. The stack has to be inserted in the electron optical column of the SEM through the $10mm$ VA port, and it needs electrical feedthroughs. A mechanism is needed to align the MBU to the electron beam, allowing movements on the plane perpendicular to the optical axis as well as correction for the tilt and rotation.

8.2 Experimental setup

We carried out experiments to demonstrate a proof of principle of the beam splitting of the multi beam unit.

An initial step of conditioning was necessary for the macro electrodes in the multi beam unit to hold the high voltages. The set up shown in figure 8.2 was used for testing the high voltage and perform the conditioning of the electrodes. The MBU was inserted in a vacuum chamber, for which we used an old FEI FIB 200, equipped with a high voltage feedthrough flange. We connected the electrodes to a high voltage tester and the electric field between each pair of electrodes was gradually increased. No leakage current and no flashovers were detected in between Dec and E1 and in between E1 and E2. However, it was not possible to reach the $9kV/mm$ electric field necessary in between E2 and the MLA. This might be caused by dirt and particles or by the non-ideal design of the insulating spacers, where the electron path might be too short, allowing flashovers to occur. The maximum electric field that could be reached in between E2 and the MLA was $4kV/mm$.

Figure 8.3 shows the schematic of the experimental set up. The set up consists of an FEI Nova Nano Lab 650 scanning electron microscope, where the variable aperture stick is replaced with the multi beam unit (MBU). The three macro electrodes (Dec, E1 and E2) are provided with the high voltages through HV BNC connectors, that are connected to three current limiting high voltage power supplies. The electron column of the SEM is controlled via the microscope PC, where the current running through the magnetic lens coils and the voltages on the electrostatic lenses can be manually set. Also, it is possible to precisely control the gun shift and gun tilt coils to align the beam on top of the multi lens array.

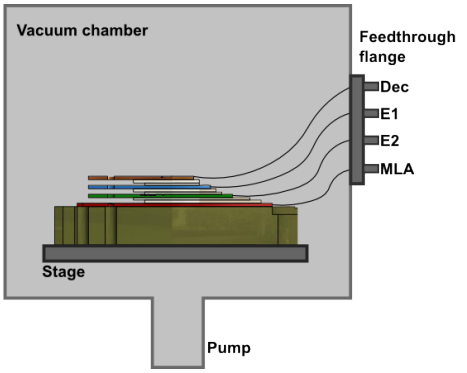

Figure 8.2: Set up for the high voltage conditioning.

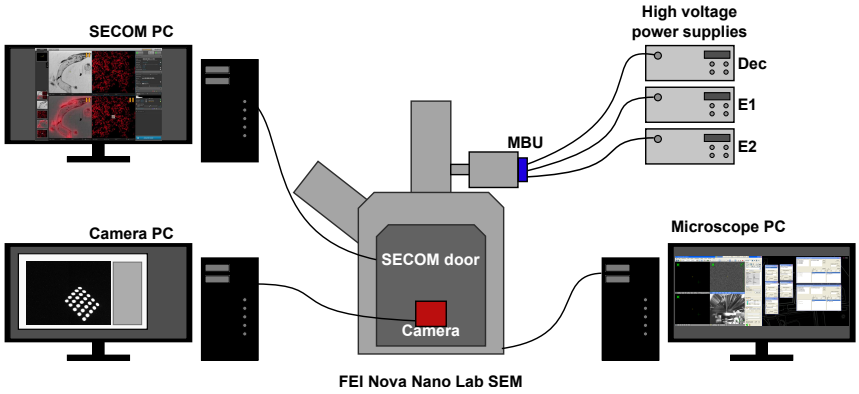

Figure 8.3: Schematics of the experimental setup. The microscope PC controls the strength of the lenses of an FEI Nova Nano Lab SEM, where the variable aperture stick is replaced with the MBU, that is connected to three high voltage power supplies for the macro electrode voltages. The SEM is equipped with a SECOM door, connected to a PC to control the sample and the optical objective lens piezo stage. A camera records the optical images that are displayed on the screen of the camera PC.

The FEI scanning electron microscope is equipped with a SECOM platform [157], that provides correlative light and electron microscopy, as shown in figure 8.4a. It consists of a vacuum compatible optical system mounted on

a custom made door. The optical objective lens collects the light emitted by the sample and collimates it into a beam that is made go outside the vacuum system by an optical path consisting of a mirror, placed below the objective lens and an optical window. Outside the chamber, a tube lens is positioned in front of the optical window and focuses the light beam onto the CMOS sensor of a camera. The SECOM platform allows simultaneous light and electron microscopy of samples that are cathodoluminescent or fluorescent. In our experimental set up, the sample consists of a YAG screen, which is a scintillator that converts the transmitted electrons, generated by the interaction of the primary beam with the sample, into photons. The YAG screen is covered with a $10nm$ layer of aluminum, to provide a conductive metal layer that is thin enough to let most of the transmitted electrons reach the YAG. Figure 8.4b shows the FEI Nova Nano Lab 650 scanning electron microscope equipped with the SECOM platform, where the optical objective and the sample stage connectors and the optical window are highlighted. The MBU is mounted in place of the variable aperture and connected to the high voltage power supplies.

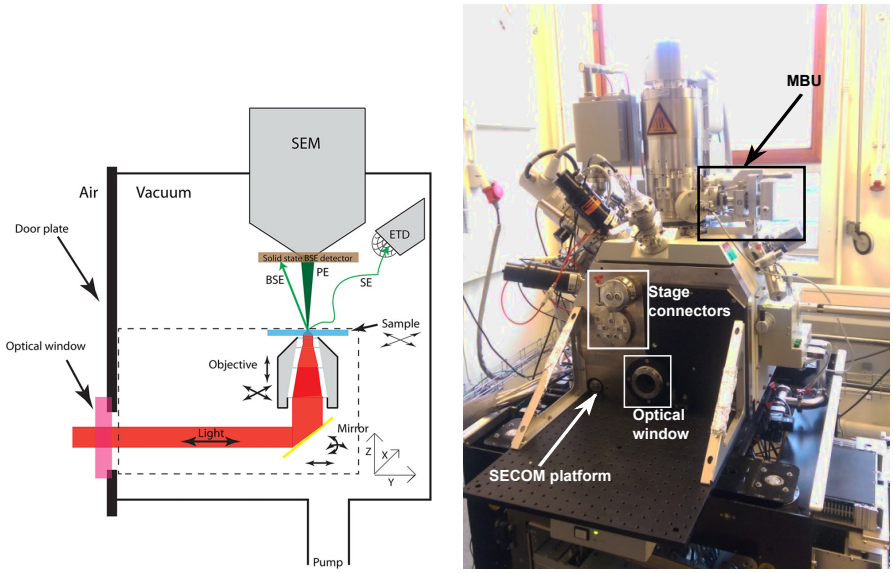

(a) (b)

Figure 8.4: (a) Schematics of a SECOM platform, that allows correlative light and electron microscopy. (b) Experimental set up.

The first part of the experiment consists in aligning the light and the electron optical systems. To achieve that, all the macro electrodes in the MBU need to be grounded and the MLA needs to be aligned with the electron optical axis, by controlling the gun tilt coils in crossover mode, using the same procedure as for aligning a standard single beam aperture. In crossover mode, the intermediate and objective lenses are switched off and the beam is focused and scanned on top of the aperture lens by the gun tilt coils. The image obtained in this mode is the shadow projection of the variable apertures. We used a 10x vacuum compatible dry objective lens and a $200mm$ tube lens in front of the optical window and mounted to a Allied Vision Prosilica GE680 camera, with a CCD sensor with resolution $640x480$ pixels, with $7.4\mu m$ pixel size. This is not sufficient, of course to judge the spot size, but it is sufficient to judge the focusing capability of the chip stack. First, the light optics system needs to be adjusted such that the sample is in the object plane of the objective lens, by moving the objective lens up or down with the objective stage controller. Then, in single beam mode, achieved by focusing all the beamlets in the same spot, the beam is kept in spot mode onto the sample surface, such that the recorded optical image shows a bright spot (corresponding to the electron beam) on a black screen. The position of the electron beam spot needs to be at the centre of the field of view, which is achieved by moving the sample stage of the SECOM platform with the stage controllers. A fine focusing of the light optical system can be done, by minimizing the size of the electron beam bright spot in the camera image.

8.3 Initial results

The macro electrodes and the multi lens array (MLA) were fabricated in the Kavli insittute nanofacility using microfabrication techniques. The electrodes were stacked together using a 6D aligner, that can achieve an accuracy of $500nm$. The macro-electrodes are electrically separated from each other by double layers of glass spacers, to reduce the risk of voltage breakdown and flashover. All electrodes were fixed by gluing them together using UV-hardening glue. Figure 8.5a shows an SEM image of the beam splitting optics stack. The electrodes are bonded to a specially designed flexible print with $30\mu m$ wires, as shown in figure 8.5b, and connected to three voltage power supplies with high voltage BNC connectors.

The MBU stack is inserted in the variable aperture port of the FEI Nova Nano Lab 650 SEM and mechanically aligned to the optical axis. First the MLA

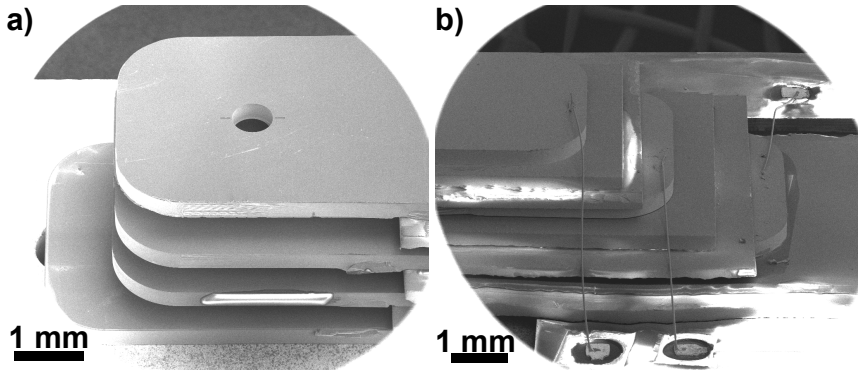

Figure 8.5: (a) An SEM image of the beam splitting optics stack, consisting of 3 macro-electrodes (on top) and the MLA (bottom). (b) An SEM image of the wire bondings that connect the electrodes to the flex print.

was imaged in crossover mode of the microscope. By changing the strength of the lens it is possible to position the C2 image plane and thus focus the beam spot exactly on the MLA plane, as shown in figure 8.6a. Figure 8.6b shows the cross-over image of the MLA, that is obtained by sufficiently reducing the scan field by decreasing the deflection range of the gun shift coils. This step is of importance, as it allows to align the aperture array to the optical axis, mechanically or by tuning the gun tilt coils. We noticed that there is some contamination visible in the central aperture, which might influence the focusing of the central beam.

Switching to imaging mode, the intermediate and the objective lenses are turned on, as shown in figure 8.7. The electrodes in the multi beam unit are still grounded, therefore there is no lens effect on the MLA, meaning that the beamlets are not focused on the blanker plane. On the contrary, the beamlets will continue diverging until they reach the intermediate lens, that will collimate the beam into the objective lens, which will focus it onto the sample surface, as depicted in figure 8.7, on the left. It is possible to collect the single beam image of the sample with the secondary electron ETD detector or the transmission image, when the sample is a scintillator covered with a thin metal film. If the beam is defocused, by weakening the strength of the objective lens for instance, as shown on the right of figure 8.7, it is possible to see the separate beams in the optical image.

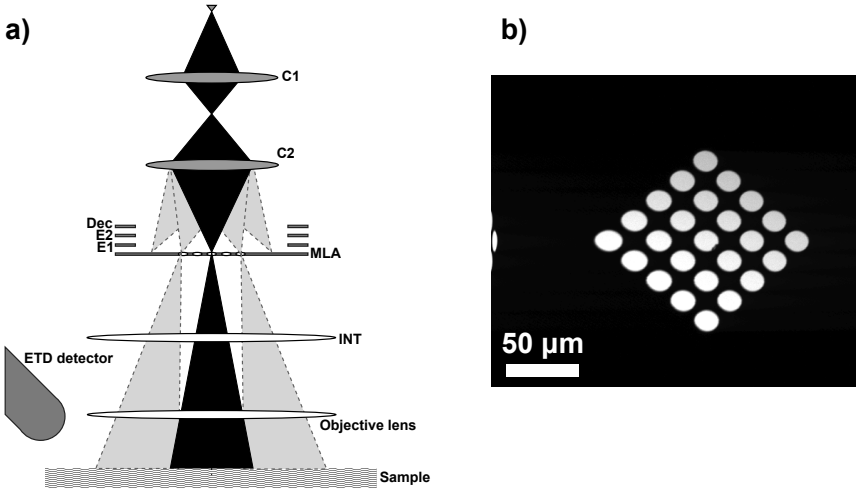

Figure 8.6: (a) Optical schematics of the system in crossover mode. (b) Cross-over mode image of the MLA, detected using the Everhart Thornly Detector, the standard SE-detector.

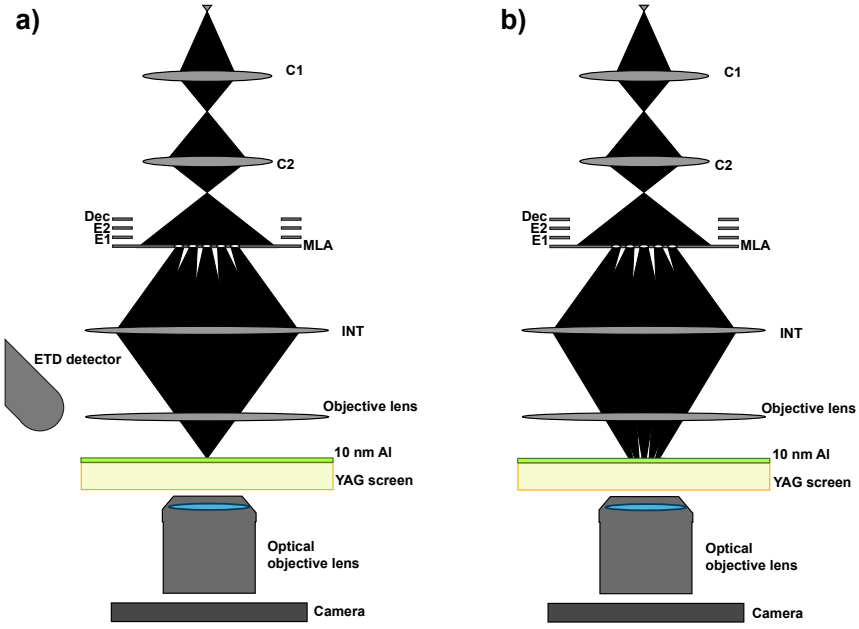

Figure 8.7: a) Optics schematics of single beam imaging in an SEM equipped with a MBU and b) the optics schematics of a defocused beam, showing the shadow image of the MLA.

Figure 8.8 shows the shadow image of the MLA, when the beam is defocused on the sample, according to the schematics of the left of figure 8.7. The lens settings adopted in this case are summarized in table 8.1. The MBU electrodes are grounded, such that there is no effect on the electron beam and the MBU behaves as a standard current limiting aperture. The INT, HR and UHR lenses are tweaked in order to defocus the beam on the sample and create the shadow image of the MLA.

MBU		Microscope	
Dec	$0V$	C1	$11306V$
E1	$0V$	C2	-
E2	$0V$	INT	0
		HR	1.775
		UHR	1

Table 8.1: Settings for the electrodes in the MBU and the lens in the microscope to create the shadow image of the MLA.

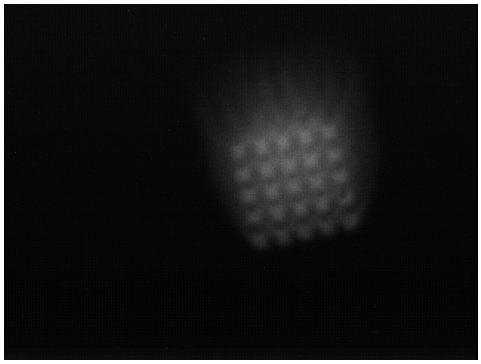

Figure 8.8: Shadow image of the MLA for the lens settings shown in table 8.1.

To test the focusing optics of the stack, the system was configured as in figure 8.9, where the beamlets are focused on the sample surface and their intensity recorded thanks to a CCD camera placed below the sample itself. The macro electrodes Dec, E1 and E2 were connected to the high voltage power supplies, with a limit in current set to $10\mu A$. The voltages were increased simultaneously, with a step of approximately $100V$ to avoid big current leakages through the electrodes that might damage them. Increasing the voltage

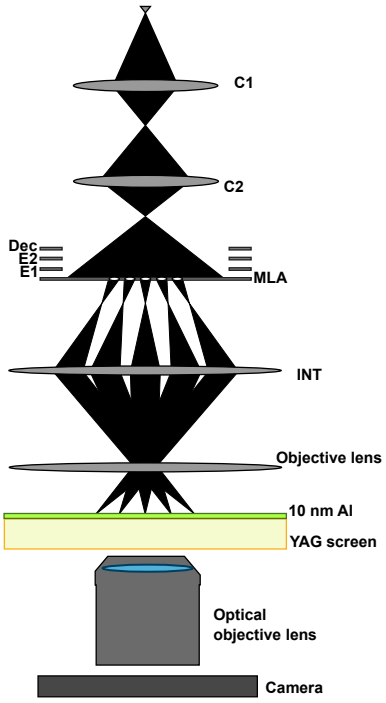

Figure 8.9: Optics schematics of the system in focusing mode.

on the first two electrodes caused the array to shift on the sample surface and eventually move out of the field of view of the optical camera. Increasing the voltage of the electrodes also caused the pitch of the beams at the sample to change. Eventually, the beams could be focused by first setting the voltages on the MBU and thereafter the strength of the intermediate and objective lens (HR and UHR). Eventually, the beams could be focused using the settings listed in table 8.2.

Figure 8.10 shows the optical image of the focused beams on the sample surface. It clearly shows 25 focused beams, having the smallest possible size that could be obtained by going through focus. Still the lens settings need to be optimized to obtain the smallest probes. In particular a thorough lens alignment procedure needs to be developed, to align the intermediate lens and the objective lens such that there is no beam shift when increasing the voltages in the MBU electrodes.

MBU		Microscope	
Dec	$180V$	C1	$1467V$
E1	$-400V$	C2	0.516
E2	$-1840V$	INT	3.798
		HR	0.17
		UHR	1.5839

Table 8.2: Settings for the electrodes in the MBU and the lens in the microscope used to focus the beams at the sample.

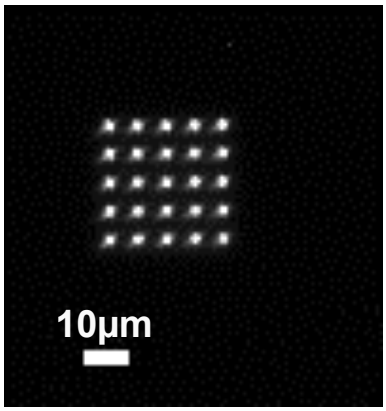

Figure 8.10: Optical image of the 25 beams focused on a YAG screen for the lens settings listed in table 8.2.

8.4 Multi beam EBID

Electron Beam Induced Deposition (EBID) is a direct write electron beam lithography technique, that does not require any resist coating nor post patterning development and processing. In EBID, a gas injection system is placed in proximity of the sample surface and a gas is let out from a nozzle. The gas is a complex molecule that can be fragmented by the interaction of a focused electron beam. From this interaction, the gas is dissociated into a volatile part that is pumped out of the system and a non volatile part that sticks to the sample surface, forming the deposit. EBID is a high resolution lithographic technique, that is also inherently slow. A way to increase the throughput of EBID is to use a multi beam scanning electron microscope (MBSEM). With the 196 MBSEM, that is briefly discussed in chapter 5, Post et al. [44] demonstrated the patterning of dots of size down to $70nm$. The new concept of multi-beam SEM that can deliver 25 focused beams at the sample, has mainly two advantages over the 196 MBSEM. First, it is flexible, meaning that the MBU can be taken out

from the microscope as a standard variable aperture stick, switching back the microscope to its original configuration. Second, it is versatile, meaning that in principle it can be used on any microscope, no matter the brand, because every microscope has a variable aperture port.

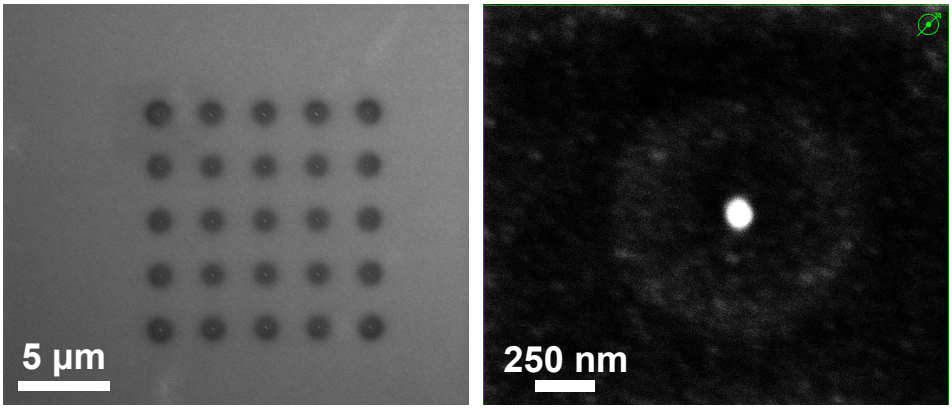

Figure 8.11: On the left, the 5x5 array of pillars deposited in the Nova Nano Lab 650 scanning electron microscope, equipped with a 25 beam MBU, in a single 5 sec exposure. On the right, zoomed-in image of one of the pillars. The diameter of the pillar is $90nm$.

We used the MBU that we designed to investigate the possibility of doing EBID in the 25 MBSEM, using the $MeCpPtMe_3$ platinum precursor. The beams were focused on the sample using the lens settings listed in table 8.2, for which we obtained the optical image of the focused beams shown in figure 8.10. The Pt-gas injection system was then inserted close to the sample surface and the gas flow was opened. The sample was exposed to the electron beam in spot mode for approximately 5 seconds. The image on the left of figure 8.11 shows a single beam SEM image, made with the TLD secondary electron detector, of a 5x5 array of pillars deposited using the Pt-precursor in a single 5 sec exposure. The pillars are visible as the white dots in the center of the black halo deposits. The image on the right of figure 8.11 shows a zoomed-in image of one of the pillars, with a diameter of approximately $90nm$.

8.5 The blanker array

It is essential that the beams can be switched on-and-off individually. First, it is possible to have only one beam down, by deflecting all the other 25, which

will effectively switch the microscope into single beam mode. This way, the focusing of the beams can be done by looking at the secondary electron image, rather than the optical image. Moreover, it is possible to use the standard door of an electron microscope, without the need of a SECOM platform. Secondly, if the beams can be driven individually, different shapes can be patterned with different beams. The possibility of implementing a blanker array in the MBU is therefore studied, as discussed in chapter 6.

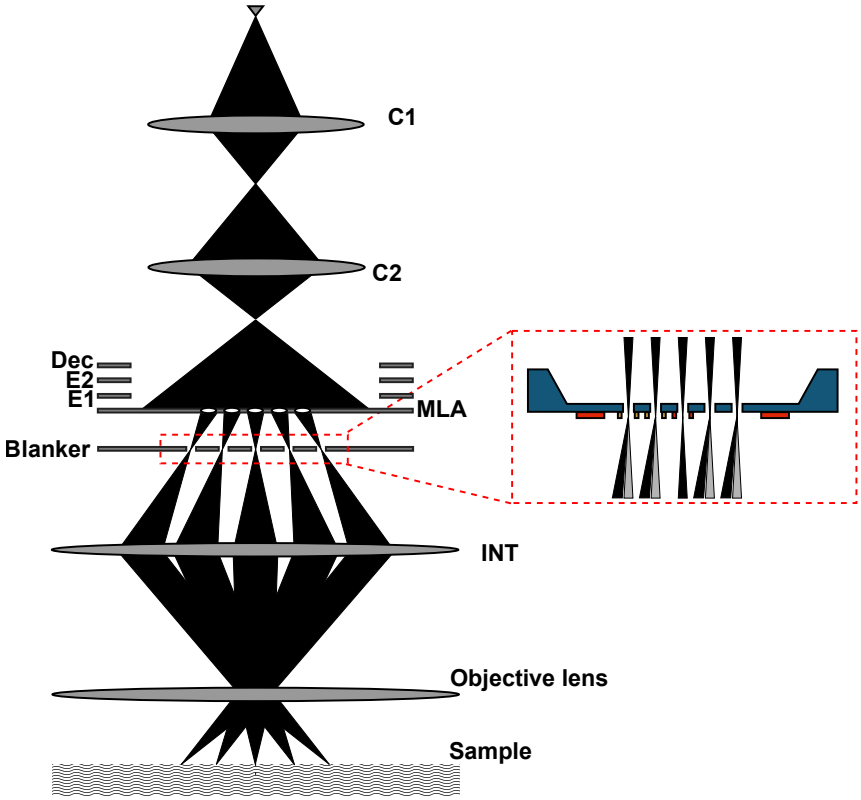

Figure 8.12: On the left, the optics schematics of a scanning electron microscope equipped with a MBU, that includes also the multi beam blanking plate. On the right, inside the red dashed box, the working principle of the multi beam blanking unit is sketched. The MBU consists of a macro electrode, that deflects all the beams, and three individual micro blankers, that can deflect one beam at the time. In red, the blankers that are switched on, in yellow the blankers that are switched off.

A second prototype is fabricated to include the blanking option as well,

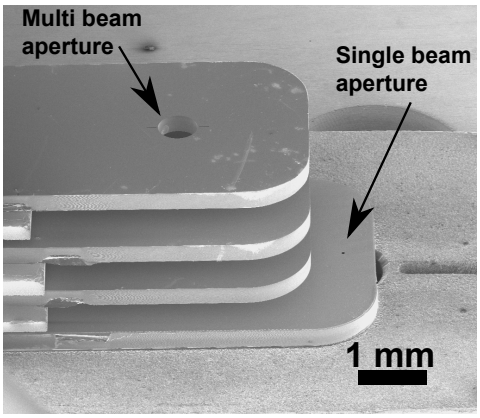

Figure 8.13: SEM micrograph of the macro electrodes stacked on top of the support of the MBU. Dec, E1, E2 and the MLA are separated by glass insulating spacers. Also, the single beam and the multi beam segments are visible.

however for the proof of concept a simpler version of a blanking unit was implemented, as described in Chapters 6 and 7, which is shown in figure 8.12. It consists of one macro blanker, that deflects all the beams, which will be stopped onto an aperture, that can be placed in the objective lens. The blanking unit consists also of three micro electrodes, placed along the diagonal from the central aperture to the outermost aperture. In this case, single beam blanking is not implemented, but in this way it will be possible to blank all the beams apart from one, which can be focused at the sample, by using the standard secondary electron detectors, rather then the optical transmission image, as if the microscope was in single beam mode.

Figure 8.13 shows the SEM micrograph of the stack of electrodes, comprising the Dec, E1 and E2 macroelectrodes and the MLA. All the elements are glued on top of the support, with glass insulating spacers in between. In this figure, the multi beam and the single beam segments are also highlighted. Next to the $30\mu m$ single beam aperture, the alignment slit, that will help in aligning the MBU to the optical axis, is also visible. Figure 8.14 shows a top view SEM image of the stack of electrodes, and a zoomed in image of the MLA, that is visible through the $600\mu m$ aperture of the macro electrodes.

The blanker plate is mounted on the back side of the MBU support, with the blanking electrodes facing down. Figure 8.15a shows an SEM image of the blanker plate, showing the region with the macro deflectors and the three micro electrodes. The electrodes are made of Al-Si (1%) and are insulated from the silicon substrate with a $1\mu m$ layer of SiC. Figure 8.15b shows the connector

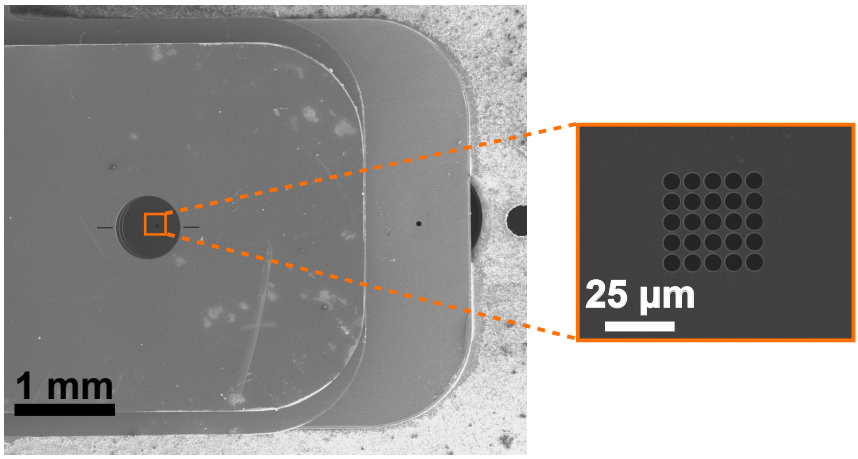

Figure 8.14: Top view SEM image of the stack of electrodes glued on top of the support of the MBU. The multi beam lens array (MLA) is visible and highlighted on the right. Next to it, the 30μm single beam aperture.

side, where the micro and macro deflectors are bonded with 30μm wires to the flex printed PCB.

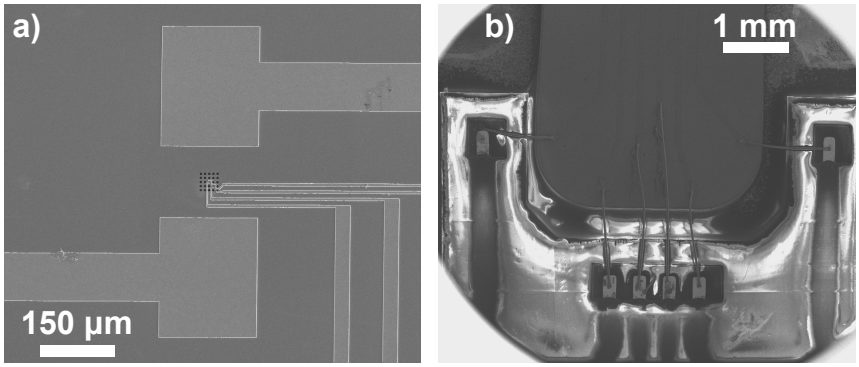

Figure 8.15: a) SEM micrograph of the macro and micro deflectors and b) the connection side of the blanker plate, where the macro and micro blankers are connected to the flex printed PCB.

Figures 8.16a and 8.16b show respectively the zoomed-in top view and tilted images of the three micro blankers, consisting of the common ground electrode and the three deflecting electrodes. The 5x5 array has apertures of a diameter of 4μm at a pitch of 8.58μm, etched away from a silicon device layer of 10μm

thickness.

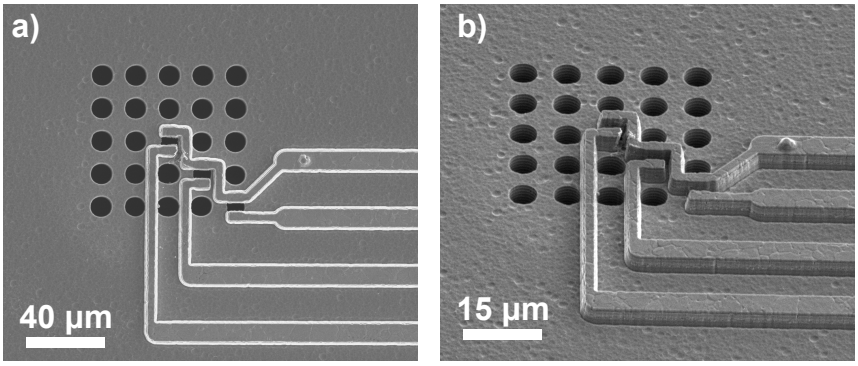

Figure 8.16: a) SEM micrograph of the 5x5 array of $4\mu m$ apertures and b) the three micro blankers, consisting of the common ground electrode and the three blanking electrodes.

Figure 8.17 shows a zoomed-in SEM image of the three blankers, with the sample tilted. The first blanking electrode on the top-left corner of the image, might be probably connected to the ground electrode, as can be seen in the SEM image. To avoid a short between the two electrodes, it is advised to mill away materials in between the two electrodes with an ion beam. The second and third micro blankers seem to be well separated. From this image it is also possible to distinguish the $1\mu m$ SiC insulating layer and the $2\mu m$ aluminum layer. The threads inside the apertures holes are characteristic of the Bosch etching process, that was used to open up the apertures.

8.5.1 Voltage test on the blanker electrodes

A test experiment was carried out to verify that the macro electrodes and micro electrodes can hold the voltages that are necessary to deflect the beams. Figure 8.18 and 8.19 show the SEM micrographs of the blanker array when a voltage is applied to the electrodes E1 and E2 respectively. In the case of E1, it was possible to apply $5V$, $10V$, $15V$ and $20V$ on E1 without having breakdowns. The SEM images of figure 8.18 are taken with the ETD detector, that collects the secondary electrons. When a voltage is applied to an electrode, it changes in intensity, meaning that the number of secondary electrons that are emitted changes. When E1 is set to $5V$, also the E2 electrode changes in contrast, meaning that the two electrodes are connected. Because there is no

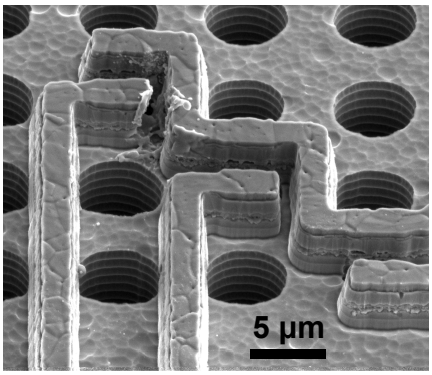

Figure 8.17: SEM micrograph of the three micro blankers. The first blanking electrode on the top left corner seems to be connected to the common ground electrode. To avoid shorts, it is advised to remove material by ion-milling.

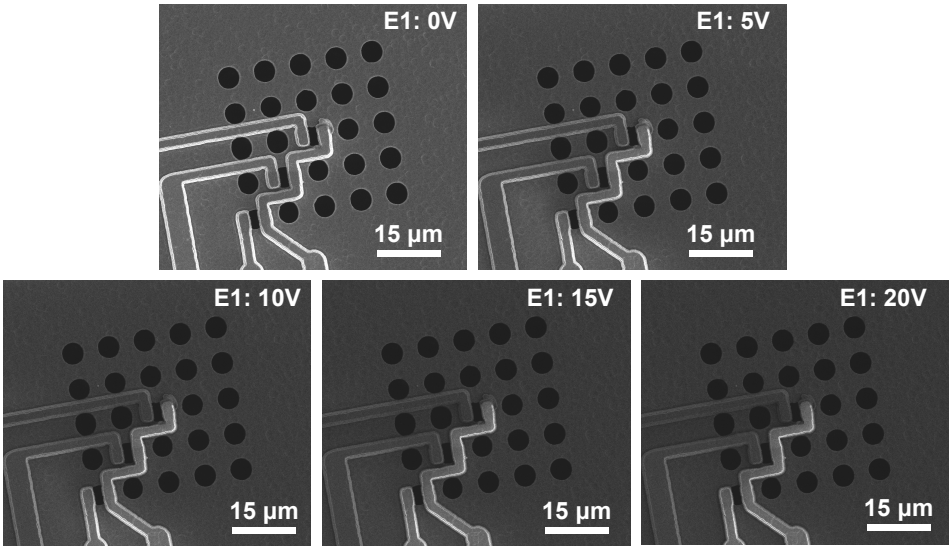

Figure 8.18: SEM micrographs of the blanker array showing the E1, E2 and E3 electrodes when a voltage is applied to the E1 electrode.

visible connection between the two wirings on the blanker plate, we suspect that the external feedthrough was not properly connected. In case of electrode E3, a voltage up to $10V$ was applied as shown in figure 8.14. In this case, no breakdown was visible.

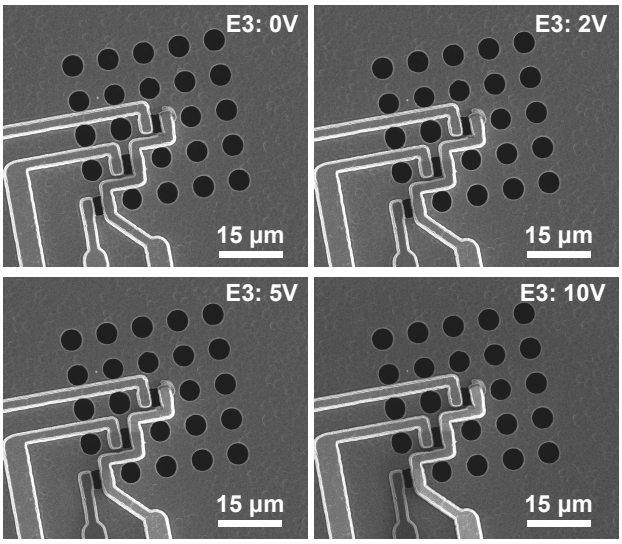

Figure 8.19: SEM micrographs of the blanker array showing the E1, E2 and E3 electrodes when a voltage is applied to the E3 electrode.

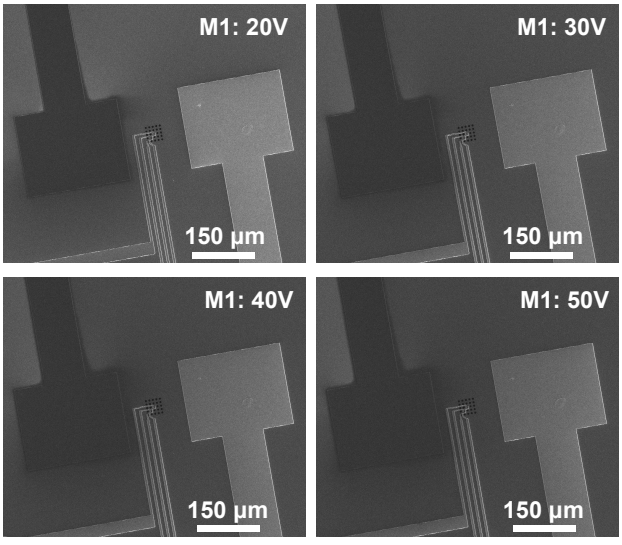

Figure 8.20: SEM micrographs of the blanker array showing the M1 and M2 electrodes and the micro electrodes when a voltage is applied to the M1 electrode.

Figures 8.20 and 8.21 show the SEM micrograph of the macro electrodes M1 and M2 when voltages are applied to M1 and M2 respectively. In figure 8.21, a

zoomed in image shows the micro blankers when a voltage of $50V$ is applied to M2. Also in this case the electrodes can hold the voltages well.

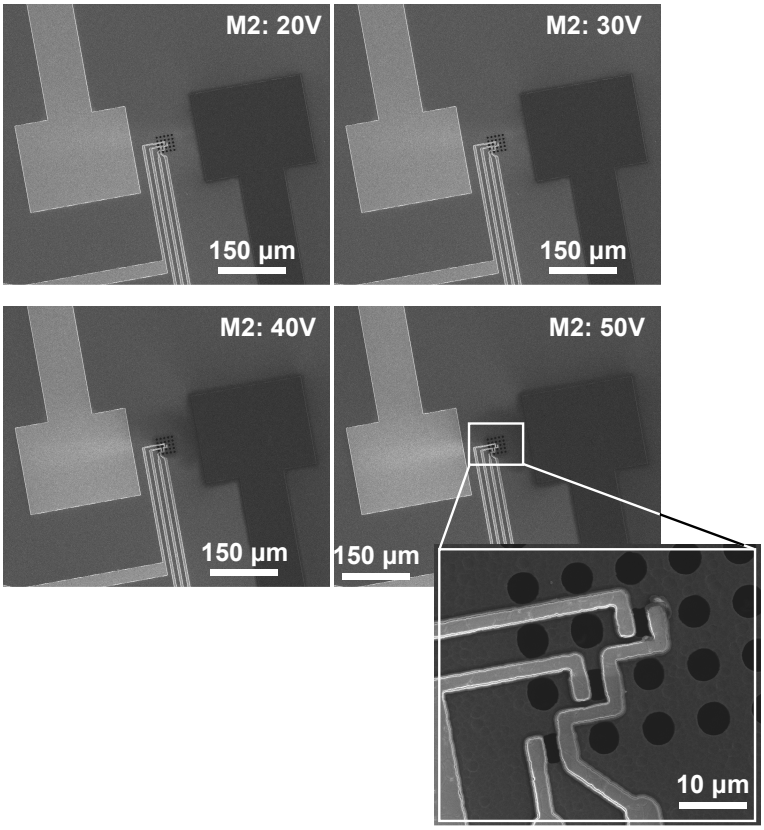

Figure 8.21: SEM micrographs of the blanker array showing the M1 and M2 electrodes and the micro electrodes when a voltage is applied to the M2 electrode.

8.6 Conclusions

A multi beam unit (MBU) was designed and developed. The MBU can be inserted in the variable aperture port of a scanning electron microscope and can split the beam into 25 beamlets. The MBU consists of three macro electrodes and a micro lens array (MLA), that has an array of 5×5 apertures of $5\mu m$ diameter at a pitch of $7.5\mu m$. First, the image of the MLA in crossover mode was shown. In this case, the macro electrodes of the MBU are connected to ground. In crossover mode, the intermediate and the objective lenses are switched off

and the beam is focused and scanned on the MLA. Secondly, we presented the shadow image of the MLA, obtained by effectively defocusing the beam at the sample, when the macro electrodes on the MBU are connected to ground. Initial EBID experiments were carried out with the MBU. The beamlets were focused on the sample surface, which was a YAG screen covered with a $10nm$ layer of aluminum. The minimum size of the deposited pillars was approximately $90nm$. Lastly, the blanker array was tested. A simplified version of the blanker was fabricated, where only three microdeflectors around three apertures were patterned, together with 2 macrodeflectors. This simplified device serves as initial proof of concept of the blanker unit. To test the microdeflectors high voltages were applied to the micro-electrodes, to test for electrical insulation. The experiments presented in this chapter are first preliminary proof-of-concept studies. Unfortunately, no further tests and experiments could be performed within this PhD program because of lack of time. Future improvements and studies may include:

1. The **optimization of the MBU design**. This comprises the following items:

   (a) The aperture in the shielding. Is the aperture sufficiently large not to influence the electric field in the proximity of the optical axis above the E1 electrode?

   (b) Electrode E2. This electrode, as described in chapter 6, serves to correct for field curvature. After an experimental verification of the theoretical calculations, an evaluation on a possible removal of the E2 electrode should be carried out. This may imply less strict requirements on the geometrical design of the unit.

2. The development of a robust **alignment strategy**, with which the MBU can be aligned with the lenses in the column. Providing good alignment is essential not only for achieving the theoretical performance described in chapter 6, but most importantly to correctly align the splitter and the blanker plate to prevent the beamlets not to be stopped on the blanker plate itself.

3. The development of a **focusing strategy** to focus the beamlets onto the sample surface in the smallest probe possible, obtained by optimizing the voltages on the macro-electrodes in the MBU.

4. Experiments to determine the **probe size** of the beamlets, using a knife edge sample.

5. Experiments on the **micro and macro-blankers**. In a first prototype, the design of the blanker array was changed to a simple one, where all the beamlets were deflected by macro-blankers and only three apertures had micro-deflectors to bring the beamlets back to the original path, one beamlet at a time. The performance of such a device was studied in chapter 6 using the simulation package COMSOL and should have an experimental proof. This device will also help in the determination of the probe size of each beamlet, since it allows one beam at a time on the sample.

6. Design and fabrication of the **blanker array**. The challenge in the fabrication of the blanker array lies in the fact that the electrodes must be positioned close to each other and must be connected to the outside world with leads. Each electrode has specific requirements on the geometry to fulfill in order to deflect the beamlets with a sufficient deflecting angle. What is the best way to design the blanker array to fulfill these requirements? And what is the right process to fabricate these electrodes?

7. **Imaging of structures with improved throughput**. The MBU increases the throughput of a standard scanning electron microscope by a factor of 25. The imaging of samples can be done in transmission mode, using a YAG screen, for instance, as scintillator and a SECOM platform. With this method, however, only samples with very thin sections can be imaged. Alternatively, it is possible to implement a secondary electron imaging system to collect SE images of bulk samples, as described by Ren [32].

8. **Deposition of structures by EBID with increased throughput**. The MBU not only brings the advantage of increased throughput compared to a single beam SEM, but also the possibility of blanking each beam individually. This gives the freedom of patterning 25 different structures with the 25 beamlets.

9. **Control and integration of the MB-SEM**. The development of a control program to integrate and facilitate the use of the MBU and the microscope as if it was one element.

9

Conclusions

While the semiconductor industry is nowadays driven by the predictions of Moore's low, resist-based lithographic techniques, such as photolithography, are facing difficulties in providing sub-10nm resolution. The European project Single Nanometer Manufacturing for beyond CMOS devices (SNM) is aimed at achieving that, using Nanoimprint Lithography (NIL). NIL is a high throughput and low cost lithographic technique that is suitable for the mass production of electronic devices. Patterns are created by a mechanical deformation of the NIL resist by imprinting a stamp with pre-patterned features. NIL stamps can be fabricated using both Scanning Probe Lithography (SPL) or Electron Beam Induced Deposition (EBID). Both SPL and EBID are high resolution lithographic techniques that are, however, limited by low throughput. The speed of EBID can be enhanced by employing multi beam scanning electron microscopes (MBSEM), where up to 196 beams can be delivered to the sample.

This thesis is driven by the need of fabricating high resolution NIL stamps using EBID in combination with a high throughput multi-electron beam system.This work can be divided into three parts that are respectively focused on EBID, NIL and MBSEM. In the first part, we present the fabrication characterization of electronic devices and on the pattern transfer of EBID structures. The

second part is focused on experiments where NIL stamps were made by electron beam induced deposition. Lastly, we show the design and fabrication of a multi beam blanking unit (MBU), that is capable of turning a single beam SEM into a MBSEM.

In chapter 2 we demonstrated that electron beam induced deposition is a valid technique for the fabrication of electronic devices in the sub-10 nm range. In order to achieve high resolution patterning, it becomes necessary to optimize a large group of parameters, which include electron beam settings, geometry of the set up (such as working distance and the position of the gas nozzle), operation conditions of the SEM (such as base vacuum), the choice of gas precursor and writing strategy. We have demonstrated that a single electron transistor operating at room temperature can be made by EBID following a precise patterning strategy. This final device consists of extensions to the two pre-patterned source and drain contacts and a nanodot fabricated using EBID. The gaps are estimated to be 9.7 nm and 4.5 nm, with the dot diameter being 22.5 nm.

The pattern transfer into an underlying layer of sub-10 nm EBID patterns can enhance the aspect ratio of these structures and it is suitable for the fabrication of NIL stamps. In chapter 3, we demonstrated that EBID patterns can be transferred into an underlying silicon layer using a fluorine based etching. With this chemistry, lines as small as 7.4 nm were transferred with a height ratio of about 8, achieving good results in terms of surface smoothness.

The pattern transfer is suitable for the fabrication of NIL stamps, where the thin sub-10 nm EBID structures can be transferred into an underlying UV-transparent layer. Typically, glass substrates are used as a NIL stamp, but they are not suitable for electron beam induced deposition because they are not conductive. While ITO (indium-tin-oxide) was proven to have a good etching selectivity with respect to the EBID deposits, it presents a surface roughness that is not compatible with sub-10 nm patterning. TiN is preferred not only because it is a conductive UV-transparent material but also because it can be deposited by ALD, leading to atomically flat surfaces. It is finally shown that a promising approach to fabricate NIL stamps is to pattern EBID structures on top of a TiN layer, deposited on a silicon dioxide covered wafer.

Chapter 4 focused on the fabrication of NIL stamps, which was done in two ways: by direct writing on the NIL stamp material or by replicating a master containing the structures to imprint. We fabricated a master containing EBID structures from which a replica was made and used as a NIL stamp. We measured that the width of the patterned EBID lines was larger than that of the

imprinted ones. This could be an artifact introduced in the fabrication of the replica, where the lateral fidelity is lost. On the other hand, the height remained constant, from the first imprint to the last imprint, within the 1σ value. In a second stage, we decided to investigate the direct write approach. The preferred material to coat the glass template with, to make it conducting, is molybdenum. In this case, lines with width down to 8 nm were patterned. After the imprint, we measured that the line width was in general maintained within the 1σ value of the original measurement, but the height of the structures was considerably reduced, up to a factor of about 50%.

In the first MBSEM developed in Delft, the source module was modified to contain a multi beam splitter, capable of generating 196 beams. The control of such a multi beam source module requires an additional FEG Source Control Unit (FGSU), resulting in a complicated system to operate. Chapter 5 reports on the integration of the electronic control, which was successfully implemented by running a Labview program that allows the user to easily control the multi-beam source module.

At the time when this work started, the 196 MBSEM did not include the option to individually blank the beamlets. The demand of a blanking unit gave rise to the study into a new design of a multi-beam SEM. While we soon realized that the source module was not the preferred location for the blanking unit, the idea of having a multi beam splitting and blanking unit (MBU) that could be easily inserted in, and retracted from, the variable aperture port was more attractive. Integrating a single beam aperture in the MBU as well, allows for easily switching between single-beam mode and multi-beam mode.

Chapter 6 deals with the design of a multi beam unit with the following requirements: each beamlet should carry a current of a 50 pA current in a total probe size smaller than 5 nm and there should be at least 25 beamlets. The system must be designed to have a common cross-over in the final lens, to minimize the off-axis aberration contributions of the final lens to the probe size. Moreover, if the cross-over is positioned in the coma-free plane of the objective lens, then the contribution of coma of this lens to the probe size is negligible. At the beginning of this chapter, we compared three different versions of MBU, where the main difference is the inclination with which the beamlets travel from the MLA to the blanker array. From this evaluation, we demonstrated that the option that gives the best performance is that where the beams are traveling outwards. In this situation, the number of beams is maximized, at the cost of having a different aperture pitch on the MLA and on the blanker plate. On the other hand, a larger pitch at the blanker translates into more

space for the blanking electrodes and the wiring. The optimization of the MBU design included the fine tuning of parameters such as the distance between the MLA and the blanker, the position of the MLA from the top edge of the variable aperture, the acceleration voltage and the beam current, the size of the MLA apertures and the working distance. The final design was then characterized in terms of on-axis aberrations and off-axis aberrations. The MBU can split a 5 kV beam into 25 beamlets and focus them at the sample with 50 pA current into a 1.63 nm probe. A pessimistic simplified calculation of the stochastic Coulomb interactions between the MLA and the sample resulted in a negligible contribution to the total probe size.

Given the limited time left before the end of this work, the design of the blanker was dramatically simplified to limit the challenges in the fabrication step. The blanker was designed to have one macro electrode and three micro electrodes on the center apertures and the two diagonal neighboring apertures. In this way, all the beams can be deflected away and stopped onto an aperture positioned in the final lens, while one is "un-blanked" by the micro-blanker and exposes the sample. Simulations of this device prove the working principle of this device and demonstrate that the crosstalk is negligible.

The mechanical design and the fabrication of the MBU components is presented in Chapter 7. The MBU consists of three macro electrodes, a multi lens array (MLA) and a blanker array. The elements are assembled together and mounted on a support connected to an alignment tool for the positioning of the unit at the center of the optical axis of the electron optical system. The alignment can be done in X, Y and Z and correction of the rotation around X and Y is also allowed for with an accuracy of 0.005 mm and 3 mrad respectively. Because a single beam aperture is placed on the splitter plate, the total stroke in X is as long as 2.5 mm to be able to reach it. A process flow was developed for the fabrication of the MLA, using a SOI (silicon on insulator) wafer, where the 5 μm apertures were fabricated using a Bosch etch. A good process was also found to fabricate the blanker arrays in silicon, were the electrodes are patterned using a wafer stepper.

Initial proof-of-concept experiments were carried out to demonstrate the main functionality of the MBU. Using a first prototype that did not include the blanker array, a shadow image of the MLA was obtained by using the microscope in single beam mode, with the macro electrodes in the MBU connected to ground and defocusing the beam. As a sample, we used a YAG screen coated with aluminum. The YAG screen is a scintillator that converts electrons into photons, that are then collected by an objective lens and detected by a CCD

camera of a SECOM platform. Focusing the beam is not trivial and initial attempts show that pillars of 90 nm width could be patterned by EBID.

Despite the initial promising results, we foresee many improvements to the current design of MBU. First of all, we did not consider the influence of the shielding on the beam at ground potential and to what extent the beam is disturbed by it. Then, a robust alignment procedure must be developed in order to align the MBU to the electron optical axis as well as a focusing strategy to find the best focus settings. Initial voltage tests on the blanker unit demonstrate the functionality of this device, which can in the future be used to determine for instance the probe size of one beam at a time.

We believe that the development of a versatile multi-beam add-on for SEM will attract great attention in the future and can find its application also in the field of biology research as well as in the semiconductor industry. The development of multi-beam SEM will speed up not only lithography, but also the imaging of large structures at high resolution, provided a good electron detection system is available.

References

[1] "Single Nanometer Manufacturing for beyond CMOS devices (SNM)." https://www.tu-ilmenau.de/snm-project. Accessed: 2019-01-28.

[2] G. E. Moore, "Cramming more components onto integrated circuits," *Electronics*, vol. 38, p. 114, 1965.

[3] R. P. Feynman, "There's plenty of room at the bottom: An invitation to enter a new field of physics," in *Handbook of Nanoscience, Engineering, and Technology, Third Edition*, pp. 26–35, CRC Press, 2012.

[4] R. H. Dennard, F. H. Gaensslen, V. L. Rideout, E. Bassous, and A. R. LeBlanc, "Design of ion-implanted mosfet's with very small physical dimensions," *IEEE Journal of Solid-State Circuits*, vol. 9, no. 5, pp. 256–268, 1974.

[5] M. Bohr, "A 30 year retrospective on dennard's mosfet scaling paper," *IEEE Solid-State Circuits Society Newsletter*, vol. 12, no. 1, pp. 11–13, 2007.

[6] R. R. Schaller, "Moore's law: past, present and future," *IEEE spectrum*, vol. 34, no. 6, pp. 52–59, 1997.

[7] C. A. Mack, "Keynote: Moore's law 3.0," in *Microelectronics and Electron Devices (WMED), 2013 IEEE Workshop on*, pp. xiii–xiii, IEEE, 2013.

[8] J. H. Bruning, "Optical lithography: 40 years and holding," in *Optical Microlithography XX*, vol. 6520, p. 652004, International Society for Optics and Photonics, 2007.

[9] C. Mack, *Fundamental principles of optical lithography: the science of microfabrication*. John Wiley & Sons, 2008.

[10] S. Owa and H. Nagasaka, "Immersion lithography; its potential performance and issues," in *Optical Microlithography XVI*, vol. 5040, pp. 724–734, International Society for Optics and Photonics, 2003.

[11] M. Mirsaeedi, J. A. Torres, and M. Anis, "Self-aligned double-patterning (sadp) friendly detailed routing," in *Design for Manufacturability through Design-Process Integration V*, vol. 7974, p. 79740O, International Society for Optics and Photonics, 2011.

[12] C. Wagner and N. Harned, "Euv lithography: Lithography gets extreme," *Nature Photonics*, vol. 4, no. 1, p. 24, 2010.

[13] S. Y. Chou, P. R. Krauss, and P. J. Renstrom, "Nanoimprint lithography," *Journal of Vacuum Science & Technology B: Microelectronics and Nanometer Structures Processing, Measurement, and Phenomena*, vol. 14, no. 6, pp. 4129–4133, 1996.

[14] L. Guo, "Nanoimprint Lithography: Methods and Material Requirements," *Advanced Materials*, vol. 19, pp. 495–513, feb 2007.

[15] H. Schift, "Nanoimprint lithography: An old story in modern times? a review," *Journal of Vacuum Science & Technology B: Microelectronics and Nanometer Structures Processing, Measurement, and Phenomena*, vol. 26, no. 2, pp. 458–480, 2008.

[16] D. Wagner and A. Jayatissa, "Nanoimprint lithography: Review of aspects and applications," in *Nanofabrication: Technologies, Devices, and Applications II*, vol. 6002, p. 60020R, International Society for Optics and Photonics, 2005.

[17] S. Zankovych, T. Hoffmann, J. Seekamp, J. Bruch, and C. S. Torres, "Nanoimprint lithography: challenges and prospects," *Nanotechnology*, vol. 12, no. 2, p. 91, 2001.

[18] C. Vieu, F. Carcenac, A. Pepin, Y. Chen, M. Mejias, A. Lebib, L. Manin-Ferlazzo, L. Couraud, and H. Launois, "Electron beam lithography: resolution limits and applications," *Applied surface science*, vol. 164, no. 1-4, pp. 111–117, 2000.

[19] W. Van Dorp and C. W. Hagen, "A critical literature review of focused electron beam induced deposition," *Journal of Applied Physics*, vol. 104, no. 8, p. 10, 2008.

[20] S. Randolph, J. Fowlkes, and P. Rack, "Focused, nanoscale electron-beam-induced deposition and etching," *Critical reviews in solid state and materials sciences*, vol. 31, no. 3, pp. 55–89, 2006.

[21] I. Utke, P. Hoffmann, and J. Melngailis, "Gas-assisted focused electron beam and ion beam processing and fabrication," *Journal of Vacuum Science and Technology B: Microelectronics and Nanometer Structures Processing, Measurement, and Phenomena*, vol. 26, no. 4, pp. 1197–1276, 2008.

[22] N. Silvis-Cividjian and C. W. Hagen, "Electron-beam–induced nanometer-scale deposition," *Advances in Imaging and Electron Physics*, vol. 143, pp. 1–235, 2006.

[23] C. Hagen, "The future of focused electron beam-induced processing," *Applied Physics A*, vol. 117, no. 4, pp. 1599–1605, 2014.

[24] I. Utke, S. Moshkalev, and P. Russell, *Nanofabrication using focused ion and electron beams: principles and applications*. Oxford University Press, 2012.

[25] M. Huth, F. Porrati, C. Schwalb, M. Winhold, R. Sachser, M. Dukic, J. Adams, and G. Fantner, "Focused electron beam induced deposition: A perspective," *Beilstein journal of nanotechnology*, vol. 3, no. 1, pp. 597–619, 2012.

[26] M. Huth, F. Porrati, and O. V. Dobrovolskiy, "Focused electron beam induced deposition meets materials science," *Microelectronic Engineering*, vol. 185, pp. 9–28, 2018.

[27] P. D. Prewett, C. W. Hagen, C. Lenk, S. Lenk, M. Kaestner, T. Ivanov, A. Ahmad, I. W. Rangelow, X. Shi, S. A. Boden, *et al.*, "Charged particle single nanometre manufacturing," *Beilstein journal of nanotechnology*, vol. 9, no. 1, pp. 2855–2882, 2018.

[28] M. Wieland, G. de Boer, G. ten Berge, R. Jager, T. van de Peut, J. Peijster, E. Slot, S. Steenbrink, T. Teepen, A. van Veen, *et al.*, "Mapper: high-throughput maskless lithography," in *Alternative Lithographic Technologies*, vol. 7271, p. 72710O, International Society for Optics and Photonics, 2009.

[29] G. de Boer, M. Dansberg, R. Jager, J. Peijster, E. Slot, S. Steenbrink, and M. Wieland, "Mapper: progress toward a high-volume manufacturing system," in *Alternative Lithographic Technologies V*, vol. 8680, p. 86800O, International Society for Optics and Photonics, 2013.

[30] I. Servin, M.-L. Pourteau, J. Pradelles, P. Essomba, L. Lattard, P. Brandt, and M. Wieland, "Progress and process improvements for multiple electron-beam direct write," *Japanese Journal of Applied Physics*, vol. 56, no. 6S1, p. 06GC03, 2017.

[31] A. Eberle, S. Mikula, R. Schalek, J. Lichtman, M. K. Tate, and D. Zeidler, "High-resolution, high-throughput imaging with a multibeam scanning electron microscope," *Journal of microscopy*, vol. 259, no. 2, pp. 114–120, 2015.

[32] Y. Ren, *Imaging systems for the Delft multi-beam scanning electron microscope 1*. PhD thesis, Delft University of Technology, 2017.

[33] I. Utke, P. Hoffmann, B. Dwir, K. Leifer, E. Kapon, and P. Doppelt, "Focused electron beam induced deposition of gold," *Journal of Vacuum Science & Technology B: Microelectronics and Nanometer Structures Processing, Measurement, and Phenomena*, vol. 18, no. 6, pp. 3168–3171, 2000.

[34] W. Van Dorp, X. Wu, J. Mulders, S. Harder, P. Rudolf, and J. De Hosson, "Gold complexes for focused-electron-beam-induced deposition," *Langmuir*, vol. 30, no. 40, pp. 12097–12105, 2014.

[35] R. Córdoba, N. Sharma, S. Kölling, P. M. Koenraad, and B. Koopmans, "High-purity 3d nano-objects grown by focused-electron-beam induced deposition," *Nanotechnology*, vol. 27, no. 35, p. 355301, 2016.

[36] R. Córdoba, J. Sesé, J. De Teresa, and M. R. Ibarra, "High-purity cobalt nanostructures grown by focused-electron-beam-induced deposition at low current," *Microelectronic Engineering*, vol. 87, no. 5-8, pp. 1550–1553, 2010.

[37] W. F. van Dorp, B. van Someren, C. W. Hagen, P. Kruit, and P. A. Crozier, "Approaching the Resolution Limit of Nanometer-Scale Electron Beam-Induced Deposition," *Nano Letters*, vol. 5, pp. 1303–1307, jul 2005.

[38] J. C. van Oven, F. Berwald, K. K. Berggren, P. Kruit, and C. W. Hagen, "Electron-beam-induced deposition of 3-nm-half-pitch patterns on bulk Si," *Journal of Vacuum Science and Technology B: Microelectronics and Nanometer Structures*, vol. 29, no. 6, p. 06F305, 2011.

[39] N. Silvis-Cividjian, C. Hagen, L. Leunissen, and P. Kruit, "The role of secondary electrons in electron-beam-induced-deposition spatial resolution," *Microelectronic engineering*, vol. 61, pp. 693–699, 2002.

[40] N. Silvis-Cividjian, C. Hagen, and P. Kruit, "Spatial resolution limits in electron-beam-induced deposition," *Journal of Applied Physics*, vol. 98, no. 8, p. 084905, 2005.

[41] H. Plank, D. A. Smith, T. Haber, P. D. Rack, and F. Hofer, "Fundamental proximity effects in focused electron beam induced deposition," *ACS nano*, vol. 6, no. 1, pp. 286–294, 2011.

[42] K. Mitsuishi, M. Shimojo, M. Takeguchi, M. Tanaka, and K. Furuya, "Proximity effect in electron-beam-induced deposition," *Japanese journal of applied physics*, vol. 45, no. 6S, p. 5517, 2006.

[43] W. Van Dorp, S. Lazar, C. Hagen, and P. Kruit, "Solutions to a proximity effect in high resolution electron beam induced deposition," *Journal of Vacuum Science & Technology B: Microelectronics and Nanometer Structures Processing, Measurement, and Phenomena*, vol. 25, no. 5, pp. 1603–1608, 2007.

[44] P. C. Post, A. Mohammadi-Gheidari, C. W. Hagen, and P. Kruit, "Parallel electron-beam-induced deposition using a multi-beam scanning electron microscope," *Journal of Vacuum Science and Technology B: Microelectronics and Nanometer Structures*, vol. 29, no. 6, p. 06F310, 2011.

[45] A. Mohammadi-Gheidari and P. Kruit, "Electron optics of multi-beam scanning electron microscope," *Nuclear Instruments and Methods in Physics Research Section A: Accelerators, Spectrometers, Detectors and Associated Equipment*, vol. 645, pp. 60–67, jul 2011.

[46] A. Mohammadi-Gheidari, C. W. Hagen, and P. Kruit, "Multibeam scanning electron microscope: Experimental results," *Journal of Vacuum Science & Technology B: Microelectronics and Nanometer Structures*, vol. 28, no. 6, p. C6G5, 2010.

[47] J. Mulders, "Practical precursor aspects for electron beam induced deposition," *Nanofabrication*, vol. 1, no. 1, 2014.

[48] A. Botman, J. Mulders, and C. Hagen, "Creating pure nanostructures from electron-beam-induced deposition using purification techniques: a technology perspective," *Nanotechnology*, vol. 20, no. 37, p. 372001, 2009.

[49] A. Botman, J. Mulders, R. Weemaes, and S. Mentink, "Purification of platinum and gold structures after electron-beam-induced deposition," *Nanotechnology*, vol. 17, no. 15, p. 3779, 2006.

[50] H. Plank, J. H. Noh, J. D. Fowlkes, K. Lester, B. B. Lewis, and P. D. Rack, "Electron-beam-assisted oxygen purification at low temperatures for electron-beam-induced pt deposits: towards pure and high-fidelity nanostructures," *ACS applied materials & interfaces*, vol. 6, no. 2, pp. 1018–1024, 2014.

[51] B. B. Lewis, M. G. Stanford, J. D. Fowlkes, K. Lester, H. Plank, and P. D. Rack, "Electron-stimulated purification of platinum nanostructures grown via focused electron beam induced deposition," *Beilstein journal of nanotechnology*, vol. 6, no. 1, pp. 907–918, 2015.

[52] S. Mehendale, J. Mulders, and P. Trompenaars, "Purification of au ebid structures by electron beam post-irradiation under oxygen flux at room temperature," *Microelectronic Engineering*, vol. 141, pp. 207–210, 2015.

[53] B. Geier, C. Gspan, R. Winkler, R. Schmied, J. D. Fowlkes, H. Fitzek, S. Rauch, J. Rattenberger, P. D. Rack, and H. Plank, "Rapid and highly compact purification for focused electron beam induced deposits: a low temperature approach using electron stimulated h2o reactions," *The Journal of Physical Chemistry C*, vol. 118, no. 25, pp. 14009–14016, 2014.

[54] N. A. Roberts, J. D. Fowlkes, G. A. Magel, and P. D. Rack, "Enhanced material purity and resolution via synchronized laser assisted electron beam induced deposition of platinum," *Nanoscale*, vol. 5, no. 1, pp. 408–415, 2013.

[55] M. G. Stanford, B. B. Lewis, J. H. Noh, J. D. Fowlkes, N. A. Roberts, H. Plank, and P. D. Rack, "Purification of nanoscale electron-beam-induced platinum deposits via a pulsed laser-induced oxidation reaction," *ACS applied materials & interfaces*, vol. 6, no. 23, pp. 21256–21263, 2014.

[56] E. Villamor, F. Casanova, P. Trompenaars, and J. Mulders, "Embedded purification for electron beam induced pt deposition using mecpptme3," *Nanotechnology*, vol. 26, no. 9, p. 095303, 2015.

[57] M. M. Shawrav, P. Taus, H. D. Wanzenboeck, M. Schinnerl, M. Stöger-Pollach, S. Schwarz, A. Steiger-Thirsfeld, and E. Bertagnolli, "Highly conductive and pure gold nanostructures grown by electron beam induced deposition," *Scientific reports*, vol. 6, p. 34003, 2016.

[58] M. Prestigiacomo, F. Bedu, F. Jandard, D. Tonneau, H. Dallaporta, L. Roussel, and P. Sudraud, "Purification and crystallization of tungsten wires fabricated by focused-ion-beam-induced deposition," *Applied Physics Letters*, vol. 86, no. 19, p. 192112, 2005.

[59] T. Lukasczyk, M. Schirmer, H.-P. Steinrück, and H. Marbach, "Electron-beam-induced deposition in ultrahigh vacuum: lithographic fabrication of clean iron nanostructures," *Small*, vol. 4, no. 6, pp. 841–846, 2008.

[60] J.-H. Noh, M. G. Stanford, B. B. Lewis, J. D. Fowlkes, H. Plank, and P. Rack, "Nanoscale electron beam-induced deposition and purification of ruthenium for extreme ultraviolet lithography mask repair," *Applied Physics A*, vol. 117, no. 4, pp. 1705–1713, 2014.

[61] E. Begun, O. V. Dobrovolskiy, M. Kompaniiets, R. Sachser, C. Gspan, H. Plank, and M. Huth, "Post-growth purification of co nanostructures prepared by focused electron beam induced deposition," *Nanotechnology*, vol. 26, no. 7, p. 075301, 2015.

[62] R. Garcia, A. W. Knoll, and E. Riedo, "Advanced scanning probe lithography," *Nature nanotechnology*, vol. 9, no. 8, p. 577, 2014.

[63] Z. Durrani, M. Jones, M. Kaestner, M. Hofer, E. Guliyev, A. Ahmad, T. Ivanov, J.-P. Zoellner, and I. W. Rangelow, "Scanning probe lithography approach for beyond cmos devices," in *Alternative Lithographic Technologies V*, vol. 8680, p. 868017, International Society for Optics and Photonics, 2013.

[64] B. E. Maile, W. Henschel, H. Kurz, B. Rienks, R. Polman, and P. Kaars, "Sub-10 nm linewidth and overlay performance achieved with a fine-tuned ebpg-5000 tfe electron beam lithography system," *Japanese Journal of Applied Physics*, vol. 39, no. 12S, p. 6836, 2000.

[65] V. R. Manfrinato, A. Stein, L. Zhang, C.-Y. Nam, K. G. Yager, E. A. Stach, and C. T. Black, "Aberration-corrected electron beam lithography at the one nanometer length scale," *Nano letters*, vol. 17, no. 8, pp. 4562–4567, 2017.

[66] S. Barcelo and Z. Li, "Nanoimprint lithography for nanodevice fabrication," *Nano convergence*, vol. 3, no. 1, p. 21, 2016.

[67] M. C. Traub, W. Longsine, and V. N. Truskett, "Advances in nanoimprint lithography," *Annual review of chemical and biomolecular engineering*, vol. 7, pp. 583–604, 2016.

[68] C. Wang, M. E. Jones, and Z. A. K. Durrani, "Single-electron and quantum confinement limits in length-scaled silicon nanowires," *Nanotechnology*, vol. 26, no. 30, p. 305203, 2015.

[69] T. Brintlinger, M. Fuhrer, J. Melngailis, I. Utke, T. Bret, A. Perentes, P. Hoffmann, M. Abourida, and P. Doppelt, "Electrodes for carbon nanotube devices by focused electron beam induced deposition of gold," *Journal of Vacuum Science & Technology B: Microelectronics and Nanometer Structures Processing, Measurement, and Phenomena*, vol. 23, no. 6, pp. 3174–3177, 2005.

[70] M. Croitoru, G. Bertsche, D. Kern, C. Burkhardt, S. Bauerdick, S. Şahakalkan, and S. Roth, "Visualization and in situ contacting of carbon nanotubes in a scanning electron microscope," *Journal of Vacuum Science & Technology B: Microelectronics and Nanometer Structures Processing, Measurement, and Phenomena*, vol. 23, no. 6, pp. 2789–2792, 2005.

[71] H. Steinberg, Y. Lilach, A. Salant, O. Wolf, A. Faust, O. Millo, and U. Banin, "Anomalous temperature dependent transport through single colloidal nanorods strongly coupled to metallic leads," *Nano letters*, vol. 9, no. 11, pp. 3671–3675, 2009.

[72] A. Persano, B. Nabet, A. Taurino, P. Prete, N. Lovergine, and A. Cola, "Polarization anisotropy of individual core/shell gaas/algaas nanowires by photocurrent spectroscopy," *Applied Physics Letters*, vol. 98, no. 15, p. 153106, 2011.

[73] T. Schwamb, B. R. Burg, N. C. Schirmer, and D. Poulikakos, "On the effect of the electrical contact resistance in nanodevices," *Applied physics letters*, vol. 92, no. 24, p. 243106, 2008.

[74] F. Wakaya, Y. Tsukatani, N. Yamasaki, K. Murakami, S. Abo, and M. Takai, "Transport properties of beam-deposited pt nanowires," in *Journal of Physics: Conference Series*, vol. 38, p. 120, IOP Publishing, 2006.

[75] D. Spoddig, K. Schindler, P. Rödiger, J. Barzola-Quiquia, K. Fritsch, H. Mulders, and P. Esquinazi, "Transport properties and growth parameters of pdc and wc nanowires prepared in a dual-beam microscope," *Nanotechnology*, vol. 18, no. 49, p. 495202, 2007.

[76] L. Dong, F. Arai, M. Nakajima, P. Liu, and T. Fukuda, "Nanotube devices fabricated in a nano laboratory," in *2003 IEEE International Conference on Robotics and Automation (Cat. No. 03CH37422)*, vol. 3, pp. 3624–3629, IEEE, 2003.

[77] E. Sadki, S. Ooi, and K. Hirata, "Focused-ion-beam-induced deposition of superconducting nanowires," *Applied Physics Letters*, vol. 85, no. 25, pp. 6206–6208, 2004.

[78] A. Fernández-Pacheco, L. Serrano-Ramón, J. M. Michalik, M. R. Ibarra, J. M. De Teresa, L. O'brien, D. Petit, J. Lee, and R. P. Cowburn, "Three dimensional magnetic nanowires grown by focused electron-beam induced deposition," *Scientific reports*, vol. 3, p. 1492, 2013.

[79] S. Frabboni, G. Gazzadi, L. Felisari, and A. Spessot, "Fabrication by electron beam induced deposition and transmission electron microscopic characterization of sub-10-nm freestanding pt nanowires," *Applied physics letters*, vol. 88, no. 21, p. 213116, 2006.

[80] K. Klein, S. Randolph, J. Fowlkes, L. Allard, H. Meyer Iii, M. Simpson, and P. Rack, "Single-crystal nanowires grown via electron-beam-induced deposition," *Nanotechnology*, vol. 19, no. 34, p. 345705, 2008.

[81] W. Jarupoonphol, C. Ochiai, M. Takai, A. Hosono, and S. Okuda, "Prototyping of field emitter array using focused ion and electron beams," *Japanese journal of applied physics*, vol. 41, no. 6S, p. 4311, 2002.

[82] K. Murakami, W. Jarupoonphol, K. Sakata, and M. Takai, "Fabrication of nano electron source using beam-assisted process," *Japanese journal of applied physics*, vol. 42, no. 6S, p. 4037, 2003.

[83] C. Schößler, A. Kaya, J. Kretz, M. Weber, and H. Koops, "Electrical and field emission properties of nanocrystalline materials fabricated by electron-beam induced deposition," *Microelectronic engineering*, vol. 30, no. 1-4, pp. 471–474, 1996.

[84] X. Yang, M. Simpson, S. Randolph, P. Rack, L. Baylor, H. Cui, and W. Gardner, "Integrated tungsten nanofiber field emission cathodes selectively grown by nanoscale electron beam-induced deposition," *Applied Physics Letters*, vol. 86, no. 18, p. 183106, 2005.

[85] R. Kox, C. Chen, G. Maes, L. Lagae, and G. Borghs, "Shrinking solid-state nanopores using electron-beam-induced deposition," *Nanotechnology*, vol. 20, no. 11, p. 115302, 2009.

[86] Y. Lau, P. Chee, J. Thong, and V. Ng, "Properties and applications of cobalt-based material produced by electron-beam-induced deposition," *Journal of Vacuum Science & Technology A: Vacuum, Surfaces, and Films*, vol. 20, no. 4, pp. 1295–1302, 2002.

[87] T. Mukawa, S. Okada, R. Kobayashi, J.-i. Fujita, M. Ishida, T. Ichihashi, Y. Ochiai, T. Kaito, and S. Matsui, "Position-controlled carbon fiber growth catalyzed using electron beam-induced chemical vapor deposition ferrocene nanopillars," *Japanese journal of applied physics*, vol. 44, no. 7S, p. 5639, 2005.

[88] T. Liang, E. Frendberg, B. Lieberman, and A. Stivers, "Advanced photolithographic mask repair using electron beams," *Journal of Vacuum Science & Technology B: Microelectronics and Nanometer Structures Processing, Measurement, and Phenomena*, vol. 23, no. 6, pp. 3101–3105, 2005.

[89] J. De Teresa, A. Fernández-Pacheco, R. Córdoba, L. Serrano-Ramón, S. Sangiao, and M. R. Ibarra, "Review of magnetic nanostructures grown by focused electron beam induced deposition (febid)," *Journal of Physics D: Applied Physics*, vol. 49, no. 24, p. 243003, 2016.

[90] L. Keller, M. K. Al Mamoori, J. Pieper, C. Gspan, I. Stockem, C. Schröder, S. Barth, R. Winkler, H. Plank, M. Pohlit, *et al.*, "Direct-write of free-form building blocks for artificial magnetic 3d lattices," *Scientific reports*, vol. 8, no. 1, p. 6160, 2018.

[91] B. B. Lewis, R. Winkler, X. Sang, P. R. Pudasaini, M. G. Stanford, H. Plank, R. R. Unocic, J. D. Fowlkes, and P. D. Rack, "3d nanoprinting via laser-assisted electron beam induced deposition: growth kinetics, enhanced purity, and electrical resistivity," *Beilstein journal of nanotechnology*, vol. 8, no. 1, pp. 801–812, 2017.

[92] R. Winkler, B. B. Lewis, J. D. Fowlkes, P. D. Rack, and H. Plank, "High-fidelity 3d-nanoprinting via focused electron beams: Growth fundamentals," *ACS Applied Nano Materials*, vol. 1, no. 3, pp. 1014–1027, 2018.

[93] K. Höflich, R. B. Yang, A. Berger, G. Leuchs, and S. Christiansen, "The direct writing of plasmonic gold nanostructures by electron-beam-induced deposition," *Advanced materials*, vol. 23, no. 22-23, pp. 2657–2661, 2011.

[94] A. Perentes, A. Bachmann, M. Leutenegger, I. Utke, C. Sandu, and P. Hoffmann, "Focused electron beam induced deposition of a periodic transparent nano-optic pattern," *Microelectronic engineering*, vol. 73, pp. 412–416, 2004.

[95] K. a. Kanaya and S. Okayama, "Penetration and energy-loss theory of electrons in solid targets," *Journal of Physics D: Applied Physics*, vol. 5, no. 1, p. 43, 1972.

[96] Z. A. K. Durrani, *Single-electron devices and circuits in silicon*. World Scientific, 2010.

[97] Z. A. Durrani, M. E. Jones, C. Wang, D. Liu, and J. Griffiths, "Excited states and quantum confinement in room temperature few nanometre scale silicon single electron transistors," *Nanotechnology*, vol. 28, no. 12, p. 125208, 2017.

[98] G. Di Prima, R. Sachser, P. Trompenaars, H. Mulders, and M. Huth, "Direct-write single electron transistors by focused electron beam induced deposition," *Nano Futures*, vol. 3, no. 2, p. 025001, 2019.

[99] S. Hari, *High resolution resist-free lithography in the SEM*. PhD thesis, Delft University of Technology, 2017.

[100] E. Meyer, "Atomic force microscopy," *Progress in surface science*, vol. 41, no. 1, pp. 3–49, 1992.

[101] W. R. (NIH). `https://imagej.nih.gov/ij/`.

[102] D. Morecroft, J. K. Yang, S. Schuster, K. K. Berggren, Q. Xia, W. Wu, and R. S. Williams, "Sub-15 nm nanoimprint molds and pattern transfer," *Journal of Vacuum Science & Technology B: Microelectronics and Nanometer Structures Processing, Measurement, and Phenomena*, vol. 27, no. 6, pp. 2837–2840, 2009.

[103] Y. Guan, J. D. Fowlkes, S. T. Retterer, M. L. Simpson, and P. D. Rack, "Nanoscale lithography via electron beam induced deposition.," *Nanotechnology*, vol. 19, p. 505302, dec 2008.

[104] A. Notargiacomo, E. Giovine, and L. Di Gaspare, "Ion and electron beam deposited masks for pattern transfer by reactive ion etching," *Microelectronic Engineering*, vol. 88, pp. 2710–2713, aug 2011.

[105] C. Heerkens, M. Kamerbeek, W. van Dorp, C. Hagen, and J. Hoekstra, "Electron beam induced deposited etch masks," *Microelectronic Engineering*, vol. 86, pp. 961–964, apr 2009.

[106] A. Weber-Bargioni, A. Schwartzberg, M. Schmidt, B. Harteneck, D. F. Ogletree, P. J. Schuck, and S. Cabrini, "Functional plasmonic antenna scanning probes fabricated by induced-deposition mask lithography," *Nanotechnology*, vol. 21, no. 6, p. 65306, 2010.

[107] M. Fleischer, A. Weber-Bargioni, S. Cabrini, and D. Kern, "Fabrication of metallic nanocones by induced deposition of etch masks and ion milling," *Microelectronic Engineering*, vol. 88, pp. 2247–2250, aug 2011.

[108] I. Weppelman, P. Post, C. Heerkens, C. Hagen, and J. Hoogenboom, "Fabrication of narrow-gap nanostructures using electron-beam induced deposition etch masks," *Microelectronic Engineering*, vol. 153, pp. 77–82, 2016.

[109] A. L. Goodyear, S. Mackenzie, D. L. Olynick, and E. H. Anderson, "High resolution inductively coupled plasma etching of 30 nm lines and spaces in tungsten and silicon," *Journal of Vacuum Science & Technology B: Microelectronics and Nanometer Structures*, vol. 18, no. 6, p. 3471, 2000.

[110] A. Kossam, C. Meadowcroft, C. A. T. Salama, and P. Ratnam, "Characterization of BCI3-CI2 Silicon Trench Etching," *Journal of The Electrochemical Society*, vol. 137, no. 5, pp. 5–9, 1990.

[111] D. L. Flamm, "Mechanisms of silicon etching in fluorine- and chlorine-containing plasmas," *Pure and Applied Chemistry*, vol. 62, no. 9, pp. 1709–1720, 1990.

[112] S. Hari, C. W. Hagen, T. Verduin, and P. Kruit, "Size and shape control of sub-20 nm patterns fabricated using focused electron beam-induced

processing," *Journal of Micro/Nanolithography, MEMS, and MOEMS*, vol. 13, p. 033002, jul 2014.

[113] M. Mohri, H. Kakinuma, M. Sakamoto, and H. Sawai, "Plasma Etching of ITO Thin Films Using a CH 4 /H 2 Gas Mixture," *Japanese Journal of Applied Physics*, vol. 29, no. Part 2, No. 10, pp. L1932–L1935, 1990.

[114] D. Kim, J. Ko, M. Park, and N.-E. Lee, "Infinitely high etch selectivity during CH4/H2/Ar inductively coupled plasma (ICP) etching of indium tin oxide (ITO) with photoresist mask," *Thin Solid Films*, vol. 516, pp. 3512–3516, apr 2008.

[115] H. B. Andagana and X. A. Cao, "Fast and smooth etching of indium tin oxides in BCl3/Cl2 inductively coupled plasmas," *Journal of Vacuum Science & Technology A: Vacuum, Surfaces, and Films*, vol. 28, no. 2, p. 189, 2010.

[116] A. Mackus, J. Mulders, M. Van De Sanden, and W. Kessels, "Local deposition of high-purity pt nanostructures by combining electron beam induced deposition and atomic layer deposition," 2010.

[117] D. Shindo and T. Oikawa, "Energy dispersive x-ray spectroscopy," in *Analytical Electron Microscopy for Materials Science*, pp. 81–102, Springer, 2002.

[118] M. Cooke and A. Goodyear, "Development of plasma atomic layer etching in close-to-conventional etch tools," *ECS Transactions*, vol. 85, no. 6, pp. 71–76, 2018.

[119] V. Bakshi, *EUV lithography*, vol. 178. Spie Press, 2009.

[120] G. Brewer, *Electron-beam technology in microelectronic fabrication*. Elsevier, 2012.

[121] A. Broers, A. Hoole, and J. Ryan, "Electron beam lithography—resolution limits," *Microelectronic Engineering*, vol. 32, no. 1-4, pp. 131–142, 1996.

[122] R. Pease, "Electron beam lithography," *Contemporary Physics*, vol. 22, no. 3, pp. 265–290, 1981.

[123] A. A. Tseng, K. Chen, C. D. Chen, and K. J. Ma, "Electron beam lithography in nanoscale fabrication: recent development," *IEEE Transactions on electronics packaging manufacturing*, vol. 26, no. 2, pp. 141–149, 2003.

[124] H. Schift, "Nanoimprint lithography: an old story in modern times? a review," *Journal of Vacuum Science & Technology B: Microelectronics and Nanometer Structures Processing, Measurement, and Phenomena*, vol. 26, no. 2, pp. 458–480, 2008.

[125] E. A. Costner, M. W. Lin, W.-L. Jen, and C. G. Willson, "Nanoimprint lithography materials development for semiconductor device fabrication," *Annual Review of Materials Research*, vol. 39, pp. 155–180, 2009.

[126] M. Malloy and L. C. Litt, "Technology review and assessment of nanoimprint lithography for semiconductor and patterned media manufacturing," *Journal of Micro/Nanolithography, MEMS, and MOEMS*, vol. 10, no. 3, pp. 032001–032001, 2011.

[127] M. D. Austin, W. Zhang, H. Ge, D. Wasserman, S. A. Lyon, and S. Y. Chou, "6 nm half-pitch lines and 0.04 μm2 static random access memory patterns by nanoimprint lithography," *Nanotechnology*, vol. 16, no. 8, p. 1058, 2005.

[128] M. C. McAlpine, R. S. Friedman, and C. M. Lieber, "Nanoimprint lithography for hybrid plastic electronics," *Nano Letters*, vol. 3, no. 4, pp. 443–446, 2003.

[129] L. J. Guo, "Nanoimprint lithography: methods and material requirements," *Advanced materials*, vol. 19, no. 4, pp. 495–513, 2007.

[130] T. Mårtensson, P. Carlberg, M. Borgström, L. Montelius, W. Seifert, and L. Samuelson, "Nanowire arrays defined by nanoimprint lithography," *Nano Letters*, vol. 4, no. 4, pp. 699–702, 2004.

[131] G. Calafiore, A. Koshelev, S. Dhuey, S. Sassolini, M. Messerschmidt, A. Schleunitz, A. Goltsov, C. Piña-Hernandez, F. C. Pirri, V. Yankov, *et al.*, "Step-and-repeat nanoimprint on pre-spin coated film for the fabrication of integrated optical devices," *Journal of Micro/Nanolithography, MEMS, and MOEMS*, vol. 14, no. 3, pp. 033506–033506, 2015.

[132] S.-W. Ahn, K.-D. Lee, J.-S. Kim, S. H. Kim, J.-D. Park, S.-H. Lee, and P.-W. Yoon, "Fabrication of a 50 nm half-pitch wire grid polarizer using nanoimprint lithography," *Nanotechnology*, vol. 16, no. 9, p. 1874, 2005.

[133] S. H. Kim, K.-D. Lee, J.-Y. Kim, M.-K. Kwon, and S.-J. Park, "Fabrication of photonic crystal structures on light emitting diodes by nanoimprint lithography," *Nanotechnology*, vol. 18, no. 5, p. 055306, 2007.

[134] H. Schift, S. Park, B. Jung, C.-G. Choi, C.-S. Kee, S.-P. Han, K.-B. Yoon, and J. Gobrecht, "Fabrication of polymer photonic crystals using nanoimprint lithography," *Nanotechnology*, vol. 16, no. 5, p. S261, 2005.

[135] A. Cattoni, P. Ghenuche, A.-M. Haghiri-Gosnet, D. Decanini, J. Chen, J.-L. Pelouard, and S. Collin, "$\lambda 3/1000$ plasmonic nanocavities for biosensing fabricated by soft uv nanoimprint lithography," *Nano letters*, vol. 11, no. 9, pp. 3557–3563, 2011.

[136] S. Zankovych, T. Hoffmann, J. Seekamp, J. Bruch, and C. S. Torres, "Nanoimprint lithography: challenges and prospects," *Nanotechnology*, vol. 12, no. 2, p. 91, 2001.

[137] S. Y. Chou and P. R. Krauss, "Imprint lithography with sub-10 nm feature size and high throughput," *Microelectronic Engineering*, vol. 35, no. 1-4, pp. 237–240, 1997.

[138] G.-Y. Jung, E. Johnston-Halperin, W. Wu, Z. Yu, S.-Y. Wang, W. M. Tong, Z. Li, J. E. Green, B. A. Sheriff, A. Boukai, *et al.*, "Circuit fabrication at 17 nm half-pitch by nanoimprint lithography," *Nano Letters*, vol. 6, no. 3, pp. 351–354, 2006.

[139] G. Calafiore, S. Dhuey, S. Sassolini, N. Alayo, D. Gosselin, M. Vogler, D. Olynick, C. Peroz, and S. Cabrini, "Multilayer lift-off process for sub-15-nm patterning by step-and-repeat ultraviolet nanoimprint lithography," *Journal of Micro/Nanolithography, MEMS, and MOEMS*, vol. 13, no. 3, pp. 033013–033013, 2014.

[140] M. D. Austin, H. Ge, W. Wu, M. Li, Z. Yu, D. Wasserman, S. Lyon, and S. Y. Chou, "Fabrication of 5 nm linewidth and 14 nm pitch features by nanoimprint lithography," *Applied Physics Letters*, vol. 84, no. 26, pp. 5299–5301, 2004.

[141] C. Peroz, S. Dhuey, M. Cornet, M. Vogler, D. Olynick, and S. Cabrini, "Single digit nanofabrication by step-and-repeat nanoimprint lithography," *Nanotechnology*, vol. 23, no. 1, p. 015305, 2011.

[142] F. Hua, Y. Sun, A. Gaur, M. A. Meitl, L. Bilhaut, L. Rotkina, J. Wang, P. Geil, M. Shim, J. A. Rogers, *et al.*, "Polymer imprint lithography with molecular-scale resolution," *Nano letters*, vol. 4, no. 12, pp. 2467–2471, 2004.

[143] I. Maximov, E.-L. Sarwe, M. Beck, K. Deppert, M. Graczyk, M. Magnusson, and L. Montelius, "Fabrication of si-based nanoimprint stamps with sub-20 nm features," *Microelectronic Engineering*, vol. 61, pp. 449–454, 2002.

[144] K. Ansari, J. Van Kan, A. Bettiol, and F. Watt, "Fabrication of high aspect ratio 100 nm metallic stamps for nanoimprint lithography using proton beam writing," *Applied Physics Letters*, vol. 85, no. 3, pp. 476–478, 2004.

[145] K. Ansari, J. A. van Kan, A. A. Bettiol, and F. Watt, "Stamps for nanoimprint lithography fabricated by proton beam writing and nickel electroplating," *Journal of Micromechanics and Microengineering*, vol. 16, no. 10, p. 1967, 2006.

[146] Y. Zhao, E. Berenschot, M. De Boer, H. Jansen, N. Tas, J. Huskens, and M. Elwenspoek, "Fabrication of a silicon oxide stamp by edge lithography reinforced with silicon nitride for nanoimprint lithography," *Journal of Micromechanics and Microengineering*, vol. 18, no. 6, p. 064013, 2008.

[147] J. Sakamoto, T. Nishino, H. Kawata, M. Yasuda, and Y. Hirai, "High aspect ratio nano mold fabrication by advanced edge lithography without cvd," *Microelectronic Engineering*, vol. 88, no. 8, pp. 1992–1996, 2011.

[148] H.-W. Sun, J.-Q. Liu, D. Chen, and P. Gu, "Optimization and experimentation of nanoimprint lithography based on fib fabricated stamp," *Microelectronic Engineering*, vol. 82, no. 2, pp. 175–179, 2005.

[149] W. Dauksher, K. Nordquist, D. Mancini, D. Resnick, J. Baker, A. Hooper, A. Talin, T. Bailey, A. Lemonds, S. Sreenivasan, *et al.*, "Characterization of and imprint results using indium tin oxide-based step and flash imprint lithography templates," *Journal of Vacuum Science & Technology B: Microelectronics and Nanometer Structures Processing, Measurement, and Phenomena*, vol. 20, no. 6, pp. 2857–2861, 2002.

[150] S. Zankovych, T. Hoffmann, J. Seekamp, J. Bruch, and C. S. Torres, "Nanoimprint lithography: challenges and prospects," *Nanotechnology*, vol. 12, no. 2, p. 91, 2001.

[151] M. N. Polyanskiy, "Refractive index database." `https://refractiveindex.info`. Accessed on 2016-10-14.

[152] M. Van Bruggen, B. Van Someren, and P. Kruit, "Development of a multi-electron-beam source for sub-10 nm electron beam induced deposition," *Journal of Vacuum Science & Technology B: Microelectronics and Nanometer Structures Processing, Measurement, and Phenomena*, vol. 23, no. 6, pp. 2833–2839, 2005.

[153] B. Van Someren, M. Van Bruggen, Y. Zhang, C. Hagen, and P. Kruit, "Multi-beam electron source using mems electron optical components," in *Journal of Physics: Conference Series*, vol. 34, p. 1092, IOP Publishing, 2006.

[154] Y. Zhang, C. H. Heerkens, M. van Bruggen, and P. Kruit, "Integrated multi-electron-beam blanker array for sub-10-nm electron beam induced deposition," *Journal of Vacuum Science & Technology B: Microelectronics and Nanometer Structures Processing, Measurement, and Phenomena*, vol. 24, no. 6, pp. 2857–2860, 2006.

[155] Y. Ren and P. Kruit, "Transmission electron imaging in the delft multi-beam scanning electron microscope 1," *Journal of Vacuum Science & Technology B, Nanotechnology and Microelectronics: Materials, Processing, Measurement, and Phenomena*, vol. 34, no. 6, p. 06KF02, 2016.

[156] N. Instruments, "Labview." v. 13.0f2.

[157] A. Zonnevylle, R. Van Tol, N. Liv, A. Narvaez, A. Effting, P. Kruit, and J. Hoogenboom, "Integration of a high-na light microscope in a scanning electron microscope," *Journal of microscopy*, vol. 252, no. 1, pp. 58–70, 2013.

[158] Y. Zhang, *A 100-electron-beam source from a high brightness Schottky emitter for fast patterning applications*. PhD thesis, Delft University of Technology, 2008.

[159] M. J. Van Bruggen, *multi-electron beam system for high resolution electron beam induced deposition*. PhD thesis, Delft University of Technology, 2008.

[160] A. Mohammadi-Gheidari, *196 Beams in a Scanning Electron Microscope*. PhD thesis, Delft University of Technology, 2013.

[161] M. Bronsgeest, *Physics of Schottky electron sources*. PhD thesis, Delft University of Technology, 2009.

[162] P. Kruit, *Introduction to Charged Particle Optics*. TuDelft, 2015.

[163] J. Barth and P. Kruit, "Addition of different contributions to the charged particle probe size," *Optik*, vol. 101(3), 1996.

[164] M. MacNaughton, "The focal properties and spherical aberration constants of aperture electron lenses," *Proceedings of the Physical Society. Section B*, vol. 65, no. 8, p. 590, 1952.

[165] J. Orloff, *Handbook of charged particle optics*. CRC press, 2008.

[166] D. Tuggle and L. Swanson, "Emission characteristics of the zro/w thermal field electron source," *Journal of Vacuum Science & Technology B: Microelectronics Processing and Phenomena*, vol. 3, no. 1, pp. 220–223, 1985.

[167] S. (Brno), "Eod, electron optical design." v. E4.004.

[168] A. Zonnevylle, C. T. H. Heerkens, C. Hagen, and P. Kruit, "Multi-electron-beam deflector array," *Microelectronic Engineering*, vol. 123, pp. 140–148, 2014.

[169] I. COMSOL, "Comsol multiphysics." v. 5.2.

[170] A. C. Zonnevylle, *Individual beam control in multi electron beam systems*. PhD thesis, Delft University of Technology, 2017.

Curriculum Vitæ

Marijke Scotuzzi

01-02-1987	Born in Brescia, Italy.

Education

2006–2010	Information Engineering Brescia, Università degli studi di Brescia *Thesis:* Tomography in a Scanning Electron Microscope
2010–2013	Electronics Engineering Brescia, Università degli studi di Brescia *Thesis:* Design and fabrication of microdevices by Electron Beam Lithography
2013–2017	PhD. Applied Physics Delft University of Technology, Delft (2013–2017)

Work experience

2017–2018	Application engineer Phenom World B.V., Eindhoven (NL)
2018–Present	Patterning engineer ASML B.V., Eindhoven (NL)

Awards

2015	Best Presentation Award 2nd Single Nanometer Manufacturing Workshop

List of Publications

1. **M. Scotuzzi**, M. J. Kamerbeek, A. Goodyear, M. Cooke and C. W. Hagen, *Pattern transfer into silicon using sub-10 nm masks made by electron beam-induced deposition*, J. Micro/Nanolith. MEMS MOEMS 14(3), 031206 (Jul – Sep 2015).

2. **M. Scotuzzi**, J. Kuipers, D. I. Wensveen, P. de Boer, C. W. Hagen, J. P. Hoogenboom, B. N. G. Giepmans, *Multi-color electron microscopy by element-guided identification of cells, organelles and molecules*, Scientific Reports 7, Article number: 45970 (2017).

3. Z.A.K. Durrani, ME Jones, C Wang, **M. Scotuzzi**, C. W. Hagen, *Electron transport and room temperature single-electron charging in 10 nm scale PtC nanostructures formed by electron beam induced deposition*, Nanotechnology 28 (47), 474002.

4. R.J. Moerland, G. Weppelman, **M. Scotuzzi**, J.P. Hoogenboom, *Nanoscale imaging of light-matter coupling inside metal-coated cavities with a pulsed electron beam*, Nano Lett., 2018, 18 (10), pp 6107–6112.

5. P.D. Prewett, C.W. Hagen, C. Lenk, S. Lenk, M. Kaestner, T. Ivanov, A. Ahmad, I.W. Rangelow, X. Shi, S.A. Boden, A.P.G. Robinson, D. Yang, S. Hari, **M. Scotuzzi**, E. Huq, *Charged particle single nanometre manufacturing*, Beilstein journal of nanotechnology 9 (1), 2855-2882

Acknowledgements

First and foremost, I would like to express my deepest gratitude to Pieter, not only for welcoming me in the Charged Particle Optics group, but also for guiding me and offering me insights throughout my PhD. His immense knowledge in Physics and unwavering enthusiasm for research kept me motivated and engaged to my project.

I would like to sincerely thank Kees for his constant lively interest and daily support during these four years, for keeping me abreast of the scientific developments and for his unceasing encouragement. Thank you for giving me the chance to pursue this journey and being the compass all the way, for our endless discussions and for being the source of wisdom a PhD needs. Above all, thanks for being the person I could turn to during moments of despair.

One does not fully enjoy the PhD without fun projects to work on and Jacob definitely hit the mark when he asked me to join the Multi-color EM project. Thank you not only for introducing me to the world of cellular biology and giving me the chance to work with many people in this field, but also for your support when I needed it and all the pleasant discussions during the 11 o'clock coffee break.

Despite the struggles, the hard work, the tight deadlines, the office was the place where I could find support and moments of pure fun. Sangeetha, you are the first person I met during my interview in Delft and I was immediately impressed by your sharp intelligence and your sweet kindness. Thank you for being my rock, my source of strength and, above all, my shopping-mate. Thanks for bringing a lovely flavor of India in my daily life. Talking about hilarious moments, there is only one person I can think of: Gerward. You have been a guidance for me, your interest in Science and research is so broad, and you are such a fun person to be around. I have admired you for all the difficult decisions you took, it demonstrated your maturity and wisdom which you childishly try to hide. The picture is far from complete if I do not mention Robert. Thank you for your encouragement, support and guidance. Your experience and wisdom

have shaped you into an anchor of my journey. I will never forget the long afternoons behind the microscope fine-tuning milling recipes, fighting all sorts of technical problems that seemed to persecute this experiment.

The work described in this thesis could not have been done without Martin. He was not just a simple technician, he taught me how to tackle engineering problems in a scientific way and he introduced me to the cleanroom magic. To me, you are a living encyclopedia of microfabrication processes, thanks for teaching me so much and giving me the help I needed to complete this PhD. But more than anything, thanks for making Fridays the funnier day of the week and Bristol the best business trip of all.

Supervising students has proved to be a valuable experience, during which I learned not only to help other people develop, but also spread my passion for science and research. Dasha was my first student, but soon became a trusted friend. I was always impressed by her brilliant mind, her simplicity and her kindness. I loved our Saturdays and Sundays sitting behind the microscope, running endless analyses, while enjoying a movie on Netflix or chitchatting about everything.

The list of people I would like to express my gratitude to is still long. Thanks to Nalan and Angela, the senior PhDs who have paved my way and given me the most useful tips and tricks to survive the PhD. Yan, your humble intelligence and your inclination to helping others have always inspired me. Thank you for your patient help in teaching me how to operate the multi beam SEM, and also for being a fun colleague to spend time with. Thomas, I joined CPO shortly after you did, but you have always been miles ahead. Your true passion for Computer Science and Physics make you a special researcher. I will never forget how fast you could type on your keyboard. Shammi, your politeness and kindness are unique. It was fun to share with you the disgrace of being the first test samples of the graduate school, the courses and all obligations it brought along. Thanks to all the colleagues who made life in CPO remarkable, Ali, Takashi, Minoru, Sebastiaan, Leon, Jason, Dusan, Christiaan, Wilco, Aditi, Kerim, Maurice, Annemarie, Connie and Neda. Gaudham, thanks for being my nerd-buddy, for sharing the passion for The Force and, above all, for being my guide during my Indian trip. Thanks to all people that I have met shortly, but in some way helped me out, Aya and Laura. Thanks to the students who have contributed to this work, Siebe and Niels.

In experimental physics research, the role of technicians is crucial. Their help in their field of expertise is essential to bridge the gap and realize the experimental set-ups that are vital for achieving the goals. In CPO, we could all rely on a team of valuable technicians, who were undoubtedly helpful. Thank you Frans for helping me with the integration of the MBSEM control electronics; Ruud, for the mechanical design and drawings of the MBU; Han, for everything that requires an oscilloscope; Carel, for the expertise in the cleanroom processes; Paul, for the LabView heads-up; Dustin, for his extensive knowledge about FEI microscopes. A special note of gratitude to Jan de Looff, who was always there to help me whenever I needed it, with his kindness and his funny stories. Thanks to Anjella, for making all the bureaucracy much simpler and for your sweet smile. Thanks to Margaret, for arranging the business trips, listening to our curious wish-lists (mainly mine and Sangeetha's) and making our plans come true.

I am very grateful to Prof. Matteo Ferroni and dr. Caterina Soldano, who supervised me during my MSc thesis at University of Brescia. Thanks for introducing me to the world of electron microscopy and nanofabricaiton and encouraging me to jump into this adventure. A thankful thought also to all staff members of Sensor Lab, in particular to Prof. Elisabetta Comini and dr. Dario Zappa.

For sure, I would not be here defending my PhD if it was not for the constant support and encouragement of my parents. Mom, you are my role model. I have always looked up to you and your strength, and I can only hope that I have managed to make you proud. You taught me that success comes when you start believing in your own capabilities and that life is nicer when you smile at it. You could not have been more right, but it was not an easy journey and I could not have done it without your support, our calls and our messages. Thank you for inspiring me to dream big. Papa, from you I have learned to work hard and to keep going, no matter what, without giving up. You taught me to be committed, engaged and responsible for all the new tasks I take in and together with Mom's advice I jumped into this new experience with enthusiasm and commitment, willing to work and learn. Igor, your strength and maturity have always been a source of inspiration, I am sure you would have kept calm during moments of despair that crept up on me! Denise and Desiree, you are the brightest stars in the sky, I know you will shine even brighter in the future, and I can only hope

that my journey can be an inspiration to you. Marlies, Giuliano and Jessica, you are my second family. Thanks for your encouragements, your help and all the happy moments we have lived togheter. I'd like to express my deepest gratitude to my best friends, Elisa and Francesca. Thanks for being there when I needed you the most, for listening and advising me. Ours is a special bond that distance only made stronger. Thanks also to all my friends from university, Marco B., Andrea, Marco G., Filippo, Bruno, Marco P, Pietro, Matteo, Annamaria, Angela. Loredana and Cristian, we worked together to help others and, yes, also save people's life. During those years I have learnt a lot, you taught me to be strong and how to cope with the toughest situations one could possibly run into. And, on top of it, you became trusted friends. Thank you.

Last, but not least, I would like to express my deepest gratitude to Nicola. You are my rock, my shoulder to lean on, my best friend and my person. You helped me find confidence and ambition, and above all, strive for balance. Thank you for giving me the freedom to explore, for reassuring me in the difficult moments and for encouraging me to improve. I hope we can continue growing together and make each other the better people we can be.